

Copyright  
by  
Grant Thomas Offord  
2013

**The Dissertation Committee for Grant Thomas Offord Certifies that this is the approved version of the following dissertation:**

**Multilayered Membranes for Modified Atmosphere Packaging**

**Committee:**

---

Donald R. Paul, Co-Supervisor

---

Benny D. Freeman, Co-Supervisor

---

Isaac C. Sanchez

---

Christopher J. Ellison

---

Desiderio Kovar

**Multilayered Membranes for Modified Atmosphere Packaging**

**by**

**Grant Thomas Offord, B.S.; M.S.E.**

**Dissertation**

Presented to the Faculty of the Graduate School of

The University of Texas at Austin

in Partial Fulfillment

of the Requirements

for the Degree of

**Doctor of Philosophy**

**The University of Texas at Austin**

**May 2013**

## Acknowledgements

I have read a number of dissertation acknowledgements sections. I mention this because I'd like to save the space where I say this was a hard thing to do, and that I was the reason it was hard. I am not unique.

I stand here at the end today because I learned a few things being immersed in this process. One watches colleagues make presentations, hears them discuss science, and sees them make mistakes. I certainly made mine. The successful conclusion of this process marks my greatest achievement to this point, and I am proud that I made it through.

I'll paraphrase Dr. Freeman on two related ideas: the most important thing is to be kind, and achievements are never diminished by giving credit. Hopefully, my shortcomings in the first area can be rectified by effusive praise in these acknowledgements. My advisers, Professors Don Paul and Benny Freeman, have been indispensable resources during my Ph.D. studies. They provided me with research funding, access to well-equipped labs, opportunities for travel and collaboration, and guidance in my studies as well as in life. In some ways, Dr. Paul has served as the "how" and Dr. Freeman as the "why." They have also displayed otherworldly patience with me during my studies. I would like to believe that their patience in the first several years has been rewarded by the achievements of the last. Their personal assistants, Susan Chapman and Carol Assadourian, were also extraordinarily helpful.

The encouragement of several of my undergraduate advisers was integral to my development as a student and as an engineer. I am grateful for perspective from Professors Arland Johannes, Rob Whiteley, Randy Lewis, Khaled Gasem, and Karen

High. Dr. High in particular showed me that graduate studies were not out of reach, and for that, I am indebted to her.

My research collaborators at Case Western Reserve University also deserve mention, because without their help and novel capabilities, this dissertation would not have been possible. Shannon Armstrong spent long hours extruding polymer films for this project, for which I am thankful. Professors Eric Baer and the late Anne Hiltner are congratulated for their helpful research advice. Dr. Steve Swinnea of the Texas Materials Institute also proved a valuable collaborator in the characterization of semicrystalline polymers. This work was supported by the U.S. National Science Foundation (Grant DMR-0423914) as part of the Center for Layered Polymeric Systems (CLiPS).

The remaining members of my committee also deserve credit for participating in this process. Professors Isaac Sanchez, Christopher Ellison, and Desiderio Kovar are greatly appreciated.

I would also like to acknowledge the contributions of several members of my research group and other colleagues who entered graduate school with me. Fellow CLiPS colleagues Dan Miller, Dr. Tom Murphy, and Kevin “kT” Tung have celebrated victories, commiserated over failures, and have generally been fixtures in my life. Dr. J. Adam Stephens was a constant companion and a sterling exemplar of graceful aging. Dr. Scott Owens encouraged me to improve myself through his consistent, affectionate disapproval.

Senior members of the research group played important roles in my scientific and personal development. Dr. Hua “Richard” Li, Dr. Claudio Ribeiro, Dr. Kristofer Gleason, and Dr. Victor Kusuma proved invaluable to my understanding of my materials and our labs. Dr. Brandon Rowe was equally invaluable in those regards, but also clued me in to the value of “networking.” Dr. Norman Horn taught me something new every day I spent

with him, and he is the closest thing to a polymath this department has ever seen. David Sanders<sup>†</sup> has taught me the value of economy.

Other members of the group have left a lasting impression on me. Sirirat “Peach” Kasemset always brightened my days with her infectious enthusiasm. Hee Jeung Oh is a master of plausibly deniable humor. Zachary “Zack” Smith and Dr. Geoffrey Geise gave me years of guilt-fueled motivation. Zhengwang “Lisa” He and Ni Yan engaged me in many conversations about China and the English language. Maj. Corey James inspired me with his great dedication. Katrina Czenkusch was a good friend, a better person, and a participant in many of the best conversations I have had these last several years.

On a final personal note, I would like to acknowledge my family for their love, support, and patience during this long process. Their pride in my educational attainment has been a source of great motivation. I am grateful for my father Spencer, my mother Suzi, my brother Paul, my cousin Jeff, and both of my grandparents. They may all now safely call me an egghead.

---

<sup>†</sup>David is technically a junior student, but he began his undergraduate research in Dr. Freeman’s lab before I arrived. What is meant by “economy” here is that he is the most consistent critic of the way I phrase my ideas, and I thought I might offend his sensibilities by explaining this fully in the main text.

# **Multilayered Membranes for Modified Atmosphere Packaging**

Grant Thomas Offord, Ph.D.

The University of Texas at Austin, 2013

Co-Supervisors: Donald R. Paul, Benny D. Freeman

This dissertation discusses, in brief, the production and transport property characterization of films made from the extrusion and biaxial stretching of  $\beta$  nucleated isotactic polypropylene and the extrusion of PEBAX block copolymers. Multilayered films for modified atmosphere packaging applications were also produced by coextrusion and biaxial stretching of these two materials and similarly characterized. Current membranes for packaging applications are generally produced by coating a porous support with a polymeric solution to deposit an active layer for separation. The goal of this project is to displace membranes produced by solvent-based processes, which are environmentally hazardous and thus costly, with equivalent or superior materials produced using melt extrusion.

## Table of Contents

List of Tables .....	xii
List of Figures .....	xiii
Chapter 1. Introduction .....	1
1.1 Dissertation Goals .....	1
1.2 Dissertation Organization .....	1
Chapter 2. Background and Theory .....	4
2.1 Porous and Composite Membranes by Extrusion .....	4
2.1.1 Porous Membrane Applications .....	4
2.1.2 Isotropic Membranes .....	5
2.1.3 Composite Membranes .....	7
2.2 Crystallinity in Polymorphic iPP .....	8
2.3 Gas Permeability in Membranes .....	10
2.3.1 Porous Membranes .....	10
2.3.2 Dense Film Polymeric Membranes .....	11
2.4 Polymers Exhibiting High CO <sub>2</sub> Solubility .....	12
2.4.1 Material Properties of Polymers with Affinity for CO <sub>2</sub> .....	12
2.4.2 Design of Polymers with Affinity for CO <sub>2</sub> .....	13
2.5 Multilayered Coextrusion .....	15
2.6 Multilayered Membranes for Modified Atmosphere Packaging .....	16
2.6.1 Produce Preservation .....	16
2.6.2 Materials for MAP .....	17
2.6.3 MAP Membranes by Coextrusion .....	19
2.7 References .....	20
Chapter 3. Materials and Experimental Methods .....	29
3.1 Introduction .....	29
3.2 Extruded $\beta$ -iPP Precursor and Stretched Films .....	29
3.2.1 Materials Selection .....	29

3.2.2	Film Preparation.....	30
3.2.3	Differential Scanning Calorimetry (DSC) .....	33
3.2.4	X-Ray Diffraction (XRD) .....	34
3.2.5	Film Thickness Determination.....	35
3.2.6	Film Density and Porosity Determination .....	35
3.2.7	Scanning Electron Microscopy (SEM) .....	36
3.2.8	Capillary Flow Porometry (CFP).....	36
3.2.9	Gas Permeability.....	37
3.3	Extruded PEBAX Single Layer Films .....	39
3.3.1	Materials Selection.....	39
3.3.2	Film Preparation.....	41
3.3.3	Elemental Analysis .....	42
3.3.4	Differential Scanning Calorimetry (DSC) .....	42
3.3.5	Film Thickness Determination.....	43
3.3.6	Gas Permeability.....	43
3.4	Coextruded Multilayered $\beta$ -iPP/PEBAX Films .....	45
3.4.1	Materials Selection.....	45
3.4.2	Film Preparation.....	45
3.4.3	Film Thickness Determination.....	47
3.4.4	Scanning Electron Microscopy (SEM) .....	48
3.4.5	Gas Permeability.....	48
3.4.6	Modeling of MAP Performance.....	48
3.5	References.....	49
Chapter 4. Porosity Enhancement in $\beta$ Nucleated Isotactic Polypropylene		
	Stretched Films by Thermal Annealing .....	53
4.1	Summary .....	53
4.2	Results and Discussion .....	54
4.2.1	$\beta$ -Crystallinity in Precursor and Stretched iPP Films .....	54
4.2.2	Pore Formation by Stretching in $\beta$ -iPP Films .....	71
4.3	References.....	83

Chapter 5. Influence of Processing Strategies on Porosity and Permeability of $\beta$ Nucleated Isotactic Polypropylene Stretched Films .....	87
5.1 Summary .....	87
5.2 Results and Discussion .....	88
5.2.1 The Effect of Thermal Annealing on Porosity and Gas Permeability of Stretched $\beta$ -iPP Films.....	88
5.2.2 The Effect of Stretching Temperature on the Porosity of Stretched $\beta$ -iPP Films .....	94
5.2.3 Influence of Processing on the Porosity, Permeability and Separation Properties of Stretched $\beta$ -iPP Films.....	100
5.2.4 Pore Size Distribution and its Influence on the Permeation Properties of Stretched $\beta$ -iPP Films.....	111
5.3 References.....	119
Chapter 6. Transport Properties of PEBAX Copolymers and their use in Multilayered Membranes for Modified Atmosphere Packaging .....	122
6.1 Summary .....	122
6.2 Results and Discussion .....	123
6.2.1 Basic Characterization of PEBAX Copolymers .....	123
6.2.2 Permeability of Single Layer PEBAX Films .....	126
6.2.3 Prediction of Parameters for PEBAX Films for MAP.....	133
6.2.4 Multilayered $\beta$ -iPP/PEBAX Films for MAP Applications.....	142
6.3 References.....	155
Chapter 7. Conclusions and Recommendations.....	158
7.1 Conclusions.....	158
7.1.1 Porosity of Thermally Annealed $\beta$ -iPP Films.....	158
7.1.2 Factors Influencing Permeability of $\beta$ -iPP Films.....	159
7.1.3 Production and Characterization of Multilayered Membranes for Modified Atmosphere Packaging (MAP) .....	160
7.2 Recommendations for Future Studies.....	161
7.2.1 Improved Crystallinity for Pore Formation in $\beta$ -iPP .....	161
7.2.2 Microporous $\beta$ -iPP Films for Liquid Separations.....	162
7.2.3 Pore Formation of $\beta$ -iPP in Confined Environments.....	162

7.2.4 Optimized Multilayered Membranes for MAP Applications ...	164
7.2.5 Coextruded Membranes with Porous Supports.....	165
7.3 References.....	168
Bibliography .....	170
Vita.....	186

## List of Tables

Table 3.1.	Structure and property data for materials used to produce $\beta$ -iPP films. ....	30
Table 3.2.	Selected Characteristics of $\beta$ -iPP Precursor Films. ....	32
Table 3.3.	Structure of PEBAX copolymers and constituent blocks. ....	40
Table 3.4.	Selected characteristics of PEBAX copolymers. ....	41
Table 4.1.	Selected Crystalline Properties of $\beta$ -iPP Precursor Films Determined by DSC. ....	54
Table 4.2.	Selected Properties of $\beta$ -iPP Precursor Films Determined by X-Ray Diffraction. ....	61
Table 4.3.	Porosity and Permeability Characterization of Films Biaxially Stretched at 100 °C After Differing Thermal Annealing Treatments. ....	77
Table 5.1.	Porosity and Permeability Characterization of Biaxially Stretched Films Subjected to Differing Thermal Annealing Treatments, with Comparison to Celgard 2400 Properties. ....	93
Table 6.1.	Property data for PEBAX films. ....	123
Table 6.2.	Arrhenius parameters for the temperature dependence of gas permeation in PEBAX copolymers. ....	133
Table 6.3.	Model parameters for transport in multilayered $\beta$ -iPP/PEBAX membranes. Each ( $\varepsilon$ , $l_{PP}$ ) pair for a given layer configuration and PEBAX content corresponds to the value for an individual sample of those specifications. ....	149

## List of Figures

Figure 1.1.	The 300 most frequent words written in this dissertation, where larger typeset indicates greater frequency. Similar words were consolidated for display purposes. Image rendered by Wordle (www.wordle.net). .....	3
Figure 2.1.	Pore formation in PP following several of the techniques described previously. ....	6
Figure 2.2.	Enhanced solubility selectivity of PEO and PTMO-containing PE-b-PA copolymers relative to prediction based on gas condensability as represented by Lennard-Jones well depth. This figure has been adapted with permission from an article published in the <i>Journal of Polymer Science Part B: Polymer Physics</i> [74]. ....	14
Figure 2.3.	General schematic of a multilayer coextruded membrane composed of a porous support layer and a dense selective layer. ....	16
Figure 2.4.	Relationship between CO <sub>2</sub> and O <sub>2</sub> content at equilibrium for a container using modified atmosphere packaging technology. Performance is displayed for membranes with different CO <sub>2</sub> /O <sub>2</sub> selectivities $\alpha$ , including those produced using PEO ( $\alpha = 19$ ) [62], silicone rubber ( $\alpha = 4.8$ ) [99], or non-selective materials ( $\alpha = 1$ ). Illustration adapted from Murphy <i>et al.</i> [90] .....	18
Figure 3.1.	Constant pressure, variable volumetric flow gas permeation system [21] used to measure the permeability of a single gas through high flux membranes. ....	37

Figure 3.2. Scheme for masking polymer film samples to a specified area and mounting the sample into a Millipore filtration cell, which is used for gas permeation experiments. ....	38
Figure 3.3. Constant volume, variable pressure gas permeation system [30] used to measure the permeability of a single gas through low to moderate flux membranes. ....	45
Figure 3.4. Coextrusion process used to produce multilayered membranes. In the AB feedblock configuration, two rheologically compatible polymers are combined in the melt, using $n$ layer multiplication elements to produce $2^{(n+1)}$ layers. The AB feedblock delivering the polymer melt can also be exchanged to an ABA feedblock so that $2^{(n+1)} + 1$ layers are produced. Outside skin layers may also be introduced after layer multiplication is complete. ....	46
Figure 4.1. DSC first heating scans of: a) precursor films extruded from $\beta$ -iPP having a MFI of 2.1, 3.5, and 12 that were then annealed at 23 °C (as-extruded), 130 °C, and 140 °C for 30 minutes, and accompanying scans for b) microporous films produced by biaxially stretching these precursor films at 100 °C. Thermograms are displaced vertically for ease of viewing, and significant melting peaks corresponding to $\beta_1$ , and $\beta_2$ and $\alpha$ endotherms are labeled. ....	55

- Figure 4.2. XRD patterns of Exxon 1572 (MFI 2.1)  $\beta$ -iPP precursor films annealed at 23 °C (as-extruded), 130 °C, and 140 °C for 30 minutes (top scans) and accompanying patterns for these films stretched at 100 °C (bottom scans). Significant reflections corresponding to  $\alpha$  and  $\beta$  peaks are labeled, and patterns are displaced vertically for ease of comparison.....63
- Figure 4.3. Growth of  $\beta$  crystal size as indicated by increase in  $\beta_1$  melting peak temperature determined by DSC, and the increase in the largest  $\beta$  crystal dimension as calculated from the Scherrer equation based on observed XRD  $(300)_\beta$  peak broadening, both as a function of precursor film annealing temperature. Results are shown for MFI 2.1 ( $\blacklozenge, \blacklozenge$ ), MFI 3.5 ( $\blacksquare, \square$ ) and MFI 12 ( $\blacktriangle, \triangle$ ) films. ....68
- Figure 4.4. Several measures of precursor film  $\beta$  crystallinity determined by DSC as a function of  $K_{\beta,A}$  from XRD patterns. Values are plotted for  $K_{\beta,DSC}$  ( $\blacklozenge$ ), crystalline fraction in  $\beta_1$  state ( $\blacktriangle$ ), and volume fraction of  $\beta_1$  material ( $\blacksquare$ ) in the films. Dashed lines are best fits meant to guide the eye. ....71

Figure 4.5. Physical changes in amorphous, interphase and crystalline regions during annealing and subsequent biaxial stretching of $\beta$ -iPP. As-extruded films (a) are annealed, which result in larger lamellae of $\beta$ crystalline material and reduced tie chain density between lamellae (b). When annealed films are biaxially stretched, lamellae rotate so they are perpendicular to the drawing direction, initial cavitation occurs between already perpendicular large $\beta$ lamellae as they separate, while smaller lamellae shear (c). As stretching continues, initially formed cavities develop into larger pores as lamellae further separate, less stable $\beta$ lamellae begin to transform to the $\alpha$ phase, and stress-induced lamellar breakup begins (d). .....	74
Figure 4.6. SEM micrographs of representative regions in stretched films. Films were prepared from precursors extruded from $\beta$ -iPP having a MFI of 12 that were subsequently annealed at 23 °C (as-extruded), 130 °C, and 140 °C for 30 minutes and then stretched at 100 °C.....	78
Figure 4.7. Porosity calculated from densities measured by Archimedes' principle in biaxially stretched films as a function of $\beta_1$ crystallinity in the corresponding precursor $\beta$ -iPP films. Values are plotted for precursor films of MFI 2.1 (◆), MFI 3.5 (■), and MFI 12 (▲). Uncertainties represent $\pm 1$ standard deviation. The dashed line is the least squares line to the data set. ....	82

Figure 5.1. Porosity increase observed in  $\beta$ -iPP films biaxially stretched at 100 °C when the volume fraction of  $\beta_1$  crystallinity present in precursor films is increased by employing a thermal annealing process. Values are plotted for stretched films produced from precursors annealed for 30 minutes at 23 °C (as-extruded) (◆), 130 °C (▲), and 140 °C (■). Uncertainties represent  $\pm 1$  standard deviation. The dashed line is the least squares line to the data set.....90

Figure 5.2. SEM micrographs of representative surface regions in stretched films. Films were prepared from extruded  $\beta$ -iPP precursors having a MFI of 2.1, 3.5, and 12 that were subsequently annealed at 23 °C (as-extruded), 130 °C, and 140 °C for 30 minutes and then stretched at 100 °C.....91

Figure 5.3. Thickness normalized  $N_2$  flux as a function of transmembrane pressure measured for biaxially stretched  $\beta$ -iPP films whose precursors have been subjected to different thermal annealing treatments. Values are plotted for 3.5M-23A-100S (◆), 3.5M-130A-100S (▲), and 3.5M-140A-100S (■) films, and Celgard 2400 (●) has been included for comparison. The porosity of each film is labeled, and dashed lines represent least squares fits through the origin.....94

Figure 5.4. Porosity calculated from densities measured by Archimedes' principle in biaxially stretched films as a function of  $\beta_1$  crystallinity in the corresponding precursor  $\beta$ -iPP films. Values are plotted for films stretched at 90 °C (■), 100 °C (◆), and 110 °C (▲). Uncertainties represent  $\pm 1$  standard deviation. Dashed lines with matching colors are the least squares fit to the data sets. Extrapolation to zero  $\beta_1$  content should not be taken to be predictive (see Figure 5.1).....97

Figure 5.5. SEM micrographs of representative surface regions in stretched films. Films were prepared from precursors extruded from  $\beta$ -iPP having a MFI of 2.1, 3.5, and 12 that were subsequently annealed at 140 °C for 30 minutes and then stretched at 100 °C (top) or 110 °C (bottom). .....99

Figure 5.6. Permeability of stretched films to N<sub>2</sub> (closed symbols) and He (open symbols) as a function of porosity. Values are plotted for stretched films produced from precursors annealed for 30 minutes at 23 °C (as-extruded) (◆, ◇), 130 °C (▲, △), and 140 °C (■, □). Uncertainties represent  $\pm 1$  standard deviation. The solid line is a best fit to N<sub>2</sub> permeability data, and the dashed line is a best fit to He permeability data. The point at ~ 15% porosity was not used to generate these fits for reasons presented in the text. ....102

Figure 5.7. Comparison of polypropylene microporous film  $N_2$  permeability as a function of porosity. Films from this study ( $\blacklozenge$ ) are compared to  $\beta$ -iPP films that have been biaxially stretched (gas:  $O_2$ ) ( $\blacksquare$ ) [5], ( $\blacktriangle$ ) [14], as well as to those that have been uniaxially stretched (gas:  $O_2$ ) ( $\bullet$ ) [5]. Commercial Celgard films ( $\square$ ) [15] and extruded PP films made by a process similar to Celgard ( $\circ$ ) [22,23] are also included. Dashed lines represent best fits to the permeability data and are meant to guide the eye. ....104

Figure 5.8.  $N_2$  permeability and He/ $N_2$  selectivity of stretched films produced from precursors annealed at 23 °C (as-extruded) as a function of a) strain rate at a stretching temperature of 100 °C and b) stretching temperature at a strain rate of 100% $s^{-1}$ . Results are shown for MFI 2.1 ( $\blacklozenge, \blacklozenge$ ), MFI 3.5 ( $\blacksquare, \square$ ) and MFI 12 ( $\blacktriangle, \triangle$ ) films. Uncertainties represent  $\pm 1$  standard deviation. ....108

Figure 5.9.  $N_2$  permeability and He/ $N_2$  selectivity of a) stretched films produced from precursors annealed at 140 °C as a function of stretching temperature and b) films stretched at 100 °C as a function of precursor annealing temperature. Results are shown for MFI 2.1 ( $\blacklozenge, \blacklozenge$ ), MFI 3.5 ( $\blacksquare, \square$ ) and MFI 12 ( $\blacktriangle, \triangle$ ) films. Uncertainties represent  $\pm 1$  standard deviation. ....110

Figure 5.10. SEM micrographs demonstrating phenomena affecting gas transport through  $\beta$ -iPP stretched films. Surface fissures are observed in films whose precursors have been annealed at 140 °C and stretched (left). These fissures are formed in the machine and transverse direction relative to the biaxial stretcher, and possess a length scale that is long relative to the pores characterized. Observing a film edge-on (right) it can be seen that a continuous pore structure is created through the thickness of the stretched film. ....112

Figure 5.11. Pore size distribution in microporous films determined by capillary flow porometry for a) films of different MFI annealed at 140 °C and stretched at 100 °C, b) films of MFI 2.1 annealed at 140 °C and stretched at different temperatures, and c) films annealed at different temperatures. Films are color-coded for identification, and the pore size distribution of Celgard 2400 is included for comparison. ....115

Figure 5.12. Comparison of He/N<sub>2</sub> selectivities measured for stretched films produced from precursors annealed for 30 minutes at 23 °C (as-extruded) (◆), 130 °C (▲), and 140 °C (■) to values expected from a model combining Knudsen and Poiseuille permeability as a function of film mean pore size. Results for several values of  $\Delta p$  are displayed. Expected selectivities,  $\alpha$ , are shown for both flow regimes. Permeabilities in this study were measured with  $\Delta p$  from 5 to 30 psi. Uncertainties represent  $\pm 1$  standard deviation. ....118

Figure 6.1. Second heating scans of PTMO and PEO-based PEBAX copolymers showing melting peaks for PE blocks at low temperature and PA12 blocks at high temperature. ....	126
Figure 6.2. Permeability of CO <sub>2</sub> , O <sub>2</sub> , and N <sub>2</sub> in PTMO-based PEBAX copolymers as a function of transmembrane pressure at 35 °C. Pure gas selectivities are also presented. ....	128
Figure 6.3. Permeability and selectivity of PTMO-based PEBAX copolymers shown in Figure 6.2 as a function of PTMO block content (top). Similar data is also presented from a companion study of PTMO-based xx33 series PEBAX copolymers at 23 °C, displaying rapid loss of permeability and selectivity at low PTMO content (bottom). This latter figure has been adapted with permission from an article published in <i>Polymer</i> [5]. Solid lines are meant to guide the eye. ....	130
Figure 6.4. Comparison of permeability and selectivity in PEO and PTMO-based PEBAX copolymers at temperatures from 5 to 35 °C. Dashed lines represent the best fit to the Arrhenius relationship between permeability and temperature. ....	132
Figure 6.5. The O <sub>2</sub> permeance of extruded PEBAX copolymer films compared to that of a commercially produced Landec Intellipac MAP composite film at temperatures from 5 to 35 °C (top). The thickness required of a PEBAX separating layer to provide O <sub>2</sub> flux equivalent to the Intellipac composite film was then calculated (bottom). ....	135

Figure 6.6.	O <sub>2</sub> permeance of PEBAX membranes with different O <sub>2</sub> permeabilities as a function of total film thickness. The target O <sub>2</sub> permeance (30 GPU) is outlined in solid black.....	137
Figure 6.7.	CO <sub>2</sub> and O <sub>2</sub> compositions achievable in an enclosed package of apples upon which a PEBAX membrane of a given thickness and area has been affixed (top). The optimum atmosphere for apples can be achieved in a narrow envelope of package temperatures and membrane areas (bottom).....	141
Figure 6.8.	SEM (edge view) of multilayered PEBAX/ $\beta$ -iPP membrane.....	142
Figure 6.9.	Permeability and selectivity of 3-layer PEBAX/ $\beta$ -iPP biaxially stretched multilayer films. Permeabilities are calculated based on the composition of the selective PEBAX layer (30 vol. %) with the assumption that the support layer provides no resistance to mass transfer. Dashed lines in corresponding colors represent the permeability and selectivity of extruded single layer PEBAX films, which serve as a control.....	144
Figure 6.10.	O <sub>2</sub> permeability of multilayered films as a function of total PEBAX thickness (top) and multilayered film CO <sub>2</sub> /O <sub>2</sub> selectivity as a function of film permeance (bottom). The permeability and selectivity of a single layer 80PTMO-PA12 film is shown. Results for 3L-10 (■), 3L-30 (□), 17L-10 (▲), and 17L-30 (△) films are presented. ....	146

Figure 6.11. One possible schematic for a model of gas transport in multilayered films with a dense PEBAX layer and a porous support. Interactions between PEBAX and $\beta$ -iPP where they interface may result in areas where porosity is not formed in the $\beta$ -iPP (top). Gas transport in this model occurs in parallel, with one area ( $\epsilon$ ) experiencing resistance to mass transfer from both PEBAX and the intact dense PP, and the other area ( $1 - \epsilon$ ) experiencing resistance only from PEBAX (bottom). The area coverage $\epsilon$ and intact PP thickness $l_{pp}$ are model parameters. ....	147
Figure 6.12. Influence of transport model parameters on the O <sub>2</sub> permeability and CO <sub>2</sub> /O <sub>2</sub> selectivity of multilayered films. Results for 3L-10 (■), 3L-30 (□), 17L-10 (▲), and 17L-30 (△) films are presented. ....	151
Figure 6.13. Application performance of multilayered films (apple storage, 23 °C). The membrane area required to reach a package composition of 2.4% O <sub>2</sub> and the resulting CO <sub>2</sub> composition is calculated. The membrane areas are normalized by the value for an 80PTMO-PA12 membrane of 1 $\mu$ m thickness operating at 23 °C. Results for 3L-10 (■), 3L-30 (□), 17L-10 (▲), and 17L-30 (△) films are presented.....	153
Figure 6.14. Influence of thermal annealing on the O <sub>2</sub> permeability of 3-layer PEBAX/ $\beta$ -iPP films composed of 10 vol. % PEBAX. ....	154
Figure 7.1. Three potential multilayered membranes and their constituent materials. ....	167

## **Chapter 1. Introduction**

### **1.1 DISSERTATION GOALS**

The purpose of this research is to provide an understanding of the properties of two melt extruded polymeric membranes, and thereby develop a pathway to understand how these materials might be combined to successfully address commercial and industrial needs in separations. Specifically, microporous membranes made from polypropylene and dense film membranes made from PEBAX copolymers were characterized for their use as a multilayered composite in modified atmosphere packaging applications. More generally, the development of multilayer composite films by melt extrusion is novel, and the efforts related to fabricating successful MAP membranes may lead to the development of other membranes using this fabrication technique.

### **1.2 DISSERTATION ORGANIZATION**

The dissertation has seven chapters, including two which have been adapted from publications in *Polymer*. Chapter 2 provides background on the polypropylene and PEBAX materials used, explaining their fabrication, properties, and applications described in the literature. The transport mechanisms operative in disparate types of membranes are also discussed. Investigations and applications of multilayered coextrusion are catalogued. Finally, the produce preservation benefits of modified atmosphere packaging are detailed.

Chapter 3 sets forth the experimental and analytical techniques used to characterize the materials studied in this dissertation. It is divided, roughly speaking, into three sections discussing the techniques used in each of the following three chapters.

Chapter 4 presents a characterization of the crystallinity that exists in a specially nucleated isotactic polypropylene, how that crystallinity is influenced by thermal annealing processes, and how pore formation upon biaxial stretching is influenced by the crystalline content and the extent of its development. The complexity of the material requires the development of a new type of analysis to account for the crystalline lamellae active during pore formation and correlates this crystallinity with porosity formed.

Chapter 5 extends the analysis of Chapter 4 to transport phenomena in the same materials. The effect of thermal annealing and stretching conditions are studied for their effect on gas permeability in these films. A comparison is made between the properties of these films and those found in the literature. The pore size distribution in the films is characterized, and this information is used to compare the permeation behavior predicted by previously developed models to the materials studied.

Chapter 6 is divided into two sections. The first section discusses the permeability of PEBAX films at a variety of experimental conditions, including temperature. A comparison of O<sub>2</sub> flux between extruded PEBAX films and a commercial packaging membrane is made. Using analysis familiar to our laboratory, the process parameters for a successful PEBAX packaging membrane are calculated. The second section discusses multilayered membranes produced from polypropylene and PEBAX. Multilayered membrane performance is characterized along the lines of the first section.

Chapter 7 presents the conclusions of this research and provides recommendations to extend it. Experiments to increase understanding of pore formation in confined



## Chapter 2. Background and Theory

### 2.1 POROUS AND COMPOSITE MEMBRANES BY EXTRUSION

#### 2.1.1 Porous Membrane Applications

Microporous polymer membranes are of interest in many industrial applications. Since nitrocellulose micro- and ultrafiltration membranes were first commercialized in the 1920s [1], many types of microporous polymer membranes have been produced. Such membranes have been studied for use in filtration applications [1,2], gas exchange [3], membrane distillation [4], for use in bioreactors [5], as battery separators [6,7], and as porous supports for gas separation and desalination membranes [1,8,9], which were first made possible by the Loeb-Sourirajan phase separation process [10]. The pore size and size distribution in porous polymeric membranes largely determines their function. A range of membranes, from non-porous to the microfiltration range in pore size, can be produced in several ways. Anisotropic membranes can be obtained by phase separation processes, isotropic porous membranes can be produced through wet or dry processes, and composite films may be constructed in a variety of ways. The membranes of most interest in this research are isotropic and composite membranes produced through solvent-free processes.

---

Portions of this chapter have been adapted with permission from the following articles:  
G.T. Offord (author, primary experimentalist), S.R. Armstrong (editor, sample preparation), B.D. Freeman (editor), E. Baer (editor), A. Hiltner (editor), J.S. Swinnea (XRD experiments), D.R. Paul (editor), Polymer. 54 (2013) 2577–2589.  
G.T. Offord (author, primary experimentalist), S.R. Armstrong (editor, sample preparation), B.D. Freeman (editor), E. Baer (editor), A. Hiltner (editor), D.R. Paul (editor), Polymer. 54 (2013) 2796–2807.

### 2.1.2 Isotropic Membranes

Isotropic porous membranes generally have pores of ultrafiltration size or larger, and separation performance is determined by the pore size distribution across the entire membrane thickness [8]. Track etching of polymer films [2,11], film extrusion and blowing [2], and several stretching techniques applied to previously formed films [2,3,12] can be used to create isotropic microporous membranes. There are several pathways to produce isotropic porous films using solvent-free stretching methods. This process generally begins with the formation of a two-phase structure and is followed by a stretching step which imposes stress on the interface [13]. For example, polypropylene (PP) can be blended with inorganic fillers such as  $\text{CaCO}_3$  or other materials such as rubber and then stretched, causing cavitation through delamination of filler from the matrix. The number of pores and their sizes can be controlled by varying particle loading, particle size, and stretching conditions [12,14]. The pore formation resulting from several of these techniques is presented in Figure 2.1.

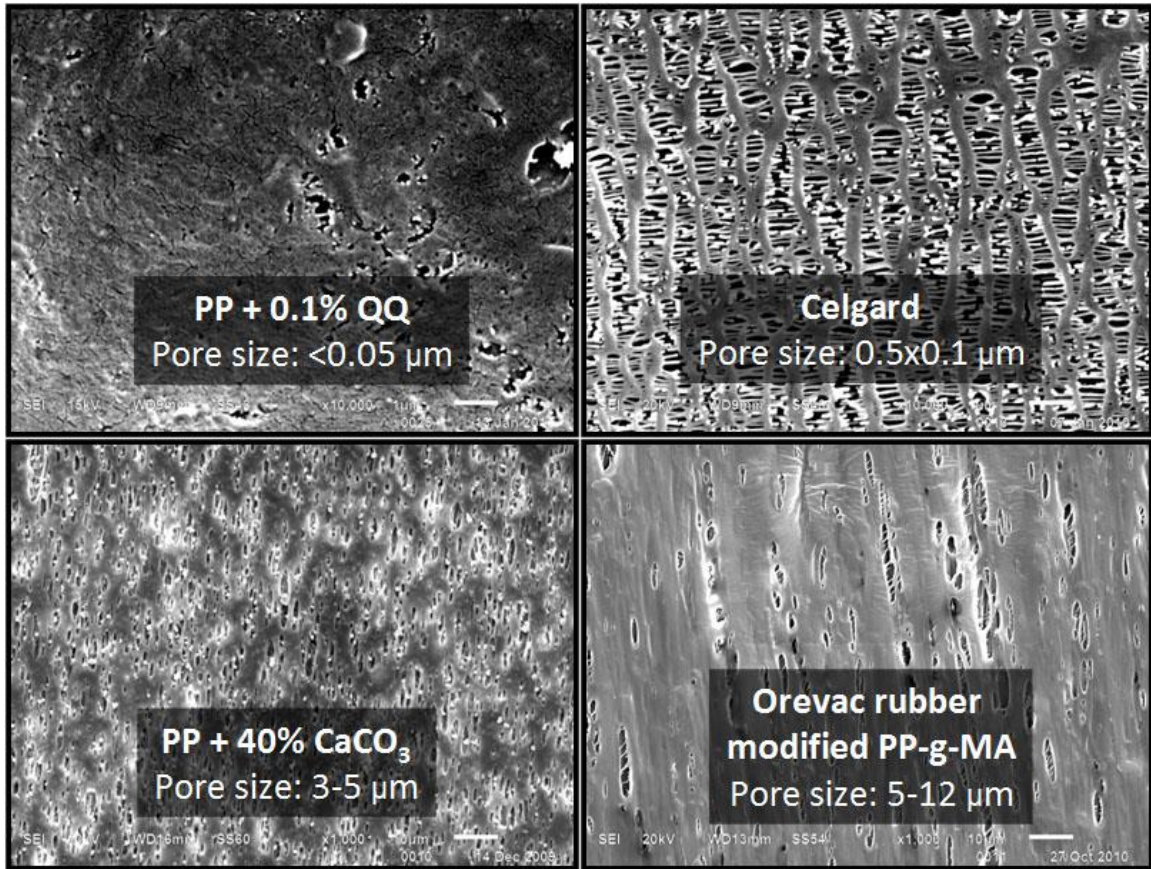


Figure 2.1. Pore formation in PP following several of the techniques described previously.

Perhaps the best-known microporous stretched film is the original Gore-Tex, a highly porous membrane produced by rapid stretching of polytetrafluoroethylene at high temperatures [15]. Other innovations in this area are isotactic polypropylene (iPP) and polyethylene (PE) microporous membranes produced by Celgard employing a “dry stretch” technique, patented by Celanese in the late 1960s [16–18] and commercialized in 1974 [19]. The extrusion, film take-up and annealing conditions for iPP prior to this “dry stretch” must be closely controlled to ensure that the film becomes highly oriented prior to crystallization. In iPP, this results in films with a stacked lamellar  $\alpha$  crystalline

structure that exhibit higher porosity and permeability upon stretching compared to films with spherulitic  $\alpha$  structures [20–23]. In addition to iPP and PE, other semicrystalline polymers that can form highly oriented stacked lamellar crystalline structures such as polyoxymethylene [24,25] and isotactic poly(4-methyl-1-pentene) [26,27] have been reported. Those studies were performed to determine the extrusion and annealing conditions required to create polymer precursors that successfully generate microporous membranes using the “dry stretch” technique.

The challenges of forming structures amenable to pore formation during stretching of a melt-extruded multilayered film have led to other approaches for iPP films, one of which is the stretching of extruded  $\beta$  nucleated isotactic polypropylene ( $\beta$ -iPP) films. This study examines extruded  $\beta$ -iPP films that have been annealed and biaxially stretched to induce pore formation, and it explored the influence of several processing variables on the gas permeation properties of  $\beta$ -iPP porous films. A comparison is made between these films and other porous films in the literature, as well as to commercially available Celgard films. If these membranes can be efficiently produced, they would be useful in many of the applications previously listed. Beyond those applications, a novel approach to incorporate  $\beta$ -iPP materials into composite membranes will be discussed next.

### **2.1.3 Composite Membranes**

In composite membranes, a thin skin layer determines separation performance, but that layer must be supported by a substrate material that provides both mechanical integrity and little resistance to mass transfer, which implies that it must be both porous and much thicker than the skin layer. These membranes have typically been produced by coating a porous substrate with a polymer in solution, or by laminating more than one

previously fabricated material together. A Celgard trilayer membrane, for instance, is fabricated in this manner [28].

Before extruded composite membranes can be produced, the production and properties of a compatible support layer must be studied. Studies of  $\beta$ -iPP isotropic films were undertaken for this purpose. Extruded  $\beta$ -iPP films, which become porous upon stretching [3,20], were produced. The aim of this part of the research is to develop a methodology by which these films may be coextruded in a multilayered configuration [29,30] with alternating layers of porous precursors and nonporous materials. These films may then be stretched to form the final composite membrane. Stand-alone  $\beta$ -iPP films made from resins with different values of melt flow index (MFI) were used to study pore formation while ensuring future rheological compatibility with other polymers during coextrusion. If useful composite membranes can ultimately be produced in this way, thus displacing solvent-based membrane production [1,8,9], large environmental and economic benefits may be realized. Specific applications for this technology will be discussed later in this chapter.

## **2.2 CRYSTALLINITY IN POLYMORPHIC IPP**

Isotactic polypropylene is a polymorphic semicrystalline polymer, manifesting crystalline modifications of the  $\alpha$ ,  $\beta$  and  $\gamma$  form [31,32]. Polymer films containing the first two modifications can be stretched under appropriate conditions to generate porosity, making these crystal forms of interest in this study [3,20]. Both  $\alpha$  and  $\beta$  crystals exist in a  $3_1$  helical conformation, but the  $\alpha$  form packs into a monoclinic unit cell while  $\beta$  packs in a hexagonal unit cell [33,34]. The  $\beta$  form is considered a metastable phase, due to its tendency to transform to  $\alpha$  when exposed to mechanical or thermal stimulation [33,35].

One reason for the instability of the  $\beta$  form and the difficulty to isolate and thus characterize the material is that  $\beta$ -iPP crystallizes with a frustrated helical packing, wherein the different azimuthal orientation of the helices ensure that at least one of the three helices in the packing is in an energetically unfavorable position [34,35]. For this reason, a nucleating additive is required to obtain any significant quantity of the  $\beta$  form, and iPP tends not to remain in that form [35]. Additionally, many  $\beta$  nucleators also serve as nucleators for the  $\alpha$  phase [35,36]. From a practical perspective, any system designed to take advantage of the properties of  $\beta$ -iPP must also account for the presence of  $\alpha$ -iPP.

The crystallinity of  $\beta$ -iPP precursor films is critical to porosity formation in the film upon stretching. This study examines porous films produced from melt-extruded  $\beta$ -iPP precursors and builds upon previous work in this area [37–39]. For example, Chu *et al.* produced  $\beta$ -iPP films crystallized in a hot press at a fixed temperature [3,40,41]. The film crystallinity was measured, then the samples were uniaxially or biaxially stretched to induce pore formation. A pore formation mechanism was proposed, and porosity, pore size distribution and gas permeability of the stretched films were measured. Several examples of melt-extruded biaxially stretched  $\beta$ -iPP microporous films are taught in the patent literature [42–45]. However, none of the previously mentioned studies examined the effect of annealing on  $\beta$  crystal structure and the resulting pore formation. There is a large body of work discussing the effect of annealing on  $\beta$ -iPP, primarily in the context of modifying the mechanical properties [46–50]. Compared to neat iPP,  $\beta$ -iPP generally exhibits greater toughness, higher impact strength, lower yield strength and reduced modulus across a variety of different iPP resins, nucleator types, and processing conditions [48,51]. Impact strength in particular is greatly enhanced when samples are annealed [49]. Of particular relevance to stretching annealed  $\beta$ -iPP films is an observed increase in resistance to necking, resulting in more homogeneous deformation [50].

Changes in mechanical properties upon annealing would likely affect the behavior of the films when stretched, including the extent of pore formation.

### 2.3 GAS PERMEABILITY IN MEMBRANES

The permeability of a membrane ( $P_i$ ) is defined as the steady state flux of a gas  $i$  ( $J_i$ ) through the membrane normalized by the driving force, a pressure gradient of gas  $i$  over the membrane thickness  $l$  ( $\Delta p_i/l$ ) [1,52]:

$$P_i = \frac{J_i}{\Delta p_i / l} \quad (2.1)$$

Likewise, the ideal permselectivity ( $\alpha_{i/j}$ ) of gas  $i$  relative to gas  $j$  is the ratio of pure gas permeabilities as follows:

$$\alpha_{i/j} = \frac{P_i}{P_j} \quad (2.2)$$

These useful formulations contain no information about the mode of transport, which is specific to the type of membrane. With these two equations, both membrane throughput and separation performance can be characterized.

#### 2.3.1 Porous Membranes

The flow of gas through porous membranes depends upon the relationship of the mean free path of the gas ( $\lambda$ ) to the characteristic size of the pore ( $D_{\text{pore}}$ ), known as the Knudsen number (Kn) [4,53]:

$$Kn = \frac{\lambda}{D_{\text{pore}}} \quad (2.3)$$

If this value is much larger than unity, gas transport through the membrane occurs by Knudsen diffusion, and the Knudsen flux ( $J_K$ ) can be represented as follows [4]:

$$J_K = \frac{D_{pore}}{3} \frac{\kappa}{\psi} \sqrt{\frac{8 \cdot R \cdot T}{\pi \cdot M}} \frac{M}{R \cdot T} \frac{\Delta p}{l} \quad (2.4)$$

When the Knudsen number is smaller than unity, transport occurs by Poiseuille flow, and the Poiseuille flux ( $J_P$ ) is represented by

$$J_P = \frac{D_{pore}^2}{32} \frac{\kappa}{\psi} \frac{M}{R \cdot T} \frac{p \cdot \Delta p}{\eta \cdot l} \quad (2.5)$$

In these models,  $\kappa$  represents the film porosity (idealized as cylindrical through-pores),  $\psi$  is flow path tortuosity,  $T$  is the gas temperature,  $M$  is the gas molecular weight,  $R$  is the gas constant,  $p$  is the mean gas pressure, and  $\eta$  is the gas viscosity.

### 2.3.2 Dense Film Polymeric Membranes

Transport in dense film polymeric membranes occurs by the solution-diffusion mechanism [54,55], where gas dissolves into the upstream face of the membrane, diffuses through the membrane, and finally desorbs from the downstream face of the membrane. In the case where a single gas  $i$  permeates through a membrane in this way, and the downstream pressure of the permeating gas is small, the permeability of gas  $i$  can be shown to be

$$P_i = D_i \cdot S_i \quad (2.6)$$

where  $D_i$  is the diffusion coefficient of gas  $i$ , and  $S_i$  is its solubility in the polymer [52]. In this formulation, diffusivity is a kinetic factor accounting for the rate gas molecules move through the polymer, and solubility is a thermodynamic property accounting for the capacity of the polymer to contain gas molecules. As before, the ideal permselectivity can also be written

$$\alpha_{i/j} = \frac{D_i}{D_j} \cdot \frac{S_i}{S_j} \quad (2.7)$$

where the ratio of diffusivities can be considered a diffusivity selectivity and the ratio of solubilities can be considered a solubility selectivity. Ideally, for a given separation the diffusivity selectivity and solubility selectivity of a membrane would be as high as possible. In practice, separations performed by membranes made of glassy polymers are usually diffusivity selectivity controlled, while those in rubbery polymers are solubility selectivity controlled [1].

## **2.4 POLYMERS EXHIBITING HIGH CO<sub>2</sub> SOLUBILITY**

### **2.4.1 Material Properties of Polymers with Affinity for CO<sub>2</sub>**

Polymers containing polar structural units (e.g., carbonates, acetates, nitriles, and ether oxygens) have the potential to exhibit strong interactions with quadrupolar CO<sub>2</sub> [56]. These strong interactions are manifested as increased solubility of CO<sub>2</sub> in the polymer relative to equivalent structures without the polar group, and further result in enhanced solubility selectivities of CO<sub>2</sub> over nonpolar light gases [57]. In particular, polymers with structures containing polar ether oxygens have been widely shown to exhibit this property [58–61]. For membrane applications where high CO<sub>2</sub> solubility or CO<sub>2</sub> solubility selectivity will result in the desired transport properties, the incorporation of ether oxygen linkages into the polymer is an obvious route to improved performance. Rubbery polymers containing ether oxygens are of particular interest, because the solubility selective behavior provided by the ether oxygens can offset the weak size-sieving behavior characteristic of rubbery polymers while retaining their high permeability. In fact, so-called “reverse selective” membranes that exhibit higher permeabilities to larger gases (e.g. CO<sub>2</sub>) over smaller gases (e.g. He, H<sub>2</sub>) are only made possible when polymer solubility behavior is the controlling factor [52,56].

#### 2.4.2 Design of Polymers with Affinity for CO<sub>2</sub>

Several approaches are available to produce membranes made of rubbery polymers containing ether oxygens [57]. Poly(ethylene oxide) (PEO), poly(tetramethylene oxide) (PTMO), or other structures that are essentially polyolefins with ether oxygen linkages can be synthesized and cast from solution as membranes. These polyethers (PE) tend to have high crystallinity, and therefore exhibit low gas permeability [62,63]. PEO is also soluble in water, greatly limiting the range of applications for which it is well-suited as a membrane [64,65]. Further, the mechanical properties of PEO are quite poor [30]. The high crystallinity and water solubility of these materials can be addressed by crosslinking the polymer network after casting from solution, an approach which has been extensively studied previously for PEO [66–68]. An intriguing method to exploit the properties of PE units in gas separation membranes that has been widely used since the mid-1990s is to synthesize block copolymers composed of a “soft” PE block and a second “hard” structural block. PEO-based materials with “hard” polyimide [58,69], polyamide [70,71], polyester [72,73], and polyurethane [60,69] segments have all been measured for CO<sub>2</sub>, N<sub>2</sub>, and other light gas permeabilities. PTMO-based materials along these lines have been studied concurrently. This class of materials exhibits significantly better material properties than solution-cast polyethers or their crosslinked derivatives, and depending upon the hard block, these copolymers may also be melt extruded. A commercially available line of polyether-block-polyamide (PE-b-PA) segmented copolymers, sold under the name PEBAX, possess these excellent processing characteristics and still retain an enhanced solubility selectivity toward CO<sub>2</sub>, shown in Figure 2.2.

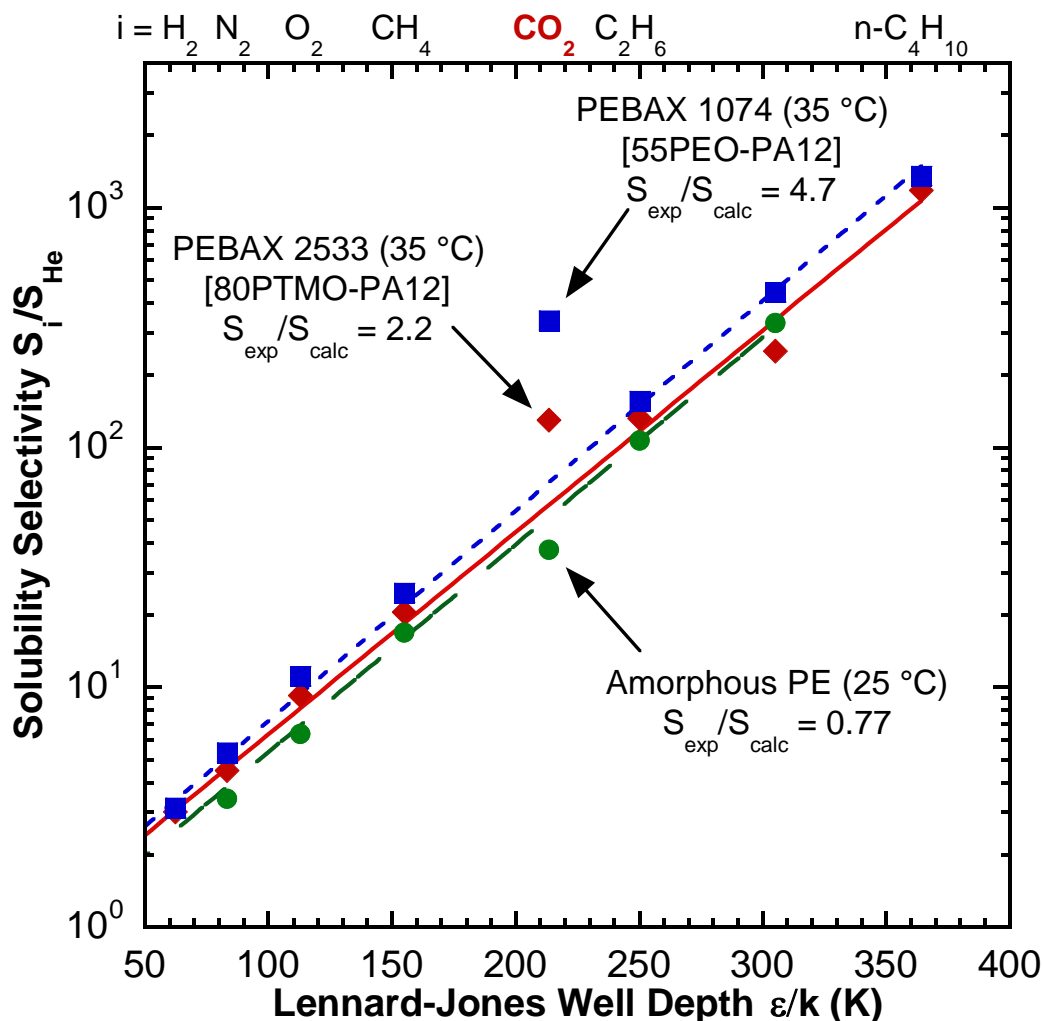


Figure 2.2. Enhanced solubility selectivity of PEO and PTMO-containing PE-b-PA copolymers relative to prediction based on gas condensability as represented by Lennard-Jones well depth. This figure has been adapted with permission from an article published in the *Journal of Polymer Science Part B: Polymer Physics* [74].

As would be expected from the solubility selectivities, PTMO-b-PA materials tend to exhibit lower permselectivities for  $CO_2$  over light gases compared to PEO-b-PA materials. The PTMO-based materials exhibit higher permeabilities, which could make them useful for high throughput applications [70,75]. Research on PEO and PTMO-based

materials has primarily been directed toward hydrogen purification, natural gas sweetening, and flue gas CO<sub>2</sub> recovery [56]. There are interesting possibilities in several other areas, which will be outlined below.

## **2.5 MULTILAYERED COEXTRUSION**

Extruded polymer films made from two or more polymers arranged in several or many layers can be produced by a technique pioneered by Dow called multilayer coextrusion. This technology is currently being advanced by the Center for Layered Polymeric Systems (CLiPS) NSF Science and Technology Center, of which this dissertation is a product. Fundamental studies of these layered polymeric systems have been performed to understand polymer interdiffusion of microlayers [76], their mechanical properties [77,78], layer morphology [79], the behavior of material at the polymer interphase [80,81], and physical aging of confined polymers [82]. Additionally, these systems have been studied for applications such as barrier materials [83–85], breathable films [30], advanced optical [86,87] and electrical properties [88], as well as for modified atmosphere packaging [89–92]. A schematic for a multilayered membrane intended for this last category, which is the primary application for which this technology platform has been developed, is depicted in Figure 2.3.

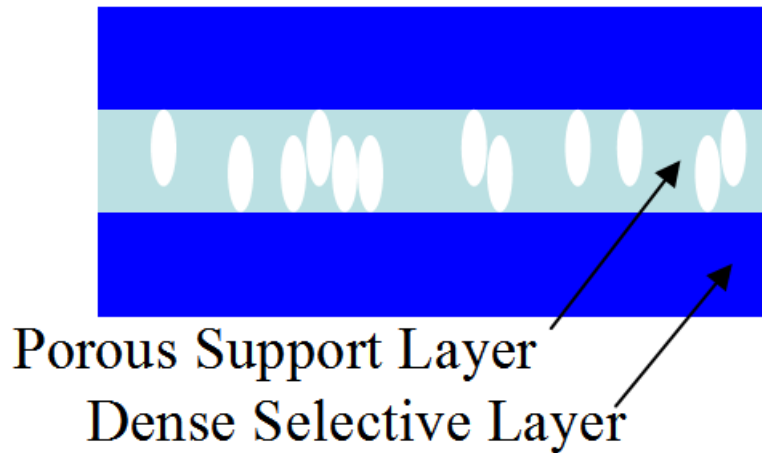


Figure 2.3. General schematic of a multilayer coextruded membrane composed of a porous support layer and a dense selective layer.

## 2.6 MULTILAYERED MEMBRANES FOR MODIFIED ATMOSPHERE PACKAGING

### 2.6.1 Produce Preservation

The preservation of fresh produce as it passes through the supply chain is an important economic and health issue. Over 20% of vegetables grown are lost to spoilage, which decreases agricultural productivity and the availability of nutritious food to the public [93]. Ripening (and thus eventual spoilage) is ultimately caused by produce respiration, which can be summarized chemically as follows [64]:



where  $C_6H_{12}O_6$  is a representative organic substrate (in this case, glucose) and heat,  $\Delta$ , is produced in the course of the reaction. The usual approach to retard the spoilage of produce is refrigeration, which reduces the rate of this reaction. A less energy-intensive method to reduce the rate is to use the reaction products and an appropriate membrane to reach elevated levels of  $CO_2$  and decreased levels of  $O_2$  inside the produce package. This approach, known as modified atmosphere packaging (MAP), can be employed with or

without refrigeration, and it has opened up significant opportunities for membrane technology [64,93–95]. The steady state gas composition in a modified atmosphere package can be modeled given the respiratory behavior of the packaged produce and the transport properties of the selected membrane material [64,90,94,96,97].

### **2.6.2 Materials for MAP**

Recent literature reports that membranes made of poly(ethylene oxide) (PEO) materials have exceptionally high CO<sub>2</sub>/O<sub>2</sub> permselectivity [56,62,63,98]. This results from the favorable interaction of quadrupolar CO<sub>2</sub> with polar ether oxygens, described previously. The achievable steady state concentration of gases in a package are represented in the form of operating lines corresponding to different polymeric membrane materials, as shown in Figure 2.4.

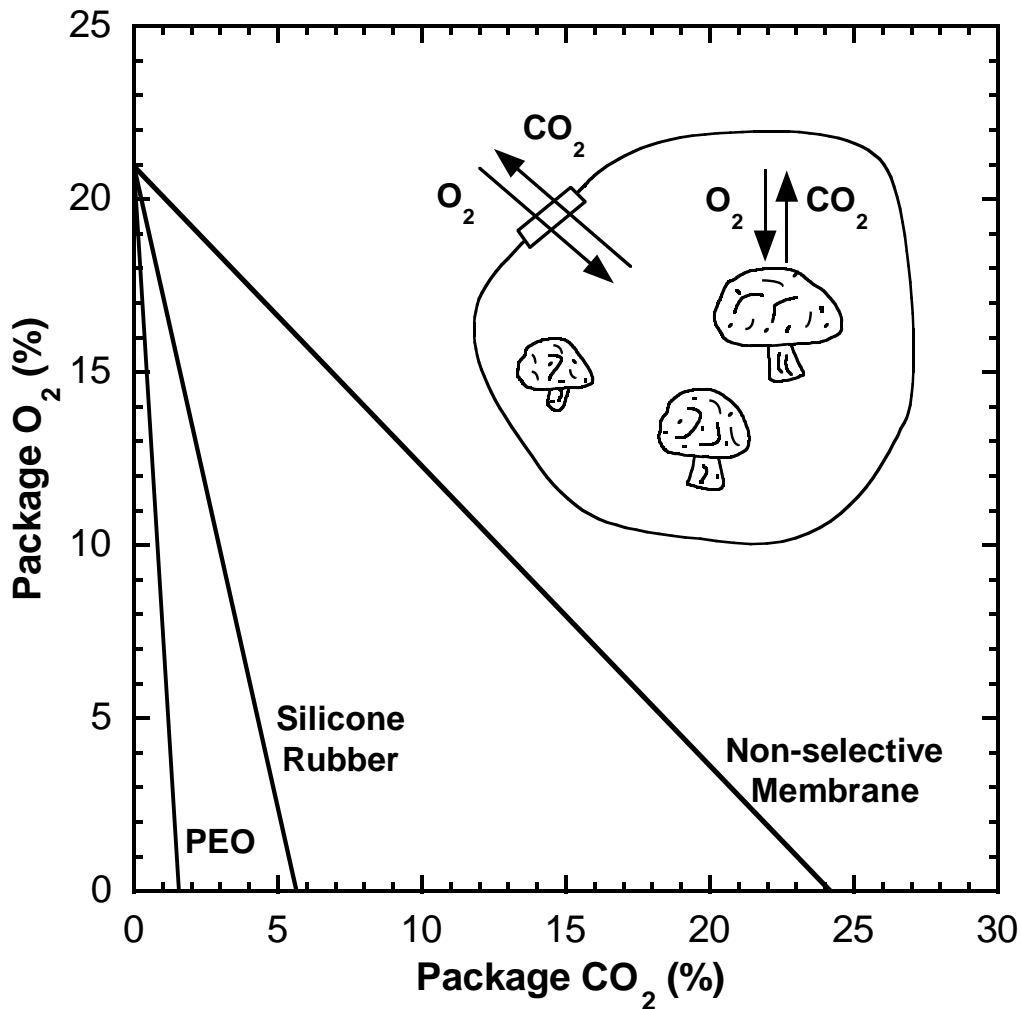


Figure 2.4. Relationship between CO<sub>2</sub> and O<sub>2</sub> content at equilibrium for a container using modified atmosphere packaging technology. Performance is displayed for membranes with different CO<sub>2</sub>/O<sub>2</sub> selectivities  $\alpha$ , including those produced using PEO ( $\alpha = 19$ ) [62], silicone rubber ( $\alpha = 4.8$ ) [99], or non-selective materials ( $\alpha = 1$ ). Illustration adapted from Murphy *et al.* [90]

Modeling results show that membrane materials with PEO-like properties are required to generate low (< 5%) equilibrium package concentrations of CO<sub>2</sub> and O<sub>2</sub>, which extend the shelf life of high-volume produce like apples, pears, grapes, and tomatoes [64,97]. The slope of the operating line depends primarily upon the CO<sub>2</sub>/O<sub>2</sub>

permselectivity, while the position on that line depends primarily on the membrane O<sub>2</sub> flux and the produce respiratory behavior [96,97]. Any composition between the PEO line and the non-selective membrane line can in principle be reached through the proper combination of selective and non-selective materials. Consequently, optimal atmospheric conditions can be achieved for a wide variety of produce.

### **2.6.3 MAP Membranes by Coextrusion**

There is no commercially available MAP product employing a high selectivity membrane. Indeed, very little work on high selectivity materials for this application has been performed, as evidenced by the sparsely available O<sub>2</sub> permeability data for such materials in the literature. This project addresses several of the deficiencies of current membranes for MAP that may be solved by selecting improved materials and microlayer coextrusion techniques [29,30]. A novel multilayer structure composed of  $\beta$ -nucleated polypropylene and PE-b-PA copolymer materials will be coextruded and biaxially stretched to produce high flux, high selectivity MAP membranes. This approach has the additional advantage of avoiding the expensive and environmentally hazardous casting of membranes from solution, which is the industry standard for the production of gas separation membranes [1,8,9].

## 2.7 REFERENCES

- [1] R.W. Baker, *Membrane Technology and Applications*, 2nd ed., West Sussex, John Wiley & Sons, Ltd., 2004.
- [2] O.W. Reif, *Microfiltration Membranes: Characteristics and Manufacturing*, *Adv. Biochem. Engin/Biotechnol.* (2006) 73–103.
- [3] F. Chu, *Structure and gas permeability of microporous films prepared by biaxial drawing of  $\beta$ -form polypropylene*, *Polymer*. 37 (1996) 573–579.
- [4] R.W. Schofield, A.G. Fane, C.J.D. Fell, *Gas and Vapour Transport Through Microporous Membranes. I. Knudsen-Poiseuille Transition*, *Journal of Membrane Science*. 53 (1990) 159–171.
- [5] A.G. Fane, *Membrane bioreactors: design & operational options*, *Filtration & Separation*. 39 (2002) 26–29.
- [6] G. Venugopal, J. Moore, J. Howard, S. Pendalwar, *Characterization of microporous separators for lithium-ion batteries*, *Journal of Power Sources*. 77 (1999) 34–41.
- [7] P. Arora, Z.J. Zhang, *Battery separators.*, *Chemical Reviews*. 104 (2004) 4419–62.
- [8] M. Ulbricht, *Advanced functional polymer membranes*, *Polymer*. 47 (2006) 2217–2262.
- [9] P. Bernardo, E. Drioli, G. Golemme, *Membrane Gas Separation: A Review/State of the Art*, *Industrial & Engineering Chemistry Research*. 48 (2009) 4638–4663.
- [10] S. Loeb, S. Sourirajan, *Sea Water Demineralization by Means of an Osmotic Membrane*, in: R.F. Gould (Ed.), *Saline Water Conversion II*, *Advances in Chemistry Series Number 38*, American Chemical Society, 1963: pp. 117–132.
- [11] S. Takahashi, M. Yoshida, M. Asano, T. Nakagawa, *Gas-Permeation Control by PET Membranes with Nanosized Pores*, *Polymer Journal*. 36 (2004) 50–53.
- [12] Y. Mizutani, S. Nakamura, S. Kaneko, K. Okamura, *Microporous Polypropylene Sheets*, *Industrial & Engineering Chemistry Research*. 32 (1993) 221–227.

- [13] F. Sadeghi, Study of Polypropylene Morphology Obtained from Blown and Cast Film Processes: Initial Morphology Requirements for Making Porous Membrane by Stretching, *Journal of Plastic Film and Sheeting*. 21 (2005) 199–216.
- [14] S. Nagō, Y. Mizutani, Microporous polypropylene sheets containing CaCO<sub>3</sub> filler: Effects of stretching ratio and removing CaCO<sub>3</sub> filler, *Journal of Applied Polymer Science*. 68 (1998) 1543–1553.
- [15] R.W. Gore, Process for producing porous products, U.S. Patent 3,953,566, 1976.
- [16] H. Bierenbaum, R. Plainfield, R. Isaacson, P. Lantos, Breathable Medical Dressing, U.S. Patent 3,426,754, 1969.
- [17] R.B. Isaacson, H.S. Bierenbaum, Process for Preparing Microporous Film, U.S. Patent 3,558,764, 1971.
- [18] M.L. Druin, J.T. Loft, S.G. Plovan, Novel Open-Celled Microporous Film, U.S. Patent 3,679,538, 1972.
- [19] Celgard, Celgard Overview Brochure, Company Literature Item #10003, 2010.
- [20] S.H. Tabatabaei, P.J. Carreau, A. Aji, Effect of processing on the crystalline orientation, morphology, and mechanical properties of polypropylene cast films and microporous membrane formation, *Polymer*. 50 (2009) 4228–4240.
- [21] S.H. Tabatabaei, P.J. Carreau, A. Aji, Structure and properties of MDO stretched polypropylene, *Polymer*. 50 (2009) 3981–3989.
- [22] F. Sadeghi, A. Aji, P.J. Carreau, Analysis of row nucleated lamellar morphology of polypropylene obtained from the cast film process: Effect of melt rheology and process conditions, *Polymer Engineering & Science*. 47 (2007) 1170–1178.
- [23] K.-Y. Lin, M. Xanthos, K.K. Sirkar, Novel polypropylene-based microporous membranes via spherulitic deformation, *Journal of Membrane Science*. 330 (2009) 267–278.
- [24] M.B. Johnson, G.L. Wilkes, Microporous membranes of polyoxymethylene from a melt-extrusion process: (I) effects of resin variables and extrusion conditions, *Journal of Applied Polymer Science*. 81 (2001) 2944–2963.
- [25] M.B. Johnson, G.L. Wilkes, Microporous membranes of polyoxymethylene from a melt-extrusion process: (II) Effects of thermal annealing and stretching on porosity, *Journal of Applied Polymer Science*. 84 (2002) 1762–1780.

- [26] M.B. Johnson, G.L. Wilkes, Microporous membranes of isotactic poly(4-methyl-1-pentene) from a melt-extrusion process. I. Effects of resin variables and extrusion conditions, *Journal of Applied Polymer Science*. 83 (2002) 2095–2113.
- [27] M.B. Johnson, G.L. Wilkes, Microporous membranes of isotactic poly(4-methyl-1-pentene) from a melt-extrusion process. II. Effects of thermal annealing and stretching on porosity, *Journal of Applied Polymer Science*. 84 (2002) 1076–1100.
- [28] Celgard, Celgard Product Comparison, Company Literature Item #10002, 2009.
- [29] C.D. Mueller, J. Kerns, T. Ebeling, S. Nazarenko, A. Hiltner, E. Baer, Microlayer Coextrusion: Processing and Applications, in: *Polymer Process Engineering 97*, 1997: pp. 137–157.
- [30] C.D. Mueller, V. Topolkaev, D. Soerens, A. Hiltner, E. Baer, Breathable Polymer Films Produced by the Microlayer Coextrusion Process, *Journal of Applied Polymer Science*. 78 (2000) 816–828.
- [31] G. Natta, P. Corradini, Structure and Properties of Isotactic Polypropylene, *Del Nuovo Cimento*. 15 (1960) 40–51.
- [32] A. Turner Jones, J.M. Aizlewood, D.R. Beckett, Crystalline Forms of Isotactic Polypropylene, *Die Makromolekulare Chemie*. 75 (1964) 134–158.
- [33] S. V. Meille, D.R. Ferro, S. Brueckner, A.J. Lovinger, F.J. Padden, Structure of  $\beta$ -Isotactic Polypropylene: A Long-Standing Structural Puzzle, *Macromolecules*. 27 (1994) 2615–2622.
- [34] B. Lotz, J.C. Wittmann, A.J. Lovinger, Structure and morphology of poly(propylenes): a molecular analysis, *Polymer*. 37 (1996) 4979–4992.
- [35] W. Stocker, M. Schumacher, S. Graff, A. Thierry, J.-C. Wittmann, B. Lotz, Epitaxial Crystallization and AFM Investigation of a Frustrated Polymer Structure: Isotactic Poly(propylene),  $\beta$  Phase, *Macromolecules*. 31 (1998) 807–814.
- [36] M. Gahleitner, C. Grein, S. Kheirandish, J. Wolfschwenger, Nucleation of Polypropylene Homo- and Copolymers, *International Polymer Processing: The Journal of the Polymer Processing Society*. XXVI (2011) 2–20.
- [37] G. Shi, F. Chu, G. Zhou, Z. Han, Plastic Deformation and Solid-Phase Transformation in  $\beta$ -Phase Polypropylene, *Die Makromolekulare Chemie*. 190 (1989) 907–913.

- [38] W. Zhu, X. Zhang, C. Zhao, W. Wu, J. Hou, M. Xu, A Novel Polypropylene Microporous Film, *Polymers for Advanced Technologies*. 7 (1996) 743–748.
- [39] S. Ran, M. Xu, Studies on the Pore Formation Mechanism of  $\beta$ -Crystalline Polypropylene Under Stretching, *Chinese Journal of Polymer Science*. 22 (2004) 123–130.
- [40] F. Chu, T. Yamaoka, H. Ide, Y. Kimura, Microvoid formation process during the plastic deformation of  $\beta$ -form polypropylene, *Polymer*. 35 (1994) 3442–3448.
- [41] F. Chu, T. Yamaoka, Y. Kimura, Crystal transformation and micropore formation during uniaxial drawing of  $\beta$ -form polypropylene film, *Polymer*. 36 (1995) 2523–2530.
- [42] M. Xu, S. Hu, J. Guan, X. Sun, W. Wu, W. Zhu, et al., Polypropylene microporous film, U.S. Patent 5,134,174, 1992.
- [43] P. Jacoby, C.W. Bauer, S.R. Clingman, W.T. Tapp, Oriented polymeric microporous films, U.S. Patent 5,317,035, 1994.
- [44] P. Jacoby, C.W. Bauer, S.R. Clingman, W.T. Tapp, Oriented polymeric microporous films, U.S. Patent 5,594,070, 1997.
- [45] H.M. Fisher, G.C. Wensley, Polypropylene microporous membrane for battery separator, U.S. Patent 6,368,742, 2002.
- [46] J. Varga, F. Tóth, D.O. Hummel, Annealing of the  $\beta$ -modification of polypropylene, *Makromolekulare Chemie. Macromolecular Symposia*. 5 (1986) 213–223.
- [47] J. Varga,  $\beta$ -Modification of polypropylene and its two-component systems, *Journal of Thermal Analysis*. 35 (1989) 1891–1912.
- [48] J. Varga,  $\beta$ -Modification of Isotactic Polypropylene: Preparation, Structure, Processing, Properties, and Application, *Journal of Macromolecular Science, Part B*. 41 (2002) 1121–1171.
- [49] H. Bai, Y. Wang, Z. Zhang, L. Han, Y. Li, L. Liu, et al., Influence of Annealing on Microstructure and Mechanical Properties of Isotactic Polypropylene with  $\beta$ -Phase Nucleating Agent, *Macromolecules*. 42 (2009) 6647–6655.

- [50] H. Bai, F. Luo, T. Zhou, H. Deng, K. Wang, Q. Fu, New insight on the annealing induced microstructural changes and their roles in the toughening of  $\beta$ -form polypropylene, *Polymer*. 52 (2011) 2351–2360.
- [51] C. Grein, Toughness of Neat, Rubber Modified and Filled  $\beta$ -Nucleated Polypropylene: From Fundamentals to Applications, *Advances in Polymer Science*. 188 (2005) 43–104.
- [52] S. Matteucci, Y.P. Yampolskii, B.D. Freeman, I. Pinnau, Transport of Gases and Vapors in Glassy and Rubbery Polymers, in: Y. Yampolskii, I. Pinnau, B.D. Freeman (Eds.), *Materials Science of Membranes for Gas and Vapor Separation*, 1st ed., Wiley, 2006.
- [53] A. Hernandez, Pore size distributions in microporous membranes. A critical analysis of the bubble point extended method, *Journal of Membrane Science*. 112 (1996) 1–12.
- [54] H.K. Lonsdale, U. Merten, R.L. Riley, Transport properties of cellulose acetate osmotic membranes, *Journal of Applied Polymer Science*. 9 (1965) 1341–1362.
- [55] J.G. Wijmans, R.W. Baker, The solution-diffusion model: a review, *Journal of Membrane Science*. 107 (1995) 1–21.
- [56] H. Lin, B.D. Freeman, Materials selection guidelines for membranes that remove CO<sub>2</sub> from gas mixtures, *Journal of Molecular Structure*. 739 (2005) 57–74.
- [57] H. Lin, *Solubility Selective Membrane Materials for Carbon Dioxide Removal from Mixtures with Light Gases*, The University of Texas at Austin, 2005.
- [58] K. Okamoto, M. Fuji, S. Okamoto, H. Suzuki, K. Tanaka, H. Kita, Gas permeation properties of poly(ether imide) segmented copolymers, *Macromolecules*. 28 (1995) 6950–6956.
- [59] H. Lin, B.D. Freeman, Gas and Vapor Solubility in Cross-Linked Poly(ethylene Glycol Diacrylate), *Macromolecules*. 38 (2005) 8394–8407.
- [60] H. Li, B.D. Freeman, O.M. Ekiner, Gas permeation properties of poly(urethane-urea)s containing different polyethers, *Journal of Membrane Science*. 369 (2010) 49–58.
- [61] S.R. Reijerkerk, K. Nijmeijer, C.P. Ribeiro, B.D. Freeman, M. Wessling, On the effects of plasticization in CO<sub>2</sub>/light gas separation using polymeric solubility selective membranes, *Journal of Membrane Science*. 367 (2011) 33–44.

- [62] H. Lin, B.D. Freeman, Gas solubility, diffusivity and permeability in poly (ethylene oxide), *Journal of Membrane Science*. 239 (2004) 105–117.
- [63] S. Kalakkunnath, D.S. Kalika, H. Lin, B.D. Freeman, Segmental Relaxation Characteristics of Cross-Linked Poly(ethylene oxide) Copolymer Networks, *Macromolecules*. 38 (2005) 9679–9687.
- [64] K.L. Yam, D.S. Lee, Design of modified atmosphere packaging for fresh produce, in: M.L. Rooney (Ed.), *Active Food Packaging*, Blackie Academic & Professional, 1995: pp. 55–73.
- [65] R. Kjellander, E. Florin, Water structure and changes in thermal stability of the system poly(ethylene oxide)-water, *Journal of the Chemical Society, Faraday Transactions 1*. 77 (1981) 2053–2077.
- [66] H. Lin, B.D. Freeman, Gas Permeation and Diffusion in Cross-Linked Poly(ethylene glycol diacrylate), *Macromolecules*. 39 (2006) 3568–3580.
- [67] V.A. Kusuma, B.D. Freeman, M.A. Borns, D.S. Kalika, Influence of chemical structure of short chain pendant groups on gas transport properties of cross-linked poly(ethylene oxide) copolymers, *Journal of Membrane Science*. 327 (2009) 195–207.
- [68] V.A. Kusuma, G. Gunawan, Z.P. Smith, B.D. Freeman, Gas permeability of cross-linked poly(ethylene-oxide) based on poly(ethylene glycol) dimethacrylate and a miscible siloxane co-monomer, *Polymer*. 51 (2010) 5734–5743.
- [69] M. Yoshino, K. Ito, H. Kita, K. Okamoto, Effects of hard-segment polymers on CO<sub>2</sub>/N<sub>2</sub> gas-separation properties of poly(ethylene oxide)-segmented copolymers, *Journal of Polymer Science Part B: Polymer Physics*. 38 (2000) 1707–1715.
- [70] V.I. Bondar, B.D. Freeman, I. Pinnau, Gas transport properties of poly(ether-b-amide) segmented block copolymers, *Journal of Polymer Science Part B: Polymer Physics*. 38 (2000) 2051–2062.
- [71] J.H. Kim, S.Y. Ha, Y.M. Lee, Gas permeation of poly (amide-6b-ethylene oxide) copolymer, *Journal of Membrane Science*. 190 (2001) 179–193.
- [72] S.J. Metz, M.H. V Mulder, M. Wessling, Gas-Permeation Properties of Poly(ethylene oxide) Poly(butylene terephthalate) Block Copolymers, *Macromolecules*. 37 (2004) 4590–4597.

- [73] A. Car, C. Stropnik, W. Yave, K.-V. Peinemann, Tailor-made Polymeric Membranes based on Segmented Block Copolymers for CO<sub>2</sub> Separation, *Advanced Functional Materials*. 18 (2008) 2815–2823.
- [74] V.I. Bondar, B.D. Freeman, I. Pinnau, Gas sorption and characterization of poly(ether-b-amide) segmented block copolymers, *Journal of Polymer Science Part B: Polymer Physics*. 37 (1999) 2463–2475.
- [75] V. Barbi, S.S. Funari, R. Gehrke, N. Scharnagl, N. Stribeck, SAXS and the Gas Transport in Polyether- block -polyamide Copolymer Membranes, *Macromolecules*. 36 (2003) 749–758.
- [76] T.L. Schuman, E. V Stepanov, S. Nazarenko, G. Capaccio, A. Hiltner, E. Baer, Interdiffusion of Linear and Branched Polyethylene in Microlayers Studied via Melting Behavior, *Macromolecules*. 31 (1998) 4551–4561.
- [77] J. Kerns, A. Hsieh, A. Hiltner, E. Baer, Mechanical Behavior of Polymer Microlayers, *Macromolecular Symposium*. 147 (1999) 15–25.
- [78] E. Baer, A. Hiltner, D. Jarus, Relationship of Hierarchical Structure to Mechanical Properties, *Macromolecular Symposium*. 147 (1999) 37–61.
- [79] T.E. Bernal-Lara, R. Masirek, A. Hiltner, E. Baer, E. Piorkowska, A. Galeski, Morphology studies of multilayered HDPE/PS systems, *Journal of Applied Polymer Science*. 99 (2006) 597–612.
- [80] R.Y.F. Liu, A.P. Ranade, H.P. Wang, T.E. Bernal-Lara, A. Hiltner, E. Baer, Forced Assembly of Polymer Nanolayers Thinner Than the Interphase, *Macromolecules*. 38 (2005) 10721–10727.
- [81] R.Y.F. Liu, T.E. Bernal-Lara, A. Hiltner, E. Baer, Polymer Interphase Materials by Forced Assembly, *Macromolecules*. 38 (2005) 4819–4827.
- [82] T.M. Murphy, D.S. Langhe, M. Ponting, E. Baer, B.D. Freeman, D.R. Paul, Physical aging of layered glassy polymer films via gas permeability tracking, *Polymer*. 52 (2011) 6117–6125.
- [83] D. Jarus, Barrier properties of polypropylene/polyamide blends produced by microlayer coextrusion, *Polymer*. 43 (2002) 2401–2408.
- [84] J. Greener, K.C. Ng, K.M. Vaeth, T.M. Smith, Moisture permeability through multilayered barrier films as applied to flexible OLED display, *Journal of Applied Polymer Science*. 106 (2007) 3534–3542.

- [85] H. Wang, J.K. Keum, A. Hiltner, E. Baer, B.D. Freeman, A. Rozanski, et al., Confined Crystallization of Polyethylene Oxide in Nanolayer Assemblies, *Science*. 323 (2009) 757–760.
- [86] Y. Jin, H. Tai, A. Hiltner, E. Baer, J.S. Shirk, New class of bioinspired lenses with a gradient refractive index, *Journal of Applied Polymer Science*. 103 (2007) 1834–1841.
- [87] R. Tangirala, E. Baer, A. Hiltner, C. Weder, Photopatternable Reflective Films Produced by Nanolayer Extrusion, *Advanced Functional Materials*. 14 (2004) 595–604.
- [88] S. Nazarenko, A. Hiltner, E. Baer, Polymer microlayer structures with anisotropic conductivity, *Journal of Materials Science*. 34 (1999) 1461 – 1470.
- [89] S. Armstrong, B. Freeman, A. Hiltner, E. Baer, Gas permeability of melt-processed poly(ether block amide) copolymers and the effects of orientation, *Polymer*. 53 (2012) 1383–1392.
- [90] T.M. Murphy, G.T. Offord, D.R. Paul, Fundamentals of Membrane Gas Separation, in: E. Drioli, L. Giorno (Eds.), *Membrane Operations: Innovative Separations and Transformations*, Wiley-VCH, 2009: pp. 63–82.
- [91] G.T. Offord, S.R. Armstrong, B.D. Freeman, E. Baer, A. Hiltner, J.S. Swinnea, et al., Porosity Enhancement in  $\beta$  Nucleated Isotactic Polypropylene Stretched Films by Thermal Annealing, *Polymer*. Accepted (2013).
- [92] G.T. Offord, S.R. Armstrong, B.D. Freeman, E. Baer, A. Hiltner, D.R. Paul, Influence of Processing Strategies on Porosity and Permeability of  $\beta$  Nucleated Isotactic Polypropylene Stretched Films, *Polymer*. Accepted (2013).
- [93] Sandhya, Modified atmosphere packaging of fresh produce: Current status and future needs, *LWT - Food Science and Technology*. 43 (2010) 381–392.
- [94] A. Exama, J. Arul, R.W. Lencki, L.Z. Lee, C. Toupin, Suitability of Plastic Films for Modified Atmosphere Packaging of Fruits and Vegetables, *Journal of Food Science*. 58 (1993) 1365–1370.
- [95] S. Mangaraj, T.K. Goswami, P. V. Mahajan, Applications of Plastic Films for Modified Atmosphere Packaging of Fruits and Vegetables: A Review, *Food Engineering Reviews*. 1 (2009) 133–158.

- [96] D.R. Paul, R. Clarke, Modeling of modified atmosphere packaging based on designs with a membrane and perforations, *Journal of Membrane Science*. 208 (2002) 269–283.
- [97] B.S. Kirkland, R. Clarke, D.R. Paul, A versatile membrane system for bulk storage and shipping of produce in a modified atmosphere, *Journal of Membrane Science*. 324 (2008) 119–127.
- [98] H. Lin, E. Van Wagner, J.S. Swinnea, B.D. Freeman, S. Pas, A.J. Hill, et al., Transport and structural characteristics of crosslinked poly(ethylene oxide) rubbers, *Journal of Membrane Science*. 276 (2006) 145–161.
- [99] T.C. Merkel, V.I. Bondar, K. Nagai, B.D. Freeman, I. Pinnau, Gas sorption, diffusion, and permeation in poly(dimethylsiloxane), *Journal of Polymer Science Part B: Polymer Physics*. 38 (2000) 415–434.

## Chapter 3. Materials and Experimental Methods

### 3.1 INTRODUCTION

The studies presented in this dissertation have significant differences in materials and experimental techniques, so this section will therefore be presented in order of subject matter: extruded  $\beta$ -iPP precursor and stretched films, extruded single layer PEBAX films, and finally, coextruded multilayered  $\beta$ -iPP/PEBAX films.

### 3.2 EXTRUDED B-IPP PRECURSOR AND STRETCHED FILMS

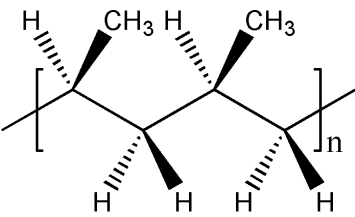
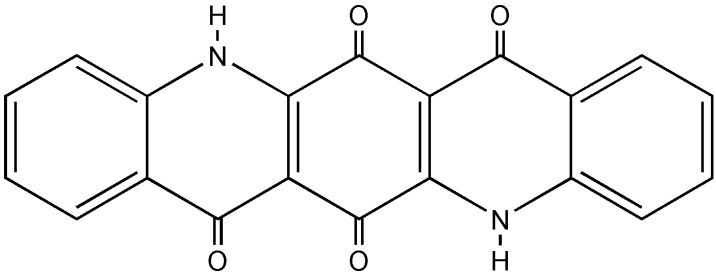
#### 3.2.1 Materials Selection

Three grades of iPP were included in this study. Dow H700-12, with an ASTM D1238 melt flow index (MFI) of 12 g/10 min., Exxon 2252 (MFI = 3.5), and Exxon 1572 (MFI = 2.1) were selected as the model iPP materials, and they were received in pellet form. A highly active [1,2]  $\beta$  nucleating agent for iPP, quinacridone quinone (QQ), was purchased from Sigma Aldrich and was used without further modification. The chemical structures of the polymer and nucleating agent are presented in Table 3.1.

---

Portions of this chapter have been adapted with permission from the following articles:  
G.T. Offord (author, primary experimentalist), S.R. Armstrong (editor, sample preparation), B.D. Freeman (editor), E. Baer (editor), A. Hiltner (editor), J.S. Swinnea (XRD experiments), D.R. Paul (editor), *Polymer*. 54 (2013) 2577–2589.  
G.T. Offord (author, primary experimentalist), S.R. Armstrong (editor, sample preparation), B.D. Freeman (editor), E. Baer (editor), A. Hiltner (editor), D.R. Paul (editor), *Polymer*. 54 (2013) 2796–2807.

Table 3.1. Structure and property data for materials used to produce  $\beta$ -iPP films.

Sample Name	MFI (g/10 min.)	Chemical Structure
Dow H700-12 iPP	12	
Exxon 2252 iPP	3.5	
Exxon 1572 iPP	2.1	
Sigma Aldrich Quinacridone Quinone	--	

### 3.2.2 Film Preparation

A master batch of each iPP grade containing 0.5 wt.% QQ was prepared by melt blending at 190 °C using a Haake Rheomix 600 twin screw extruder and pelletizing the extrudate. These pellets were then mixed with additional iPP in the hopper before film extrusion to reach the desired concentration of 0.1 wt.% QQ. This two-step process ensured good control over the QQ content in the  $\beta$ -iPP films and a uniform distribution of QQ  $\beta$  nucleator in the iPP.

Dow H700-12  $\beta$ -iPP films were extruded at a temperature of 210 °C, while films of the lower MFI Exxon grades were extruded at 250 °C. To promote the formation of  $\beta$ -iPP by controlling the extruded film cooling rate, and thus crystallization behavior, the iPP was coextruded with a low density polyethylene (LDPE) sacrificial surface layer on each side of the iPP layer. This approach reflects guidance from a prior study which showed that in injection molded tensile bars, the core of the bar had a significantly higher

$\beta$  fraction due to its slower cooling rate [3]. Each multilayered film was extruded from a 14" film die in series with a chill roll operated at a constant temperature of 95 °C in close proximity to the die. Melt flow rates and roll take-up speeds were controlled and uniform between samples so that nominal film thicknesses of 100  $\mu$ m and consistent crystallization conditions upon film cooling were achieved. Control iPP films were translucent and white, while the  $\beta$ -iPP films were translucent and yellow in color due to the addition of QQ.

Test samples 8.5×8.5 cm in size were cut from the center of the extruded film for consistency of thickness, and the LDPE sacrificial layer was carefully peeled away to obtain  $\beta$ -iPP films. Each of the three grades of  $\beta$ -iPP films were subjected to three different thermal annealing treatments to produce nine unique precursor films varying in both iPP MFI and thermal history. After conditioning the films for at least two hours at room temperature (23 °C), films were maintained at 23 °C or annealed in an oven in air at either 130 °C or 140 °C for 30 minutes. The oven was allowed to equilibrate for several hours before annealing, and samples were placed in the same location. Previous studies demonstrated that any structural changes in films of the thickness used in this study are complete by the end of a 30 minute annealing process [4,5]. The samples were free-standing during heat treatment, and they were allowed to cool to room temperature by leaving the oven door open. Control iPP films were maintained at room temperature after extrusion. All precursor films were stored in sealed plastic bags at room temperature until they were stretched or characterized.

The nomenclature for films produced in this study is as follows. For  $\beta$ -iPP precursor films, the sample code is [MFI]M-[T<sub>anneal</sub>]A-P, where, for example, 12M-23A-P refers to a precursor film with an iPP MFI of 12 and an annealing temperature of 23 °C. Selected characteristics of  $\beta$ -iPP precursor films produced for this study are displayed in

Table 3.2. For biaxially stretched films, the sample code is [MFI]M-[T<sub>anneal</sub>]A-[T<sub>stretch</sub>]S, where 3.5M-140A-100S refers to a stretched film whose precursor had an iPP MFI of 3.5, an annealing temperature of 140 °C, and a stretching temperature of 100 °C.

Table 3.2. Selected Characteristics of  $\beta$ -iPP Precursor Films.

Sample Code	iPP Grade	MFI (g/10 min.)	Annealing Treatment	$\rho$ (g/cm <sup>3</sup> )
12M-23A-P	Dow H700-12	12	23 °C	0.900 ± 0.002
3.5M-23A-P	Exxon 2252	3.5	23 °C	0.904 ± 0.004
2.1M-23A-P	Exxon 1572	2.1	23 °C	0.902 ± 0.003
12M-130A-P	Dow H700-12	12	130 °C/30 min.	0.904 ± 0.003
3.5M-130A-P	Exxon 2252	3.5	130 °C/30 min.	0.906 ± 0.002
2.1M-130A-P	Exxon 1572	2.1	130 °C/30 min.	0.907 ± 0.001
12M-140A-P	Dow H700-12	12	140 °C/30 min.	0.902 ± 0.002
3.5M-140A-P	Exxon 2252	3.5	140 °C/30 min.	0.905 ± 0.003
2.1M-140A-P	Exxon 1572	2.1	140 °C/30 min.	0.902 ± 0.004

Each of the  $\beta$ -iPP precursor films was biaxially stretched to generate porosity, as demonstrated in several other studies [6–10]. A Brückner Karo IV biaxial stretching device with temperature control was used to produce porous stretched films from the precursor films. To investigate the properties of annealed films in this study, such films were stretched to an elongation of 100% in the machine and transverse directions simultaneously at a rate of 100% $s^{-1}$  and at a temperature of 100 °C. The exposure of as-extruded samples to this temperature in the biaxial stretcher occurs for only 1 to 2 minutes, minimizing any effect of thermal annealing. Other as-extruded and annealed precursor films were stretched at temperatures of 80 to 110 °C in 10 degree increments, and the samples were stretched at strain rates of 20, 100, and 500% $s^{-1}$  to investigate the effect of processing conditions on pore formation. Stretched films were stored in sealed plastic bags at room temperature until they were characterized.

### 3.2.3 Differential Scanning Calorimetry (DSC)

Thermal analysis of precursor and stretched samples was performed using a TA Instruments Q100 DSC. The DSC was calibrated for temperature using an indium standard. Measurements were taken on samples weighing around 7 mg, which were sealed in aluminum pans and purged with nitrogen gas during experiments. First heating scans were performed using a heating rate of 20 °C/min. from 40 to 100 °C and then heating from 100 to 200 °C at 10 °C/min. Samples were then cooled from 200 °C to 40 °C at 20 °C/min. Second heating scans were performed using the same procedure as first scans. The initially faster heating rate was used to expedite the experiment and to limit the amount of time precursor films would spend under conditions not found in the biaxial stretching step.

The fraction of crystallinity of a given type  $i$  ( $X_i$ ) for a particular sample was calculated using the equation

$$X_i = \frac{\Delta H_i}{\Delta H_i^0} \quad (3.1)$$

where  $\Delta H_i$  is the heat of fusion measured for an endotherm in a given sample corresponding to one of three crystalline iPP modifications ( $\alpha$ ,  $\beta_1$ , or  $\beta_2$ ), and  $\Delta H_i^0$  is the heat of fusion for a completely crystalline material of a particular modification. As reported elsewhere [11,12],  $\Delta H_\alpha^0 = 177.0$  J/g, and  $\Delta H_\beta^0 = 168.5$  J/g, with  $\Delta H_\beta^0$  used to characterize melting in both  $\beta_1$  and  $\beta_2$  endotherms. The sample crystallinity ( $X_c$ ) was then determined as follows:

$$X_c = X_\alpha + X_{\beta_1} + X_{\beta_2} \quad (3.2)$$

Stretched film properties are dependent upon the fraction of precursor  $X_c$  that is in the  $\beta_1$  or  $\beta_2$  form, and this point will be discussed in more depth later.

### 3.2.4 X-Ray Diffraction (XRD)

XRD experiments were performed on 3×3 cm precursor and stretched samples using a Scintag X1 diffractometer using  $\text{CuK}_\alpha$  radiation with  $\lambda = 0.154$  nm. Scans were run in the range  $2\theta = 10\text{-}30^\circ$  at a rate of  $4^\circ/\text{min}$  with an angle increment of  $0.04^\circ$ . The software package Jade (Materials Data Inc.) was used to generate best fits to peak areas and to account for background scatter.

A widely used measure of the  $\beta$  crystalline content in iPP materials is the Turner-Jones parameter,  $K_{\beta,H}$  [13]. This parameter can be determined from XRD scans as follows:

$$K_{\beta,H} = \frac{H(300)_\beta}{H(300)_\beta + H(110)_\alpha + H(040)_\alpha + H(130)_\alpha} \quad (3.3)$$

where  $H(300)_\beta$  is the intensity of the equatorial  $\beta$  diffraction peak and  $H(110)_\alpha$ ,  $H(040)_\alpha$ , and  $H(130)_\alpha$  are the intensities of the equatorial  $\alpha$  diffraction peaks. A related parameter [14,15] using the areas corresponding to these peaks rather than their intensities will also be used in this study, and it will be referred to as  $K_{\beta,A}$ . This parameter is only a relative measure of the amount of  $\beta$  material in a sample, and it should not be taken to represent the absolute quantity of  $\beta$  material [16]. Only equatorial peaks are used in this analysis because the  $(111)_\alpha$  and  $(301)_\beta$  peaks are found near the same  $2\theta$  value, and their inclusion would make determination of relative  $\alpha$  and  $\beta$  content difficult [17]. Sample crystallinity,  $X_c$ , can also be estimated from the ratio of crystalline peak area to the total peak area [17].

The relative size of the largest dimension of the  $\beta$  crystal,  $D_{300}$ , can be estimated based on the peak broadening associated with the  $(300)_\beta$  peak. This estimate is based on the Scherrer equation [10,18] as follows:

$$D_{300} = \frac{\lambda_x}{B_{300} \cdot \cos(\theta)} \quad (3.4)$$

In this equation,  $\lambda_x$  is the x-ray wavelength,  $B_{300}$  is the  $(300)_\beta$  peak width at half the maximum intensity, and  $\theta$  is half the scattering angle.

### 3.2.5 Film Thickness Determination

Thicknesses of precursor and stretched films were measured using a Mitutoyo handheld micrometer and a Mitutoyo low-force micrometer, respectively. Prior to permeation testing, thickness measurements at five equally spaced points on the exposed membrane area were performed.

### 3.2.6 Film Density and Porosity Determination

Densities of precursor and stretched films were measured using the density kit for a Mettler Toledo Excellence balance. Pure water was used as the liquid medium for measurement. Samples were measured for wet and dry weight in triplicate and densities were calculated from these weights based on Archimedes' principle.

Precursor film densities were also estimated from DSC and XRD measurements, since both experiments yielded crystalline  $\alpha$  and  $\beta$  content as well as amorphous content. These estimates were based on the equation

$$\rho_{iPP} = X_\alpha \cdot \rho_\alpha + X_\beta \cdot \rho_\beta + (1 - X_c) \cdot \rho_a \quad (3.5)$$

where  $\rho$  is density, and the subscripts "iPP" and "a" refer to bulk iPP material and amorphous phase, respectively. Densities of amorphous,  $\alpha$ , and  $\beta$ -iPP material have been reported to be 0.852, 0.936, and 0.922 g/cm<sup>3</sup>, respectively [19].

The bulk porosity,  $\Phi$ , of the stretched film was determined by tracking the reduction in density upon stretching a given precursor film. Porosity was calculated as follows:

$$\Phi = 1 - \frac{\rho_{stretch}}{\rho_0} \quad (3.6)$$

where  $\rho_{stretch}$  is the stretched film density and  $\rho_0$  is the precursor film density.

### 3.2.7 Scanning Electron Microscopy (SEM)

Surface SEM was performed to examine pore formation resulting from stretching precursor films. Film cross-sections were prepared by cryo-fracturing following more than an hour of exposure to liquid nitrogen. Stretched films of 30-70  $\mu\text{m}$  in thickness were sputter-coated with  $\sim 10$  nm of iridium and images of representative areas were captured on a Zeiss SEM.

### 3.2.8 Capillary Flow Porometry (CFP)

Analytical services were provided by LabQMC, who used a Quantachrome Porometer 3Gzh for CFP to determine the size distribution of through-pores in stretched film samples. Dry stretched films were wetted with a proprietary fluorinated hydrocarbon (Porofil) having a low surface tension and vapor pressure, then placed into the CFP device. Differential air pressure,  $\Delta p_{air}$ , was applied to the film until the force applied was great enough to overcome the capillary force in the largest pore (the bubble point) and expel the liquid. As pressure was further increased, the flow of air through the porous film was monitored, and liquid was expelled from decreasingly small pores until either all pores were dry or the pressure limit of the device had been reached. The accessed through-pore diameter,  $D_{pore}$ , was calculated using the equation for capillary pressure [20]

$$D_{pore} = \frac{4 \cdot \gamma_{liq} \cdot \cos(\theta_{liq})}{\Delta p_{air}} \quad (3.7)$$

where  $\gamma_{liq}$  is the surface tension of Porofil, and  $\theta_{liq}$  is the contact angle of the Porofil on the stretched film.  $D_{pore}$  values greater than 18 nm could be detected using this method.

To display histograms of pore size distributions, pressure and flow data were processed to show the fraction of pores present in a given size range (or bin), which was selected to be 0.5 nm. This bin size was selected because it provided a reasonable compromise between observing the distribution within a given sample and the changes in distributions between samples. For example, if bin sizes were too large, a given distribution would appear to occupy a single or small number of pore sizes, giving poor resolution of a given sample; if they were too small, a given distribution would appear to be flat over a large number of pore sizes, and would be difficult to differentiate visually from other distributions.

### 3.2.9 Gas Permeability

The permeabilities of pure N<sub>2</sub> and He gases through stretched films were measured using a constant pressure, variable volume device described previously [21]. A schematic of this device is presented in Figure 3.1.

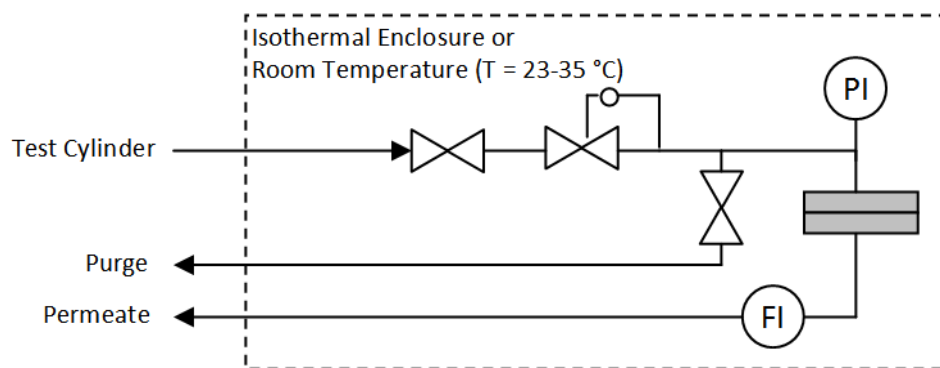


Figure 3.1. Constant pressure, variable volumetric flow gas permeation system [21] used to measure the permeability of a single gas through high flux membranes.

Stretched films were masked with aluminum tape prior to placement in the permeation system, as outlined in Figure 3.2.

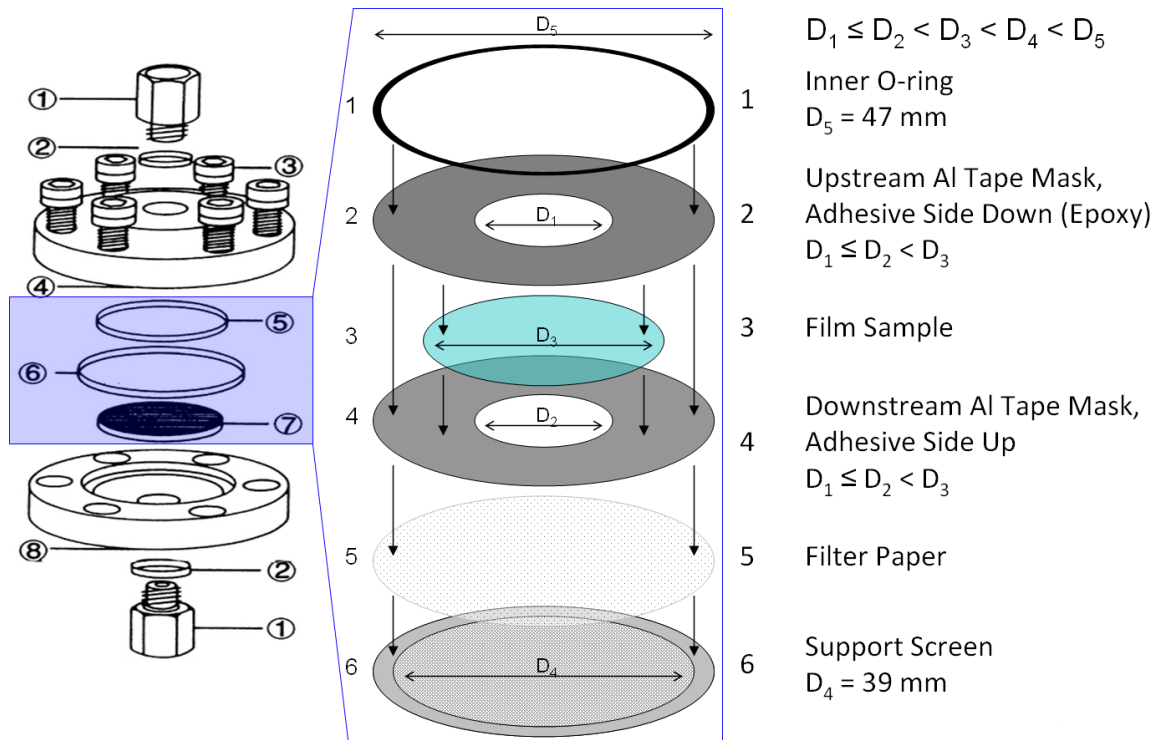


Figure 3.2. Scheme for masking polymer film samples to a specified area and mounting the sample into a Millipore filtration cell, which is used for gas permeation experiments.

After masking, stretched films were placed into the permeation cell, the upstream side of the sample was exposed to flowing gas at test pressure, and the downstream side was maintained at atmospheric pressure. To ensure the purity of gas on each side of the sample, the upstream volume was purged five times, and permeation measurements were not started until five downstream volumes had passed through the stretched film. The volumetric flow rate of the permeate gas was measured using a bubble flow meter and a stopwatch. Permeability measurements were conducted in triplicate at several differential pressures from 5 to 30 psig (0.34 to 2.07 barg) at room temperature. The gas permeability,  $P_{\text{gas}}$ , was calculated as follows [22]:

$$P_{gas} = \frac{l}{A} \cdot \frac{T_0}{T} \cdot \frac{p_{atm}}{p_0 \cdot \Delta p} \cdot \left( \frac{dV}{dt} \right)_{ss} \quad (3.8)$$

where  $l$  is the film thickness. The exposed film area ( $0.32 \text{ cm}^2$ ) is  $A$ ,  $T_0$  is the standard temperature (273.15 K),  $T$  is the experiment temperature (295.15 K),  $p_{atm}$  is atmospheric pressure,  $p_0$  is the standard pressure (76 cmHg),  $\Delta p$  is the differential pressure across the stretched film, and  $(dV/dt)_{ss}$  is the steady state volumetric flow rate of permeate gas. Permeability in this study is reported in Barrer, where  $1 \text{ Barrer} = 10^{-10} \text{ cm}^3(\text{STP}) \cdot \text{cm}/(\text{cm}^2 \cdot \text{s} \cdot \text{cmHg})$ .

### 3.3 EXTRUDED PEBAX SINGLE LAYER FILMS

#### 3.3.1 Materials Selection

The properties of a commercially available series of polyether-block-amide (PE-b-PA) copolymers produced by Arkema, Inc., PEBAX, were studied for MAP applications in this project. Because PEBAX is commercially available, the large quantities required for extrusion were readily procured in pellet form. The structures of the polymer blocks and that of the copolymer are presented in Table 3.3.

Table 3.3. Structure of PEBAX copolymers and constituent blocks.

Polymer	Structure
PEBAX Block Copolymer	$\text{HO}-\left[ \begin{array}{c} \text{O} \\ \parallel \\ \text{C} \end{array} \text{-PA-} \begin{array}{c} \text{O} \\ \parallel \\ \text{C} \end{array} \text{-O-PE-O} \right]_n \text{-H}$
Poly[imino(1-oxodo-decamethylene)] (PA = Nylon-12 / PA12)	$\left[ \begin{array}{c} \text{O} \\ \parallel \\ \text{C} \end{array} \text{---} (\text{CH}_2)_{11} \text{---} \begin{array}{c} \text{H} \\   \\ \text{N} \end{array} \right]_n$
Poly(ethylene oxide) (PE = PEO)	$\left[ (\text{CH}_2)_2 \text{---} \text{O} \right]_n$
Poly(tetramethylene oxide) (PE = PTMO)	$\left[ (\text{CH}_2)_4 \text{---} \text{O} \right]_n$

All grades of PEBAX contain a Nylon-12 (PA12) polyamide block. Grades containing poly(ethylene oxide) (PEO) (1074, 3000) and poly(tetramethylene oxide) (PTMO) (1041, 1205, 2533) polyether blocks were obtained. The nomenclature for films produced in this study is as follows. [wt. % PE][PE]-PA12 is the sample code, where, for example, 80PTMO-PA12 is a PEBAX film containing 80 wt. % of the polyether PTMO by weight, and the polyamide block is PA12 (as it is for all samples in this study). Basic properties of these polymers are presented in Table 3.4.

Table 3.4. Selected characteristics of PEBAX copolymers.

PEBAX Grade	PE Block	Water Uptake (wt. %, 50% RH)	$\rho$ , g/cm <sup>3</sup>	T <sub>m</sub> , °C
1074	PEO	1.4	1.07	158
3000	PEO	1.0	1.02	158
1041	PTMO	0.9	1.04	170
1205	PTMO	0.4	1.01	147
2533	PTMO	1.2	1.00	134

Values from Arkema Product Literature

A related study [23,24] performed by research collaborators used the PEBAX xx33 series, which were block copolymers with a Shore D hardness “xx” and contain PTMO polyether blocks. Some of the results from that study will be compared with results obtained here to provide context.

### 3.3.2 Film Preparation

Pelletized PEBAX was spread out on trays in a vacuum oven and dried at 100 °C for at least 6 hours. The polyether block in PEBAX is hydrophilic and results in water uptake, which could generate water vapor in the extruder at high temperature and lead to problems with film quality and consistency. The drying step is, therefore, necessary to ensure that as little water remains in the polymer as possible prior to extrusion. Each grade of pelletized PEBAX was placed in a hopper and fed into the extruder. The extrusion temperature for each grade was 190 °C, and a 14” film die was used to extrude a uniform film onto a chill roll at 55 °C. The melt pump rate was set at a fixed value between grades, and the chill roll take-up rate was set to produce films between 25 and 40  $\mu$ m in thickness. Films were unwound from the roll and wound onto wax paper to prevent self-cling. The wound rolls were stored at room temperature until needed for further characterization.

All films were clear in appearance, with visible extrusion die lines present on all samples. Films with a PEO polyether block tended to have a tackier feel than those with a

PTMO block, and films with higher polyether block contents were tackier than those with lower contents. For all characterization techniques, samples were taken from as close as possible to the center of the extruded film, and away from die lines.

### 3.3.3 Elemental Analysis

Analytical services provided by Galbraith Labs were used to determine the nitrogen content of PEBAX copolymers. As outlined previously [25], since the polyamide blocks present in PEBAX are the only part of the structure containing nitrogen, analysis of combustion products for nitrogen can be used to calculate the weight fraction of the polyamide block, PA12 in this case, and thus the polyether block weight fraction by difference. Transport properties in this class of materials are largely determined by the polyether content. The calculation of PA12 weight fraction is performed as follows:

$$\omega_{PA12} = \frac{MW_{PA12}}{MW_N / \omega_N} \quad (3.9)$$

where  $MW_{PA12}$  is the molecular weight of a PA12 repeat unit (197 g/mol),  $MW_N$  is the molecular weight of elemental nitrogen (14 g/mol), and  $\omega_N$  is the measured weight fraction of nitrogen from combustion analysis.

### 3.3.4 Differential Scanning Calorimetry (DSC)

Extruded film samples having masses between 10 and 12 mg were sealed in aluminum pans and placed in the DSC. First heating scans were performed by heating at 5 °C/min from 40 to 200 °C. From this scan, the crystallinity of the PA block was determined as follows:

$$X_{c,PA12} = \frac{\Delta H_{PA12}}{\omega_{PA12} \cdot \Delta H_{PA12}^0} \quad (3.10)$$

where  $\Delta H_{\text{PA12}}$  is the measured heat of fusion of PA12, and  $\Delta H^0_{\text{PA12}}$  is the value for entirely crystalline PA12 (246 J/g) [25]. Samples were cooled at the same rate to -60 °C, and a second heating scan was performed at the same rate. Polyether  $T_g$  values were too low to be recorded, and the glass transition for the polyamide block in these materials is typically too weak to be detected. Other studies indicate that they are present at approximately 65 to 75 °C [26].  $T_m$  values for the PE and PA blocks were collected.

### **3.3.5 Film Thickness Determination**

The thicknesses of extruded PEBAX films were determined using a Mitutoyo handheld micrometer. Prior to permeation testing, thickness measurements at five equally spaced points on the exposed membrane area were performed and averaged.

### **3.3.6 Gas Permeability**

Extruded PEBAX films were measured for gas permeability using two rapid screening techniques. Films were masked using a method similar to that presented previously, and they were then measured for O<sub>2</sub> permeability using a Mocon Ox-tran device. For CO<sub>2</sub> permeability, a Mocon Permatran-C device was used. These permeation systems use coulometric or infrared detection techniques [27,28], respectively. A test gas is flowed past the upstream face of the membrane, and a sweep gas carries the permeate from the downstream face of the membrane to the detector. The system is operated at atmospheric pressure, so the permeability of membranes cannot be tested at higher partial pressures. Additionally, test temperatures are limited to room temperature (23 °C) with this technique. Because these systems are fully automated, they require little attention to obtain basic permeation properties.

A more traditional technique to measure permeability was also used to obtain more detailed permeation properties. After masking the film as shown in Figure 3.2, a

constant volume, variable pressure system, depicted in Figure 3.3, was used to measure the permeability of extruded PEBAX membranes. These measurements were performed over a variety of upstream applied pressures of CO<sub>2</sub>, O<sub>2</sub>, and N<sub>2</sub>, and at temperatures ranging from 5 to 35 °C. The system was operated by evacuating the volume downstream of the membrane in the permeation cell using a vacuum pump, and applying a fixed test gas pressure to the upstream face of the membrane. The temperature of the membrane was controlled using a water bath, and the temperature of the downstream volume was enclosed in an insulated box fixed at 35 °C. Once enough time passed for the flux through the membrane to have reached steady state, the line to the vacuum pump was closed. The rate of pressure increase in the downstream volume was monitored and used to calculate the number of moles of gas transported through the membrane over time using the ideal gas law. This technique is not dependent upon the proper calibration and operation of detector-based systems like Mocon devices. In all cases, the driving force did not change significantly during the course of the experiment because the upstream ballast volume was large, and the pressure of the downstream volume never exceeded 10 torr, which was a small fraction of the pressure in the upstream. This information was then coupled with the membrane thickness and area to calculate the permeability of the test gas at a fixed temperature and upstream pressure [29].

Because of the potential for CO<sub>2</sub> to plasticize membranes, which leads to increased gas permeability and decreased gas pair selectivity, the gases were tested in the following order: N<sub>2</sub>, O<sub>2</sub>, CO<sub>2</sub>.

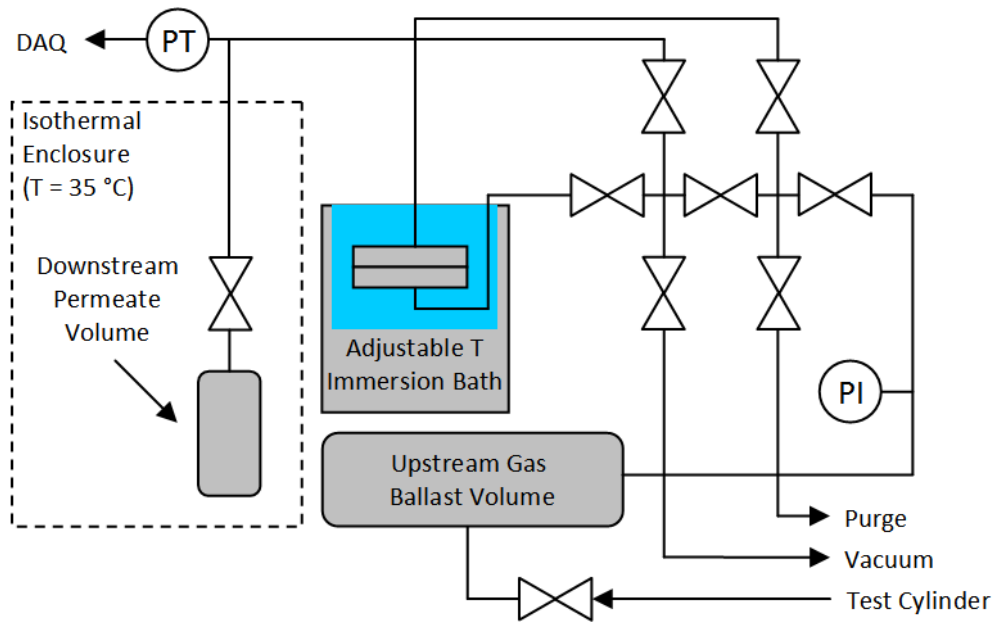


Figure 3.3. Constant volume, variable pressure gas permeation system [30] used to measure the permeability of a single gas through low to moderate flux membranes.

### 3.4 COEXTRUDED MULTILAYERED B-iPP/PEBAX FILMS

#### 3.4.1 Materials Selection

A grade of iPP (Dow H7012-35RN) with lower viscosity (MFI = 35) than the other iPP samples considered earlier was selected for multilayering with the highest permeability PEBAX sample, PEBAX 2533, to coextrude multilayered films suitable for modified atmosphere packaging applications. This grade of iPP was selected to ensure a viscosity match between the  $\beta$ -iPP and PEBAX 2533 during coextrusion.

#### 3.4.2 Film Preparation

The multilayered membranes characterized in this project were coextruded at Case Western Reserve University using their microlayering coextrusion system. This

device is capable of splitting and stacking flows of polymer melt an arbitrary number of times using layer multiplication elements to create as many layers as desired. It is typical to produce multilayered films with hundreds or even thousands of layers at layer thicknesses under 100 nm. A schematic of this approach is shown in Figure 3.4 [31].

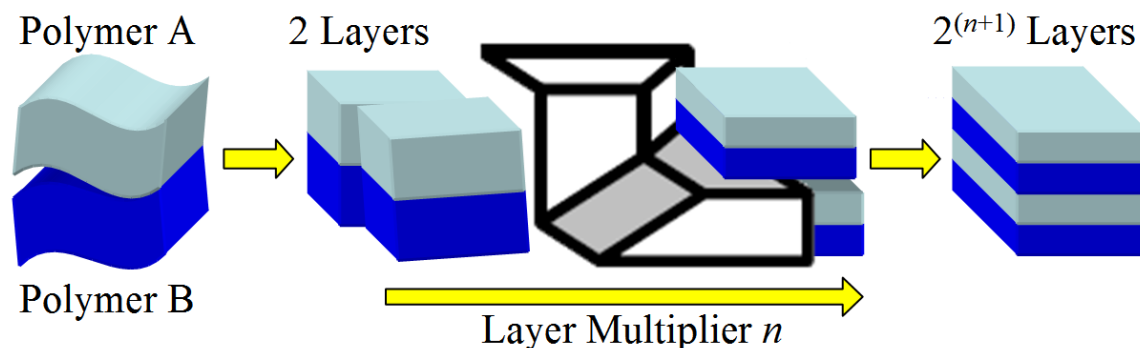


Figure 3.4. Coextrusion process used to produce multilayered membranes. In the AB feedblock configuration, two rheologically compatible polymers are combined in the melt, using  $n$  layer multiplication elements to produce  $2^{(n+1)}$  layers. The AB feedblock delivering the polymer melt can also be exchanged to an ABA feedblock so that  $2^{(n+1)} + 1$  layers are produced. Outside skin layers may also be introduced after layer multiplication is complete.

In this study, the coextruder was fitted with the ABA feedblock, producing  $2^{(n+1)} + 1$  layers. These multilayer films were produced at compositions of 10 and 30 vol. % PEBAX. These low concentrations of PEBAX were selected to minimize the total thickness of the layer (or layers) intended to provide the most resistance to mass transfer. Two different layer configurations were examined:

1. 3-layer films, with two layers of PEBAX sandwiching a single  $\beta$ -iPP layer;
2. 17-layer films, with nine layers of PEBAX sandwiching eight  $\beta$ -iPP layers.

In the first case, the ABA feedblock was used to directly produce a 3-layer film. In the second case, three layer multiplication elements were used in concert with the ABA feedblock to increase the number of layers of PEBAX present. It was hypothesized that increasing the number of layers might decrease the possibility that defects in any given layer would significantly diminish the separation performance of the composite membrane. The nomenclature for these films is [Layers]L-[vol. % PEBAX], where, for example, 3L-10 is a multilayered film with three total layers and 10 vol. % PEBAX in the film. Films were extruded at 190 °C, like the PEBAX single layer films, and at a nominal thickness of 100 µm.

Test samples 8.5×8.5 cm in size were cut from the center of the extruded film for consistency of thickness, and they were subjected to biaxial stretching at 100 °C and 100 %s<sup>-1</sup>. 3L-30 films were stretched at draw ratios of 1.6, 1.8, 2.0, and 2.2. These films were tested for permeability at the University of Texas using a constant volume, variable pressure device. Additional films of the 3L-10, 3L-30, 17L-10, and 17L-30 types were stretched at a draw ratio of 2.0. 3L-10 films underwent thermal annealing at 140 °C for 30 min. and were stretched at a draw ratio of 2.0 for comparison to as-extruded films. These additional films were tested for permeability by our collaborators at Case Western Reserve University using Mocon devices.

Landec Intellipac MAP composite membranes were obtained for comparison to PEBAX-based materials in this study. These membranes were measured for thickness and tested for permeability using the constant volume, variable pressure technique.

### **3.4.3 Film Thickness Determination**

Multilayer film thicknesses were determined as described for single layer PEBAX films. The total thickness of a single component is estimated to be the volume fraction of

that component multiplied by the multilayered film thickness. To estimate the thicknesses of single layers in the films, the total thickness of a single component is divided by the number of layers of that component.

#### **3.4.4 Scanning Electron Microscopy (SEM)**

SEM of cross-sections was performed to confirm the expected multilayer structure was intact after the extrusion and stretch process.

#### **3.4.5 Gas Permeability**

Gas permeability was measured using Mocon devices and constant volume, variable pressure techniques described for single layer PEBA films.

#### **3.4.6 Modeling of MAP Performance**

The performance of multilayered films in achieving suitable atmospheric compositions in a produce package was modeled using techniques developed previously in our laboratories [32,33]. In particular, headspace gas compositions achieved when packaging a standard quantity of apples at various temperatures were examined, and the required membrane area was calculated. These calculations were performed under the simplifying condition that package pressure is constant.

### 3.5 REFERENCES

- [1] J. Varga,  $\beta$ -Modification of Isotactic Polypropylene: Preparation, Structure, Processing, Properties, and Application, *Journal of Macromolecular Science, Part B*. 41 (2002) 1121–1171.
- [2] M. Fujiyama, Structures and properties of injection moldings of beta-crystal nucleator-added polypropylenes., *International Polymer Processing*. 11 (1996) 271–274.
- [3] H. Bai, Y. Wang, Z. Zhang, L. Han, Y. Li, L. Liu, et al., Influence of Annealing on Microstructure and Mechanical Properties of Isotactic Polypropylene with  $\beta$ -Phase Nucleating Agent, *Macromolecules*. 42 (2009) 6647–6655.
- [4] H. Bai, F. Luo, T. Zhou, H. Deng, K. Wang, Q. Fu, New insight on the annealing induced microstructural changes and their roles in the toughening of  $\beta$ -form polypropylene, *Polymer*. 52 (2011) 2351–2360.
- [5] L. Poussin, Y.A. Bertin, J. Parisot, C. Brassy, M. De, D. Physique, et al., Influence of thermal treatment on the structure of an isotactic polypropylene, *Polymer*. 39 (1998) 4261–4265.
- [6] F. Chu, Structure and gas permeability of microporous films prepared by biaxial drawing of  $\beta$ -form polypropylene, *Polymer*. 37 (1996) 573–579.
- [7] W. Zhu, X. Zhang, C. Zhao, W. Wu, J. Hou, M. Xu, A Novel Polypropylene Microporous Film, *Polymers for Advanced Technologies*. 7 (1996) 743–748.
- [8] S. Ran, M. Xu, Studies on the Pore Formation Mechanism of  $\beta$ -Crystalline Polypropylene Under Stretching, *Chinese Journal of Polymer Science*. 22 (2004) 123–130.
- [9] G. Shi, X. Zhang, J. Zheng, G. Zhou, Microporous Film, Made from  $\beta$ -Crystalline Phase Polypropylene, *International Polymer Processing*. 10 (1995) 330–333.
- [10] F. Chu, T. Yamaoka, H. Ide, Y. Kimura, Microvoid formation process during the plastic deformation of  $\beta$ -form polypropylene, *Polymer*. 35 (1994) 3442–3448.
- [11] J.X. Li, W.L. Cheung, D. Jia, A study on the heat of fusion of  $\beta$ -polypropylene, *Polymer*. 40 (1999) 1219–1222.

- [12] J.X. Li, W.L. Cheung, A Correction Function to Determine the  $\beta$ -Fusion Heat in a Mixture of  $\alpha$ - and  $\beta$ -PP, *Journal of Thermal Analysis and Calorimetry*. 61 (2000) 757–762.
- [13] A. Turner Jones, J.M. Aizlewood, D.R. Beckett, Crystalline Forms of Isotactic Polypropylene, *Die Makromolekulare Chemie*. 75 (1964) 134–158.
- [14] M. Dong, Z. Guo, J. Yu, Z. Su, Study of the assembled morphology of aryl amide derivative and its influence on the nonisothermal crystallizations of isotactic polypropylene, *Journal of Polymer Science Part B: Polymer Physics*. 47 (2009) 314–325.
- [15] M. Dong, Z. Guo, Z. Su, J. Yu, The effects of crystallization condition on the microstructure and thermal stability of isotactic polypropylene nucleated by  $\beta$ -form nucleating agent, *Journal of Applied Polymer Science*. 119 (2011) 1374–1382.
- [16] P. Jacoby, B.H. Bersted, W.J. Kissel, C.E. Smith, Studies on the  $\beta$ -Crystalline form of Isotactic Polypropylene, *Journal of Polymer Science Part B: Polymer Physics*. 24 (1986) 461–491.
- [17] G. Zhou, Z. He, J. Yu, Z. Han, Characterization of the  $\beta$ -form and study of the  $\beta$ - $\alpha$  transition during heating by wide angle X-ray diffraction, *Die Makromolekulare Chemie*. 187 (1986) 633–642.
- [18] J. Kotek, M. Raab, J. Baldrian, W. Grellmann, The effect of specific  $\beta$ -nucleation on morphology and mechanical behavior of isotactic polypropylene, *Journal of Applied Polymer Science*. 85 (2002) 1174–1184.
- [19] F. Bai, F. Li, B.H. Calhoun, R.P. Quirk, S.Z.D. Cheng, Physical Constants of Poly(propylene), in: J. Brandrup, E.H. Immergut, E.A. Grulke (Eds.), *Polymer Handbook*, 4th ed., New York, John Wiley & Sons, Inc., 1999: p. V/21–V/30.
- [20] E.W. Washburn, The Dynamics of Capillary Flow, *Physical Review*. 17 (1921) 273–283.
- [21] S.D. Kelman, S. Matteucci, C.W. Bielawski, B.D. Freeman, Crosslinking poly(1-trimethylsilyl-1-propyne) and its effect on solvent resistance and transport properties, *Polymer*. 48 (2007) 6881–6892.
- [22] R.D. Raharjo, B.D. Freeman, D.R. Paul, G.C. Sarti, E.S. Sanders, Pure and mixed gas CH<sub>4</sub> and n-C<sub>4</sub>H<sub>10</sub> permeability and diffusivity in poly (dimethylsiloxane ), *Journal of Membrane Science*. 306 (2007) 75–92.

- [23] S.R. Armstrong, D.R. Paul, A. Hiltner, Permeability of Poly (ether block amide) (PEBAX): Effect of Orientation, in: Abstracts of Papers, 240th ACS National Meeting, Boston, MA, American Chemical Society, 2010: p. PMSE – 193.
- [24] S. Armstrong, B. Freeman, A. Hiltner, E. Baer, Gas permeability of melt-processed poly(ether block amide) copolymers and the effects of orientation, *Polymer*. 53 (2012) 1383–1392.
- [25] V.I. Bondar, B.D. Freeman, I. Pinnau, Gas sorption and characterization of poly(ether-b-amide) segmented block copolymers, *Journal of Polymer Science Part B: Polymer Physics*. 37 (1999) 2463–2475.
- [26] M.E. Rezac, T. John, P.H. Pfromm, Effect of copolymer composition on the solubility and diffusivity of water and methanol in a series of polyether amides, *Journal of Applied Polymer Science*. 65 (1997) 1983–1993.
- [27] ASTM, D3985: Standard Test Method for Oxygen Gas Transmission Rate Through Plastic Film and Sheeting Using a Coulometric Sensor, *ASTM Book of Standards*. 15.10 (n.d.).
- [28] ASTM, F2476: Test Method for the Determination of Carbon Dioxide Gas Transmission Rate (CO<sub>2</sub> TR) Through Barrier Materials Using An Infrared Detector, *ASTM Book of Standards*. 15.10 (n.d.).
- [29] H. Lin, B.D. Freeman, *Springer Handbook Part C: Measurement Methods for Materials Properties*, Ch. 7 Sect. 6, Permeation and Diffusion, in: *Springer Handbook*, 2006.
- [30] W.J. Koros, D.R. Paul, A.A. Rocha, Carbon Dioxide Sorption and Transport in Polycarbonate, *Journal of Polymer Science Part B: Polymer Physics*. 14 (1976) 687–702.
- [31] C.D. Mueller, S. Nazarenko, T. Ebeling, T.L. Schuman, A. Hiltner, E. Baer, Novel Structures by Microlayer Coextrusion - Talc-Filled PP, PC/SAN, and HDPE/LLDPE, *Polymer Engineering & Science*. 37 (1997) 355–362.
- [32] B.S. Kirkland, R. Clarke, D.R. Paul, A versatile membrane system for bulk storage and shipping of produce in a modified atmosphere, *Journal of Membrane Science*. 324 (2008) 119–127.
- [33] D.R. Paul, R. Clarke, Modeling of modified atmosphere packaging based on designs with a membrane and perforations, *Journal of Membrane Science*. 208 (2002) 269–283.

- [34] G.T. Offord, S.R. Armstrong, B.D. Freeman, E. Baer, A. Hiltner, J.S. Swinnea, et al., Porosity Enhancement in  $\beta$  Nucleated Isotactic Polypropylene Stretched Films by Thermal Annealing, *Polymer*. Accepted (2013).
- [35] G.T. Offord, S.R. Armstrong, B.D. Freeman, E. Baer, A. Hiltner, D.R. Paul, Influence of Processing Strategies on Porosity and Permeability of  $\beta$  Nucleated Isotactic Polypropylene Stretched Films, *Polymer*. Accepted (2013).

## **Chapter 4. Porosity Enhancement in $\beta$ Nucleated Isotactic Polypropylene Stretched Films by Thermal Annealing**

### **4.1 SUMMARY**

Microporous polymer membranes were fabricated by extrusion, thermal annealing, and subsequent biaxial stretching of  $\beta$  nucleated isotactic polypropylene. Fabrication conditions were optimized based on prior studies so that the influence of annealing on precursor film crystallinity and pore formation in such films upon stretching could be investigated. Annealing perfected the crystalline structure of these materials, as evidenced by thermal and x-ray techniques. A mechanism detailing the annealing and pore formation process during biaxial stretching is presented. An appropriate metric was developed to relate the crystallinity of the precursor films to the porosity of the films after biaxially stretching. The porosity developed in biaxially stretched films increased substantially when its precursor was annealed near the melting temperature of  $\beta$  crystalline material, enabling the production of high permeability microporous membranes.

---

This chapter has been adapted with permission from the following article:  
G.T. Offord (author, primary experimentalist), S.R. Armstrong (editor, sample preparation), B.D. Freeman (editor), E. Baer (editor), A. Hiltner (editor), J.S. Swinnea (XRD experiments), D.R. Paul (editor), *Polymer*. 54 (2013) 2577–2589.

## 4.2 RESULTS AND DISCUSSION

### 4.2.1 $\beta$ -Crystallinity in Precursor and Stretched iPP Films

Thermal analysis of precursor and stretched  $\beta$ -iPP films was performed by DSC. These experiments provided insight about the populations of crystals in a given film as they melted during the scan. The evolution of the crystalline material in precursor films for each of the three annealing conditions was tracked, and further changes in the crystalline material were observed as the films were stretched. Several key properties arising from the crystallinity of the precursor films are presented in Table 4.1.

Table 4.1. Selected Crystalline Properties of  $\beta$ -iPP Precursor Films Determined by DSC.

Sample Code	$T_m(\beta_1)$ ( $^{\circ}\text{C}$ )	$X_c$	$K_{\beta,\text{DSC}}$	$X_{\beta_1}/X_c$	$\Phi_{\beta_1}$	$\rho_{\text{DSC}}$ ( $\text{g}/\text{cm}^3$ )
12M-23A-P	141.8	0.65	0.50	0.249	0.158	0.902
3.5M-23A-P	143.8	0.61	0.47	0.298	0.176	0.899
2.1M-23A-P	143.6	0.58	0.43	0.299	0.169	0.897
12M-130A-P	143.3	0.62	0.48	0.342	0.207	0.900
3.5M-130A-P	144.9	0.60	0.46	0.378	0.219	0.898
2.1M-130A-P	144.6	0.58	0.42	0.374	0.213	0.898
12M-140A-P	143.7	0.66	0.49	0.371	0.240	0.903
3.5M-140A-P	145.9	0.73	0.50	0.430	0.307	0.908
2.1M-140A-P	145.1	0.70	0.48	0.409	0.279	0.906

Heat flows measured during first heating DSC scans of precursor films are presented in Figure 4.1. In each precursor film scan, distinct melting peaks for  $\beta_1$ ,  $\beta_2$  and  $\alpha$  endotherms were observed. Double  $\beta$  peaks, seen in the form of  $\beta_1$  and  $\beta_2$  endotherms, are typical of polymorphic  $\beta$ -iPP. These peaks occur when the polymer has been crystallized at temperatures below  $125\text{ }^{\circ}\text{C}$ , and are due to the instability of the  $\beta_1$  crystals formed at high cooling rates and their propensity to recrystallize to  $\beta_2$  [1–3]. This phenomenon has also been seen to occur during nonisothermal crystallization [4], as is used in this study.

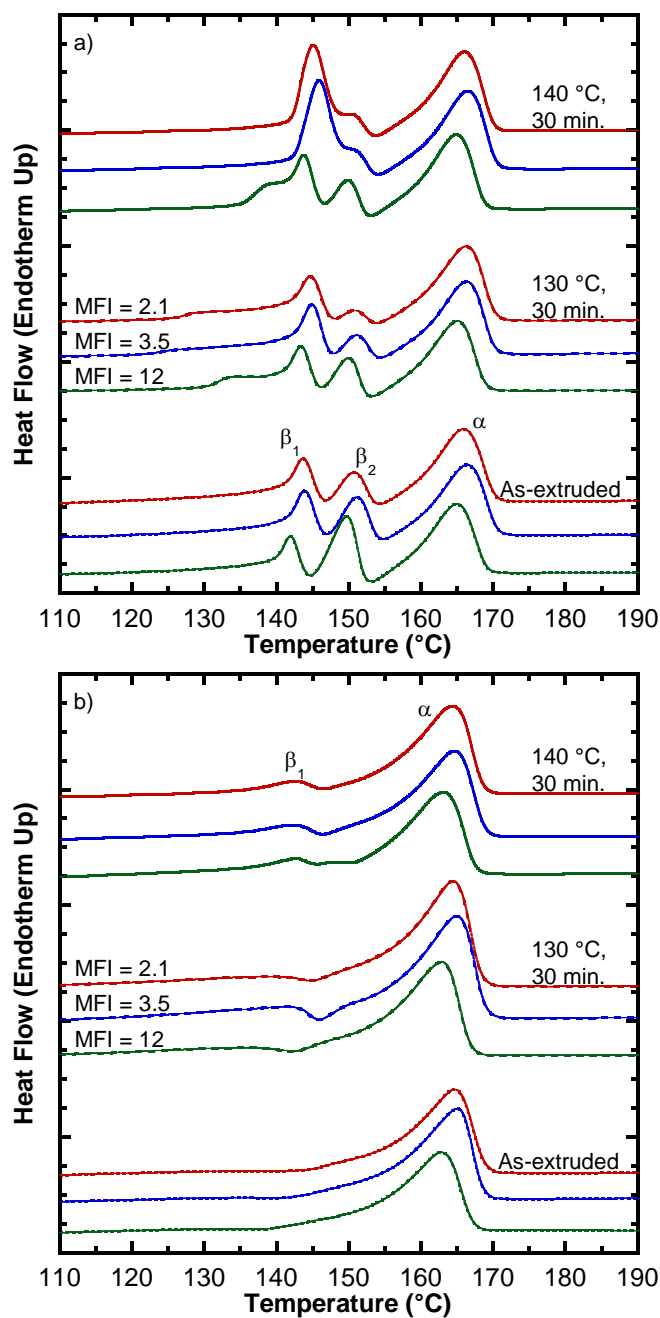


Figure 4.1. DSC first heating scans of: a) precursor films extruded from  $\beta$ -iPP having a MFI of 2.1, 3.5, and 12 that were then annealed at 23 °C (as-extruded), 130 °C, and 140 °C for 30 minutes, and accompanying scans for b) microporous films produced by biaxially stretching these precursor films at 100 °C. Thermograms are displaced vertically for ease of viewing, and significant melting peaks corresponding to  $\beta_1$ , and  $\beta_2$  and  $\alpha$  endotherms are labeled.

Melting peak temperatures for  $\beta_1$  material in the precursor films increased with increasing annealing temperature, as shown in Table 4.1. The nonisothermal crystallization of  $\beta$ -iPP was achieved with temperatures at or above the chill roll temperature of 95 °C, and films were cooled to room temperature before characterization. Thus, the critical temperature of recooling (100 to 110 °C) [5] was reached in all samples. This temperature is defined as that below which  $\alpha$  nuclei are formed in the  $\beta$  phase, resulting in  $\alpha$  recrystallization during  $\beta$  melting. This bears mentioning here, because re-cooled samples that are then annealed below the melting temperature of the  $\beta_1$  material exhibit greater stability and a correspondingly higher melting point for the  $\beta_1$  material [6], consistent with observations in this study. At a given annealing temperature, melting peak temperatures observed were about 2 °C lower in 12 MFI iPP precursors than in the two lower MFI iPP precursors. Few studies examine the effect of iPP homopolymer MFI on  $\beta$  crystal melting peak temperature, but two related papers by Varga *et al.* show that a 5.5 MFI iPP has a melting temperature about 1 °C lower than that of a 0.76 MFI iPP [1,2]. This result was obtained under controlled crystallization conditions, contrasting with crystallization during extrusion and chill roll take-up used in this study. Precursor annealing temperature did not influence the melting peak temperatures of  $\beta_2$  ( $T_m = 150$  °C) or of  $\alpha$  ( $T_m = 166$  °C) material, but 12 MFI iPP precursors exhibited a peak at about 165 °C, roughly 1 °C lower than the two lower MFI iPP precursors. The lower melting temperatures observed in the 12 MFI iPP can be attributed to the reduced chain entanglement that accompanies lower molecular weight. Observed melting temperatures were consistent with similar materials previously studied [7,8].

The sizes of the  $\beta_1$ ,  $\beta_2$  and  $\alpha$  endotherms associated with the melt-recrystallization processes occurring during the first heat were used to calculate most of the properties in Table 4.1. Because of the melt-recrystallization that occurs in polymorphic  $\beta$ -iPP during

the heating scan, the calculated crystallinity,  $X_c$ , may not be equal to the crystallinity of the precursor film just after the annealing step. It is more useful to observe the crystallinities  $X_i$  individually to track changes in  $\beta$ -iPP materials as they are annealed. A quantity analogous to  $K_{\beta,A}$  for XRD measurements can be defined as follows:

$$K_{\beta,DSC} = \frac{X_{\beta_1} + X_{\beta_2}}{X_c} \quad (4.1)$$

which is meant to provide a measure of the relative content of  $\beta$ -crystalline material in the film [9]. A technique employing simultaneous DSC and XRD of polymorphic  $\beta$ -iPP has been previously performed to decouple melting and crystallization of the  $\alpha$  and  $\beta$  crystalline material [8,10], but the results of this study can be interpreted using simpler techniques. As the annealing temperature is increased, there is no apparent trend in either the calculated precursor  $X_c$  or  $K_{\beta,DSC}$ , although there is a slight increase in  $X_c$  at an annealing temperature of 140 °C. The most apparent effect of increasing the precursor annealing temperature was an accompanying enlargement of the  $\beta_1$  endotherm and a decrease in  $\beta_2$  endotherm size. The size of the  $\alpha$  endotherm remained relatively constant across all annealing treatments, likely due to the ability of the  $\beta$  crystals to melt and then recrystallize to  $\alpha$  phase crystals in samples cooled below the critical temperature of recooling [5]. This effect is especially pronounced when the sample undergoes crystallization at a large supercooling [6,11,12], and in this study, crystallization was performed at a large supercooling and the final crystallization temperature was below the critical temperature of recooling. Recrystallization may mask any change in the amount of  $\alpha$  material present prior to annealing. The slight increase in calculated  $X_c$  at an annealing temperature of 140 °C results from a greater increase in  $\beta_1$  endotherm size than the corresponding decrease in  $\beta_2$  endotherm size.

The evolution of the  $\beta$  endotherms as annealing temperature increases proceeds in the following way. Initially, a low temperature “shoulder” in the endotherm develops as the  $\beta_1$  melting peak is approached, and it is accompanied by both an increase in peak heat flow and area in the  $\beta_1$  region and a decrease in  $\beta_2$  peak heat flow and area. When annealing temperature is further increased, the shoulder develops at temperatures closer to the  $\beta_1$  melting peak, and it eventually disappears as it is incorporated into an increasingly smooth  $\beta_1$  endotherm. The  $\beta_2$  endotherm concurrently decreases in size and becomes a shoulder to the  $\beta_1$  endotherm. Similar behavior has been reported previously, and it can be reasonably characterized as the perfection of the  $\beta$  crystal structure [13]. The  $\beta_1$  endotherm grows due to an increased size and quantity of  $\beta$  crystals, and the  $\beta_2$  endotherm decreases in size due to the higher melting point of the  $\beta_1$  endotherm and the resulting smaller window to recrystallize to the  $\beta_2$  form [14]. The melting peak elevation of the  $\beta_1$  endotherm provides additional evidence for the growth of  $\beta$  crystals upon annealing.

In the case of films annealed at 130 °C, the onset temperature of the shoulder peaks differ from one film to the next, with a range of about 125 to 131 °C. The onset temperature is related to the annealing temperature [15], which could indicate that the true annealing temperature deviates from the reported temperature. Since the deviation is small, we believe the results are not significantly affected.

Precursor films extruded from 12 MFI iPP showed less development of the  $\beta$  endotherms than the higher MFI precursor films at all annealing temperatures. In the case of the 12M-140A-P film, the annealing temperature was sufficiently close to the peak melting temperature of the  $\beta_1$  endotherm ( $T_m(\beta_1) = 141.8$  °C) that the development of larger  $\beta$  crystals with higher melting temperatures may have been impeded. A less perfected crystal structure compared to lower MFI films may explain the remaining

shoulder at a temperature below the  $\beta_1$  melting peak as well as the more pronounced  $\beta_2$  endotherm in the 12M-140A-P film.

Contrary to other studies that examine similar extruded  $\beta$ -iPP materials [16], the precursor film density calculated from an additive model of the constituent phases based upon crystalline contents determined by DSC,  $\rho_{\text{DSC}}$ , which is shown in Table 4.1, differs by less than one percent from precursor density measured directly. Thus, for the materials examined in this study, the simple model of material composition involving only amorphous and  $\alpha$  and  $\beta$  crystalline material is consistent with the actual material composition. Because of the possibility of “double counting” crystalline material as it recrystallizes to both the  $\alpha$  and  $\beta$  phases, these values should be considered less reliable than those obtained by XRD.

First heating scans on biaxially stretched films corresponding to the precursor films discussed above are also presented in Figure 4.1. Very weak (if any)  $\beta_1$  melting peaks and strong  $\alpha$  melting peaks were observed. Compared to precursor films, the melting peak temperatures of the  $\beta_1$  and  $\alpha$  endotherms were depressed by about 1 °C. Previous studies show that mechanical deformation of  $\beta$ -iPP can destroy  $\beta$  crystals [17], result in a rearrangement from  $\beta$  to  $\alpha$  crystalline material [3,6,11,17,18], or have both a destructive and transformative effect. A reduction in crystal size resulting from these processes may account for the observed decrease in melting peak temperatures upon stretching. The change in size of these endotherms is also consistent with these crystal phase rearrangements. In films where the precursor was stretched without further precursor annealing, no  $\beta_1$  endotherm was detectable, while higher temperature annealing of precursors resulted in a small amount of residual  $\beta$  material appearing in the  $\beta_1$  endotherm. Thus, the  $\beta$  material was indeed either destroyed or transformed, and this process occurred to a greater extent when the  $\beta$  crystals had been less perfected through

the annealing process. The size of the  $\alpha$  endotherm was increased upon stretching in all cases, which is possibly evidence of either a strain-induced transformation from  $\beta$  to  $\alpha$ , recrystallization to  $\alpha$  during the scan, or both. The onset of the  $\alpha$  endotherm also occurred at a lower temperature than precursor films. The lower temperature onset could indicate either a lower melting temperature for some of the newly formed  $\alpha$  crystals or the formation of a small  $\beta_2$  endotherm that cannot be distinguished from the  $\alpha$  endotherm.

Low  $\beta$  nucleator concentration is one potential cause of the instability that results in double peaks observed in the precursor first heating scans [2]. Second heating scans of both precursor and stretched samples (not shown) were nearly identical to one another, featuring a single large  $\beta$  endotherm at about 150 °C and a diminished  $\alpha$  endotherm at about 166 °C. The single  $\beta$  endotherm observed in the second heat scan demonstrates that the crystallization process, not the nucleator concentration, most likely contributes to the double  $\beta$  peaks in the first scans [19]. Crystallization conditions induced by the extrusion and annealing process always led to double peaks and were a significant factor influencing the performance of the porous films produced by stretching in this study.

Characteristic reflections of  $\alpha$  and  $\beta$  crystals in precursor films and stretched films were generated by using XRD techniques frequently employed for characterization of similar  $\beta$ -iPP materials [18,20–22]. Compared to DSC analysis, XRD permits the quantification of crystalline material without thermal transitions as confounding factors. Solvent extraction and depolarized light intensity methods have also been used [21] to quantify  $\beta$  content, but these were not considered here because they are time-consuming techniques, and are not as prevalent in the literature as XRD. The effect of annealing on precursor film crystalline content and the effect of the stretching process on the crystalline material can then be more clearly understood relative to DSC alone. Table 4.2

summarizes some of the key properties calculated from diffraction patterns of precursor films.

Table 4.2. Selected Properties of  $\beta$ -iPP Precursor Films Determined by X-Ray Diffraction.

Sample Code	$D_{300}$ (nm)	$X_c$	$K_{\beta,H}$	$K_{\beta,A}$	$\rho_{XRD}$ (g/cm <sup>3</sup> )
12M-23A-P	41	0.68	0.99	0.98	0.900
3.5M-23A-P	42	0.68	0.99	0.95	0.900
2.1M-23A-P	42	0.70	0.99	0.95	0.902
12M-130A-P	45	0.64	0.97	0.93	0.898
3.5M-130A-P	43	0.72	0.98	0.91	0.903
2.1M-130A-P	44	0.74	0.97	0.91	0.904
12M-140A-P	48	0.71	0.97	0.90	0.903
3.5M-140A-P	46	0.73	0.93	0.86	0.904
2.1M-140A-P	53	0.71	0.95	0.89	0.903

Diffraction peaks for the MFI 2.1 precursor and stretched films are presented in Figure 4.2. There were no significant differences between the patterns from these films and those from higher MFI iPP materials, so for brevity only the MFI 2.1 patterns are shown.

The K value and double peak behavior can be altered by varying  $\beta$  nucleator content [2,22]. One study reported a maximum in K value using iPP with an MFI of 8, but this effect was observed at a very low  $\beta$  nucleator loading (0.1 – 0.3 ppm) and a low K value (below 0.6) was attained [22]. As  $\beta$  nucleator content was increased, the sensitivity of K to MFI decreased, consistent with another study where, at still higher nucleator content, no effect was observed [2]. In this study, the influence of iPP MFI on precursor crystallinity appears to be confined to the stability of the  $\beta$  crystalline material present, since no effect on the amount of  $\beta$  material or precursor K value was observed in XRD experiments.

The  $(300)_\beta$  diffraction peak was found at about  $2\theta = 16.1^\circ$ , and the  $(110)_\alpha$ ,  $(040)_\alpha$  and  $(130)_\alpha$  peaks were found at  $2\theta = 14.2$ ,  $17.0$  and  $18.6^\circ$ , respectively, consistent with a prior study [7]. Two metrics characterizing  $\beta$  crystalline content by XRD are  $K_{\beta,H}$  and  $K_{\beta,A}$ , and they are recorded for precursor films in Table 4.2. The former is calculated using the intensity of equatorial  $\beta$  peaks in a pattern, while the latter is based on the area of those same peaks. The originally conceived [20] and most widely used K value is  $K_{\beta,H}$ , but for consistency with the presentation of  $X_c$ , which is calculated based on the ratio of crystalline peak area to total area,  $K_{\beta,A}$  will be primarily used for analysis and also presented alongside  $K_{\beta,H}$ . This approach has the additional advantage of generating a broader range of K values, since the peak intensity is much greater for  $(300)_\beta$  than for the  $\alpha$  peaks.

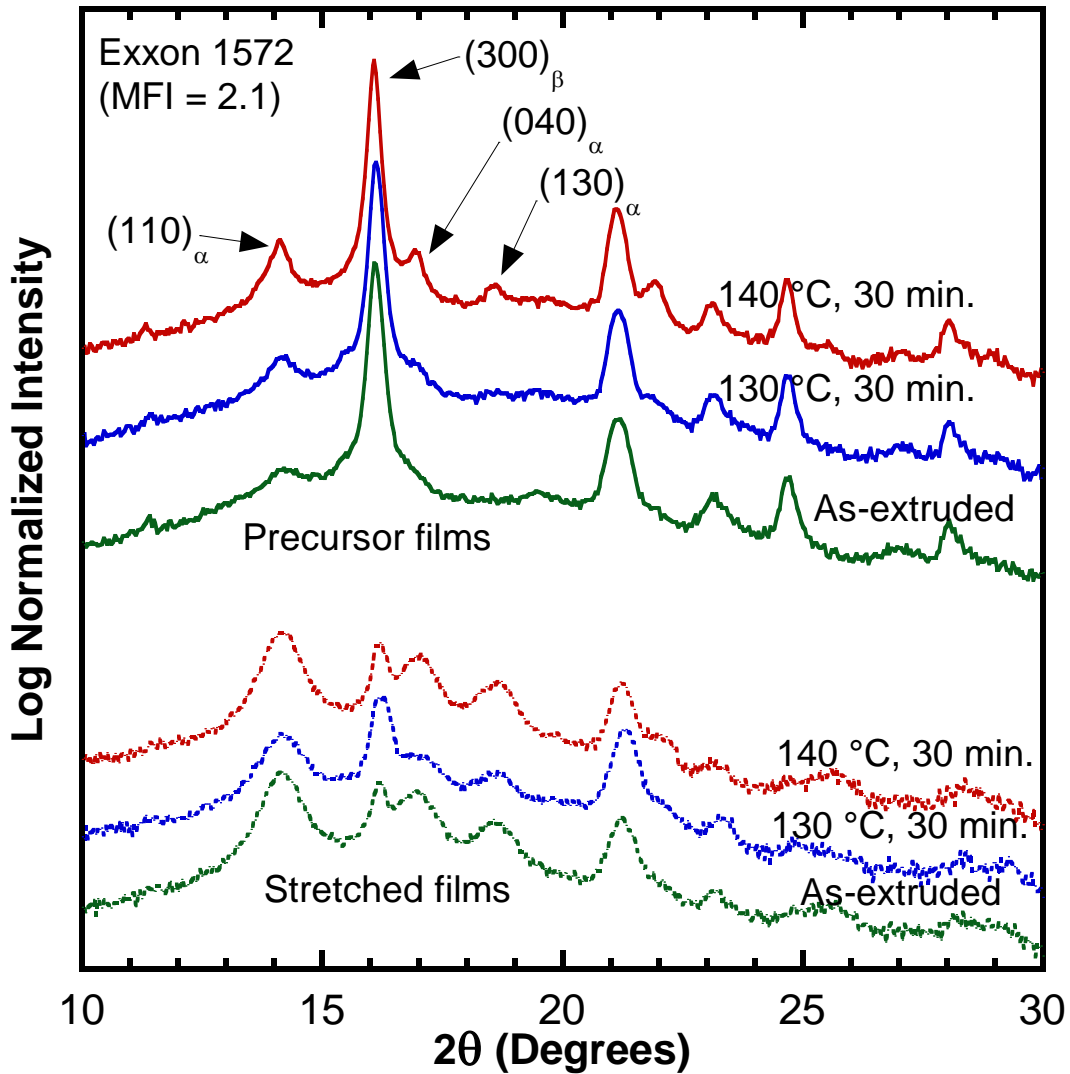


Figure 4.2. XRD patterns of Exxon 1572 (MFI 2.1)  $\beta$ -iPP precursor films annealed at 23 °C (as-extruded), 130 °C, and 140 °C for 30 minutes (top scans) and accompanying patterns for these films stretched at 100 °C (bottom scans). Significant reflections corresponding to  $\alpha$  and  $\beta$  peaks are labeled, and patterns are displaced vertically for ease of comparison.

Studies on crystallization of  $\beta$ -iPP have compared the growth rates of  $\alpha$  and  $\beta$  crystals as a function of temperature within a temperature window of 105 to 140 °C, where the growth rate of  $\beta$  crystals is faster than that of  $\alpha$  crystals [6,11]. Crystallization behavior in  $\beta$ -iPP assists in rationalizing the XRD results. The two annealing

temperatures selected in this study were situated in the temperature window where  $\beta$  grows more rapidly than  $\alpha$  to ensure  $\beta$  material remained available to induce pore formation. Precursors annealed at 130 °C correspond to samples annealed at the same temperature in another study [13] that resulted in the maximization of both the fraction of  $\beta$  material and impact strength. The maximum temperature where the growth of  $\beta$  material is preferred to  $\alpha$  is 140 °C, so a significant loss of  $\beta$  material during precursor annealing is avoided if this temperature is not exceeded.

Analysis of XRD patterns from precursor films show that the total amount of  $\beta$  crystalline material decreased slightly with increasing annealing temperature, while the total amount of  $\alpha$  crystalline material increased substantially with increasing annealing temperature. This can be verified by noting that the value of  $X_c$  is relatively stable as annealing temperatures are increased, while both  $K_{\beta,H}$  and  $K_{\beta,A}$  values decrease with increasing annealing temperature. The balance crystallinity must then be made up of crystalline material in the  $\alpha$  phase. The decrease in  $\beta$  material observed when annealing at 140 °C is likely due to some degree of melting of  $\beta$  and recrystallization to  $\alpha$  arising from the instability of low-melting  $\beta$  material, and exposure to an annealing temperature where the growth of  $\beta$  is only slightly preferred to  $\alpha$ . A smaller change along these lines is apparent at 130 °C, where  $\alpha$  growth is not as strongly preferred as at 140 °C.

The growth of  $\alpha$  content with increasing annealing temperature is anticipated by the decline in  $\beta$  content. The amount of growth of the  $\alpha$  content, however, is too great to be accounted for by only the transformation of  $\beta$  to  $\alpha$  during annealing. The value of  $X_c$  increases slightly even as  $K_{\beta,A}$  decreases, indicating an excess growth of  $\alpha$  material that must be explained by some other mechanism. The increase in both  $\alpha$  material and  $X_c$  likely results from the transformation of semi-ordered smectic iPP to ordered  $\alpha$  crystalline PP, which is known to occur in iPP that has been rapidly cooled and then heat

treated above 80 °C [23], similar to the thermal history of samples used in this study. Precursor density values calculated from crystalline composition,  $\rho_{\text{XRD}}$ , are within the uncertainty of the directly measured density values.

Patterns from films biaxially stretched at 100 °C are also shown in Figure 4.2. Significant  $\alpha$  and  $\beta$  diffraction peaks did not change position relative to precursor film scans, but large changes in intensity were observed. For all precursors and annealing conditions, the intensity of the  $(300)_{\beta}$  reflection was reduced by more than 90% after stretching. This observation, along with DSC first heat scans which show the near-complete disappearance of  $\beta_1$  endotherms, provides evidence supporting a large scale destruction of  $\beta$  material upon stretching. Prior studies show a similar large reduction in the K value of  $\beta$ -iPP films upon stretching uniaxially [16,18,24] or biaxially [16,25] under comparable crystallization conditions. The change in  $\alpha$  material is also readily apparent, with all equatorial  $\alpha$  reflections increasing in intensity relative to precursor films. This increase is consistent with the idea that  $\alpha$  crystals form upon deformation of  $\beta$ -iPP films [24]. Additionally, the XRD measurement is not confounded by the potential recrystallization to  $\alpha$  caused by the temperature ramp used in thermal analysis, which made it difficult to confirm the growth of  $\alpha$  material induced by stretching.

An interesting outcome of stretching films that were annealed under different conditions is that XRD patterns of these films do not display systematic patterns based on their annealing treatment or iPP MFI. Thus, trends existing in precursor films, such as the increase in  $\alpha$  material (or decrease in K value) with increasing annealing temperature, do not persist after stretching. There are several reasons for the inability to identify trends in post-stretch patterns. First, the  $\alpha$  material formed during stretching is much greater in quantity than that found in precursors prior to stretching. Second, existing  $\alpha$  material may be lost during stretching, even as new  $\alpha$  material is formed. Third, the amount of

additional  $\alpha$  material formed is related to the existing quantity and stability of  $\beta$  material, which differs between films having different annealing treatments. The situation is much the same for DSC first heating scans of stretched films, although in that case there are some subtle systematic differences in the  $\beta$  phase resulting from precursor annealing conditions. Overall, the morphology present in extruded precursor films is disrupted by the biaxial stretching process, which simultaneously induces pore formation and thereby reduces organization of the remaining crystallinity and alters XRD reflections. Due to the difficulty of differentiating measures of crystallinity after stretching, it seems likely that the change in crystallinity during stretching or even the precursor crystallinity itself may be a more effective predictor of stretched film properties than the crystallinity of stretched films.

The annealing process has a large influence on the composition and stability of crystalline structures in  $\beta$ -iPP films. Figure 4.3 illustrates the effect of annealing temperature on the size of  $\beta$  crystals in precursor films using two independent metrics. First, DSC was used to determine the peak melting temperature of the initially formed crystals in the  $\beta_1$  endotherm,  $T_m(\beta_1)$  (Table 4.1). The melting temperature of crystalline polymers increases with increasing crystal size, and  $\beta$  crystalline material is no exception [11]. Second, XRD was used to observe the peak broadening of the  $(300)_\beta$  reflection (Table 4.2), which can be related to the size of the largest dimension,  $D_{300}$ , of the  $\beta$  crystals in the sample using the Scherrer equation (Equation 3.4). Compared to precursor films that have not been annealed, both  $T_m(\beta_1)$  and  $D_{300}$  increase with increasing annealing temperature. This increase in both measures strongly indicates that  $\beta$  crystals grow in size when annealed at 130 and 140 °C, which is consistent with the idea that the annealing process perfects the  $\beta$  crystalline material. The size of the  $\beta_1$  endotherm also increases with annealing, indicating that crystal growth, and not only the formation of

new  $\beta$  crystals, is a likely driver of increased  $\beta$  material in annealed films. Other studies [18,26] have found  $D_{300}$  values of 18 – 35 nm for  $\beta$  crystalline materials, with little effect seen for either crystallization temperature or  $\beta$  nucleator concentration on  $D_{300}$ . The observed increase in crystal size in this study is a large effect, with  $D_{300}$  increasing by 10 to 25% over the course of annealing from an initial size of about 40 nm.

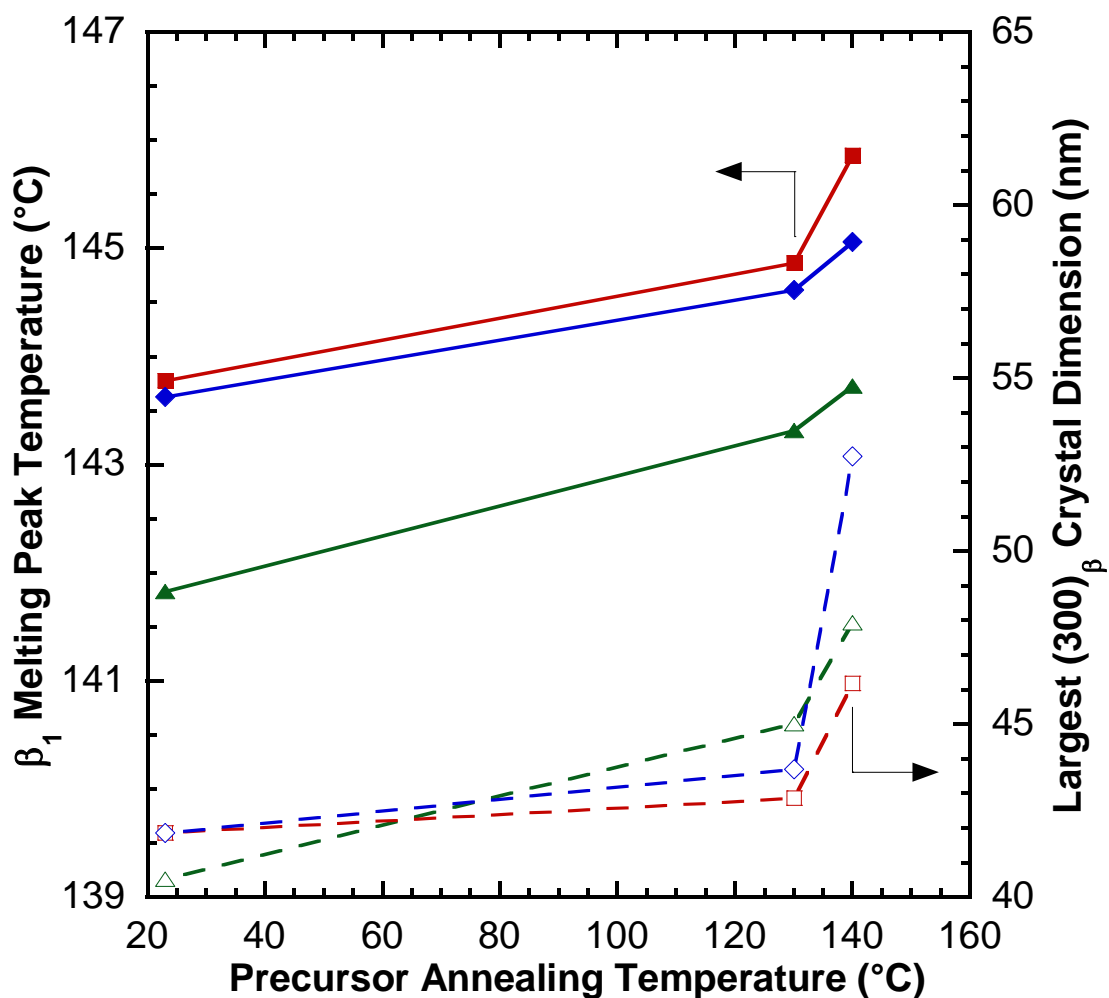


Figure 4.3. Growth of  $\beta$  crystal size as indicated by increase in  $\beta_1$  melting peak temperature determined by DSC, and the increase in the largest  $\beta$  crystal dimension as calculated from the Scherrer equation based on observed XRD  $(300)_\beta$  peak broadening, both as a function of precursor film annealing temperature. Results are shown for MFI 2.1 ( $\blacklozenge, \blacklozenge$ ), MFI 3.5 ( $\blacksquare, \blacksquare$ ) and MFI 12 ( $\blacktriangle, \blacktriangle$ ) films.

The general trend in K value presented previously for DSC and XRD analyses is as follows:  $K_{\beta, \text{DSC}}$  showed no appreciable trend with precursor film annealing temperature (Table 4.1), and  $K_{\beta, \text{A}}$  decreased with increasing annealing temperature (Table 4.2). The more likely explanation for this discrepancy lies in the counting of the  $\beta_2$  endotherm from

melt-recrystallization of the initially formed  $\beta$  material during the DSC scan in the calculation of  $K_{\beta,\text{DSC}}$ . Since the formation of the  $\beta_2$  endotherm occurs due to externally imposed heating not present in XRD measurements, it is reasonable to develop a metric based on DSC measurements that only considers the initially formed  $\beta_1$  material so that results from the two techniques may be compared on an equivalent basis. One prior metric proposed by Bai [13] with a definition nearly identical to  $K_{\beta,\text{DSC}}$  was developed to compare DSC and XRD analyses, but it was used to examine annealed  $\beta$ -iPP materials that did not exhibit double peak behavior. A comparison in this study between three measures of  $\beta$  crystallinity from DSC scans and  $K_{\beta,\text{A}}$  for all precursor films is shown in Figure 4.4. The behavior of  $K_{\beta,\text{DSC}}$  is uncorrelated with  $K_{\beta,\text{A}}$ , as would be expected from the prior discussion detailing the melt-recrystallization of  $\beta$  to  $\alpha$ . The fraction of total crystallinity in the  $\beta_1$  phase,  $X_{\beta_1}/X_c$ , is strongly correlated with  $K_{\beta,\text{A}}$ . Interestingly, it is a negative correlation, with the fraction of  $\beta_1$  material measured growing with increasing annealing temperature while  $K_{\beta,\text{A}}$  decreases. Through the annealing process,  $\beta$  material is perfected, resulting in a growth in crystal size (Figure 4.3) reflected in the growth of the  $\beta_1$  endotherm and thus the increase in  $X_{\beta_1}/X_c$ . The  $\beta$  material initially formed during the rapid cooling present in extrusion and take-up of the film is also composed of relatively small and less stable crystals, and thus is also more subject to conversion to  $\alpha$  crystalline material. The growth of some  $\beta$  crystalline material and the conversion of less stable  $\beta$  material to  $\alpha$  must proceed concurrently to explain these opposite trends and their high degree of correlation.

One shortcoming of the measure  $X_{\beta_1}/X_c$  is that  $X_c$  necessarily contains  $X_\alpha$ . Since the measure of  $\alpha$  crystallinity can be influenced by recrystallization to  $\alpha$  after the melting of  $\beta$  crystals in the DSC scan, a more robust measure of  $\beta_1$  content would avoid the

inclusion of  $X_\alpha$ . One possible alternative measure is the volume fraction of  $\beta_1$  (Table 4.1) in the precursor films, which can be simply calculated as follows:

$$\Phi_{\beta_1} = \frac{\rho_0}{\rho_\beta} \cdot X_{\beta_1} \quad (4.2)$$

This measure is also well-correlated with  $K_{\beta,A}$ , so it tracks  $X_{\beta_1}/X_c$  quite closely, shown in Figure 4.4. This is likely because calculated  $X_c$  does not change significantly during annealing, and it is therefore acting only as a scaling factor on  $X_{\beta_1}$ . Pore formation in stretched  $\beta$ -iPP films may also be related to this quantity, which will be explored in the following section.

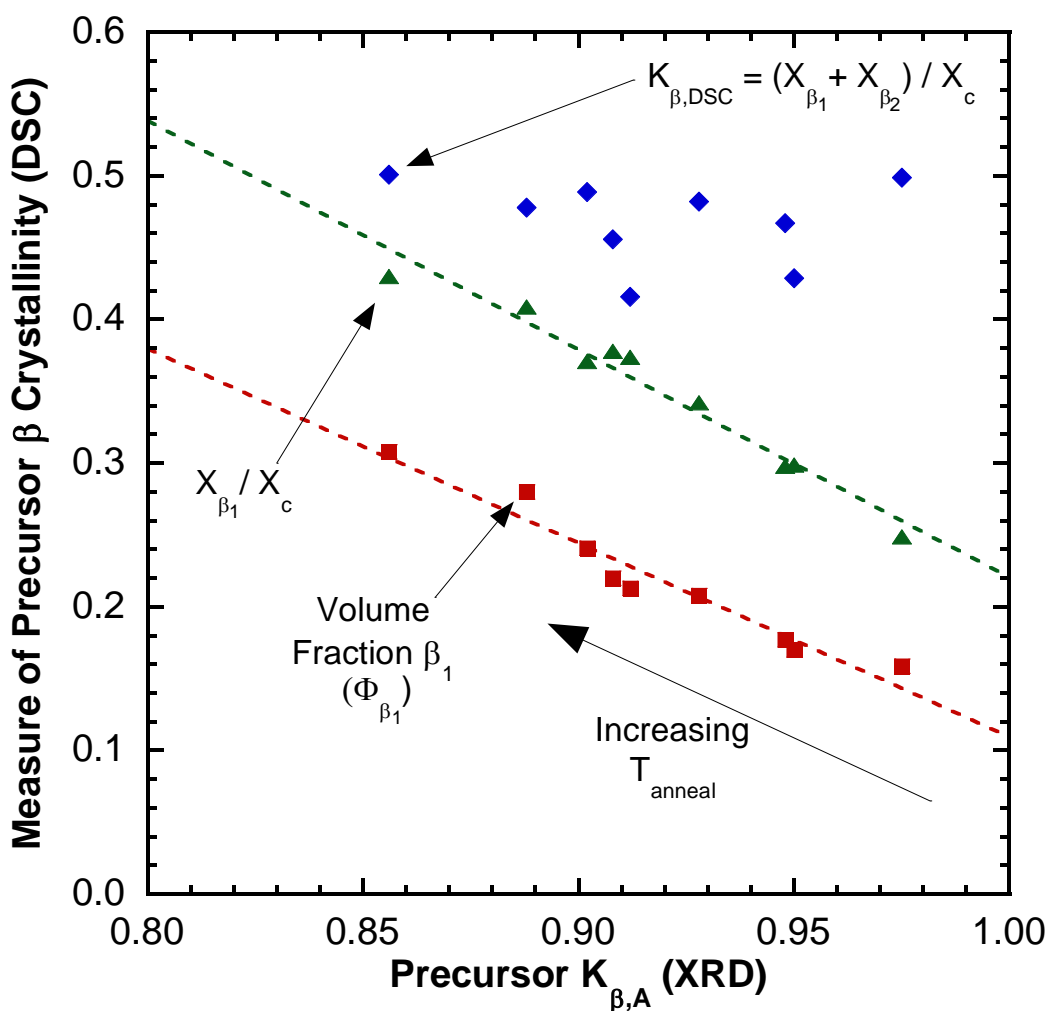


Figure 4.4. Several measures of precursor film  $\beta$  crystallinity determined by DSC as a function of  $K_{\beta,A}$  from XRD patterns. Values are plotted for  $K_{\beta,DSC}$  ( $\blacklozenge$ ), crystalline fraction in  $\beta_1$  state ( $\blacktriangle$ ), and volume fraction of  $\beta_1$  material ( $\blacksquare$ ) in the films. Dashed lines are best fits meant to guide the eye.

#### 4.2.2 Pore Formation by Stretching in $\beta$ -iPP Films

The previous section discussed the modification of several  $\beta$ -iPP precursor film parameters (crystallinity  $X_c$ ,  $\beta$  fraction  $K_{\beta,A}$ , size of  $\beta$  crystals  $D_{300}$ ) by varying the starting iPP MFI and precursor film annealing temperature. The method by which  $\beta$ -iPP materials mechanically deform is dependent upon each phase present ( $\alpha$ ,  $\beta$ , smectic,

amorphous) and how the crystallization and annealing conditions to which they have been previously exposed influence the morphology and amount of these phases. During stretching, iPP is deformed by the separation of crystalline lamellae, by shear forces between lamellae, and by slip along the glide planes of a given lamella [27,28]. This deformation can also be accompanied by a phase transformation from  $\beta$  to  $\alpha$  [20]. The lamellar structure of  $\alpha$  crystalline material is a relatively unusual cross hatched configuration of radial parent lamellae and tangential daughter lamellae, while the  $\beta$  form is structured more conventionally in the form of parallel, stacked lamellae [11]. The deformation modes are then influenced by these differing lamellar structures. A number of prior studies have used mechanical testing and other techniques to evaluate why  $\beta$ -iPP materials exhibit superior toughness and impact strength relative to neat iPP, and how this difference in properties is related to its deformation behavior.

One key difference between the two modifications is an increased tendency for  $\beta$ -iPP to cavitate as part of its deformation process during stretching relative to neat iPP [17,29]. This behavior is seen generally in semicrystalline polymers, and it occurs during elongation when stress transmitter density near lamellae is inadequate to cause lamellar shear, instead resulting in cavitation [30]. However, because  $\beta$ -iPP materials exhibit a phase transformation from  $\beta$  to  $\alpha$  or from  $\beta$  to smectic when stretched, the accompanying change in density was thought to be the primary cause of pore formation [17]. More recent studies found that the initial pore formation upon stretching of  $\beta$ -iPP films, which occurs before the yield point, is a result of the decoupling between  $\beta$  lamellae and weakly bound adjacent amorphous material [18,24]. This cavitation begins as lamellae separate during stretching of  $\beta$ -iPP, as the mobility of the amorphous phase is not restricted by cross-hatched  $\alpha$  structures [29]. Amorphous tie chains are also less abundant in  $\beta$ -iPP than in neat iPP, and this lack of stress transmitters facilitates the decoupling, presenting

a picture in line with cavitation in other semicrystalline polymers [13]. When iPP is exposed to shear forces during drawing that occur due to the inhomogeneity of the material, interlocked  $\alpha$  lamellae resist rotation [31]. Lamellae in the  $\beta$  phase rotate perpendicular to the drawing direction as strain is increased, however, and this rotation contributes to pore formation by assisting in the separation of lamellae [24,32]. After this initial cavitation, continued drawing results in enlargement of previously formed cavities, a phenomenon reflected in prior studies [16,25]. These processes are outlined in a general schematic presented in Figure 4.5.

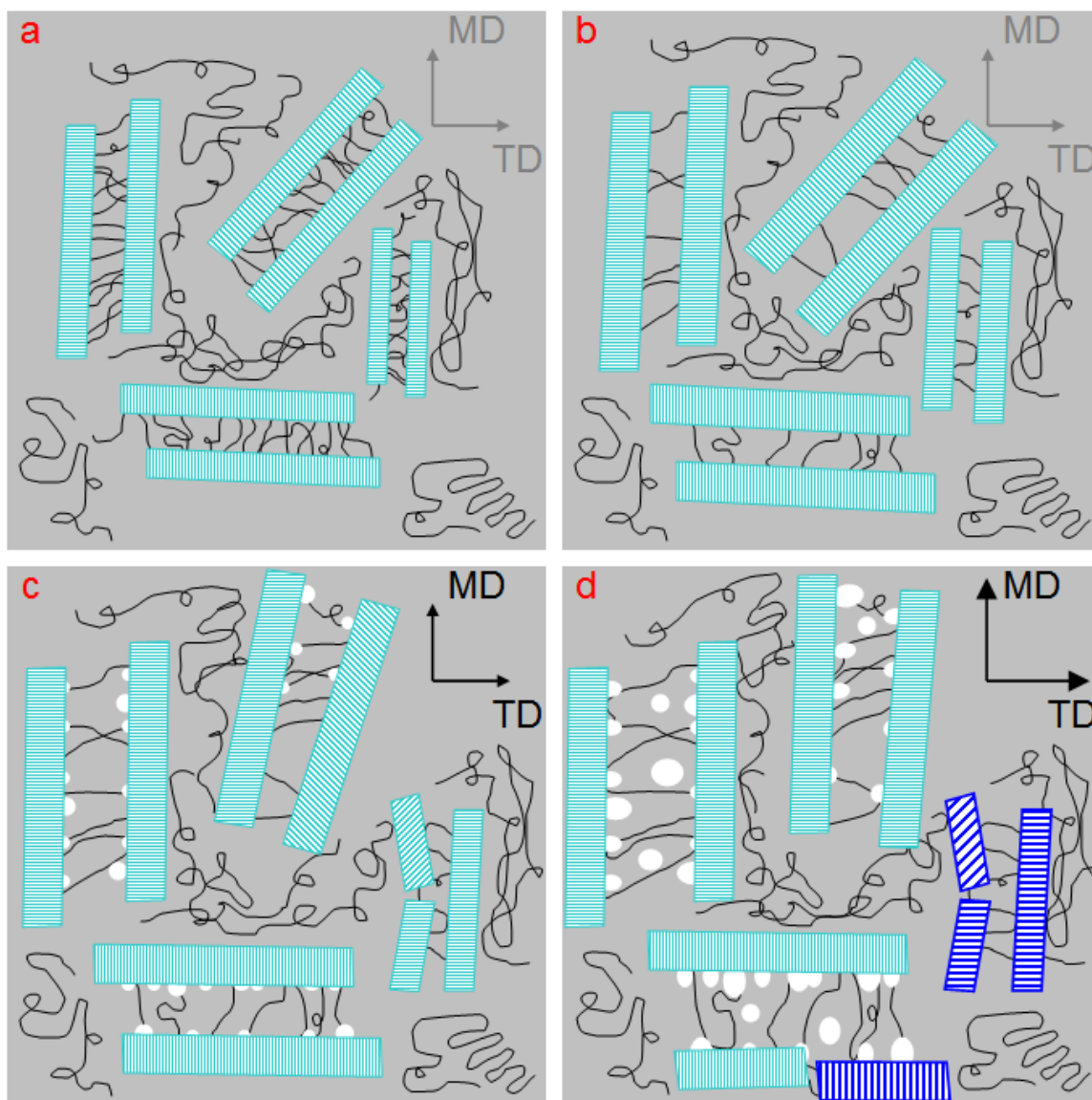


Figure 4.5. Physical changes in amorphous, interphase and crystalline regions during annealing and subsequent biaxial stretching of  $\beta$ -iPP. As-extruded films (a) are annealed, which result in larger lamellae of  $\beta$  crystalline material and reduced tie chain density between lamellae (b). When annealed films are biaxially stretched, lamellae rotate so they are perpendicular to the drawing direction, initial cavitation occurs between already perpendicular large  $\beta$  lamellae as they separate, while smaller lamellae shear (c). As stretching continues, initially formed cavities develop into larger pores as lamellae further separate, less stable  $\beta$  lamellae begin to transform to the  $\alpha$  phase, and stress-induced lamellar breakup begins (d).

Aside from pore formation by reorientation of existing  $\beta$  crystal structures, phase transformation during stretching influences the porosity of these materials. The transformation from  $\beta$  to  $\alpha$  occurs after the yield point during drawing [32,33], so this process is only related to changes in porosity after it is initially generated. This transformation may be induced thermally, but only those produced by mechanical drawing are correlated with changes in porosity [18]. While the existence of the  $\beta$  to  $\alpha$  transformation is apparent, its mechanism remains a contentious matter. At low temperatures, stretching results in a  $\beta$  to smectic transition, while at higher temperatures where  $\alpha$  crystallization is more favored,  $\beta$  to  $\alpha$  transformation occurs [24]. Both types of crystals are arranged in the same  $3_1$  helical conformation, but the  $\beta$  form is packed so that the chains are isochiral in each layer, while the  $\alpha$  form is packed in a lower energy configuration with alternating chain directionality in each layer [33]. It has been proposed that this transformation can occur in the solid state at these higher temperatures during stretching, where the additional thermal energy can activate the rewinding of helices and result in direct recrystallization to  $\alpha$  [17]. Others believe such a solid state transition is impossible, citing a lack of mobility in the ordered  $\beta$  structure and speculating that a pseudo-melt (decrystallization) and recrystallization to  $\alpha$  with energy imparted from the drawing process is required [33,34]. In any case, the transformation proceeds with increasing draw ratio, beginning at the yield point and concluding when the sample fractures, in both uniaxially [16,24,33] or biaxially stretched samples [16,18]. The local densification that this transformation causes results in void formation, but that cannot entirely account for the high porosity in stretched  $\beta$ -iPP films since the change in density is on the order of 1% [18].

A factor that strongly influences both lamellar reorientation and phase transformation as well as the resulting pore formation is the extent of  $\beta$  lamellae growth

in the sample. Both crystallization temperature and the subsequent annealing influence the size of  $\beta$  lamellae. Crystallization proceeds more slowly at elevated temperatures than when samples are quenched from the melt [24], resulting in larger lamellae. Additionally, annealing the samples at temperatures where  $\beta$  crystalline growth is favored over  $\alpha$  also results in larger lamellar blocks [13]. When the lamellae are larger, they have greater thermal and mechanical stability, making it more likely that cavitation will occur as the crystals reorient and separate from the amorphous material [24]. Annealing in particular should increase the likelihood of cavitation, since crystal growth comes directly from the adjacent amorphous region, reducing tie chain density [13]. Larger lamellae also inhibit phase transformation, such that higher draw ratios are required to complete the shift to  $\alpha$ , demonstrated by residual  $\beta$  material in DSC thermograms of annealed and stretched films. If this transformation can be retarded by more stable  $\beta$  lamellae during stretching, there are more opportunities for cavitation by lamellar reorientation, resulting in the generation of higher porosity [24].

Based on guidance provided by previous studies that outlined how various processing conditions affected the porosity of stretched  $\beta$ -iPP films, processing of parameters were fixed at values favorable to pore formation to explore the influence of the starting iPP MFI and precursor film annealing temperature on porosity. The nonisothermal crystallization of the film during extrusion was performed at an elevated temperature to yield larger initial  $\beta$  crystals [24,35]. Precursor films were stretched biaxially because prior findings show films made with this technique have higher porosity [18,36] and higher permeability [36] than uniaxially stretched films. The biaxial draw ratio was also optimized for maximum porosity [16,18,36,37]. The porosity characteristics of selected microporous membranes produced in this study are recorded in Table 4.3.

Table 4.3. Porosity and Permeability Characterization of Films Biaxially Stretched at 100 °C After Differing Thermal Annealing Treatments.

Sample Code	Film Thickness (μm)	Film Porosity (1 - ρ <sub>stretch</sub> /ρ <sub>0</sub> )	Number Mean D <sub>pore</sub> (nm)	P(N <sub>2</sub> ) (Barrer)
12M-23A-100S	32.0	0.173 ± 0.016	< 18	24,400
3.5M-23A-100S	43.1	0.255 ± 0.022	< 18	68,700
2.1M-23A-100S	54.1	0.239 ± 0.012	< 18	42,100
12M-130A-100S	43.6	0.263 ± 0.010	< 18	88,000
3.5M-130A-100S	74.5	0.308 ± 0.002	21	243,000
2.1M-130A-100S	68.4	0.280 ± 0.008	< 18	172,000
12M-140A-100S	47.5	0.368 ± 0.005	26	380,000
3.5M-140A-100S	64.2	0.375 ± 0.005	29	449,000
2.1M-140A-100S	46.6	0.346 ± 0.010	25	298,000

The most striking feature about the porosity of these films is that the strongest influence on pore formation is the precursor annealing temperature. Compared to films stretched without annealing, those annealed at 130 °C and 140 °C exhibited very large increases in porosity. This finding is reasonable because annealing affects the size of β lamellae and tie chain density in ways that assist pore formation [13,24]. Further, the measured porosity of 17 to 38% is in line with previous studies based on similar films [16,18,36]. Figure 4.6 presents surface SEM of 12M-[T<sub>anneal</sub>]A-100S films, with the associated properties presented in Table 4.3.

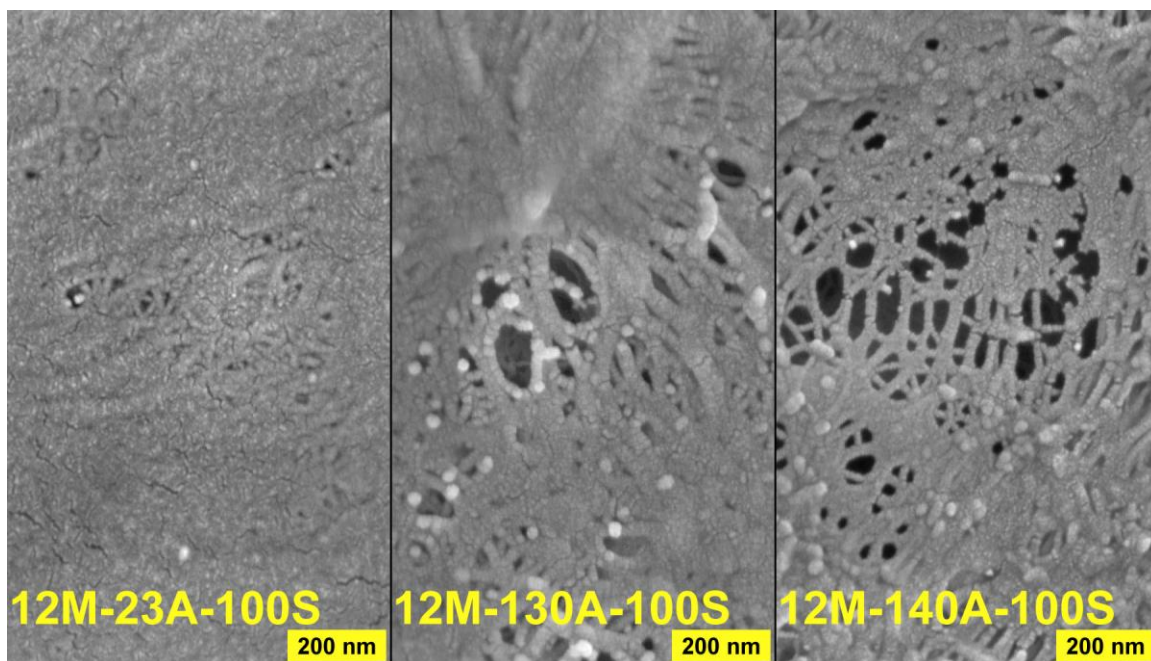


Figure 4.6. SEM micrographs of representative regions in stretched films. Films were prepared from precursors extruded from  $\beta$ -iPP having a MFI of 12 that were subsequently annealed at 23 °C (as-extruded), 130 °C, and 140 °C for 30 minutes and then stretched at 100 °C.

The increase in porosity with annealing temperature was most apparent in these 12 MFI  $\beta$ -iPP films. The increase cannot be explained in terms of greater relative increases in crystal size compared to lower MFI films (Figure 4.3) or in terms of more extensive perfection of the crystals during annealing (Figure 4.1) since the  $\beta$  endotherms are only intermediate in the transition to more stable  $\beta_1$  compared to lower MFI films. One possible explanation for the larger increase in porosity in 12 MFI films is that the formation of crystalline structures after extrusion is not as favorable in these films as in the lower MFI films, either due to its lower molecular weight or lower extrusion temperature. This disadvantage is offset by a lower density of tie chains between the  $\beta$  crystalline and amorphous phase because of the lower molecular weight of the iPP [28].

The lower tie chain density would further decrease as the crystal structure is improved by annealing, making initial cavitation more likely and resulting in the parity of porosity between films with different MFI at the highest annealing temperature. The 2.1 and 3.5 MFI films had measured porosities similar to one another at all annealing temperatures, and like the 12 MFI films, increased in porosity with annealing temperature. Regardless of annealing temperature, the intermediate 3.5 MFI films had the highest porosity. Perhaps there is a balance between tie chain density (lower in high MFI iPP) and lamellar block size (higher in low MFI iPP) that must be struck to develop the greatest porosity.

The measured thickness of these films prior to stretching was nominally 100  $\mu\text{m}$ , and the films were biaxially stretched to 100% elongation in the machine and transverse directions. If phase transformation, void formation or other phenomena do not influence the density of the films, the final thickness should be 25  $\mu\text{m}$ . Accounting for both porosity and phase change in each of the stretched films, the expected final thickness should range from 30 to 40  $\mu\text{m}$ . In all cases, the film thicknesses were greater than expected. One prior study of  $\beta$ -iPP materials [18] found a similar discrepancy between expected and measured film thicknesses, with thicknesses substantially higher than expected based on film porosity and draw ratio. This phenomenon is of limited applicability, however, because stretching was performed uniaxially with free film width, which would result in thicker films due to a reduction in width during stretching. To our knowledge, no such results have been reported for biaxially stretched films. Since the uncertainty in both film thickness and porosity is much smaller than the difference between expected and measured thickness, an alternative explanation is required.

Pore size and gas permeability for these selected films were also characterized. For the as-extruded films and some of the films annealed at 130  $^{\circ}\text{C}$ , the pore diameter was too small to measure by the technique used. One of the films annealed at 130  $^{\circ}\text{C}$  and

all of the films annealed at 140 °C were found to have pores in the ultrafiltration range, with mean pore diameters between 21 and 29 nm. This size is consistent with the surface SEM images in Figure 4.6. The N<sub>2</sub> permeability of stretched films closely tracked the porosity measured in each film, with precursor film annealing temperature again playing a key role. With one exception [16], the measured N<sub>2</sub> permeability of 449,000 Barrer is the highest reported for a microporous membrane of this type. The close relationship between permeability and porosity across the films indicates that the interconnectedness and size of pores is similar. A more complete discussion of the permeability of these microporous membranes will be provided in a publication to follow.

Having discussed both the porosity of stretched films and the quantity of stable  $\beta_1$  crystalline material in the precursor films, it is now possible to demonstrate a relationship between them. Figure 4.7 presents a correlation between the volume fraction of  $\beta_1$  material in precursor films (influenced by iPP MFI, extrusion conditions and annealing temperature) and the bulk porosity of films stretched at 100 °C. A volume fraction is a more appropriate quantity to consider than a mass fraction in this case because it yields some physical insight into how much space  $\beta_1$  crystals occupy in the bulk, and in turn, how large a volume they may cause to be converted into voids in the material. In fact, there appears to be a close correspondence between these values. Over the range of volume fractions of  $\beta_1$  present in the precursor films, each unit increase in that value results in a unit increase in film porosity, i.e., the slope of the linear fit is close to unity. The intercept of the fit does not represent a plausible extrapolation to porosity at infinite dilution of  $\beta_1$  content, since pore formation cannot occur by the mechanism discussed without  $\beta$  crystals present. Indeed, the requirements for pore formation absent  $\beta$  crystals in iPP are not met by films produced in this study [38–41]. It is more likely that below some critical value of  $\beta_1$  volume fraction, zero porosity will be developed. The low

porosity of the stretched film corresponding to the 12M-23A-100S precursor may indicate that its volume fraction of  $\beta_1$  is close to that point, because it also exhibits an especially low  $N_2$  permeability (Table 4.3).

Precursor annealing temperature appears to be the most important factor in both volume fraction of  $\beta_1$  and porosity, with little scatter between points representing a given annealing temperature. This general observation gives way to two exceptions, both occurring in the 12 MFI iPP films, and these exceptions can be rationalized based on prior observations. In the case of the as-extruded film, the porosity is lower than expected due to poor crystallization conditions during extrusion. For the film annealed at 140 °C, the annealing process induced substantial growth in the lamellae, but the higher than expected porosity can be attributed to a lower tie chain density than the other films annealed under these conditions. Additionally, the greater variability in  $\beta_1$  volume fraction for films annealed at 140 °C can be attributed to the fact that the annealing temperature is closer to the melt temperature of  $\beta$  crystals than in the other films, permitting melt-recrystallization of  $\beta$  material according to the original sizes of crystals formed during extrusion. Characterization of the volume fraction of  $\beta_1$  in these materials provides a powerful tool to predict the porosity and thus performance of microporous membranes made from  $\beta$ -iPP.

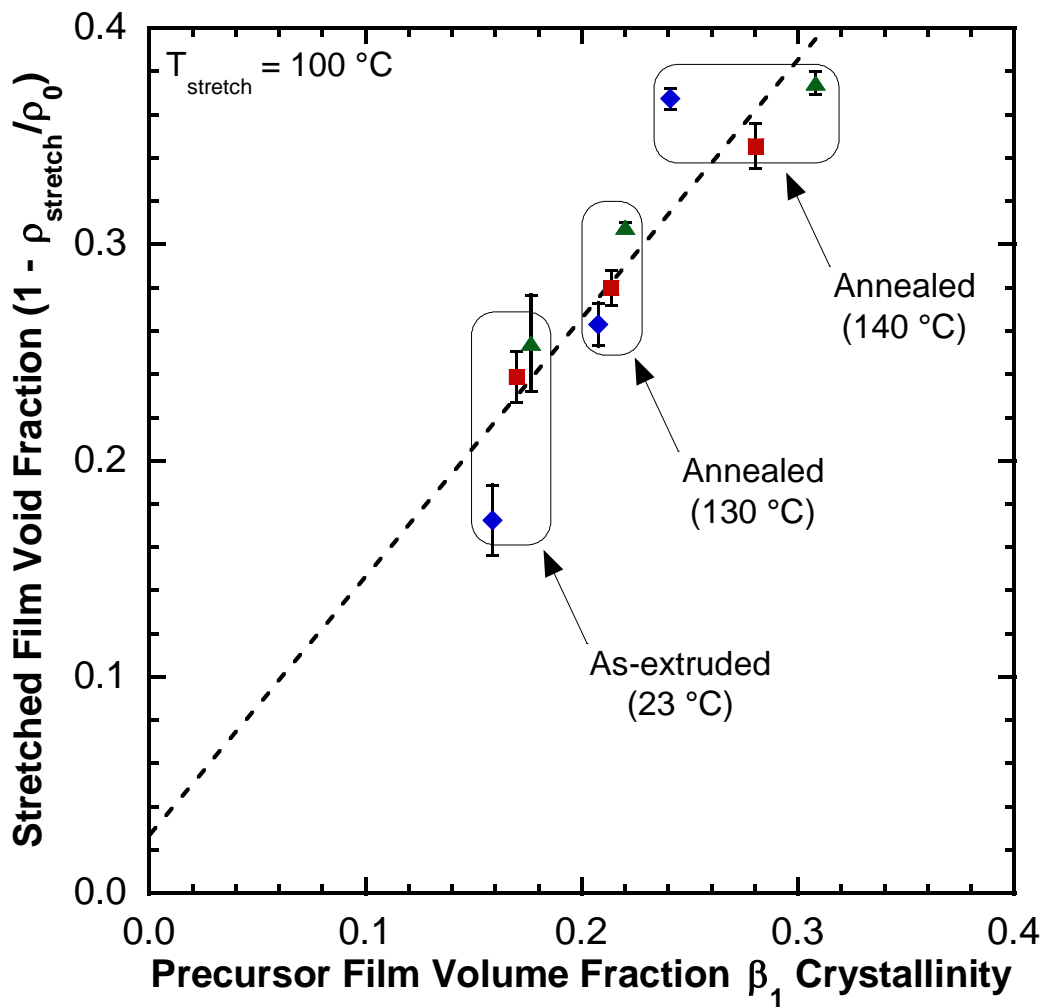


Figure 4.7. Porosity calculated from densities measured by Archimedes' principle in biaxially stretched films as a function of  $\beta_1$  crystallinity in the corresponding precursor  $\beta$ -iPP films. Values are plotted for precursor films of MFI 2.1 (◆), MFI 3.5 (■), and MFI 12 (▲). Uncertainties represent  $\pm 1$  standard deviation. The dashed line is the least squares line to the data set.

### 4.3 REFERENCES

- [1] J. Varga, I. Mudra, G.W. Ehrenstein, Highly active thermally stable  $\beta$ -nucleating agents for isotactic polypropylene, *Journal of Applied Polymer Science*. 74 (1999) 2357–2368.
- [2] J. Varga, I. Mudra, G.W. Ehrenstein, Crystallization and Melting of  $\beta$ -Nucleated Isotactic Polypropylene, *Journal of Thermal Analysis and Calorimetry*. 56 (1999) 1047–1057.
- [3] Y. Fujiwara, Das Doppelschmelzverhalten der  $\beta$ -Phase des isotaktischen Polypropylens, *Colloid and Polymer Science*. 253 (1975) 273–282.
- [4] M. Dong, Z. Guo, J. Yu, Z. Su, Study of the assembled morphology of aryl amide derivative and its influence on the nonisothermal crystallizations of isotactic polypropylene, *Journal of Polymer Science Part B: Polymer Physics*. 47 (2009) 314–325.
- [5] J. Varga,  $\beta$ -Modification of polypropylene and its two-component systems, *Journal of Thermal Analysis*. 35 (1989) 1891–1912.
- [6] J. Varga,  $\beta$ -Modification of Isotactic Polypropylene: Preparation, Structure, Processing, Properties, and Application, *Journal of Macromolecular Science, Part B*. 41 (2002) 1121–1171.
- [7] M. Dong, Z. Guo, Z. Su, J. Yu, The effects of crystallization condition on the microstructure and thermal stability of isotactic polypropylene nucleated by  $\beta$ -form nucleating agent, *Journal of Applied Polymer Science*. 119 (2011) 1374–1382.
- [8] Y. Yamamoto, Y. Inoue, T. Onai, C. Doshu, H. Takahashi, H. Uehara, Deconvolution Analyses of Differential Scanning Calorimetry Profiles of  $\beta$ -Crystallized Polypropylenes with Synchronized X-ray Measurements, *Macromolecules*. 40 (2007) 2745–2750.
- [9] X. Li, H. Wu, T. Huang, Y. Shi, Y. Wang, F. Xiang, et al.,  $\beta/\alpha$  Transformation of  $\beta$ -polypropylene during tensile deformation: effect of crystalline morphology, *Colloid and Polymer Science*. 288 (2010) 1539–1549.
- [10] T. Asano, T. Yamamoto, M.F. Mina, Y. Fujiwara, H. Takahashi, I. Hatta, Melting behavior of the oriented  $\beta$ -phase polypropylene texture crystallized by the temperature slope method, *Journal of Macromolecular Science, Part B*. 38 (1999) 163–175.

- [11] R.A. Phillips, M.D. Wolkowicz, Polypropylene Morphology, in: N. Pasquini (Ed.), Polypropylene Handbook, 2nd ed., Hanser Gardner, 2005: pp. 147–264.
- [12] A. Menyhárd, J. Varga, G. Molnár, Comparison of different  $\beta$ -nucleators for isotactic polypropylene, characterisation by DSC and temperature-modulated DSC (TMDSC) measurements, Journal of Thermal Analysis and Calorimetry. 83 (2006) 625–630.
- [13] H. Bai, Y. Wang, Z. Zhang, L. Han, Y. Li, L. Liu, et al., Influence of Annealing on Microstructure and Mechanical Properties of Isotactic Polypropylene with  $\beta$ -Phase Nucleating Agent, Macromolecules. 42 (2009) 6647–6655.
- [14] H. Bai, F. Luo, T. Zhou, H. Deng, K. Wang, Q. Fu, New insight on the annealing induced microstructural changes and their roles in the toughening of  $\beta$ -form polypropylene, Polymer. 52 (2011) 2351–2360.
- [15] L. Poussin, Y.A. Bertin, J. Parisot, C. Brassy, M. De, D. Physique, et al., Influence of thermal treatment on the structure of an isotactic polypropylene, Polymer. 39 (1998) 4261–4265.
- [16] S. Ran, M. Xu, Studies on the Pore Formation Mechanism of  $\beta$ -Crystalline Polypropylene Under Stretching, Chinese Journal of Polymer Science. 22 (2004) 123–130.
- [17] G. Shi, F. Chu, G. Zhou, Z. Han, Plastic Deformation and Solid-Phase Transformation in  $\beta$ -Phase Polypropylene, Die Makromolekulare Chemie. 190 (1989) 907–913.
- [18] F. Chu, T. Yamaoka, H. Ide, Y. Kimura, Microvoid formation process during the plastic deformation of  $\beta$ -form polypropylene, Polymer. 35 (1994) 3442–3448.
- [19] J. Varga, Melting memory effect of the  $\beta$ -modification of polypropylene, Journal of Thermal Analysis. 31 (1986) 165–172.
- [20] A. Turner Jones, J.M. Aizlewood, D.R. Beckett, Crystalline Forms of Isotactic Polypropylene, Die Makromolekulare Chemie. 75 (1964) 134–158.
- [21] P. Jacoby, B.H. Bersted, W.J. Kissel, C.E. Smith, Studies on the  $\beta$ -Crystalline form of Isotactic Polypropylene, Journal of Polymer Science Part B: Polymer Physics. 24 (1986) 461–491.
- [22] M. Fujiyama, Y. Kawamura, T. Wakino, T. Okamoto, Study on Rough-Surface Biaxially Oriented Polypropylene Film. I. Formation of  $\beta$ -Form Crystals in Sheet

Cast with T-Die Extruder, *Journal of Applied Polymer Science*. 36 (1988) 985–993.

- [23] D. Ferrer-Balas, M.L. MasPOCH, A.B. Martinez, O.O. Santana, Influence of annealing on the microstructural, tensile and fracture properties of polypropylene films, *Polymer*. 42 (2001) 1697–1705.
- [24] F. Chu, T. Yamaoka, Y. Kimura, Crystal transformation and micropore formation during uniaxial drawing of  $\beta$ -form polypropylene film, *Polymer*. 36 (1995) 2523–2530.
- [25] F. Chu, Structure and gas permeability of microporous films prepared by biaxial drawing of  $\beta$ -form polypropylene, *Polymer*. 37 (1996) 573–579.
- [26] J. Kotek, M. Raab, J. Baldrian, W. Grellmann, The effect of specific  $\beta$ -nucleation on morphology and mechanical behavior of isotactic polypropylene, *Journal of Applied Polymer Science*. 85 (2002) 1174–1184.
- [27] J.X. Li, W.L. Cheung, C.M. Chan, On deformation mechanisms of  $\beta$ -polypropylene 3. Lamella structures after necking and cold drawing, *Polymer*. 40 (1999) 3641–3656.
- [28] C. Grein, Toughness of Neat, Rubber Modified and Filled  $\beta$ -Nucleated Polypropylene: From Fundamentals to Applications, *Advances in Polymer Science*. 188 (2005) 43–104.
- [29] C. Grein, C.J.G. Plummer, H.-H. Kausch, Y. Germain, P. Béguelin, Influence of  $\beta$  nucleation on the mechanical properties of isotactic polypropylene and rubber modified isotactic polypropylene, *Polymer*. 43 (2002) 3279–3293.
- [30] S. Humbert, O. Lame, J.M. Chenal, C. Rochas, G. Vigier, New Insight on Initiation of Cavitation in Semicrystalline Polymers: In-Situ SAXS Measurements, *Macromolecules*. 43 (2010) 7212–7221.
- [31] M. Aboulfaraj, C. G'Sell, B. Ulrich, A. Dahoun, In situ observation of the plastic deformation of polypropylene spherulites under uniaxial tension and simple shear in the scanning electron microscope, *Polymer*. 36 (1995) 731–742.
- [32] Z. Cai, Y. Zhang, J. Li, F. Xue, Y. Shang, X. He, et al., Real time synchrotron SAXS and WAXS investigations on temperature related deformation and transitions of  $\beta$ -iPP with uniaxial stretching, *Polymer*. 53 (2012) 1593–1601.

- [33] J.X. Li, W.L. Cheung, On the deformation mechanisms of  $\beta$ -polypropylene: 1. Effect of necking on  $\beta$ -phase PP crystals, *Polymer*. 39 (1998) 6935–6940.
- [34] S. V. Meille, D.R. Ferro, S. Brueckner, A.J. Lovinger, F.J. Padden, Structure of  $\beta$ -Isotactic Polypropylene: A Long-Standing Structural Puzzle, *Macromolecules*. 27 (1994) 2615–2622.
- [35] M. Xu, S. Hu, J. Guan, X. Sun, W. Wu, W. Zhu, et al., Polypropylene microporous film, U.S. Patent 5,134,174, 1992.
- [36] W. Zhu, X. Zhang, C. Zhao, W. Wu, J. Hou, M. Xu, A Novel Polypropylene Microporous Film, *Polymers for Advanced Technologies*. 7 (1996) 743–748.
- [37] G. Shi, X. Zhang, J. Zheng, G. Zhou, Microporous Film, Made from  $\beta$ -Crystalline Phase Polypropylene, *International Polymer Processing*. 10 (1995) 330–333.
- [38] M.B. Johnson, G.L. Wilkes, Microporous membranes of isotactic poly(4-methyl-1-pentene) from a melt-extrusion process. II. Effects of thermal annealing and stretching on porosity, *Journal of Applied Polymer Science*. 84 (2002) 1076–1100.
- [39] M.B. Johnson, G.L. Wilkes, Microporous membranes of polyoxymethylene from a melt-extrusion process: (II) Effects of thermal annealing and stretching on porosity, *Journal of Applied Polymer Science*. 84 (2002) 1762–1780.
- [40] M.B. Johnson, G.L. Wilkes, Microporous membranes of isotactic poly(4-methyl-1-pentene) from a melt-extrusion process. I. Effects of resin variables and extrusion conditions, *Journal of Applied Polymer Science*. 83 (2002) 2095–2113.
- [41] M.B. Johnson, G.L. Wilkes, Microporous membranes of polyoxymethylene from a melt-extrusion process: (I) effects of resin variables and extrusion conditions, *Journal of Applied Polymer Science*. 81 (2001) 2944–2963.
- [42] G.T. Offord, S.R. Armstrong, B.D. Freeman, E. Baer, A. Hiltner, J.S. Swinnea, et al., Porosity Enhancement in  $\beta$  Nucleated Isotactic Polypropylene Stretched Films by Thermal Annealing, *Polymer*. Accepted (2013).

## **Chapter 5. Influence of Processing Strategies on Porosity and Permeability of $\beta$ Nucleated Isotactic Polypropylene Stretched Films**

### **5.1 SUMMARY**

Microporous polymer membranes were produced from  $\beta$  nucleated isotactic polypropylene using a solvent-free process involving extrusion and biaxial stretching. Pore formation, previously shown to depend upon the quantity of perfected  $\beta$  crystalline material in the film, was found to also depend upon stretching temperature. The pore structure of membranes produced under a variety of processing conditions was investigated by SEM, flow porometry, and gas permeation techniques. The mechanism of gas transport through these membranes was determined using permeability experiments and pore size distribution. Gas permeability was correlated with film porosity and compared to the permeability of an array of porous polypropylene films. High quality microporous membranes were produced without the use of the strict process control required for traditional extruded films, and such membranes exhibit performance comparable to commercially available Celgard films. This process flexibility provides an avenue toward coextruded composite membranes for a range of applications.

---

This chapter has been adapted with permission from the following article:  
G.T. Offord (author, primary experimentalist), S.R. Armstrong (editor, sample preparation), B.D. Freeman (editor), E. Baer (editor), A. Hiltner (editor), D.R. Paul (editor), *Polymer*. 54 (2013) 2796–2807.

## 5.2 RESULTS AND DISCUSSION

### 5.2.1 The Effect of Thermal Annealing on Porosity and Gas Permeability of Stretched $\beta$ -iPP Films

Pore formation in  $\beta$ -iPP films depends upon the type and morphology of crystalline structures in such films, and it is a consequence of the processing history of the films. Films produced under favorable conditions with appropriate nucleation tend to form  $\beta$  crystalline material in the form of parallel-stacked lamellae [1]. When these films are stretched, the stacked  $\beta$  lamellae are able to rotate and separate, causing cavitation between lamellae [2–4]. Stretching beyond the yield point causes enlargement of the voids formed [5] and a transformation of  $\beta$  phase to  $\alpha$  phase crystalline material [6]. The effectiveness of lamellar separation is strongly influenced by the extent of  $\beta$  lamellae growth in the film, because larger and more stable lamellae are more likely to dissipate stress by separating from amorphous material than by crystalline shear during the stretching process [7]. Thermal annealing of  $\beta$ -iPP films results in such lamellar growth [8], and it should therefore prove beneficial in increasing the porosity of these films when stretched relative to those of films not subjected to annealing. While the growth of the crystal size can be detected by both XRD and DSC techniques [9], information about the quantity of crystalline material affected by thermal annealing is more accessible using DSC. First heating thermograms can be analyzed to determine the extent of growth and perfection of  $\beta$  crystalline lamellae in annealed films. This is not a trivial undertaking, because many  $\beta$ -iPP materials exhibit double peak behavior in DSC thermograms, where endotherms corresponding to  $\beta$  crystalline material appear twice. An endotherm designated  $\beta_1$  corresponds to an initial melting of  $\beta$  crystals. The material can recrystallize and then melt, as indicated by a second endotherm  $\beta_2$ , as temperature is further increased.

A large population of stable  $\beta$  crystals result in a larger  $\beta_1$  endotherm, and those crystals are less likely to recrystallize to the  $\beta_2$  form after melting [10,11]. The  $\beta_1$  endotherm is related in this way to the size and stability of  $\beta$  lamellae in the films, and it is thus predictive of how well a given  $\beta$ -iPP film will form porosity upon stretching. One useful metric to quantify the amount of  $\beta_1$  crystalline material in the precursor film is the volume fraction, as follows:

$$\Phi_{\beta_1} = \frac{\rho_0}{\rho_{\beta}} \cdot X_{\beta_1} \quad (1)$$

The volume fraction of  $\beta_1$  material in a precursor film is influenced by several factors [9], but the annealing treatment proved to be the most significant. For precursor films with a crystalline configuration determined only by the extrusion and take-up process, a low level of perfected  $\beta$  crystal structure was achieved, as indicated by volume fractions of  $\beta_1$  under 18%. As the annealing temperature was increased within the temperature range where  $\beta$  crystallization is favored [8], the volume fraction of  $\beta_1$  material increases to above 30%. This quantity provides an indication of the space occupied by  $\beta_1$  crystalline material [9], and it can be related to the measured bulk porosity of the stretched film. Figure 5.1 displays the effect of precursor annealing temperature on the porosity generated in samples over a range of precursor iPP MFI values, but at a fixed stretching condition. The porosity of films stretched at 100 °C increases in a linear fashion over the range of  $\beta_1$  volume fraction investigated [9], and is consistent with the porosity developed in similar stretched films [12–14]. Below a threshold content of  $\beta_1$ , however, it cannot be expected that this relationship would continue to hold because the lamellar separation previously described could not occur in significant amounts. Thus, it would be more likely for film porosity to reach zero at non-zero  $\beta_1$  content, a concept outlined in Figure 5.1.

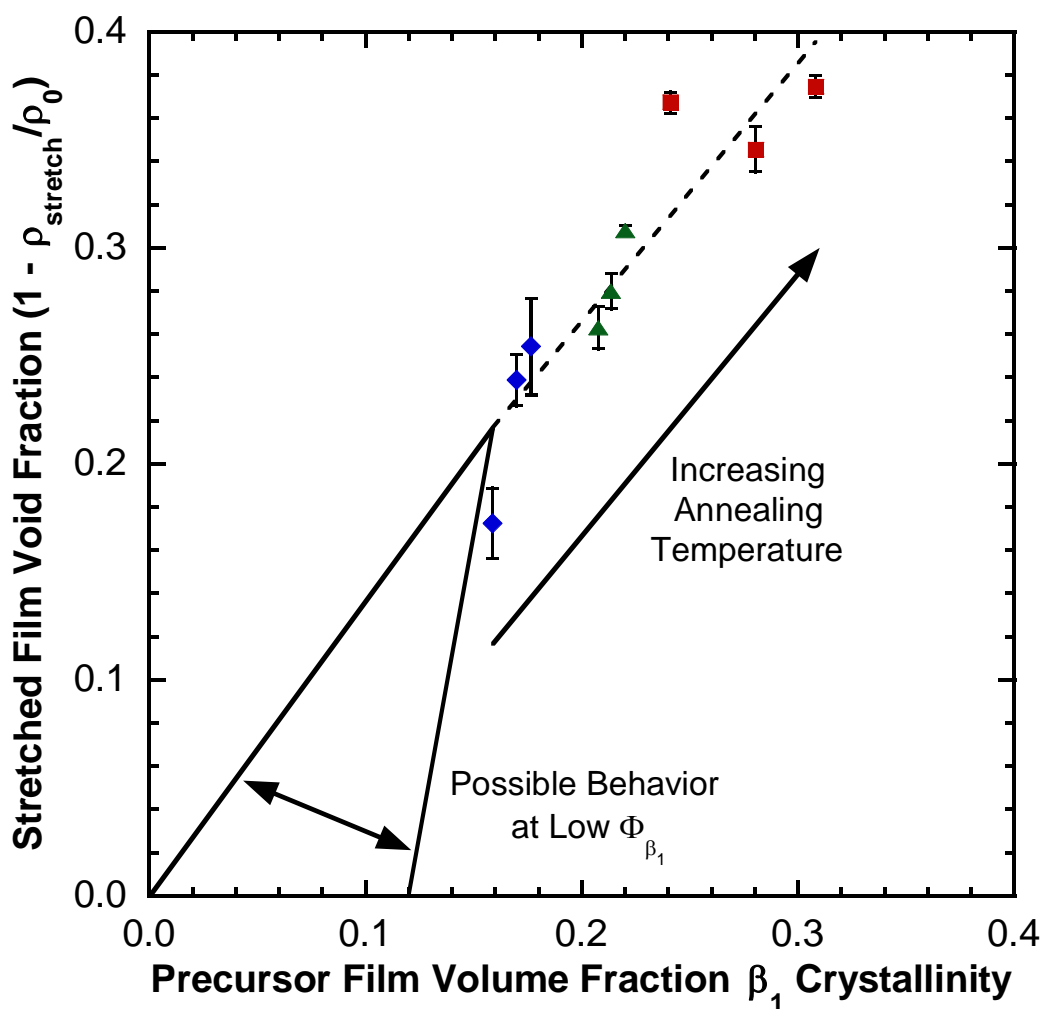


Figure 5.1. Porosity increase observed in  $\beta$ -iPP films biaxially stretched at 100 °C when the volume fraction of  $\beta_1$  crystallinity present in precursor films is increased by employing a thermal annealing process. Values are plotted for stretched films produced from precursors annealed for 30 minutes at 23 °C (as-extruded) ( $\blacklozenge$ ), 130 °C ( $\blacktriangle$ ), and 140 °C ( $\blacksquare$ ). Uncertainties represent  $\pm 1$  standard deviation. The dashed line is the least squares line to the data set.

The increase in porosity of stretched films with  $\beta_1$  content in Figure 5.1 can be verified by surface SEM, as shown in Figure 5.2.

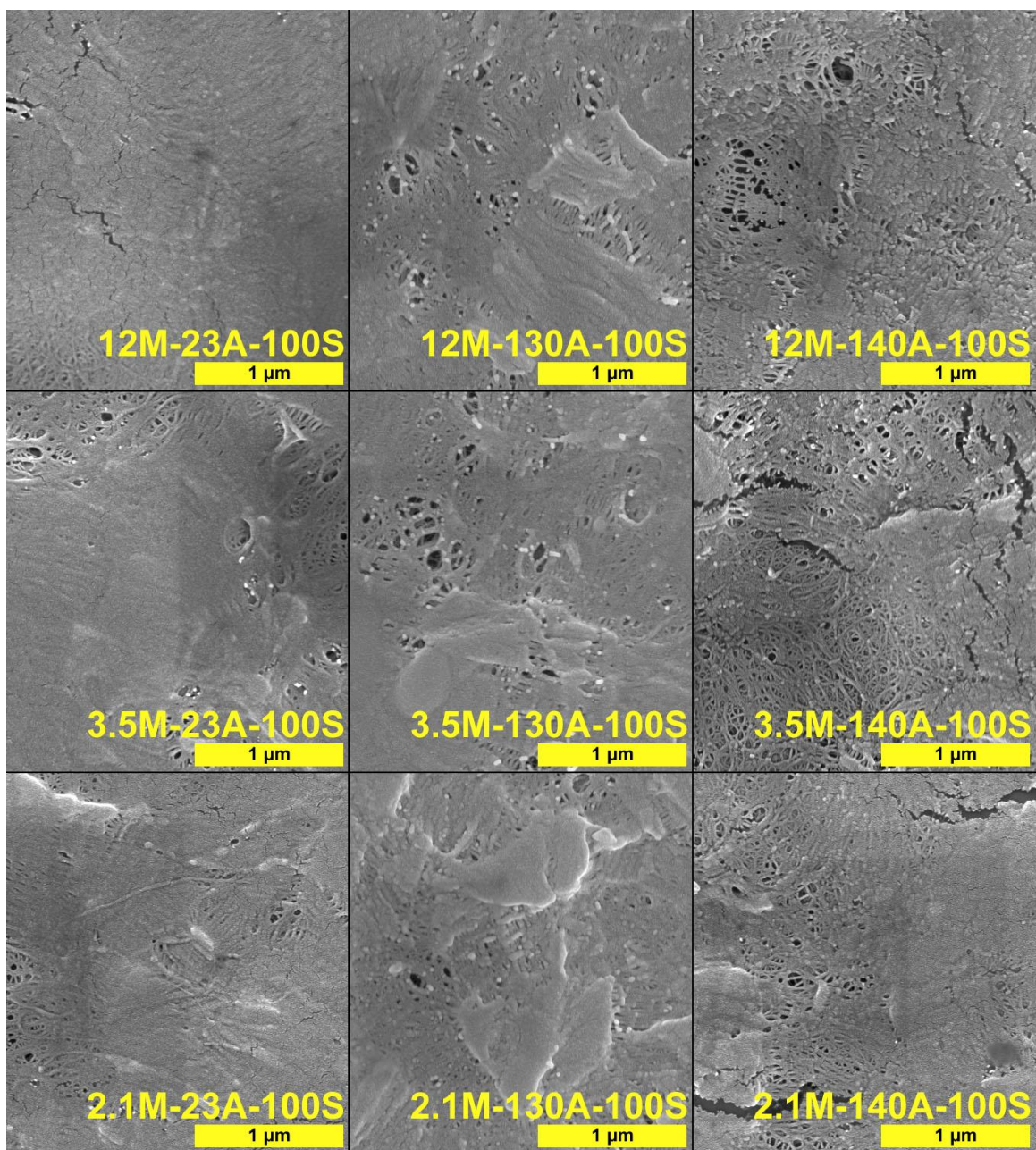


Figure 5.2. SEM micrographs of representative surface regions in stretched films. Films were prepared from extruded  $\beta$ -iPP precursors having a MFI of 2.1, 3.5, and 12 that were subsequently annealed at 23 °C (as-extruded), 130 °C, and 140 °C for 30 minutes and then stretched at 100 °C.

It is difficult to qualitatively differentiate the visible surface porosity of these stretched films at a fixed precursor annealing temperature as iPP MFI is varied. The change in porosity as annealing temperature increases is much more apparent. When precursor films are annealed at 130 °C, the number and size of pores at the surface of stretched films both increase relative to as-extruded films. Upon annealing at 140 °C, there is a further increase in pore size and quantity, and large surface fissures begin to appear.

The influence of precursor annealing temperature on porosity, pore size and N<sub>2</sub> permeability of porous films made from iPP with an MFI of 3.5 is presented in Table 5.1. These values are presented together with those of a commercially available monolayer polypropylene porous film, Celgard 2400. As precursor annealing temperature is elevated, porosity, pore size, and permeability increase in concert. These changes are consistent with the hypothesis that  $\beta$  crystalline lamellae growth in precursor films translates to larger volume fractions of  $\beta_1$ , and when such films are stretched, the separation of larger lamellae yield larger individual pores. This process leads to higher porosities, which in turn lowers the resistance to mass transfer in the stretched film. The porosity and permeability characteristics of  $\beta$ -iPP porous films annealed at 140 °C are roughly comparable to those of Celgard 2400.

Table 5.1. Porosity and Permeability Characterization of Biaxially Stretched Films Subjected to Differing Thermal Annealing Treatments, with Comparison to Celgard 2400 Properties.

Sample Code	Film Porosity ( $\Phi = 1 - \rho_{\text{stretch}}/\rho_0$ )	Number Mean $D_{\text{pore}}$ (nm)	P(N <sub>2</sub> ) (Barrer)
3.5M-23A-100S	0.255 ± 0.022	< 18	68,700
3.5M-130A-100S	0.308 ± 0.002	21	243,000
3.5M-140A-100S	0.375 ± 0.005	29	449,000
Celgard 2400	0.41 [15]	34	727,000

The thickness normalized N<sub>2</sub> flux for the porous films introduced in Table 5.1 as a function of transmembrane pressure  $\Delta p$  is presented in Figure 5.3. The permeability values recorded in Table 5.1 were calculated from the slope of the flux data for each film. As  $\Delta p$  was increased during permeation experiments, thickness normalized N<sub>2</sub> flux increased linearly. Permeabilities increased as film porosity increased, changing by an order of magnitude from the lowest permeability  $\beta$ -iPP film ( $\Phi = 0.255$ ) to that of the highest permeability film, Celgard 2400 ( $\Phi = 0.41$ ). The linear increase in N<sub>2</sub> flux with  $\Delta p$  provides some insight into the transport mechanism occurring in these porous films, which will be discussed more thoroughly below.

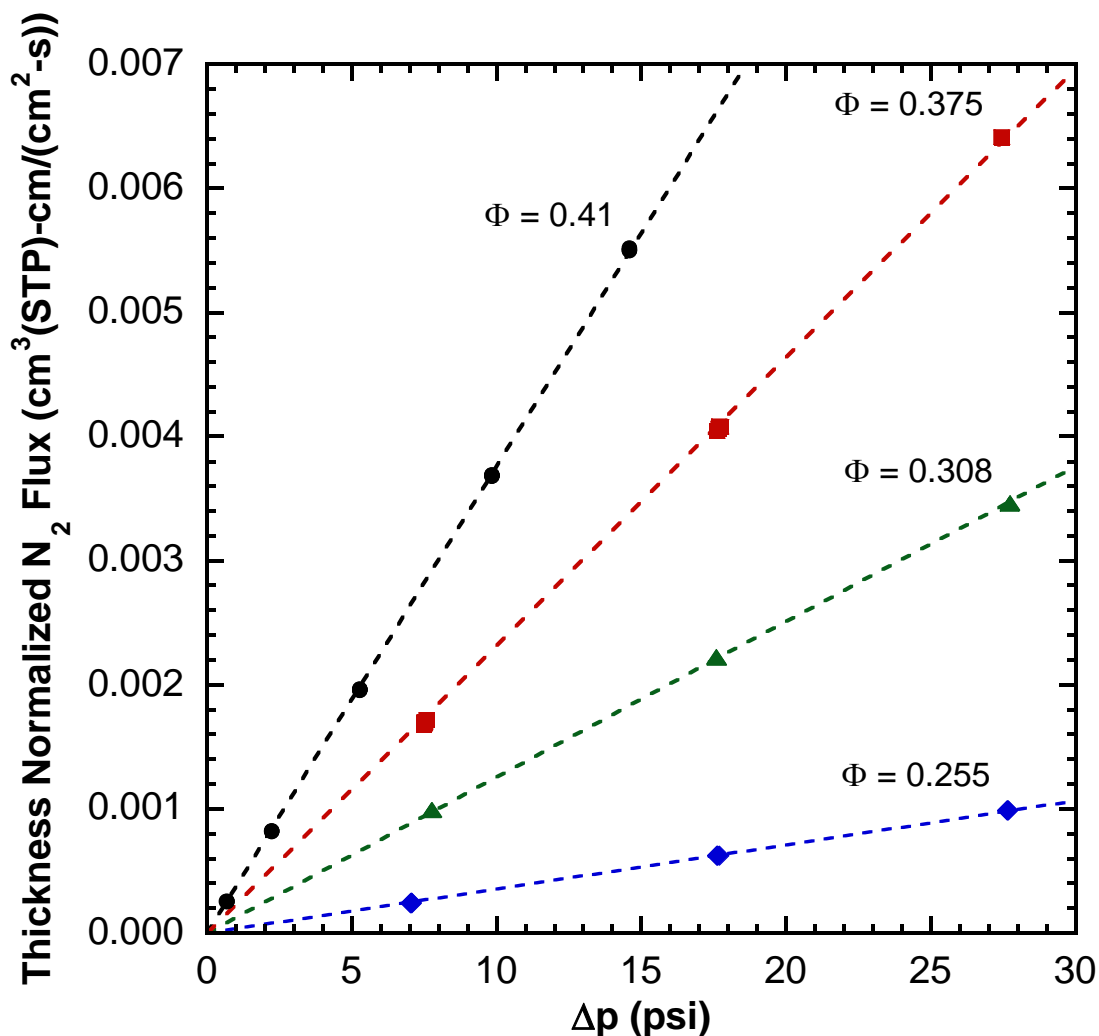


Figure 5.3. Thickness normalized  $N_2$  flux as a function of transmembrane pressure measured for biaxially stretched  $\beta$ -iPP films whose precursors have been subjected to different thermal annealing treatments. Values are plotted for 3.5M-23A-100S ( $\blacklozenge$ ), 3.5M-130A-100S ( $\blacktriangle$ ), and 3.5M-140A-100S ( $\blacksquare$ ) films, and Celgard 2400 ( $\bullet$ ) has been included for comparison. The porosity of each film is labeled, and dashed lines represent least squares fits through the origin.

### 5.2.2 The Effect of Stretching Temperature on the Porosity of Stretched $\beta$ -iPP Films

At a stretching temperature of 100 °C, the porosity of stretched films increases linearly with  $\beta_1$  content within certain bounds [9]. It is not currently known whether films

with significantly higher levels of  $\beta_1$  material can be produced, but this would be an obvious avenue to generate films of even higher porosity. One way to potentially increase  $\beta_1$  content is to operate the chill roll at a more favorable crystallization temperature of 100 to 110 °C instead of 95 °C, which was not possible in this study due to the use of water as the coolant for the chill roll. Without altering the crystallinity of the precursor, it may be possible to modify the porosity of these stretched films by employing different stretching temperatures. The relationship between porosity of stretched films and the content of well-developed  $\beta$  crystalline material in their precursors will therefore be investigated as a function of stretching temperature. It has been shown previously [16] that the stress-strain relationship in  $\beta$ -iPP films is a function of stretching temperature. Applying different stresses to  $\beta$ -iPP films of a given  $\beta_1$  content should then result in different pore formation behavior, since cavitation in polymeric films is dependent upon how stress is dissipated [17]. In films stretched at 100 °C, the highest porosity is achieved when the  $\beta_1$  content is maximized, so altering the stretching temperature will facilitate both a better understanding of the fundamentals of pore formation in  $\beta$ -iPP films and will assist in the optimization of conditions to produce films with the highest possible porosity.

The relationship between precursor  $\beta_1$  content and the porosity of films extruded from all grades of iPP and stretched at three distinct temperatures is presented in Figure 5.4. The increase in porosity in films stretched at 110 °C is similar to what has already been shown for those stretched at 100 °C. For each additional percent of volume occupied by  $\beta_1$  material, roughly speaking, an additional percent of porosity is formed when the film is stretched. The films stretched at 100 °C are slightly more sensitive to precursor  $\beta_1$  content than those stretched at 110 °C. Films stretched at 90 °C display a much lower sensitivity, with less benefit to pore formation shown when  $\beta_1$  content is

elevated. The slope for films stretched at 90 °C is lower than for those films stretched at 100 or 110 °C, and this may be an indication of a difference in the pore formation mechanism. The general behavior of  $\beta$ -iPP films during the annealing and subsequent biaxial stretching is outlined in our previous publication [9], but the stretching temperature subtly modifies this picture.

It is well-established that the stretching process involves the initiation of cavitation before the yield point of the material and the delamination of  $\beta$  lamellae from amorphous material [7,12], and this is followed by the subsequent growth of the pore structure after the yield point. Expansion of the pores is accompanied by strain-hardening owing to the deformation of  $\beta$  structures, as well as the transformation from  $\beta$  to  $\alpha$  or  $\beta$  to smectic material. At the two highest stretching temperatures, the transition from  $\beta$  to  $\alpha$  during stretching should predominate, while a  $\beta$  to smectic transition is more likely at 90 °C [7]. A further difference between the stretching of  $\beta$ -iPP films at 100 or 110 °C and stretching at 90 °C is the higher stress required to achieve the same strain rate [16]. These factors may together account for the differences in pore formation behavior between  $\beta$ -iPP films stretched at higher temperatures relative to those stretched at lower temperatures. In light of these differences in the stretching process and in the relationship between  $\beta_1$  content and porosity, a difference in the mechanism for pore formation in  $\beta$ -iPP films stretched at different temperatures may be indicated.

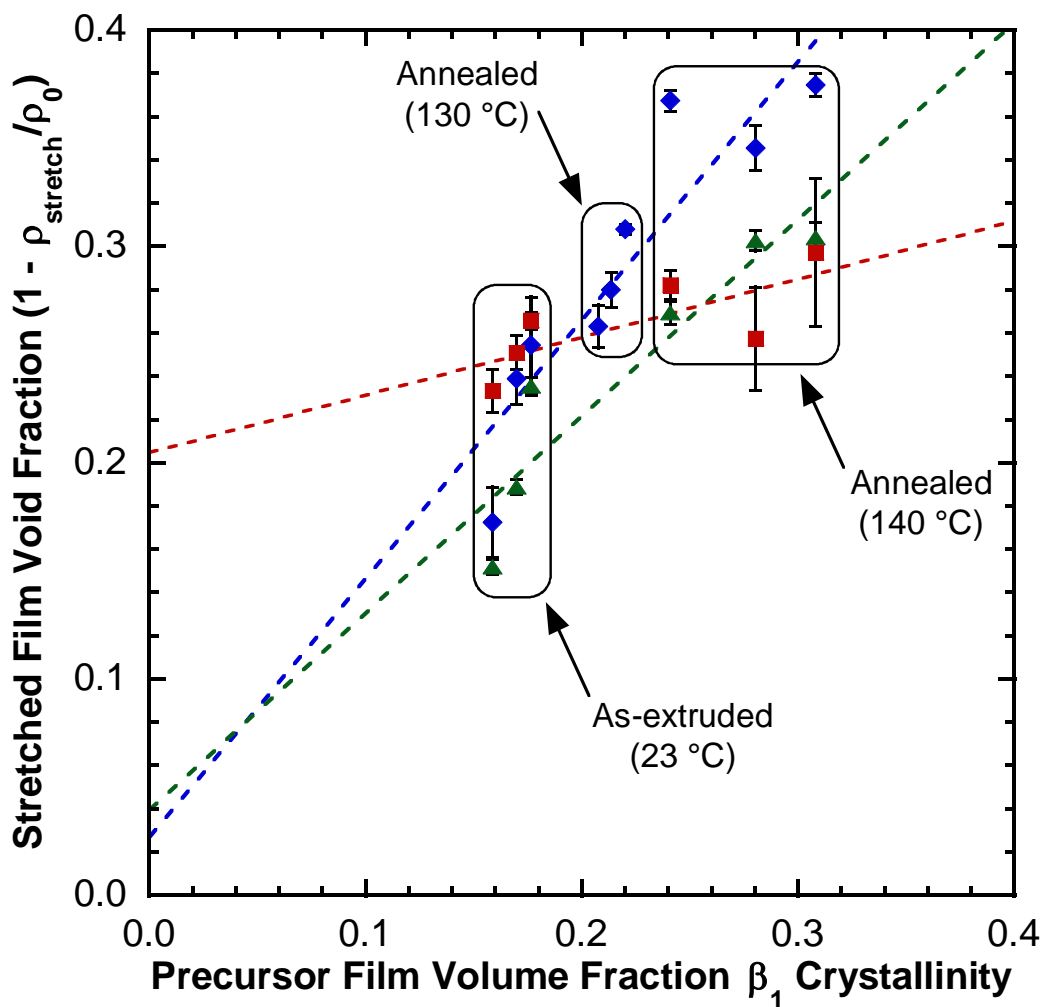


Figure 5.4. Porosity calculated from densities measured by Archimedes' principle in biaxially stretched films as a function of  $\beta_1$  crystallinity in the corresponding precursor  $\beta$ -iPP films. Values are plotted for films stretched at 90 °C (■), 100 °C (◆), and 110 °C (▲). Uncertainties represent  $\pm 1$  standard deviation. Dashed lines with matching colors are the least squares fit to the data sets. Extrapolation to zero  $\beta_1$  content should not be taken to be predictive (see Figure 5.1).

SEM micrographs of films produced from each iPP MFI used in the study that were annealed at 140 °C and then stretched at 100 and 110 °C are presented in Figure 5.5. Altering the precursor annealing temperature resulted in large differences between

surface scans of films (see Figure 5.2), but the effect of varying the stretching temperature is subtle by comparison. Little difference is visible between surfaces of films produced from different iPP MFI, but there is an apparent decrease in surface porosity when the films are stretched at 110 °C relative to films stretched at 100 °C. This observation is consistent with the measured porosities presented in Figure 5.4. The pores visible in surface SEM should not be taken as representative of the pore size distribution that will be determined later by CFP. Qualitatively comparing surface SEM images to one another provides some understanding of which conditions affect pore formation, but the internal structure of membrane cannot be revealed by surface SEM.

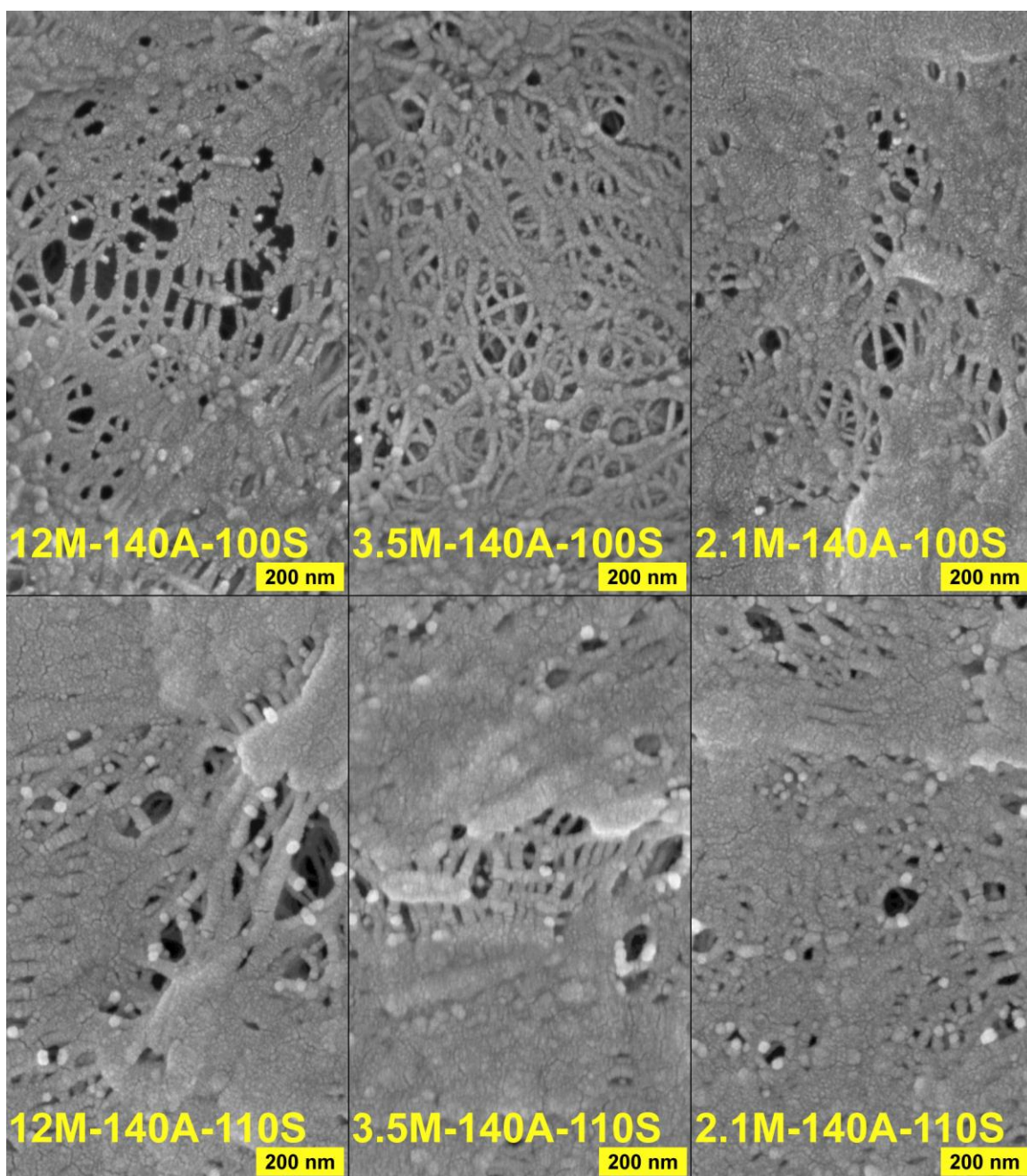


Figure 5.5. SEM micrographs of representative surface regions in stretched films. Films were prepared from precursors extruded from  $\beta$ -iPP having a MFI of 2.1, 3.5, and 12 that were subsequently annealed at 140 °C for 30 minutes and then stretched at 100 °C (top) or 110 °C (bottom).

Precursor films were overlaid with a grid pattern prior to stretching to verify the uniformity of biaxial stretching. When the annealed films were stretched at 100 or 110 °C, the expansion of the grid was even, and the thicknesses of films were relatively constant. At these stretching temperatures, films appeared consistent and opaque white in color. Annealed films stretched at 90 °C displayed inconsistencies in the expansion of the grid and in thickness. The appearance of these films was opaque white interspersed with irregular areas of slight translucency. This inconsistency over the area of the film can be quantified in terms of the uncertainty in the porosity (Figure 5.4), which is much greater than the uncertainty measured for other stretching temperatures or annealing conditions. As the stretching temperature was further decreased to 80 °C, annealed films of acceptable quality could not be produced. These results for films stretched at relatively low temperatures are consistent with the hypothesis that pore formation differs with stretching temperature. The higher degree of uncertainty in the porosity of films produced without the thermal annealing step is also apparent. In particular, films stretched at 90 and 100 °C without annealing display a relatively high variability in porosity. Whenever higher stresses are required during stretching (which occurs in films of lower iPP MFI, in thermally annealed films, or when such films are stretched at lower temperatures), the consistency of the films produced declines. Because of the similarity in appearance, stretching behavior, and porosity between films stretched at 100 and 110 °C, these films will be considered together in some of the analysis of film permeability to follow.

### **5.2.3 Influence of Processing on the Porosity, Permeability and Separation Properties of Stretched $\beta$ -iPP Films**

Prior studies of pore formation and permeability in  $\beta$ -iPP films have found that these properties are enhanced when certain processing guidelines are followed. Higher crystallization temperatures lead to larger  $\beta$  crystals, increasing porosity upon stretching

[7,12]. Biaxial stretching to 100% elongation in the machine and transverse directions of these films creates more porous films than uniaxial stretching, and these films also have higher permeability [5,13,14]. Stretching temperatures above 110 °C tend to decrease the permeability of  $\beta$ -iPP films [5]. To further improve the properties of  $\beta$ -iPP porous films, these guidelines were employed while exploring other process variables.

The variation of  $\beta_1$  content in precursor films with the porosity developed in the corresponding stretched films is similar when the stretching temperature is 100 or 110 °C. This suggests that pore formation occurs in the same way in films stretched at these conditions, and so a comparison between their permeabilities can be made. This comparison should provide an understanding of the ability to tailor the material properties of the precursor films to develop the desired function in the final produced microporous films. Permeation experiments like those shown in Figure 5.3 for 3.5 MFI films stretched at 100 °C were performed for films produced at each iPP MFI, annealing temperature, and at 100 and 110 °C stretching temperatures. The results of a comparison between the porosity in these films and their permeabilities to N<sub>2</sub> and He are presented in Figure 5.6.

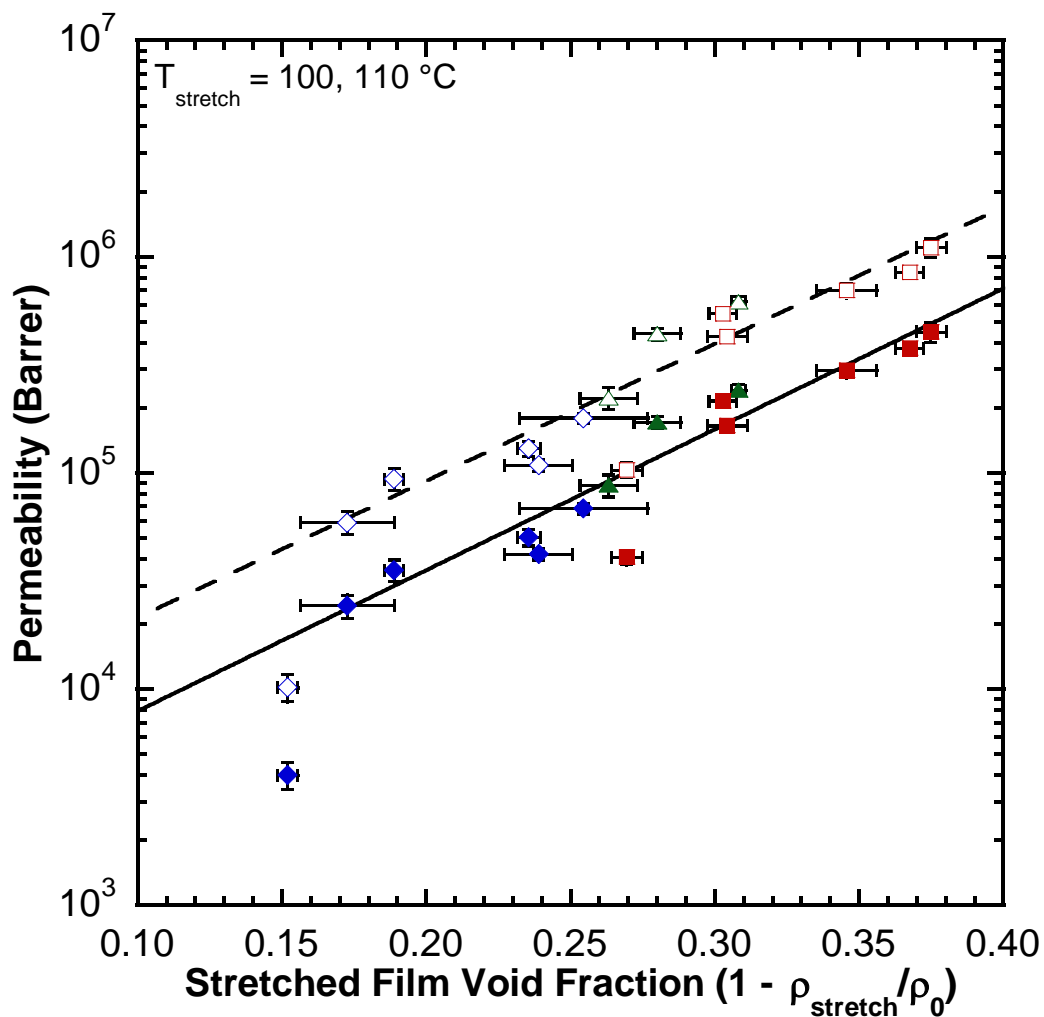


Figure 5.6. Permeability of stretched films to N<sub>2</sub> (closed symbols) and He (open symbols) as a function of porosity. Values are plotted for stretched films produced from precursors annealed for 30 minutes at 23 °C (as-extruded) (◆, ◇), 130 °C (▲, △), and 140 °C (■, □). Uncertainties represent ±1 standard deviation. The solid line is a best fit to N<sub>2</sub> permeability data, and the dashed line is a best fit to He permeability data. The point at ~15% porosity was not used to generate these fits for reasons presented in the text.

As the porosity of these stretched  $\beta$ -iPP films increased, their permeabilities increased exponentially. The porosity developed in the films increases in a regular fashion in the order of increasing annealing temperature, as would be expected based on

Figure 5.4. Remarkably, this relationship is valid over a wide variety of materials and processing conditions. This result stands in contrast to porous iPP films made by other techniques, which require strict control of processing conditions to develop high levels of porosity and permeability [18–20]. The permeabilities of both N<sub>2</sub> and He increased similarly, with the permeability of N<sub>2</sub> increasing with porosity slightly faster than that of He. This observation is related to the relationship between the pore size and porosity in the films, and it will be more fully discussed later.

Pore formation by lamellar separation might be inhibited below a certain threshold value of  $\beta_1$  content. The 12M-23A-110S porous film has the lowest porosity ( $\Phi = 0.152$ ) of all the films, which was accompanied by N<sub>2</sub> and He permeabilities that were well below the expected value based on the porosity-permeability relationship of the other films. Therefore, this data point was excluded in generating the fit to the remaining data. The significantly lower than expected permeability in this film may be a result of a less interconnected pore structure, resulting from either fewer or smaller cavities developed during stretching.

Microporous PP films are widely used industrially for a variety of separation and filtration applications [21]. To place the properties of the porous  $\beta$ -iPP films produced in this study into perspective, the porosity and gas permeability characteristics of films from Figure 5.6 have been compared with those of several types of porous PP films found in the literature or available commercially: uniaxially and biaxially stretched  $\beta$ -iPP porous films, porous PP films made with techniques similar to those used to make Celgard films, as well as commercial Celgard films. All of these films were produced using a solvent-free process and a stretching step to develop porosity. The results of this comparison are presented in Figure 5.7.

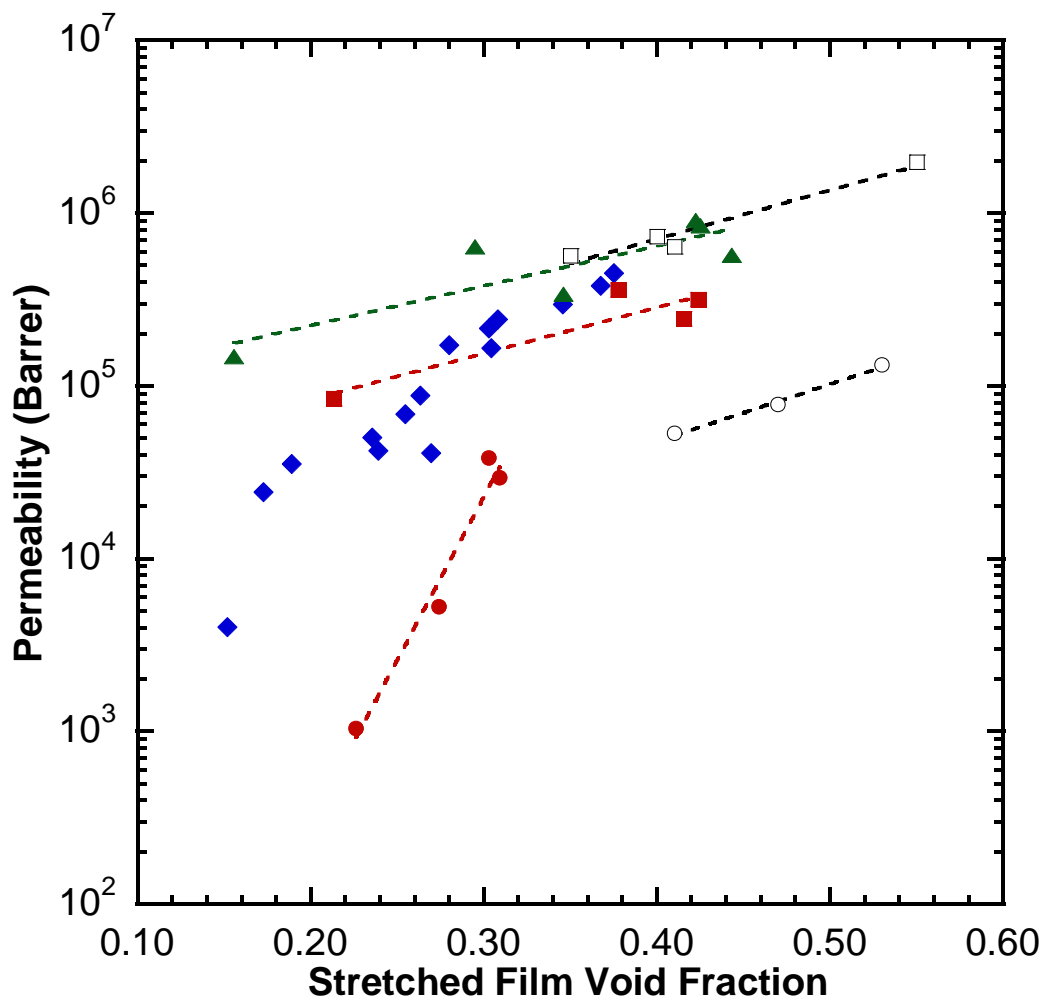


Figure 5.7. Comparison of polypropylene microporous film  $N_2$  permeability as a function of porosity. Films from this study ( $\blacklozenge$ ) are compared to  $\beta$ -iPP films that have been biaxially stretched (gas:  $O_2$ ) ( $\blacksquare$ ) [5], ( $\blacktriangle$ ) [14], as well as to those that have been uniaxially stretched (gas:  $O_2$ ) ( $\bullet$ ) [5]. Commercial Celgard films ( $\square$ ) [15] and extruded PP films made by a process similar to Celgard ( $\circ$ ) [22,23] are also included. Dashed lines represent best fits to the permeability data and are meant to guide the eye.

The permeabilities presented in Figure 5.7 are in some cases for  $O_2$ , which should have a similar permeability to  $N_2$  in these films and will therefore give a good indication of their performance. Transport data was also reported with different measurement units

in each source, and appropriate steps were taken to present permeabilities in Barrers. Compared to porous films made from  $\beta$ -iPP elsewhere, the  $N_2$  permeability of porous films in this study were quite high. One study of biaxially stretched  $\beta$ -iPP films reported a substantially higher value, but it did not present any information about the pore size distribution achieved in the porous films or the transport of other gases through the film [14]. These omissions make it difficult to understand the material properties or processing choices that resulted in the high reported permeability. An important study by Chu *et al.* reports  $O_2$  permeability data for biaxially and uniaxially stretched  $\beta$ -iPP films. In that study, the permeability is substantially higher in biaxially stretched films, and the sensitivity of porosity and permeability properties to the degree of elongation is much lower in biaxially stretched films than in uniaxially stretched films [5]. A series of porous PP films made by Sadeghi *et al.* in a fashion similar to that of Celgard films exhibit much lower  $N_2$  permeabilities than biaxially stretched  $\beta$ -iPP films, even at equivalent porosities and in spite of the fact that the pores in the film are substantially larger [22,23]. Commercially produced Celgard films generally had somewhat higher permeabilities than the highest performing  $\beta$ -iPP films at the same porosities, generally due to their larger mean pore size. The single highest performing film was Celgard 2500 (see Figure 5.7), which had a porosity of 55% and a  $N_2$  permeability just under 2,000,000 Barrer. The high performance of Celgard films relative to non-nucleated porous PP films highlights the importance of tight control of processing conditions in films made using this technique.

Although the porosity and permeability values of the examined films varied widely, each class of films exhibited a similar exponential dependence of permeability on film porosity. Uniaxially stretched  $\beta$ -iPP films showed a much higher increase in permeability with porosity than other films, but this result could be related to the low

permeability in these films when the elongation conditions were not carefully optimized to prevent pore collapse at high draw ratios [5].

Specific processing conditions employed during the production of precursor films and stretched films can also be examined for their effect on stretched film permeability and the ability of such films to perform separations. The precursor annealing temperature, the stretching temperature, and the strain rate during stretching were varied to produce porous films of each iPP MFI. The N<sub>2</sub> and He permeability of these films were measured and presented in the form of N<sub>2</sub> permeability and He/N<sub>2</sub> selectivity. Figure 5.8 presents the effect of stretch temperature and strain rate on the transport properties of stretched films produced without thermal annealing.

The applied strain rate during biaxial stretching of precursor films at 100 °C appears to have a relatively small influence on their transport properties. A prior study [3] shows that cavitation in  $\beta$ -iPP increases with strain rate, but at a lower temperature than studied here. Films produced from each iPP MFI display a small decline in permeability as strain rate is increased from 20% $s^{-1}$  to 100% $s^{-1}$ , which is within experimental uncertainty, and a larger increase as the strain rate is further increased from 100% $s^{-1}$  to 500% $s^{-1}$ . The He/N<sub>2</sub> selectivity shows the inverse of this behavior, but in this case, the selectivity of films of a given iPP MFI are within the uncertainty over the range of strain rates. The films had N<sub>2</sub> permeabilities in the order of iPP MFI 3.5 > 2.1 > 12.

Stretching temperature was found to be a more significant process variable than strain rate, based on the large changes in both permeability and selectivity that stretching under different thermal conditions caused. As the stretching temperature was increased from 90 to 100 °C, there was a significant decrease in permeability at all iPP MFI when a strain rate of 100% $s^{-1}$  was applied. As temperature was further increased to 110 °C, the 2.1M-23A-110S and 3.5M-23A-110S films displayed a modest decrease in permeability,

while the 12M-23A-110S film showed a drastic decrease. The high iPP MFI, lack of thermal annealing, and high stretching temperature in that film led to low stress during stretching, and therefore unfavorable pore formation conditions that cause low permeability. As indicated in Figure 5.6, the porosity and permeability of this porous film is the lowest in the study. The rank order of permeabilities by iPP MFI remained  $3.5 > 2.1 > 12$ . The He/N<sub>2</sub> selectivity again goes counter to the N<sub>2</sub> permeability, with higher selectivities generally measured in films with lower N<sub>2</sub> permeabilities. Increases in selectivity outside of the uncertainty occurred when the stretching temperature was increased from 90 to 100 °C in the 2.1 and 3.5 MFI films, while a similar increase in selectivity was recorded for the 12 MFI film when the stretching temperature was increased from 100 to 110 °C.

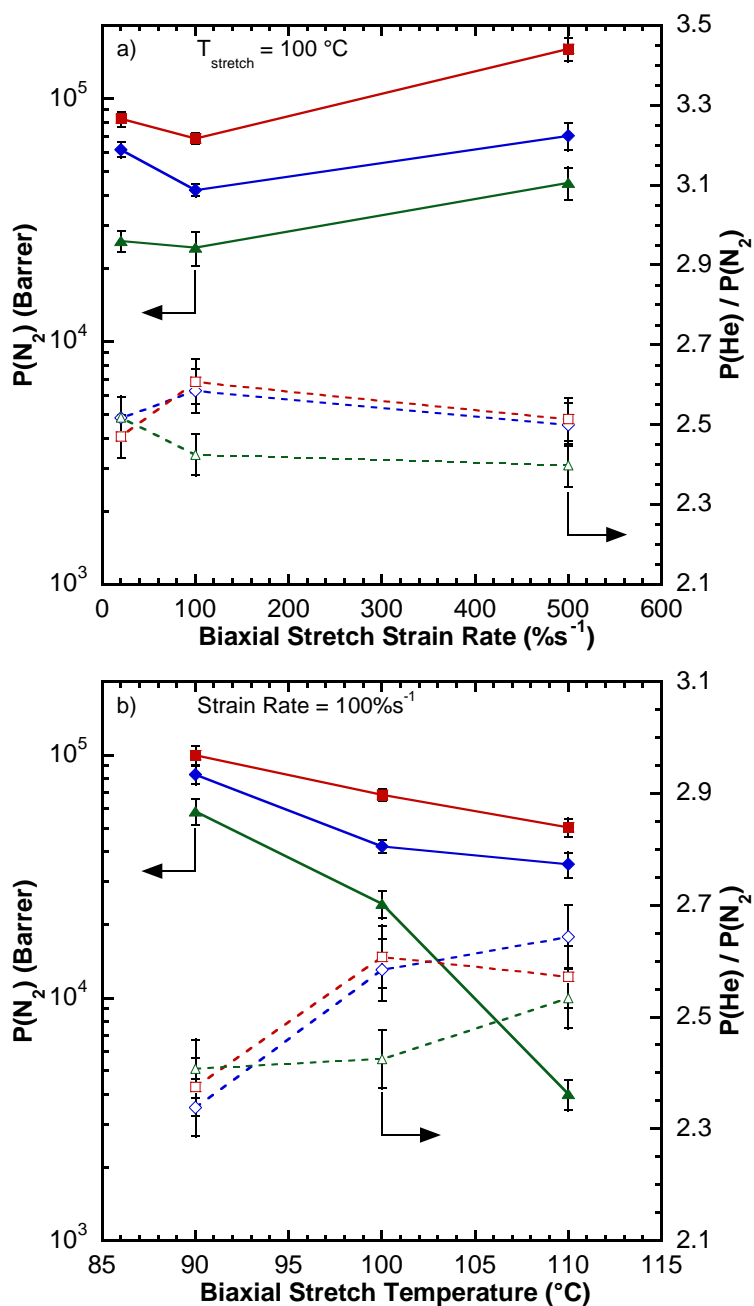


Figure 5.8.  $N_2$  permeability and He/ $N_2$  selectivity of stretched films produced from precursors annealed at  $23\text{ }^\circ\text{C}$  (as-extruded) as a function of a) strain rate at a stretching temperature of  $100\text{ }^\circ\text{C}$  and b) stretching temperature at a strain rate of  $100\%s^{-1}$ . Results are shown for MFI 2.1 ( $\blacklozenge, \blacklozenge$ ), MFI 3.5 ( $\blacksquare, \square$ ) and MFI 12 ( $\blacktriangle, \triangle$ ) films. Uncertainties represent  $\pm 1$  standard deviation.

The effect of stretching temperature in thermally annealed films and precursor annealing temperature on their transport properties is presented in Figure 5.9. The behavior of thermally annealed films at different stretching temperatures is quite different from that of as-extruded films, and this difference is exemplified by a local maximum in permeability at each iPP MFI when the films are stretched at 100 °C. Film permeabilities were lower in these films at a stretching temperature of 110 °C than they were at 90 °C. Like the as-extruded films, the He/N<sub>2</sub> selectivity appears to be lower when N<sub>2</sub> permeability is higher.

When  $\beta$ -iPP films are subjected to different thermal annealing treatments before stretching at 100 °C, N<sub>2</sub> permeability increases with annealing temperature. This is consistent with the information presented in Figure 5.1, and it reinforces the key point that thermal annealing results in the development of  $\beta$  lamellae, which lead to more porosity when stretched than the less-developed structures in as-extruded films, and the high level of porosity contributes to increased N<sub>2</sub> permeability. The He/N<sub>2</sub> selectivity remained relatively constant until the annealing temperature reached 140 °C, at which point there was a large decline.

The highest permeability films were those annealed at 140 °C and stretched at 90 or 100 °C using high MFI iPP samples. The films with the highest He/N<sub>2</sub> selectivities were those annealed at 130 °C and stretched at 110 °C using high MFI iPP samples. Consequently, processing conditions must be carefully selected to obtain porous films with the desired gas permeation properties.

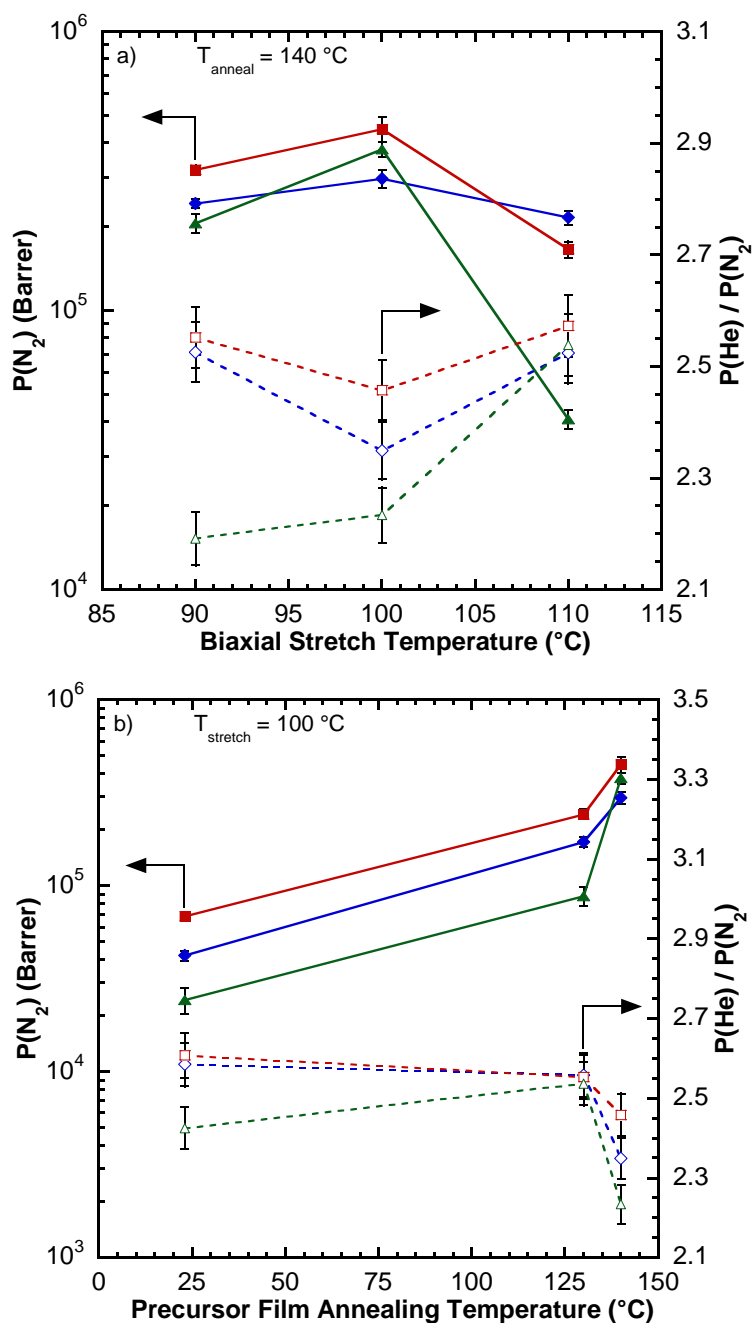


Figure 5.9.  $N_2$  permeability and He/ $N_2$  selectivity of a) stretched films produced from precursors annealed at  $140^{\circ}C$  as a function of stretching temperature and b) films stretched at  $100^{\circ}C$  as a function of precursor annealing temperature. Results are shown for MFI 2.1 ( $\blacklozenge, \diamond$ ), MFI 3.5 ( $\blacksquare, \square$ ) and MFI 12 ( $\blacktriangle, \triangle$ ) films. Uncertainties represent  $\pm 1$  standard deviation.

#### **5.2.4 Pore Size Distribution and its Influence on the Permeation Properties of Stretched $\beta$ -iPP Films**

Transport of gases through  $\beta$ -iPP porous films depends upon the probe gas, the gas pressure, the film bulk porosity, the pore size distribution, and the interconnectedness of the pore structure in the film. To more thoroughly understand the separation properties of these films, their pore structures have been investigated using SEM, CFP, and gas permeability. Figure 5.10 presents qualitative characteristics affecting the transport in thermally annealed stretched films. In several of the thermally annealed films, biaxial stretching resulted in the formation of fissures at the surface which were perpendicular to the drawing directions, and possess a length scale that is very long relative to individual surface pores presented in Figure 5.2 and Figure 5.5. If such fissures were continuous through the thickness of the film, their size would ensure that they would dominate gas transport. Cross-sections of  $\beta$ -iPP films were also observed to provide visual confirmation of a continuous pore structure through the thickness of the film. The formation of pores below the surface is apparent, indicating that a continuous structure is a possibility. To determine the nature of the pore structure, these observations can be supplemented by techniques using the passage of gas through the films.

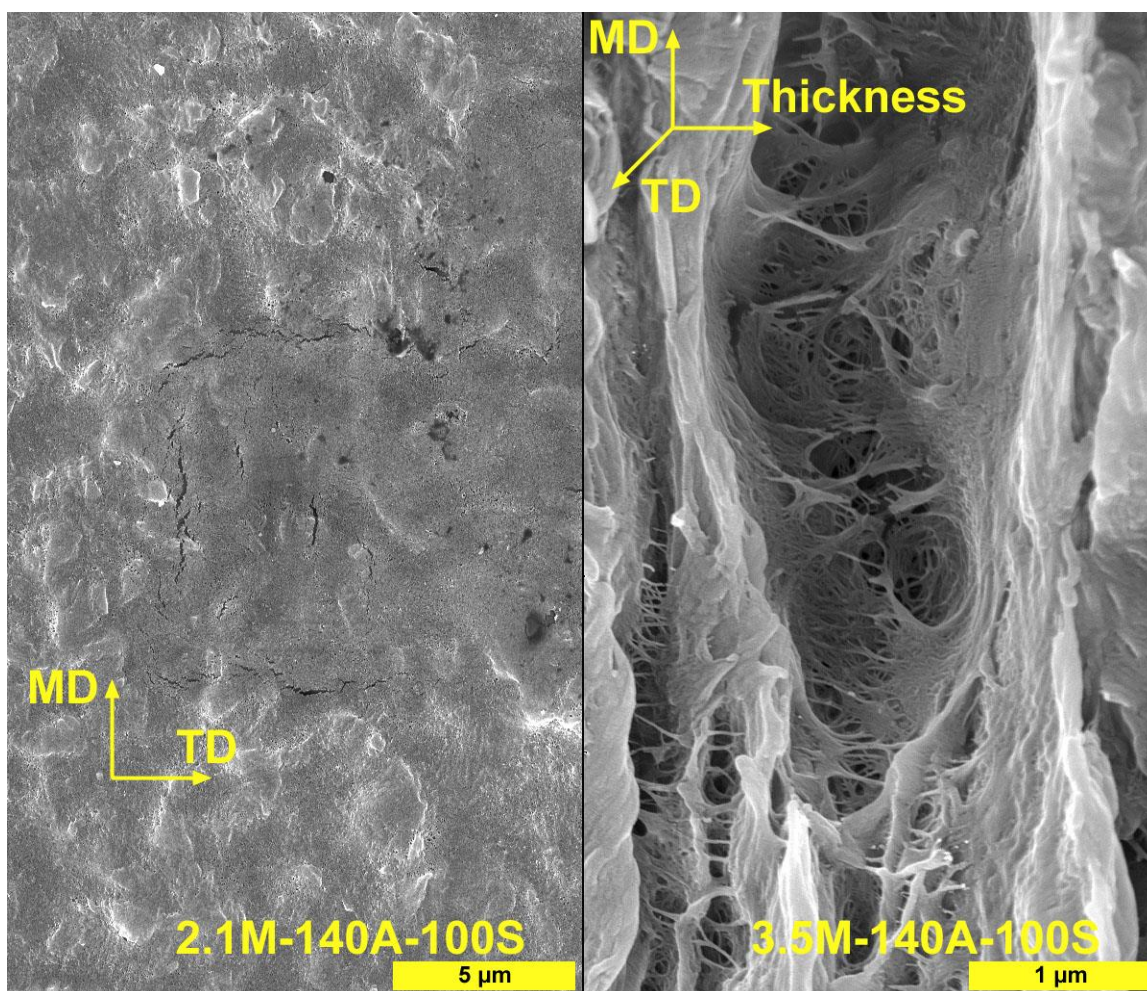


Figure 5.10. SEM micrographs demonstrating phenomena affecting gas transport through  $\beta$ -iPP stretched films. Surface fissures are observed in films whose precursors have been annealed at 140 °C and stretched (left). These fissures are formed in the machine and transverse direction relative to the biaxial stretcher, and possess a length scale that is long relative to the pores characterized. Observing a film edge-on (right) it can be seen that a continuous pore structure is created through the thickness of the stretched film.

Pore size distributions for a selection of  $\beta$ -iPP porous films were determined using a CFP technique, more broadly considered to be a bubble point technique [24,25]. Several prior studies of these materials have used mercury intrusion porometry to gather

information about their pore structure [5,7,26], a practice also employed for porous PP films in general [22,23,27]. This technique has two deficiencies in the context of transport: the high pressures required by mercury intrusion can deform the pore structure [28], and pores not involved in transport (e.g., blind pores) are detected [24]. Gas permeability measured in this study can therefore be more readily related to pore size distributions determined by CFP.

Considered as a whole, Figure 5.11 indicates that all of the pores detected in  $\beta$ -iPP films were 18 to 35 nm in diameter, which is in the ultrafiltration size range [21]. Compared to other porous films presented in Figure 5.7, the  $\beta$ -iPP films in this study had smaller pore sizes and higher permeabilities at the same porosity. Uniaxially stretched  $\beta$ -iPP films [7] had mean pore diameters of 10 to 100 nm, biaxially stretched  $\beta$ -iPP films [5] were 20 to 70 nm, and porous PP films similar to Celgard [22,23] were about 100 nm. Thus, the internal pore structure of these porous films is less well connected than those in this study, or that the high pressures used in mercury intrusion have increased the apparent pore size. Additionally, the  $\beta$ -iPP films in this study appear to have a narrower distribution than those produced elsewhere, with the majority of pores being detected within a 3 to 5 nm size window. Celgard 2400 was measured by CFP to have a mean pore diameter of 34 nm, with a comparably narrow distribution relative to other films in this study. This pore size is in reasonable agreement with the manufacturer's specification of 43 nm [15], and it is consistent with its somewhat higher permeability than our  $\beta$ -iPP films.

Processing conditions influence the pore diameter in  $\beta$ -iPP stretched films just as they influence the porosity and permeability. With one exception (2.1M-23A-90S), as-extruded films had pore sizes under 18 nm that could not be detected by CFP. The results presented in Figure 5.11 are primarily for films whose precursors were annealed at 140

°C, because their pore sizes were larger than 18 nm and were therefore detectable. The MFI of the iPP resin in annealed films had a subtle effect on stretched film pore size, with the increase in pore size tracking the increase in permeability in the order 3.5M-140A-100S > 2.1M-140A-100S > 12M-140A-100S. The balance between tie chain density, which is lowest in 12 MFI films, and lamellar block size, which is highest in 2.1 MFI films, determines this order. For stretched films made from 2.1 MFI iPP resin precursors annealed at 140 °C, increasing pore size again tracked increasing permeability in the order 2.1M-140A-100S > 2.1M-140A-90S > 2.1M-140A-110S. Because the stretching temperatures examined span two distinct types of  $\beta$  crystalline transitions, as previously discussed, properties determined by the pore formation process should not necessarily change in a regular fashion with temperature. Stretching temperature had a larger influence on mean pore diameters than iPP MFI. The largest contributor to differences in pore size is the precursor thermal annealing temperature. The 3.5M-140A-100S film had a mean pore diameter more than 7 nm larger than 3.5M-130A-100S or 2.1M-23A-90S films (3.5 MFI as-extruded films did not have detectable pore sizes), again in accord with permeability results.

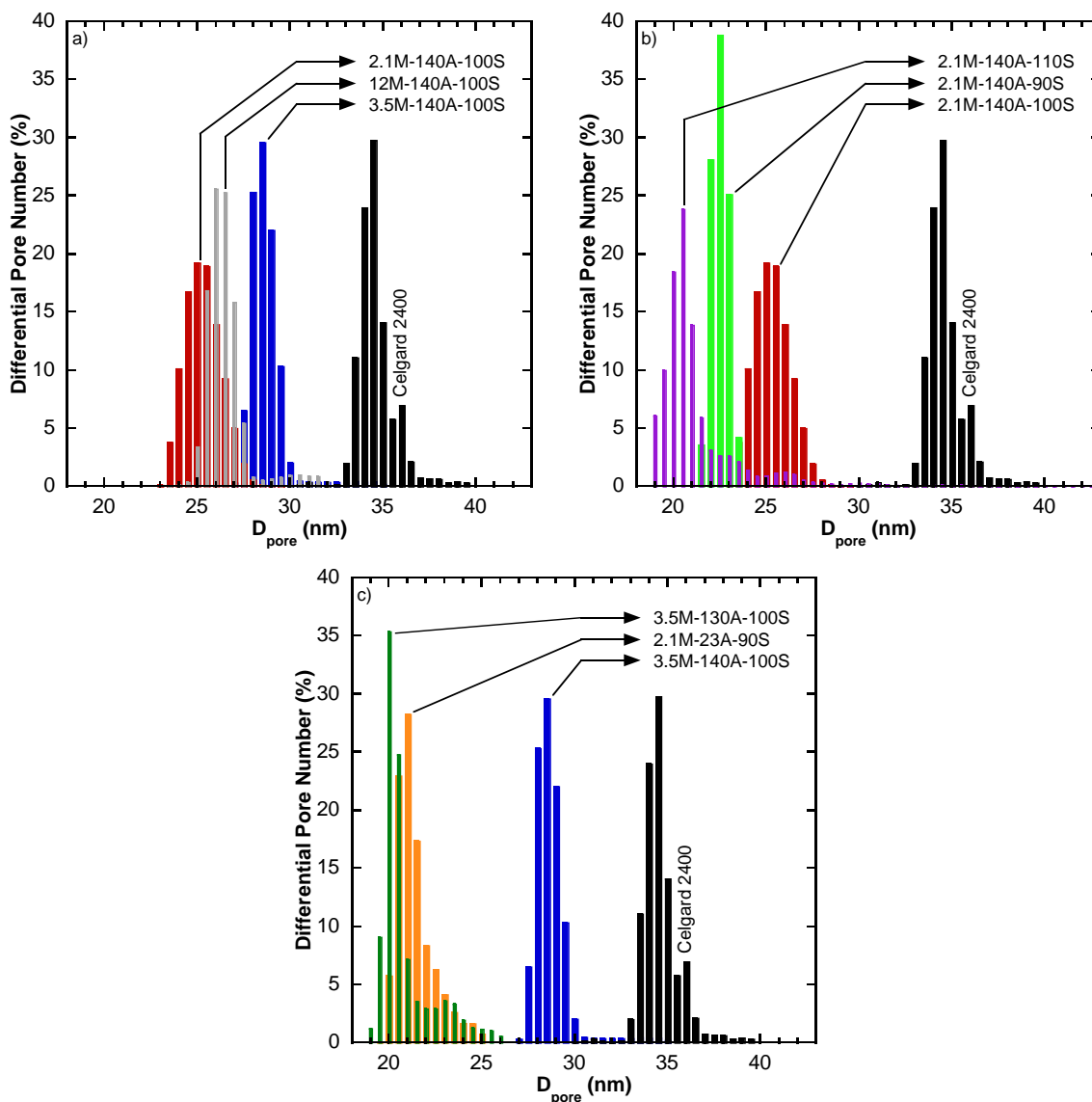


Figure 5.11. Pore size distribution in microporous films determined by capillary flow porometry for a) films of different MFI annealed at 140 °C and stretched at 100 °C, b) films of MFI 2.1 annealed at 140 °C and stretched at different temperatures, and c) films annealed at different temperatures. Films are color-coded for identification, and the pore size distribution of Celgard 2400 is included for comparison.

With the pore size distributions for these films determined, the mechanism for mass transfer can be more thoroughly investigated. For the gases and pressures tested, the

mean free path of the gas is comparable to the characteristic size of the pores, i.e. the Knudsen number is close to unity. Therefore, the flow should lie in a transition region where both Knudsen diffusion and Poiseuille flow occurs [28,29]. Inspection of the forms of the equations for transport by Knudsen diffusion is consistent with gas flux exhibiting linear variation with  $\Delta p$ , whereas Poiseuille flow would result in linear variation of gas flux with  $p\Delta p$ . Prior studies in this area have observed a distinct transition in flux behavior from Knudsen to Poiseuille mechanisms as pressure was increased [22,28]. Following Figure 5.3, linear variation of flux with  $\Delta p$  indicates that  $N_2$  transport through  $\beta$ -iPP films in this study occurs primarily by Knudsen diffusion. Similar results are seen for He flux. The selectivity of a gas pair varies with the square root of the ratio of gas molecular weights in Knudsen diffusion, while the selectivity of the same gas pair in Poiseuille flow will vary with the inverse ratio of their viscosities. In the case of the He/ $N_2$  pair, the expected Knudsen selectivity would then be 2.65, and the expected Poiseuille selectivity would be 0.898. The relatively large selectivity expected under Knudsen diffusion was the basis of the selection of He as a counterpart to  $N_2$  in this study. One prior study of similar films measured  $CO_2/O_2$  selectivity [5], but the expected Knudsen selectivity of 1.17 would be difficult to differentiate from its Poiseuille selectivity of 1.37, making this study of a single gas pair an ineffective tool to reveal the operative transport mechanism.

In reasonable agreement with the conclusion from the flux results, the selectivity of all films measured ranged from 2.19 to 2.64, indicating Knudsen diffusion is the primary mechanism for transport. An additive model [29] of the two modes of transport ( $J = J_K + J_P$ ) was constructed to determine how the selectivity of a membrane would change with pore size at a fixed differential pressure, and the results are presented in Figure 5.12. As expected from inspection of the flux equations, the transport increases in

Poiseuille character as  $D_{\text{pore}}$  and  $\Delta p$  increase. The observation that  $N_2$  flux increases more rapidly than He flux in  $\beta$ -iPP films as porosity increases is explained if that increase is attributable to larger pore sizes in more porous films. Poiseuille flow would then account for more of the transport, leading to a lower He/ $N_2$  selectivity. Several of the  $\beta$ -iPP films studied deviated significantly from the model selectivity based on their mean pore diameter, with lower than expected selectivities. This behavior could be indicative of the presence of a small number of very large pores (more along the lines of a film defect), but because such pores were not detected by CFP and the pressure-flux behavior is generally consistent with Knudsen flow, this explanation seems unlikely unless the defects were generated during the permeation experiment.

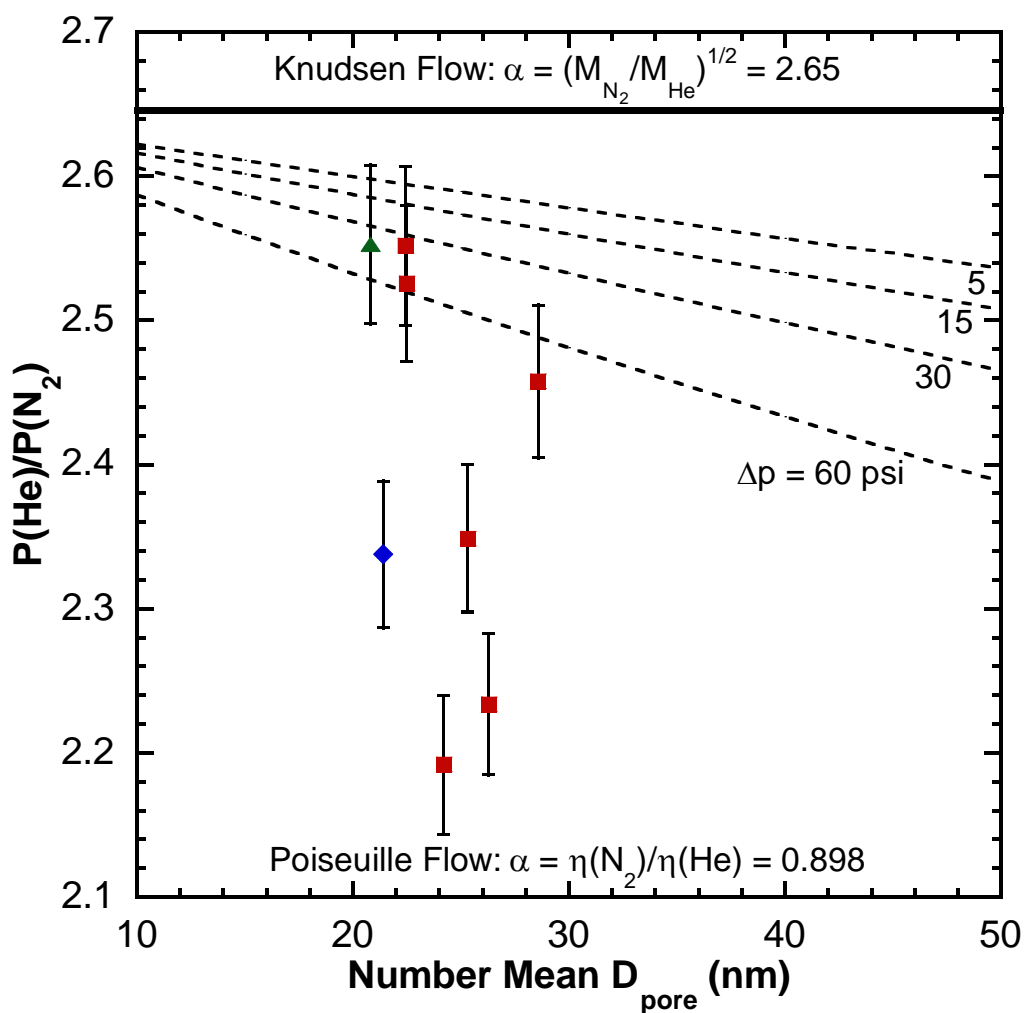


Figure 5.12. Comparison of He/N<sub>2</sub> selectivities measured for stretched films produced from precursors annealed for 30 minutes at 23 °C (as-extruded) (◆), 130 °C (▲), and 140 °C (■) to values expected from a model combining Knudsen and Poiseuille permeability as a function of film mean pore size. Results for several values of  $\Delta p$  are displayed. Expected selectivities,  $\alpha$ , are shown for both flow regimes. Permeabilities in this study were measured with  $\Delta p$  from 5 to 30 psi. Uncertainties represent  $\pm 1$  standard deviation.

### 5.3 REFERENCES

- [1] R.A. Phillips, M.D. Wolkowicz, Polypropylene Morphology, in: N. Pasquini (Ed.), Polypropylene Handbook, 2nd ed., Hanser Gardner, 2005: pp. 147–264.
- [2] G. Shi, F. Chu, G. Zhou, Z. Han, Plastic Deformation and Solid-Phase Transformation in  $\beta$ -Phase Polypropylene, *Die Makromolekulare Chemie.* 190 (1989) 907–913.
- [3] C. Grein, C.J.G. Plummer, H.-H. Kausch, Y. Germain, P. Béguelin, Influence of  $\beta$  nucleation on the mechanical properties of isotactic polypropylene and rubber modified isotactic polypropylene, *Polymer.* 43 (2002) 3279–3293.
- [4] J.X. Li, W.L. Cheung, C.M. Chan, On deformation mechanisms of  $\beta$ -polypropylene 3. Lamella structures after necking and cold drawing, *Polymer.* 40 (1999) 3641–3656.
- [5] F. Chu, Structure and gas permeability of microporous films prepared by biaxial drawing of  $\beta$ -form polypropylene, *Polymer.* 37 (1996) 573–579.
- [6] A. Turner Jones, J.M. Aizlewood, D.R. Beckett, Crystalline Forms of Isotactic Polypropylene, *Die Makromolekulare Chemie.* 75 (1964) 134–158.
- [7] F. Chu, T. Yamaoka, Y. Kimura, Crystal transformation and micropore formation during uniaxial drawing of  $\beta$ -form polypropylene film, *Polymer.* 36 (1995) 2523–2530.
- [8] H. Bai, Y. Wang, Z. Zhang, L. Han, Y. Li, L. Liu, et al., Influence of Annealing on Microstructure and Mechanical Properties of Isotactic Polypropylene with  $\beta$ -Phase Nucleating Agent, *Macromolecules.* 42 (2009) 6647–6655.
- [9] G.T. Offord, S.R. Armstrong, B.D. Freeman, E. Baer, A. Hiltner, J.S. Swinnea, et al., Porosity Enhancement in  $\beta$  Nucleated Isotactic Polypropylene Stretched Films by Thermal Annealing, *Polymer.* Accepted (2013).
- [10] J. Varga, I. Mudra, G.W. Ehrenstein, Crystallization and Melting of  $\beta$ -Nucleated Isotactic Polypropylene, *Journal of Thermal Analysis and Calorimetry.* 56 (1999) 1047–1057.
- [11] J. Varga, I. Mudra, G.W. Ehrenstein, Highly active thermally stable  $\beta$ -nucleating agents for isotactic polypropylene, *Journal of Applied Polymer Science.* 74 (1999) 2357–2368.

- [12] F. Chu, T. Yamaoka, H. Ide, Y. Kimura, Microvoid formation process during the plastic deformation of  $\beta$ -form polypropylene, *Polymer*. 35 (1994) 3442–3448.
- [13] W. Zhu, X. Zhang, C. Zhao, W. Wu, J. Hou, M. Xu, A Novel Polypropylene Microporous Film, *Polymers for Advanced Technologies*. 7 (1996) 743–748.
- [14] S. Ran, M. Xu, Studies on the Pore Formation Mechanism of  $\beta$ -Crystalline Polypropylene Under Stretching, *Chinese Journal of Polymer Science*. 22 (2004) 123–130.
- [15] Celgard, Celgard Product Comparison, Company Literature Item #10002, 2009.
- [16] C. Grein, Toughness of Neat, Rubber Modified and Filled  $\beta$ -Nucleated Polypropylene: From Fundamentals to Applications, *Advances in Polymer Science*. 188 (2005) 43–104.
- [17] S. Humbert, O. Lame, J.M. Chenal, C. Rochas, G. Vigier, New Insight on Initiation of Cavitation in Semicrystalline Polymers: In-Situ SAXS Measurements, *Macromolecules*. 43 (2010) 7212–7221.
- [18] S.H. Tabatabaei, P.J. Carreau, A. Aji, Effect of processing on the crystalline orientation, morphology, and mechanical properties of polypropylene cast films and microporous membrane formation, *Polymer*. 50 (2009) 4228–4240.
- [19] S.H. Tabatabaei, P.J. Carreau, A. Aji, Structure and properties of MDO stretched polypropylene, *Polymer*. 50 (2009) 3981–3989.
- [20] F. Sadeghi, A. Aji, P.J. Carreau, Analysis of row nucleated lamellar morphology of polypropylene obtained from the cast film process: Effect of melt rheology and process conditions, *Polymer Engineering & Science*. 47 (2007) 1170–1178.
- [21] R.W. Baker, *Membrane Technology and Applications*, 2nd ed., West Sussex, John Wiley & Sons, Ltd., 2004.
- [22] F. Sadeghi, A. Aji, P.J. Carreau, Analysis of microporous membranes obtained from polypropylene films by stretching, *Journal of Membrane Science*. 292 (2007) 62–71.
- [23] F. Sadeghi, A. Aji, P.J. Carreau, Microporous membranes obtained from polypropylene blends with superior permeability properties, *Journal of Polymer Science Part B: Polymer Physics*. 46 (2008) 148–157.

- [24] R.I. Peinador, J.I. Calvo, P. Prádanos, L. Palacio, A. Hernández, Characterisation of polymeric UF membranes by liquid–liquid displacement porosimetry, *Journal of Membrane Science*. 348 (2010) 238–244.
- [25] A. Gigova, Investigation of the porous structure of battery separators using various porometric methods, *Journal of Power Sources*. 158 (2006) 1054–1061.
- [26] G. Shi, X. Zhang, J. Zheng, G. Zhou, Microporous Film, Made from  $\beta$ -Crystalline Phase Polypropylene, *International Polymer Processing*. 10 (1995) 330–333.
- [27] S.H. Tabatabaei, P.J. Carreau, A. Ajji, Microporous membranes obtained from polypropylene blend films by stretching, *Journal of Membrane Science*. 325 (2008) 772–782.
- [28] A. Hernandez, Pore size distributions in microporous membranes. A critical analysis of the bubble point extended method, *Journal of Membrane Science*. 112 (1996) 1–12.
- [29] R.W. Schofield, A.G. Fane, C.J.D. Fell, Gas and Vapour Transport Through Microporous Membranes. I. Knudsen-Poiseuille Transition, *Journal of Membrane Science*. 53 (1990) 159–171.
- [30] G.T. Offord, S.R. Armstrong, B.D. Freeman, E. Baer, A. Hiltner, D.R. Paul, Influence of Processing Strategies on Porosity and Permeability of  $\beta$  Nucleated Isotactic Polypropylene Stretched Films, *Polymer*. Accepted (2013).

## **Chapter 6. Transport Properties of PEBAX Copolymers and their use in Multilayered Membranes for Modified Atmosphere Packaging**

### **6.1 SUMMARY**

Single layer PEBAX films were extruded and characterized for gas permeability and gas pair selectivity. PEBAX transport properties were studied for their variation with polyether block content, transmembrane pressure, and temperature. These findings were used to model the parameters required to successfully construct a package suitable for the preservation of fresh produce. Multilayered films composed of PEBAX and  $\beta$ -iPP were coextruded and biaxially stretched to fabricate composite membranes with porous support and dense selective layers. The influence of the draw ratio, layer count, and PEBAX composition in these films was measured via permeation experiments. A simple transport model was developed to account for deviations from expected membrane performance and to provide insight on what processes could lead to these deviations. The application performance of multilayered films was compared to the performance expected from earlier idealized modeling work. Finally, a thermal annealing procedure developed in earlier chapters was examined for its effect on pore formation in multilayered films.

## 6.2 RESULTS AND DISCUSSION

### 6.2.1 Basic Characterization of PEBAX Copolymers

Because the transport properties of PE-b-PA copolymers depend sensitively on their polyether content [1,2], elemental analysis was performed by Galbraith Labs to estimate the composition of the materials considered. Combustion of pelletized PEBAX was performed to determine the nitrogen content in the material, and therefore the weight fraction of PA12 in the copolymer. The compositions determined by this technique reflect findings elsewhere [3,4], and are slightly lower than those found by FTIR analysis of characteristic PTMO and PA12 peaks [5]. PEBAX compositions are displayed in Table 6.1.

Table 6.1. Property data for PEBAX films.

PEBAX Grade	Polyether (PE)			Polyamide (PA)			
	Type	PE wt. %	PE T <sub>m</sub> , °C	Type	PA wt. %	PA T <sub>m</sub> , °C	PA X <sub>c</sub> , wt. %
1074	PEO	49%	6	PA12	49%	158	22%
3000	PEO	70%	8	PA12	30%	158	23%
1041	PTMO	28%	-2	PA12	72%	172	21%
1205	PTMO	52%	-18	PA12	48%	147	19%
2533	PTMO	80%	10	PA12	20%	138	8%

PE-b-PA materials are microphase separated, with PE and PA blocks largely inhabiting separate domains in the polymer [6]. The simplest way to model transport through such a material is by treating it as a composite with two separate, non-interacting phases, each having distinct transport properties. Transport occurs primarily through the more permeable PE phase, so treating the PA phase as impermeable provides a good first approximation to the properties of the composite. Several factors can cause polymer behavior to deviate from this ideal. Interactions between the PE and PA block that compromise the phase separation can result in reduced permeability. If the less permeable

PA block is more crystalline, the interaction of amorphous PA with PE is reduced. The reduced interaction improves PE phase permeability, and the overall permeability increases in spite of higher total crystallinity [7]. When PEBAX films are cast from solution, the choice of solvent can influence the size and shape of domains in the polymer microstructure [8]. Orientation, whether from the casting process, applied strain, or from extrusion, can influence the size and shape of domains as well as crystallinity [5,8–10]. Transport properties are, therefore, influenced by both the structure of the polymer and how the polymer is processed. Efforts have been undertaken elsewhere to develop copolymer systems with based on these ideas [7,11–13], but none of these advanced materials are available in large quantities for applications involving extruded films.

First heating scans of extruded PEBAX films were performed by DSC to determine the crystallinity of the PA phase in the films, and those results are presented in Table 6.1. PTMO-based PEBAX grades exhibit higher PA crystallinity when the PA content is higher, likely due to a higher number of PA repeat units. PEO-based grades have higher crystallinity in the PA block than do PTMO-based grades. In both cases, observed crystallinity appears to be lower than in PEBAX films extruded for transport characterization in other studies [1,4]. It is difficult to say why this would be the case, because materials in those studies were received as films rather than extruded by the authors, so processing conditions are unavailable.

Second heating DSC scans of PE-b-PA copolymers are presented in Figure 6.3. Low temperature melting peaks of PE blocks and high temperature melting peaks of PA blocks are visible, and the melting temperatures are recorded in Table 6.1. Melting temperatures and shapes of characteristic peaks correspond quite well with identical grades of PEBAX studied previously [3,4], with differences likely resulting from differences in scan rates. PTMO-based grades with higher PA12 contents tended to

exhibit higher PA melting temperatures and higher PA crystallinity. 80PTMO-PA12 had a strong PTMO melting peak, likely due to its high PTMO composition. PEO-based grades had strong PEO and PA12 melting peaks. The curious thermal behavior of the 70PEO-PA12 film, which exhibits an intermediate peak at  $\sim 73$  °C, can be explained by the fact that this PEBAX grade includes an additive not present in the other grades [4]. Good quality films could not be extruded from this grade of PEBAX, so any implications arising from this additive were not further explored.

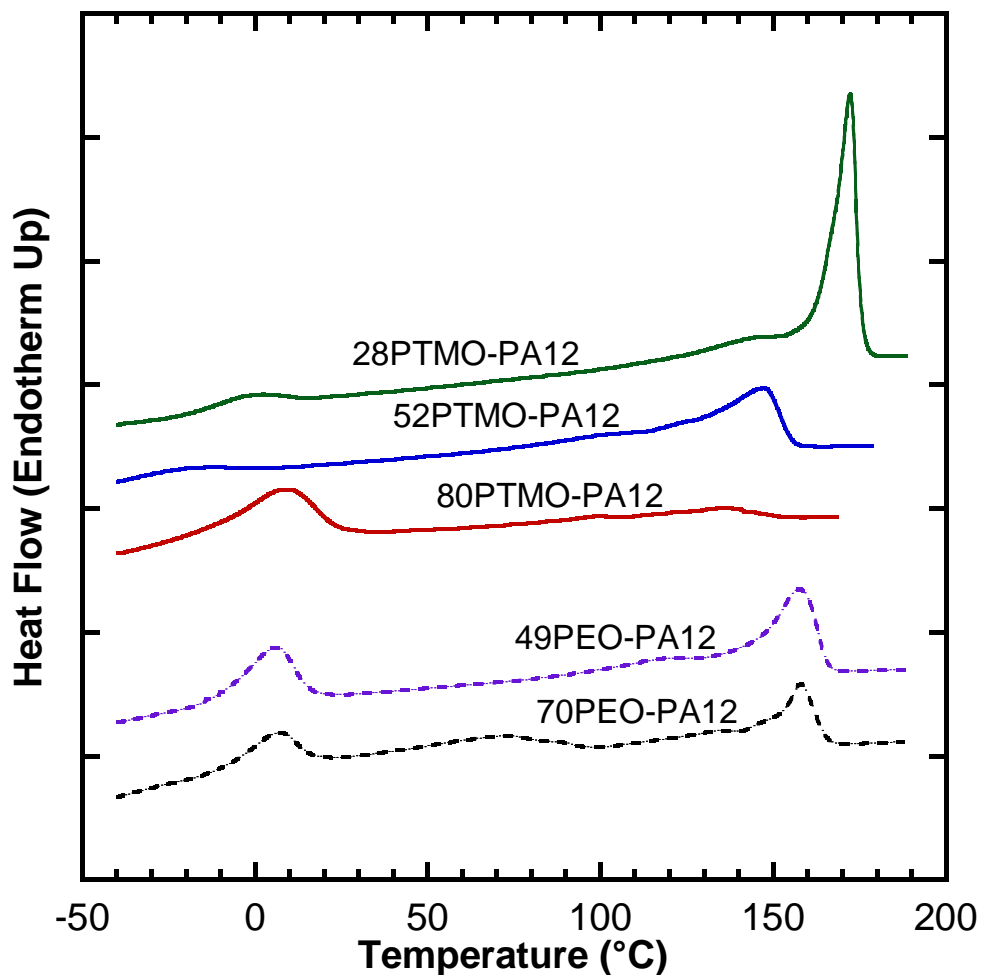


Figure 6.1. Second heating scans of PTMO and PEO-based PEBA12 copolymers showing melting peaks for PE blocks at low temperature and PA12 blocks at high temperature.

### 6.2.2 Permeability of Single Layer PEBA12 Films

The permeability of PTMO-based PEBA12 grades (28PTMO-PA12, 52PTMO-PA12, 80PTMO-PA12) were measured at 35 °C as a function of transmembrane pressure. These results are presented in Figure 6.2.

None of these PTMO-based grades exhibited measurable dependencies of permeability on transmembrane pressure. This is typical of gases that are present in low

concentrations in rubbery polymers [14,15], although plasticization occurs in rubbers when exposed to high-sorbing gases such as CO<sub>2</sub> at higher pressures [14–16]. Because the intention of this study was to determine the properties of these materials for MAP applications, high applied pressures that result in high gas concentrations are not likely to be encountered. In each PEBAX grade, the permeability was highest for CO<sub>2</sub>, significantly lower for O<sub>2</sub>, and lower still for N<sub>2</sub>. This is consistent with prior results for PEBAX [1,2,4,8], and it reflects the fact that CO<sub>2</sub> is a smaller gas than O<sub>2</sub>, which, in turn, is smaller than N<sub>2</sub> [14,17]. This gives CO<sub>2</sub> a diffusivity selectivity advantage over the other gases. More significantly, as was discussed previously, CO<sub>2</sub> is much more soluble than either gas in this class of materials. The permselectivity of these PEBAX grades also shows little dependence on transmembrane pressure, and as can be deduced from the permeability results, CO<sub>2</sub>/N<sub>2</sub> selectivities are higher than CO<sub>2</sub>/O<sub>2</sub> selectivities. In the case of the 28PTMO-PA12 membrane, both selectivities were slightly elevated at the highest transmembrane pressure. The permeability measurements show a small increase in CO<sub>2</sub> permeability and a small decrease in O<sub>2</sub> and N<sub>2</sub> permeability relative to lower pressures. One explanation consistent with these findings is that there was an undetected leak into the downstream, elevating the apparent flux at lower pressures. The permeability and selectivity values at higher pressures would then be more consistent with the properties of the materials than the values at lower pressures.

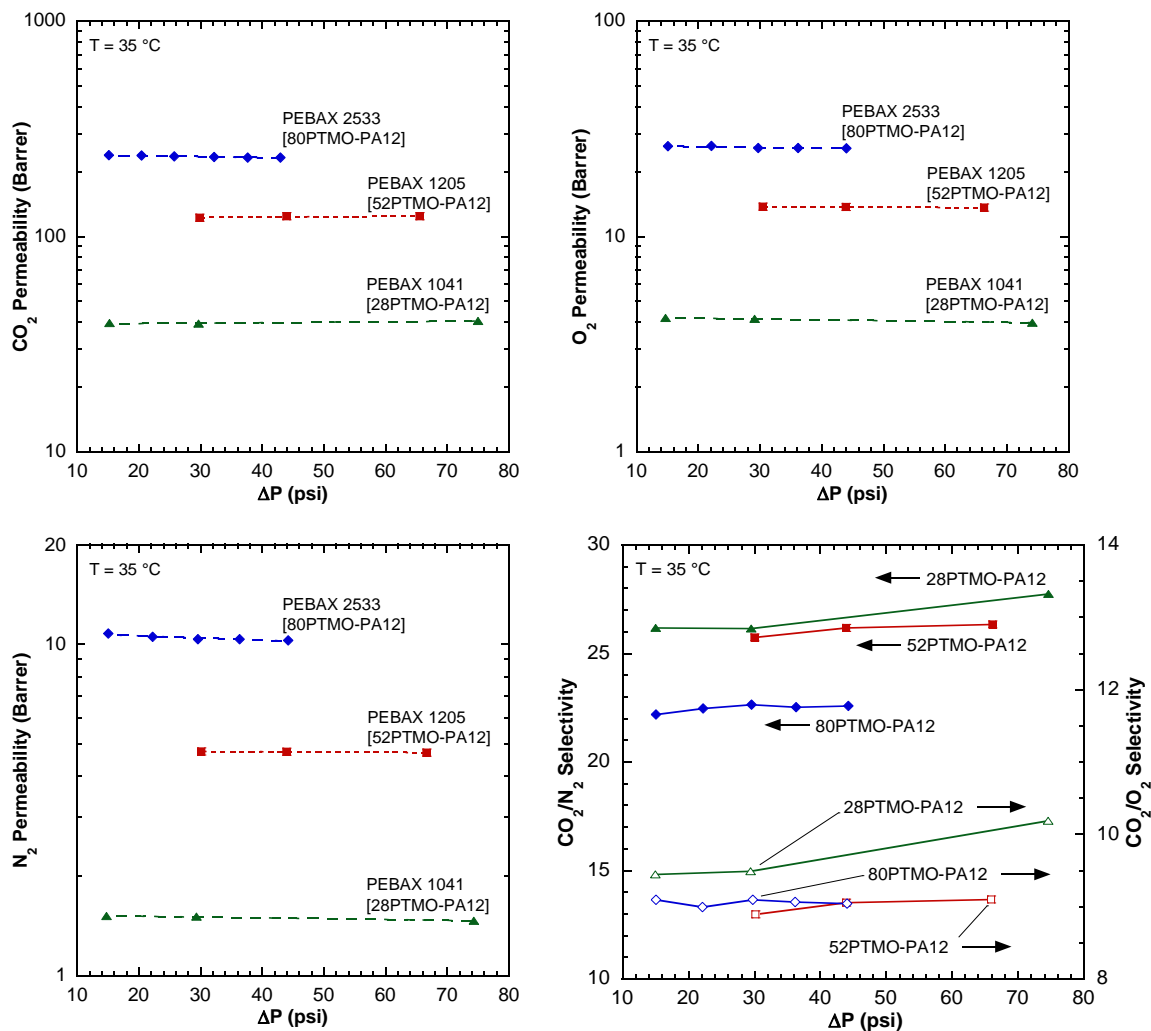


Figure 6.2. Permeability of CO<sub>2</sub>, O<sub>2</sub>, and N<sub>2</sub> in PTMO-based PEBAX copolymers as a function of transmembrane pressure at 35 °C. Pure gas selectivities are also presented.

One way of recasting the data to look at structure-property relationships in these materials is to examine the change in transport properties with PTMO block content. The results of this analysis for samples tested at 35 °C and 2 atm transmembrane pressure are presented in Figure 6.3.

As PTMO block content increases, the permeability of each gas increases, consistent with the picture that transport occurs primarily through the PE block in these materials. At levels of PTMO content above 28%, there is little change in the selectivity of either gas pair studied as a function of PTMO content. These materials are known to have a morphology featuring an interconnected PTMO phase [9]. A study performed by our colleagues at Case Western Reserve University [5,10] on a series of similar materials shows similar behavior at these levels of PTMO content, but also reveals a behavior consistent with the breakup of PTMO interconnection at low contents. The permeability of CO<sub>2</sub> and O<sub>2</sub> begin to decline rapidly with decreasing PTMO content below 25 wt. % PTMO, with the CO<sub>2</sub> permeability decreasing at a greater rate. Since CO<sub>2</sub> permeability is especially advantaged due to its high solubility in the PE phase of PE-b-PA materials, network breakup is an excellent hypothesis to explain the observed permeation phenomena.

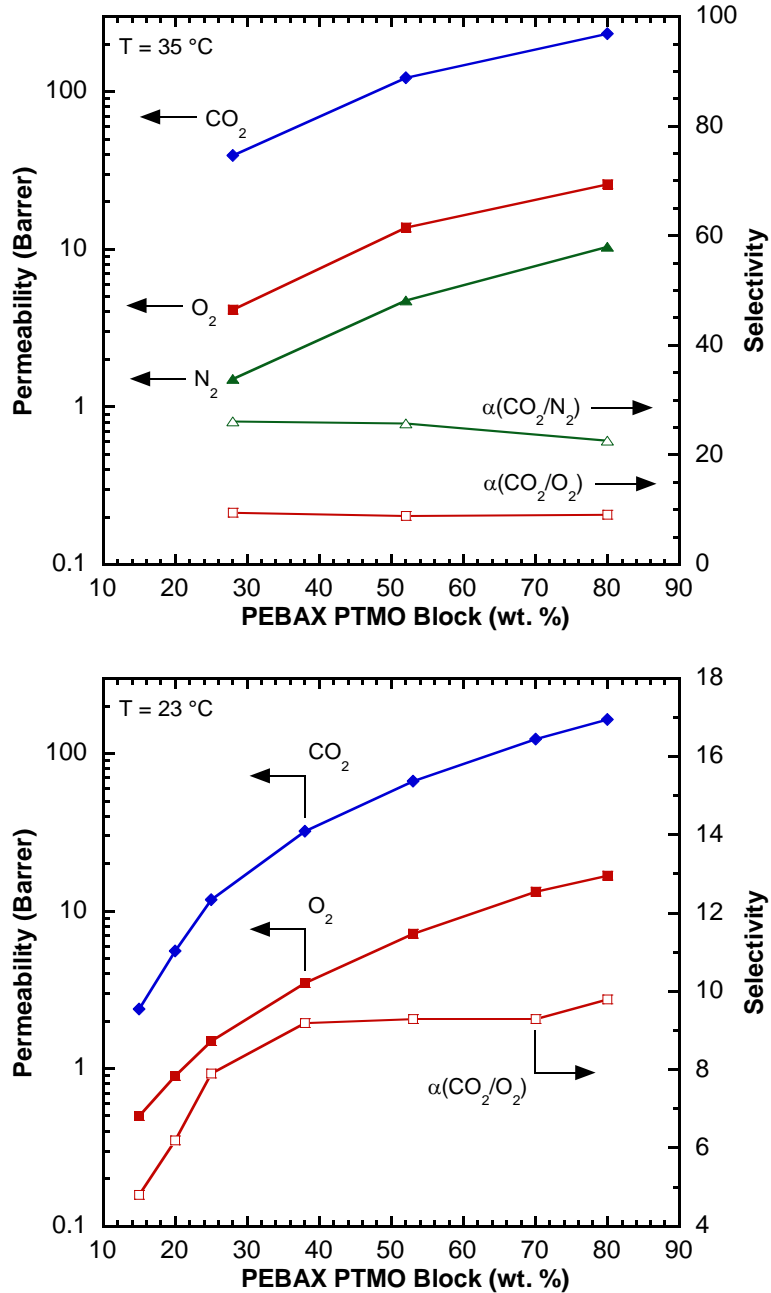


Figure 6.3. Permeability and selectivity of PTMO-based PEBAX copolymers shown in Figure 6.2 as a function of PTMO block content (top). Similar data is also presented from a companion study of PTMO-based xx33 series PEBAX copolymers at 23 °C, displaying rapid loss of permeability and selectivity at low PTMO content (bottom). This latter figure has been adapted with permission from an article published in *Polymer* [5]. Solid lines are meant to guide the eye.

The permeability of the most permeable PTMO-based PEBAX (80PTMO-PA12) and that of a PEO-based PEBAX (49PEO-PA12) were measured at a transmembrane pressure of 2 atm as a function of temperature. Temperatures from 5 to 35 °C were selected to correspond to potential temperature conditions such membranes would face in MAP scenarios. Permeabilities of CO<sub>2</sub>, O<sub>2</sub>, and N<sub>2</sub> in these materials are presented in Figure 6.4.

The permeability of each gas increases with temperature in both the 80PTMO-PA12 and 49PEO-PA12 rubbery polymers. There are no glass transitions or other phase changes over the temperature range examined, so a continuous increase in permeability with temperature is observed [2,14,18]. Both CO<sub>2</sub>/N<sub>2</sub> and CO<sub>2</sub>/O<sub>2</sub> selectivities decrease with temperature. In this type of material, the increase in CO<sub>2</sub> diffusivity is similar to that of the light gases with temperature, but a much larger decrease in solubility with temperature occurs with CO<sub>2</sub> compared to the light gases [2].

The 80PTMO-PA12 material exhibits higher permeabilities than the 49PEO-PA12 material due to its higher PE block content, as well as the fact that PTMO segments tend to be more mobile and hence promote higher diffusivity than PEO segments [19]. The PEO-based material, however, has higher selectivities for CO<sub>2</sub> over the light gases because the concentration of the ether oxygens is higher in the PE phase of PEO-based materials than in PTMO-based materials [1]. CO<sub>2</sub> permeabilities of nearly 250 Barrer are achieved in 80PTMO-PA12 membranes at 35 °C, and 49PEO-PA12 membranes exhibit CO<sub>2</sub>/O<sub>2</sub> selectivities of nearly 30 at 5 °C.

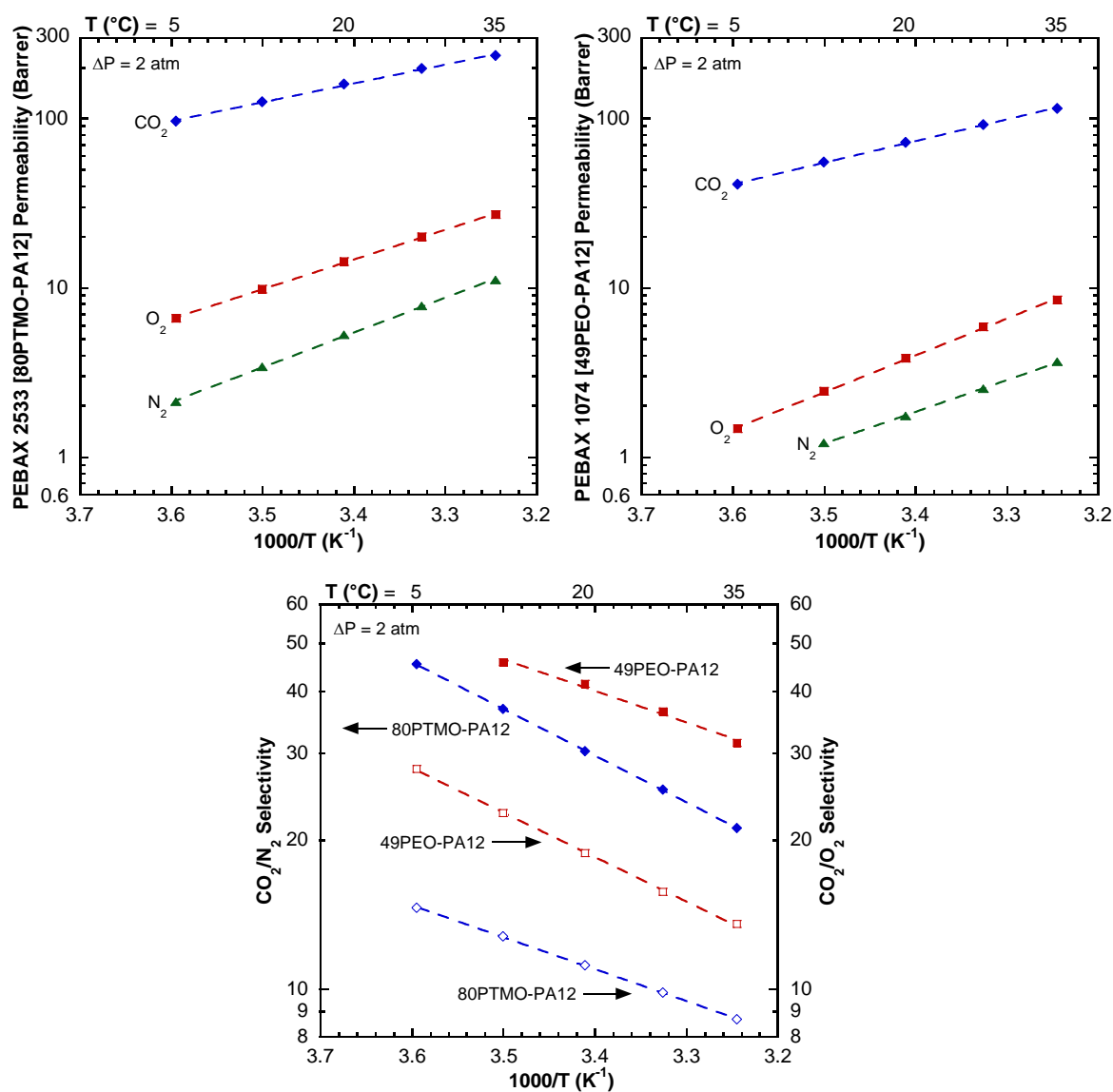


Figure 6.4. Comparison of permeability and selectivity in PEO and PTMO-based PEBAX copolymers at temperatures from 5 to 35 °C. Dashed lines represent the best fit to the Arrhenius relationship between permeability and temperature.

The temperature dependence of permeability in these materials can be modeled using a simple Arrhenius relationship as follows [14]:

$$P = P_0 \cdot e^{-E_p/R \cdot T} \quad (1)$$

where  $P_0$  is a pre-exponential factor,  $E_p$  is the activation energy of permeation, and  $R$  is the gas constant. The parameters for this equation were fit to the experimental data presented in Figure 6.4 and are shown in Table 6.2. This model will be used in the following section, which describes how PEBAX materials may be used in MAP applications.

Table 6.2. Arrhenius parameters for the temperature dependence of gas permeation in PEBAX copolymers.

Polymer	$P_0$ (Barrer)			$E_p$ (kJ/mol)		
	CO <sub>2</sub>	O <sub>2</sub>	N <sub>2</sub>	CO <sub>2</sub>	O <sub>2</sub>	N <sub>2</sub>
80PTMO-PA12	$9.87 \times 10^5$	$1.40 \times 10^7$	$5.36 \times 10^7$	21.3	33.7	39.4
49PEO-PA12	$1.66 \times 10^6$	$1.03 \times 10^8$	$4.46 \times 10^6$	24.5	41.7	35.9

### 6.2.3 Prediction of Parameters for PEBAX Films for MAP

Two material properties are most important in the construction of a MAP membrane: O<sub>2</sub> permeability, and CO<sub>2</sub>/O<sub>2</sub> selectivity [20,21]. MAP membrane O<sub>2</sub> flux (a function of O<sub>2</sub> permeability, membrane area, and active layer thickness) determines how effectively the package can replace O<sub>2</sub> depleted by produce respiration. Commercially available products, such as Landec's Intellipac MAP membrane, generate very high O<sub>2</sub> fluxes by using thin surface coatings deposited on porous substrates. This is in contrast to the approach in this project, which uses high permeability materials so that the separating layer may be thicker. It should be noted that the CO<sub>2</sub>/O<sub>2</sub> selectivity of Intellipac MAP membranes was measured to be  $\sim 4$ , indicating that the applications for which the membrane is intended are much more limited than for PEBAX materials designed to provide equivalent O<sub>2</sub> flux.

Because the Intellipac separating layer material is proprietary and exists in the form of a thin surface coating of unknown thickness, it is easiest to compare the O<sub>2</sub> permeance of the Intellipac membrane to that of PEBAX membranes. Permeance is the

pressure normalized O<sub>2</sub> flux, where 1 Gas Permeation Unit (GPU) = 1 Barrer/μm. The results of this comparison, presented as O<sub>2</sub> permeance as a function of temperature, are shown in Figure 6.5.

The O<sub>2</sub> permeance of the Intellipac membrane is substantially higher than that of either the 80PTMO-PA12 or 49PEO-PA12 PEBAX films at all temperatures. Its O<sub>2</sub> permeance increased from 34 to 71 GPU as temperature was increased from 5 to 35 °C. The separating layer of the Intellipac membrane is likely thinner than 1 μm [22], compared to the 38 to 48 μm thickness of the extruded PEBAX films. Because the thickness of the separating layer in the PEBAX films is known (in this case, it is just the total film thickness), the required thickness to match the O<sub>2</sub> permeance of the Intellipac membrane can be calculated as a function of temperature. The O<sub>2</sub> permeability of the PEBAX films increases more rapidly with temperature than does the Intellipac membrane, resulting in less stringent thickness requirements (i.e., the membrane can be thicker) at higher temperatures. 80PTMO-PA12 films can be as thick as 0.4 μm at 35 °C and exhibit equivalent O<sub>2</sub> permeance. Unfortunately, it is not currently possible to extrude a free-standing PEBAX film much thinner than about 15 μm, so a different solution must be pursued.

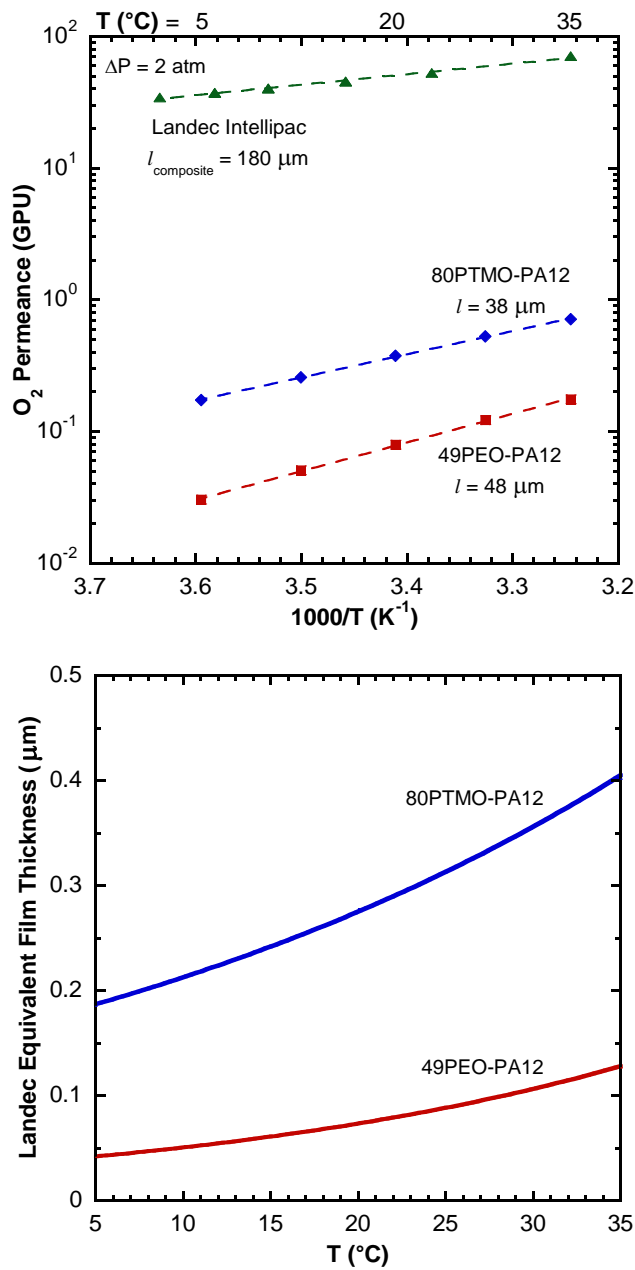


Figure 6.5. The O<sub>2</sub> permeance of extruded PEBA<sub>X</sub> copolymer films compared to that of a commercially produced Landec Intellipac MAP composite film at temperatures from 5 to 35 °C (top). The thickness required of a PEBA<sub>X</sub> separating layer to provide O<sub>2</sub> flux equivalent to the Intellipac composite film was then calculated (bottom).

To create a MAP membrane with reasonable coverage (i.e., not too large) on the package, the O<sub>2</sub> permeance of the membrane should be approximately 30 GPU. Figure 6.6 presents the required membrane thickness of the PTMO and PEO-based PEBAX grades studied at 35 °C to reach several different values of O<sub>2</sub> permeance.

To meet this performance standard, a film made of 80PTMO-PA12 would need to be about 0.9 μm in thickness, and a film made of 49PEO-PA12 would need to be about 0.3 μm in thickness. Because of the superior CO<sub>2</sub>/O<sub>2</sub> selectivity of the PEO-based PEBAX, 49PEO-PA12 will be used alongside the higher permeability 80PTMO-PA12 grade to develop package parameters that would yield an optimal atmosphere for apple storage.

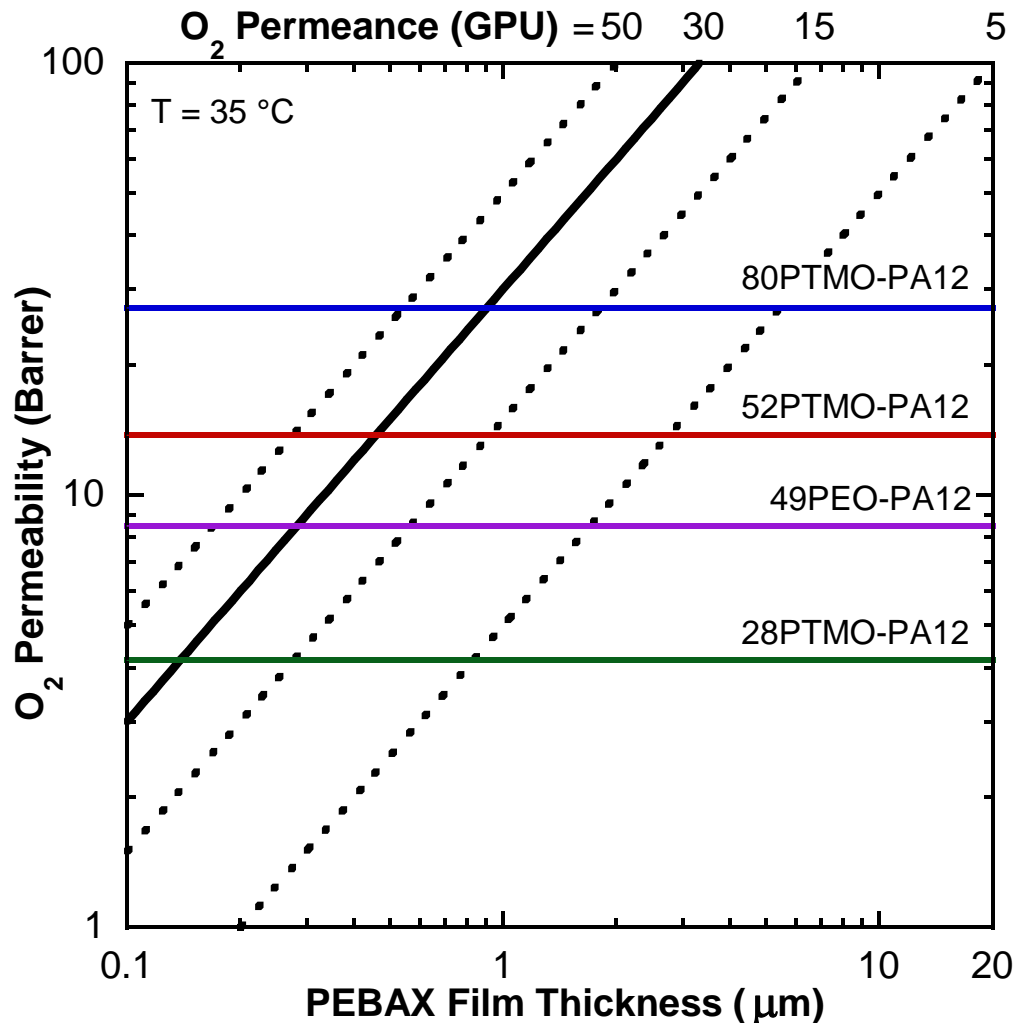


Figure 6.6. O<sub>2</sub> permeance of PEBAX membranes with different O<sub>2</sub> permeabilities as a function of total film thickness. The target O<sub>2</sub> permeance (30 GPU) is outlined in solid black.

The storage of apples is a relatively demanding application for MAP materials, with optimal conditions consisting of low levels of CO<sub>2</sub> (1 to 2%) and O<sub>2</sub> (1.8 to 3%) [21,23]. As mentioned in Chapter 2, reaching these conditions requires a membrane with both high CO<sub>2</sub>/O<sub>2</sub> selectivity and high O<sub>2</sub> flux. Ripening and eventual spoilage of apples may also be forestalled by storage at temperatures only slightly above freezing, although higher temperatures may be encountered both during shipping and when on display for

sale. Like the transport properties of PEBAX materials discussed in the previous section, the metabolic behavior of produce is temperature dependent. The purpose of the following analysis is to use a simple model developed previously [20,21] to determine package atmospheric composition. That analysis will be extended by invoking the temperature dependence of both the membrane materials (49PEO-PA12, 80PTMO-PA12) and produce (apples) to determine the required membrane area to reach an optimal package composition as a function of temperature.

A previous study focused on the storage of produce in large quantities in a container with a selective membrane in contact with a well-mixed environment and a non-selective membrane in contact with a chamber supplied with a controlled air flow [21]. By varying the air flow, the slope of the operating line defining the achievable compositions can be altered, creating a versatile system for large scale produce storage. However, when the air flow to the non-selective membrane is exactly the quantity required to create an isobaric condition in the container, the analysis is simplified, and the physical situation becomes plausible for small scale produce storage. In this case [20], the operating line, which runs between the atmospheric composition and that of the CO<sub>2</sub> concentration at zero package O<sub>2</sub> ( $x_{CO_2,0}$ ), can be defined in terms of three parameters:

$$x_{CO_2,0} = 0.21 \cdot \frac{\alpha_{O_2/N_2} + 0.266}{\alpha_{CO_2/N_2} / RQ + 0.266} \quad (2)$$

where  $\alpha$  is the selectivity of the displayed gas pair, and RQ is the ratio of the produce CO<sub>2</sub> production to that of its O<sub>2</sub> consumption, a value typically close to 1.2 [21]. The value of RQ is generally reported as a fixed value regardless of temperature [23], meaning that the slope of the operating line varies with the temperature dependent values of CO<sub>2</sub>, O<sub>2</sub>, and N<sub>2</sub> permeability. The composition in the package is set by the following equations:

$$x_{CO_2} = \frac{W \cdot R_{CO_2} \cdot l_m}{P_{O_2} \cdot A_m \cdot p_{atm} \cdot \alpha_{CO_2/O_2}} \quad (3)$$

$$x_{O_2} = 0.21 - \frac{W \cdot R_{CO_2} \cdot l_m}{P_{O_2} \cdot A_m \cdot p_{atm} \cdot \alpha_{CO_2/O_2} \cdot x_{CO_2,0}} \quad (4)$$

where  $W$  is the produce weight,  $R_{CO_2}$  is the temperature dependent  $CO_2$  production rate of the produce,  $l_m$  is the packaging membrane thickness, and  $A_m$  is the membrane area. The actual composition in the package is a function of several design parameters ( $W$ ,  $l_m$ ,  $A_m$ ), the membrane material properties, and the produce biology. The temperature dependence of the  $CO_2$  production rate obeys, like the temperature dependence of membrane permeability, an Arrhenius relationship. The pre-exponential factor and the activation energy of  $CO_2$  production for apples and other produce types are reported elsewhere [23].

Two types of analysis are presented in Figure 6.7. The first analysis assumes that a 1  $\mu m$  thick membrane made of either 49PEO-PA12 or 80PTMO-PA12 is affixed to a standard size package of apples ( $W = 2.27$  kg) [23] that respire with  $RQ = 1.2$ . The area of each membrane is fixed at a value which ensures that as the package temperature is varied, the package composition passes through the optimal range. The temperature required to reach several compositions are labeled for each membrane material. The higher permeability 80PTMO-PA12 requires much less membrane area than the 49PEO-PA12, and achieves the optimal composition at lower temperatures as well. Due to the shape of the optimal range and the way that composition varies with package temperature for these materials,  $O_2$  composition plays a larger role than  $CO_2$  composition in achieving the optimum. When the package is subjected to a temperature that causes it to depart from the optimal range, it is nearly always because the  $O_2$  requirement is not met.

The second type of analysis examines combinations of temperatures and areas where the optimal range for apple preservation can be achieved. Values for both materials are again presented for the temperatures at which PEBAX permeability has been characterized. The upper and lower area limits at a given temperature define an envelope in which the optimum conditions are achieved. These limits are calculated by varying the membrane area at a given temperature until one of the optimal compositions is no longer met. The envelope for both materials is quite narrow, primarily due to the stringent O<sub>2</sub> requirements. Both materials cannot achieve the optimal range beyond certain temperatures. 49PEO-PA12 cannot reach the optimum below about 7 °C, and 80PTMO-PA12 cannot reach it above about 17 °C. To give this analysis perspective based on existing MAP products, the Landec Intellipac membrane previously discussed has an area of 72 cm<sup>2</sup>, indicating that when an active layer thickness of 1 μm is assumed, membranes made from PEBAX range from large to enormous.

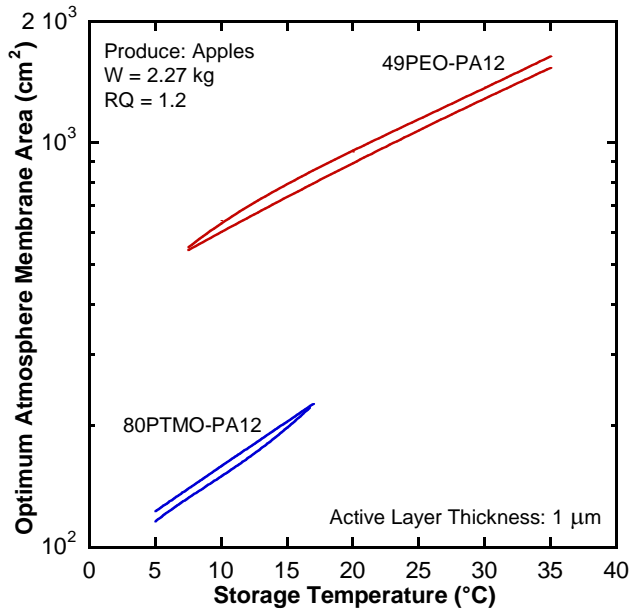
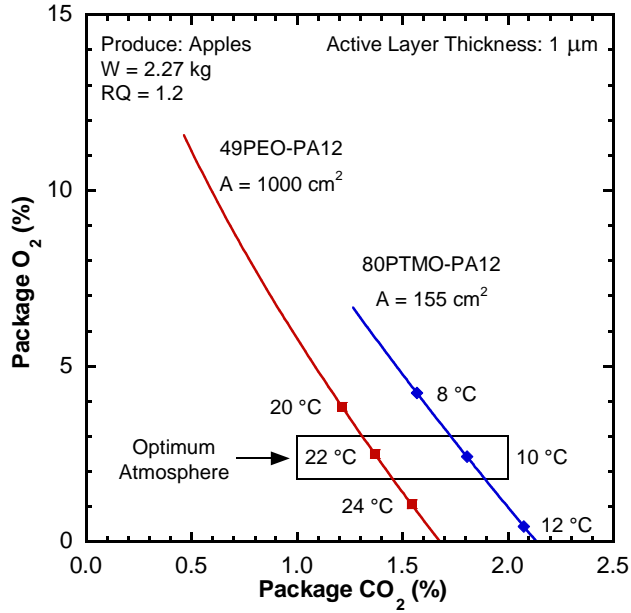


Figure 6.7. CO<sub>2</sub> and O<sub>2</sub> compositions achievable in an enclosed package of apples upon which a PEBA membrane of a given thickness and area has been affixed (top). The optimum atmosphere for apples can be achieved in a narrow envelope of package temperatures and membrane areas (bottom).

The optimal range consists not only of extending the shelf life of the produce, but also of achieving high scores in subjective evaluations (flavor, texture, scent, appearance) by tasters [24]. Conditions between the optimum and the ambient atmosphere should also produce improvements in the storage of produce, and the design of a MAP package should not be seen as a failure if the optimum is not achieved. The only strict requirement is that the O<sub>2</sub> levels may not be allowed to bottom out in the package, because this can facilitate the growth of harmful anaerobic bacteria, or anaerobic respiration in the produce, which may result in other toxins [25]. Achieving a composition between atmospheric and the optimum may result in favorable outcomes, but these are best addressed by a more complex economic analysis that is outside the scope of this dissertation.

#### 6.2.4 Multilayered $\beta$ -iPP/PEBAX Films for MAP Applications

Multilayered films made of the materials studied to this point were produced by coextrusion with the goal of creating membranes suitable for MAP applications. A representative SEM scan of such a film is depicted in Figure 6.8.

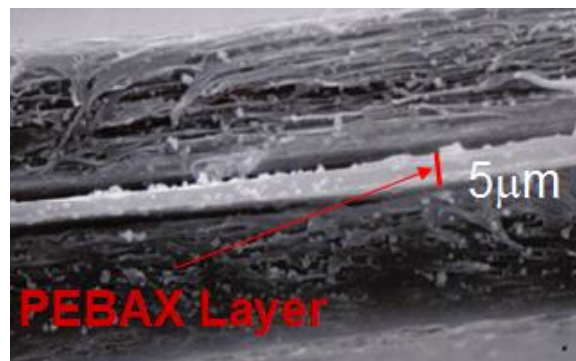


Figure 6.8. SEM (edge view) of multilayered PEBAX/ $\beta$ -iPP membrane.

Films with three layers were coextruded and biaxially stretched at several draw ratios to investigate the effect of elongation on transport properties in these films. It is

well-established that the draw ratio influences pore formation in biaxially stretched  $\beta$ -iPP films [26,27], and other work has examined the role of orientation on the transport properties of PEBAX films [5,8].

The influence of biaxial draw ratio on transport in these multilayered films is presented in Figure 6.9. Permeabilities are calculated based only on the thickness of the PEBAX layers in the film. This calculation relies on the assumption that the PEBAX layers are continuous, and that the porous layer has no resistance to mass transfer. The measured CO<sub>2</sub> permeability exhibits a substantial decrease relative to that of the control material, while the O<sub>2</sub> permeability is either equivalent to the control or shows an increase. There is no perceptible pattern to these trends as a function of draw ratio, although lower values of CO<sub>2</sub> permeability tend to correspond with lower values of O<sub>2</sub> permeability. The separation capability of these membranes is substantially reduced, with CO<sub>2</sub>/O<sub>2</sub> selectivities around 5 instead of 9. The explanation for this overall behavior, and especially that of greatly increased O<sub>2</sub> permeability, is that there are continuous defects in the dense material through the membrane of a large enough area that a significant fraction of transport occurs through them. An area fraction of approximately 0.002 of exposed porous substrate would correspond to this physical situation. The reduced CO<sub>2</sub> permeability observed in the films requires a different explanation. There is an additional resistance to mass transfer beyond that of the PEBAX layer, and it affects CO<sub>2</sub> transport more strongly than O<sub>2</sub>. The resistance must therefore be composed of a material with a lower CO<sub>2</sub>/O<sub>2</sub> selectivity than PEBAX, which is consistent with the presence of intact PP in the film. These ideas will be explored more fully in the discussion of multilayered films to follow.

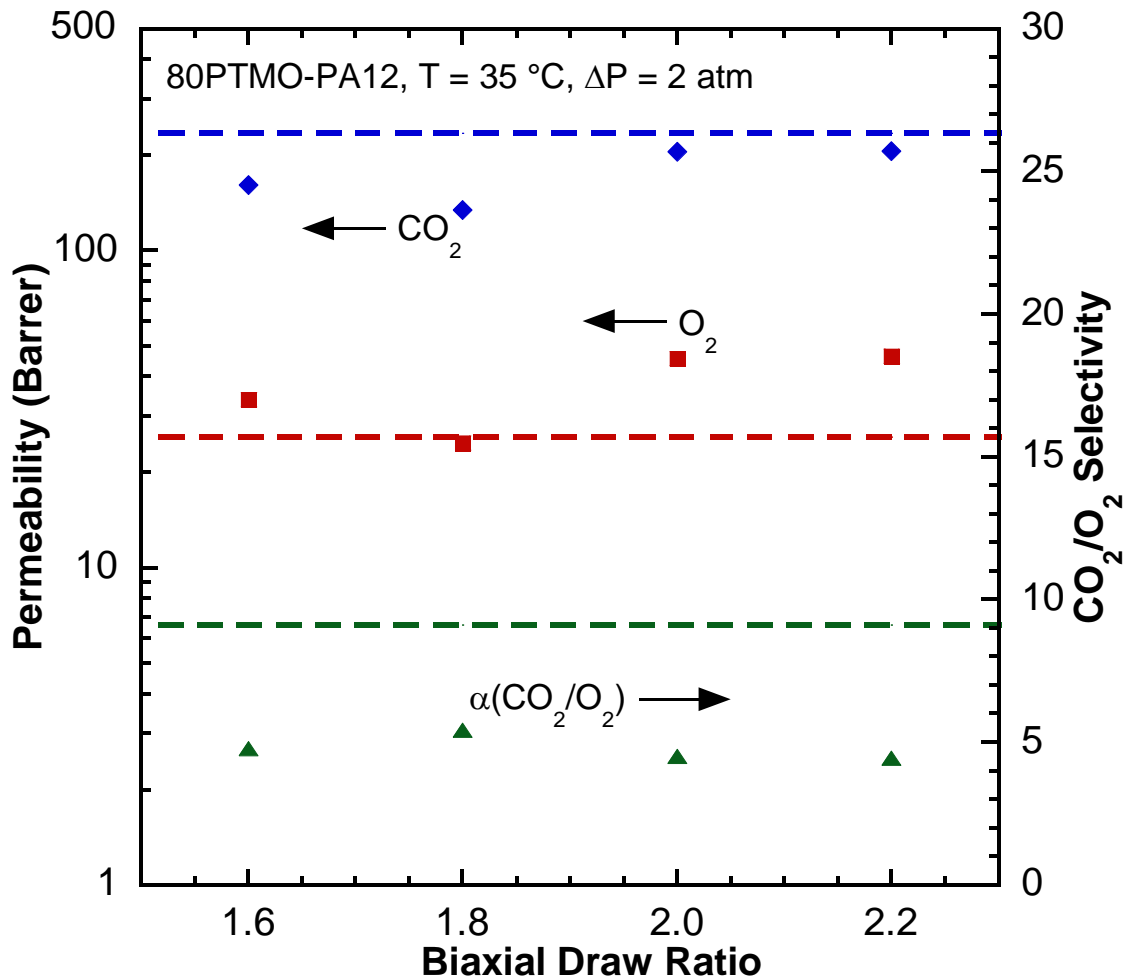


Figure 6.9. Permeability and selectivity of 3-layer PEBA/β-iPP biaxially stretched multilayer films. Permeabilities are calculated based on the composition of the selective PEBA layer (30 vol. %) with the assumption that the support layer provides no resistance to mass transfer. Dashed lines in corresponding colors represent the permeability and selectivity of extruded single layer PEBA films, which serve as a control.

Because no conclusive data about the optimum draw ratio for these multilayered films were obtained from the experiments described by Figure 6.9, the remainder of films were produced with a biaxial draw ratio of 2, which is recommended for optimum pore formation in β-iPP films [27]. Although orientation effects affect the permeability of

80PTMO-PA12 by creating PTMO structures which melt at 40 to 45 °C [5], each multilayered film was stretched at 100 °C, preventing orientation from occurring in these films. Two variables were examined for their effects on gas transport: the number of layers, and the volume fraction of PEBAX in the film, outlined previously.

Figure 6.10 displays the O<sub>2</sub> throughput and the separation ability of the multilayered films. The top figure shows the performance of the multilayered films relative to the O<sub>2</sub> permeance target (30 GPU) for MAP membranes. All films have O<sub>2</sub> permeances of less than 5 GPU, while exhibiting a substantial reduction in expected permeability compared to the control PEBAX film at a given thickness. Films with 3 layers appear to attain both higher permeabilities and permeances than 17-layer films, indicating that pore formation is likely inhibited when there are a greater number of layers. In the 3-layer films, higher PEBAX content results in greater permeability in the PEBAX layers. Permeabilities are about the same in 17-layer films with different PEBAX contents. This increase in permeability cannot offset the reduction in total PEBAX thickness, however, because the films with lower PEBAX content exhibit higher permeance. The bottom figure displays film selectivity as a function of O<sub>2</sub> permeance. The films generally have much lower selectivity than single layer PEBAX films, with the effect most pronounced in films with 17 layers and films with 10 vol. % PEBAX. Films with 17 layers, in particular, have quite low selectivity.

These are complex materials with internal structures that clearly vary depending upon layer count and layer composition, as well as from sample to sample. To understand the performance of these materials, a model that accounts for the influence of inadequate pore formation on the observed transport properties will be developed in the following pages.

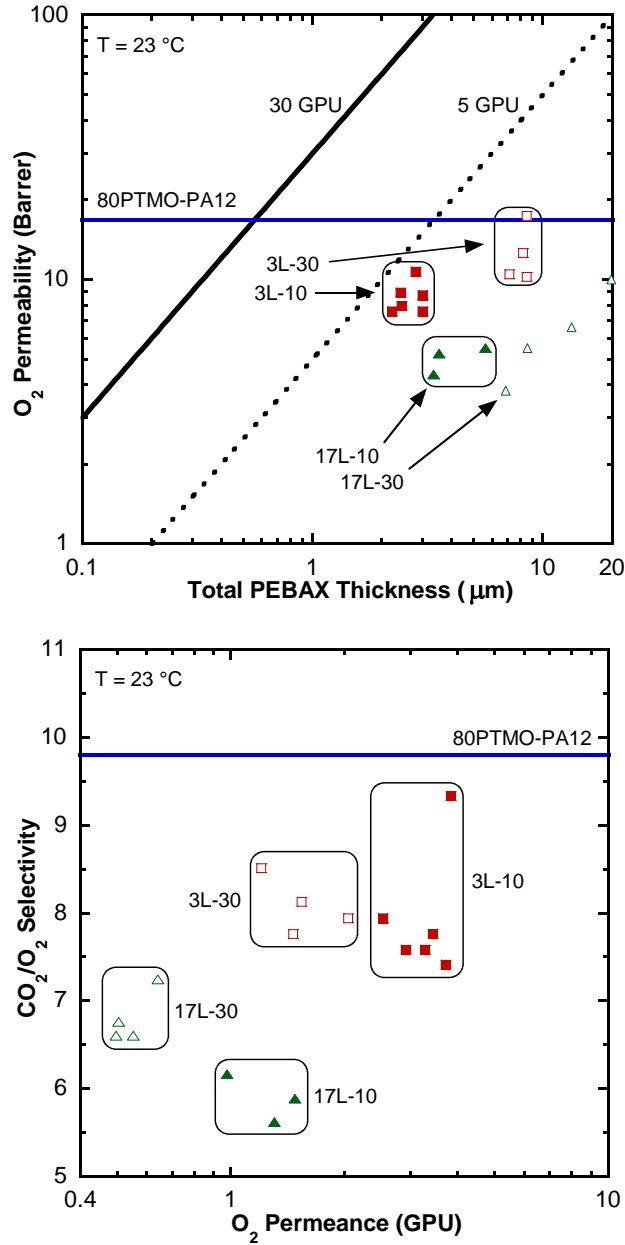


Figure 6.10. O<sub>2</sub> permeability of multilayered films as a function of total PEBAX thickness (top) and multilayered film CO<sub>2</sub>/O<sub>2</sub> selectivity as a function of film permeance (bottom). The permeability and selectivity of a single layer 80PTMO-PA12 film is shown. Results for 3L-10 (■), 3L-30 (□), 17L-10 (▲), and 17L-30 (△) films are presented.

A simple model for gas transport through multilayered membranes is presented in Figure 6.11.

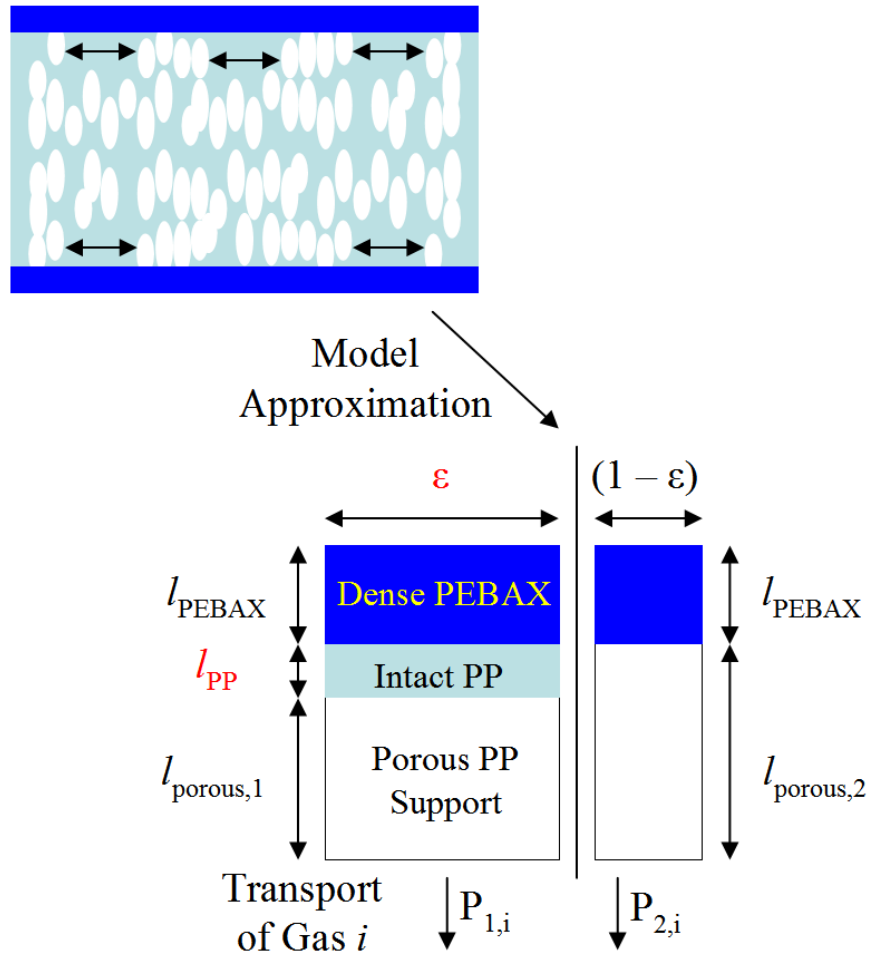


Figure 6.11. One possible schematic for a model of gas transport in multilayered films with a dense PEBAX layer and a porous support. Interactions between PEBAX and  $\beta$ -iPP where they interface may result in areas where porosity is not formed in the  $\beta$ -iPP (top). Gas transport in this model occurs in parallel, with one area ( $\epsilon$ ) experiencing resistance to mass transfer from both PEBAX and the intact dense PP, and the other area ( $1 - \epsilon$ ) experiencing resistance only from PEBAX (bottom). The area coverage  $\epsilon$  and intact PP thickness  $l_{PP}$  are model parameters.

Mathematically, this can be represented using the following three equations:

$$P_{1,i} = \frac{l_{composite}}{\left(\frac{l_{PEBAX}}{P_{PEBAX,i}}\right) + \left(\frac{l_{PP}}{P_{PP,i}}\right) + \left(\frac{l_{porous1}}{P_{porousi}}\right)} \cong \frac{l_{composite}}{\left(\frac{l_{PEBAX}}{P_{PEBAX,i}}\right) + \left(\frac{l_{PP}}{P_{PP,i}}\right)} \quad (5)$$

$$P_{2,i} = \frac{l_{composite}}{\left(\frac{l_{PEBAX}}{P_{PEBAX,i}}\right) + \left(\frac{l_{porous2}}{P_{porousi}}\right)} \cong \frac{l_{composite}}{\left(\frac{l_{PEBAX}}{P_{PEBAX,i}}\right)} \quad (6)$$

$$P_i = \varepsilon \cdot P_{1,i} + (1 - \varepsilon) \cdot P_{2,i} \quad (7)$$

This model can be understood conceptually as the transport of gas  $i$  through series resistances operating in parallel. One resistance has area fraction  $\varepsilon$ , and it is composed of a PEBAX layer of thickness  $l_{PEBAX}$  in series with an intact (i.e., dense) PP layer of thickness  $l_{PP}$  and a porous layer of thickness  $l_{porous,1}$ . The other resistance has an area fraction  $(1 - \varepsilon)$ , and it is composed of a PEBAX layer of thickness  $l_{PEBAX}$  in series with a porous layer of  $l_{porous,2}$ . The total thickness is  $l_{composite}$ . In both cases, the resistance of the porous layer is assumed to be negligible, leading to the approximations displayed above. The permeability of pure PEBAX at 23 °C to the relevant gases is known, and the permeability of dense PP (assumed here to be 50% crystalline) is reported elsewhere [28]. The total thickness of PEBAX layers is known from its volume fraction in the melt. The model, therefore, has only two parameters ( $\varepsilon$  and  $l_{PP}$ ), and it may be solved given the permeability of the composite film to two gases, CO<sub>2</sub> and O<sub>2</sub>. Other models with more sophisticated treatments of the structures present in these multilayered films (i.e., the consideration of defects) would be possible if permeability data for additional gases were available. The calculated parameters for the films are shown in Table 6.3.

Table 6.3. Model parameters for transport in multilayered  $\beta$ -iPP/PEBAX membranes. Each ( $\varepsilon$ ,  $l_{PP}$ ) pair for a given layer configuration and PEBAX content corresponds to the value for an individual sample of those specifications.

3L-10		3L-30		17L-10		17L-30	
$\varepsilon$	$l_{PP}$ ( $\mu\text{m}$ )						
0.740	0.539	0.688	0.735	0.962	0.951	0.914	3.220
0.759	0.331	0.623	0.469	0.944	0.808	0.840	2.930
0.751	0.486	0.559	1.677	0.922	1.289	0.877	2.533
0.420	1.499					0.908	1.354
0.736	0.481						
0.720	0.813						

The results of evaluating the performance of multilayered films using the model are presented in Figure 6.12. Performance is cast in terms of the ratio of multilayered film  $O_2$  permeability to 80PTMO-PA12 permeability and in terms of multilayered film  $CO_2/O_2$  selectivity to 80PTMO-PA12 selectivity. The ratio of  $l_{PP}$  to  $l_{PEBAX}$  is used to allow comparison between films with different PEBAX thicknesses, and this ratio is called  $\tau$ . For these materials, the maximum value of  $\tau$  should be 9, which corresponds to a film with 10 vol. % PEBAX and 90 vol. % intact PP. In practice,  $\tau$  was found to be less than 0.6. If a membrane's structure corresponds to the physical situation captured by the model, its properties must lie between the bounds defined by Figure 6.12. It is possible for a membrane with a different structure to exhibit these properties, but if the membrane properties lie outside of this envelope, its construction certainly does not correspond to the model physics. Generally, as  $\tau$  and  $\varepsilon$  increase, the  $O_2$  permeability of the multilayered film decreases. At a fixed value of  $\varepsilon$ , where  $\varepsilon < 1$ ,  $CO_2/O_2$  selectivity decreases as  $\tau$  increases, reaches a minimum value, and then increases. When  $\varepsilon = 1$ , selectivity decreases as  $\tau$  increases. When  $\varepsilon = 0$ , the selectivity is equal to that of PEBAX. At a fixed value of  $\tau$ , where  $\tau > 0$ , selectivity decreases as  $\varepsilon$  increases. At  $\tau = 0$ , the selectivity is equal to PEBAX. When  $\varepsilon = 1$  and  $\tau$  is very large, the selectivity is equal to PP.

These results yield physical insight about the cause of performance differences between 3-layer and 17-layer films, as well as between films having different PEBAX content. The area coverage of dense PP,  $\varepsilon$ , is a more important parameter to the separation performance of these films than the thickness of that PP layer,  $l_{pp}$ . There are more interfaces between PEBAX and PP layers (16 total) in 17-layer films than in 3-layer films (2 total). Thus, there should be more interactions per unit volume of PP in films with more layers. If interactions between PEBAX and PP layers during stretching retard pore formation, 17-layer films should have greater values of  $\varepsilon$  than 3-layer films and correspondingly lower selectivity. This is in fact what is seen in 17-layer films relative to 3-layer films, where every 17-layer film observed had a value of  $\varepsilon$  above 0.8. Additionally, when PEBAX layers are thinner, their interaction with PP should be stronger [29], potentially retarding pore formation in PP and again reducing selectivity. At a fixed number of film layers, modeling results show that films with one third the PEBAX thickness (i.e., 10 vol. % PEBAX instead of 30 vol. % PEBAX) have higher  $\varepsilon$  values. This observation could indicate that the retardation of pore formation occurs more often at the interface in films with more layers. The total thickness of the PP layers,  $l_{pp}$ , was also greater in 17-layer films than in 3-layer films, which may mean that pore formation is less efficient per PP layer. Practically, if one were to design an optimal multilayered film of this type, that film should have one separating layer and one porous layer.

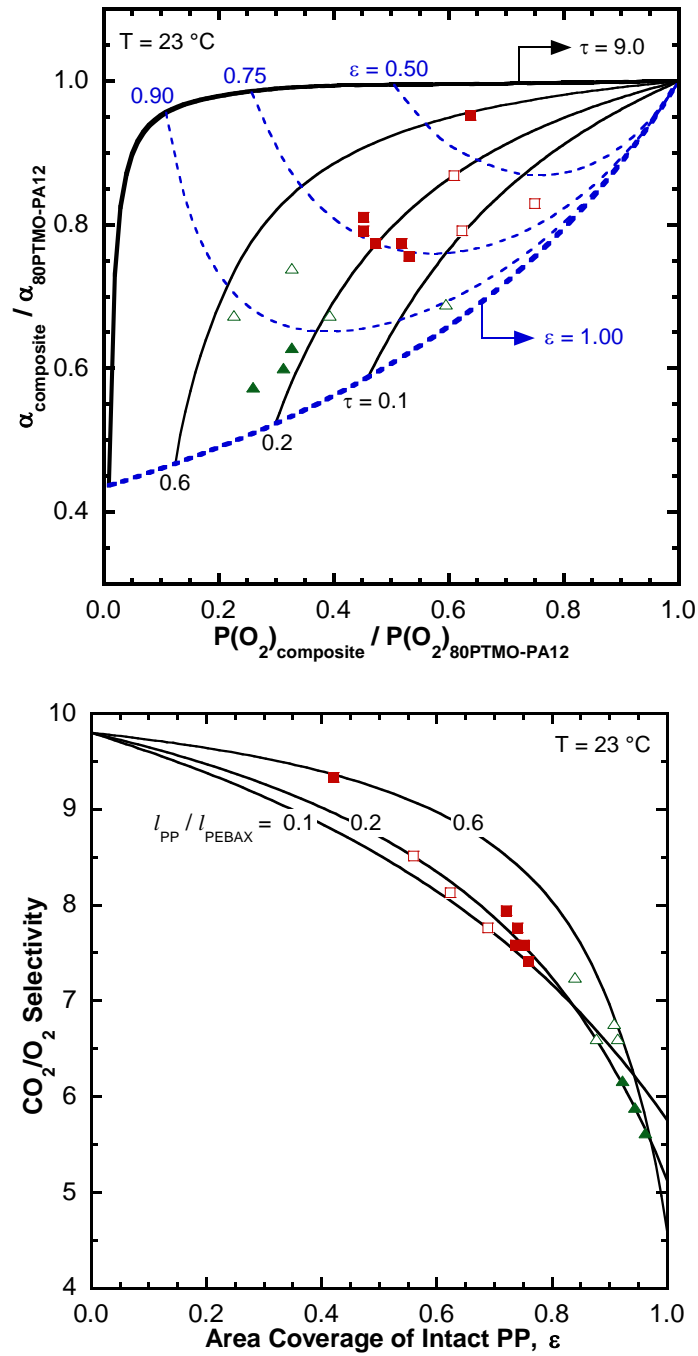


Figure 6.12. Influence of transport model parameters on the  $\text{O}_2$  permeability and  $\text{CO}_2/\text{O}_2$  selectivity of multilayered films. Results for 3L-10 (■), 3L-30 (□), 17L-10 (▲), and 17L-30 (△) films are presented.

The topic of produce preservation can also be revisited in the context of the performance of these multilayered films. Using the permeability and selectivity data for the multilayered films discussed in the previous pages, the ability of these films to approach the optimum preservation conditions for apples is examined. Figure 6.13 shows the membrane area required to achieve an optimal concentration of 2.4% O<sub>2</sub>, and the resulting deviation from the optimal CO<sub>2</sub> content. The optimal content cannot be achieved with 80PTMO-PA12 at 23 °C, but the deviation from the optimal range is fairly small. Compared to pure 80PTMO-PA12, the multilayered films develop a package CO<sub>2</sub> level over 2% higher, while requiring membrane areas 3 to 30 times larger. This is primarily due to the low permeance provided by the multilayered membranes, which is caused by PEBAX layers that are too thick and the existence of large areas of intact PP.

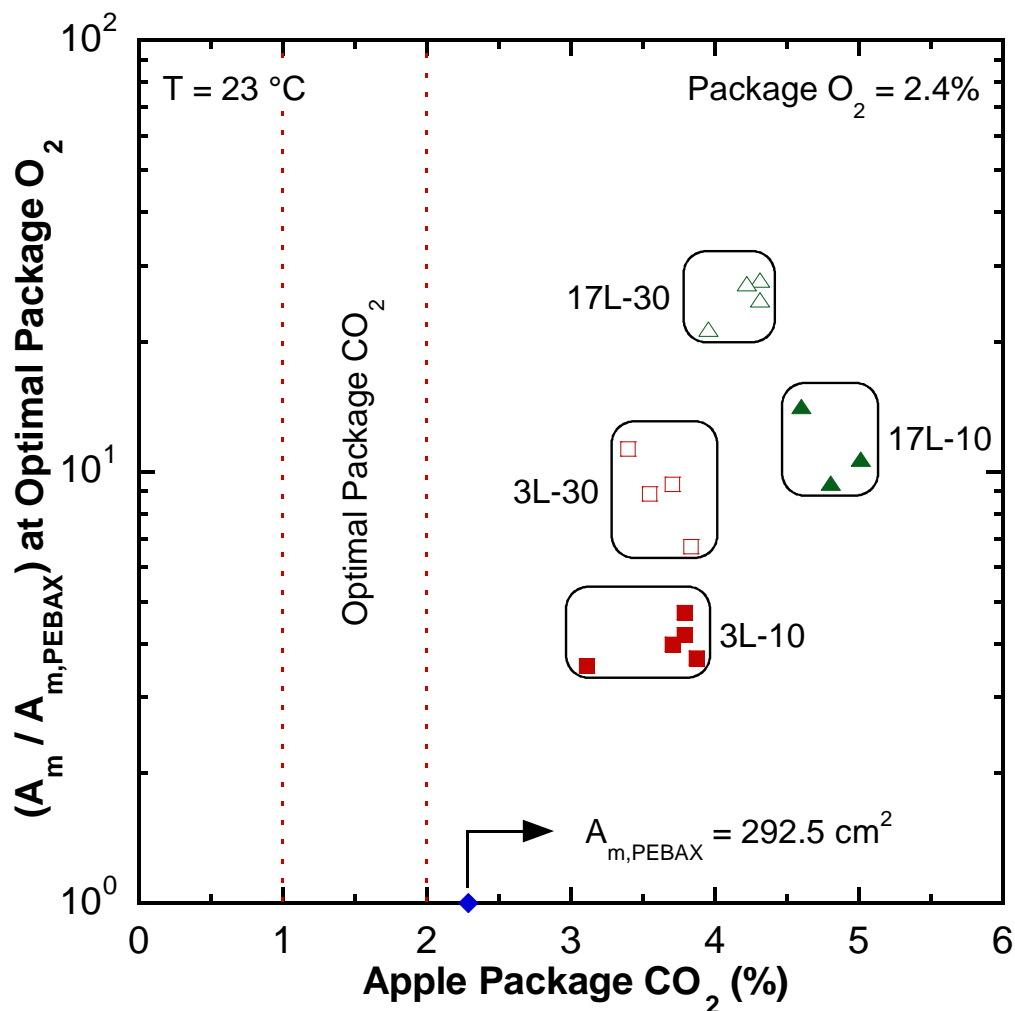


Figure 6.13. Application performance of multilayered films (apple storage, 23 °C). The membrane area required to reach a package composition of 2.4%  $O_2$  and the resulting  $CO_2$  composition is calculated. The membrane areas are normalized by the value for an 80PTMO-PA12 membrane of 1  $\mu\text{m}$  thickness operating at 23 °C. Results for 3L-10 (■), 3L-30 (□), 17L-10 (▲), and 17L-30 (△) films are presented.

Multilayered films were thermally annealed at 140 °C prior to stretching so that the benefits to pore formation witnessed in the previous chapters might be attained. The results of this experiment are presented in Figure 6.14. Compared to as-extruded films, the thickness of annealed films is decreased, but the  $O_2$  permeability also decreases. This

results in a modest improvement in permeance, but not nearly enough to overcome the shortcomings of the existing films depicted in Figure 6.13.

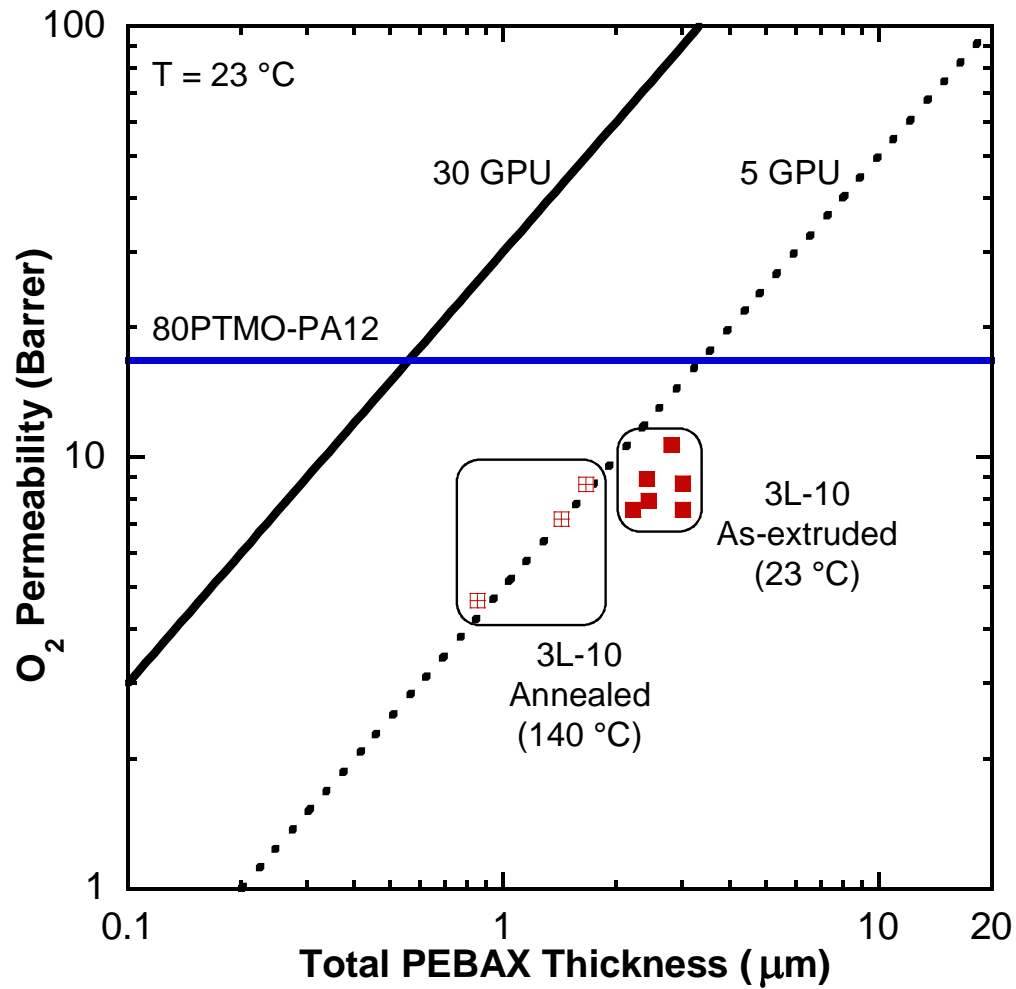


Figure 6.14. Influence of thermal annealing on the O<sub>2</sub> permeability of 3-layer PEBAK/ $\beta$ -iPP films composed of 10 vol. % PEBAK.

### 6.3 REFERENCES

- [1] V.I. Bondar, B.D. Freeman, I. Pinnau, Gas transport properties of poly(ether-b-amide) segmented block copolymers, *Journal of Polymer Science Part B: Polymer Physics*. 38 (2000) 2051–2062.
- [2] J.H. Kim, S.Y. Ha, Y.M. Lee, Gas permeation of poly (amide-6b-ethylene oxide) copolymer, *Journal of Membrane Science*. 190 (2001) 179–193.
- [3] V.I. Bondar, B.D. Freeman, I. Pinnau, Gas sorption and characterization of poly(ether-b-amide) segmented block copolymers, *Journal of Polymer Science Part B: Polymer Physics*. 37 (1999) 2463–2475.
- [4] Q.T. Nguyen, J. Sublet, D. Langevin, C. Chappey, S. Marais, J.-M. Valleton, et al., CO<sub>2</sub> Permeation with Pebax®-based Membranes for Global Warming Reduction, in: B.D. Freeman, Y. Yampolskii (Eds.), *Membrane Gas Separation*, Galley Pro, West Sussex, John Wiley & Sons, Ltd., 2010: pp. 255–278.
- [5] S. Armstrong, B. Freeman, A. Hiltner, E. Baer, Gas permeability of melt-processed poly(ether block amide) copolymers and the effects of orientation, *Polymer*. 53 (2012) 1383–1392.
- [6] M.E. Rezac, T. John, P.H. Pfromm, Effect of copolymer composition on the solubility and diffusivity of water and methanol in a series of polyether amides, *Journal of Applied Polymer Science*. 65 (1997) 1983–1993.
- [7] S.R. Reijerkerk, R. Jordana, K. Nijmeijer, M. Wessling, Highly hydrophilic, rubbery membranes for CO<sub>2</sub> capture and dehydration of flue gas, *International Journal of Greenhouse Gas Control*. 5 (2011) 26–36.
- [8] V. Barbi, S.S. Funari, R. Gehrke, N. Scharnagl, N. Stribeck, SAXS and the Gas Transport in Polyether- b lock -polyamide Copolymer Membranes, *Macromolecules*. 36 (2003) 749–758.
- [9] Y. Song, H. Yamamoto, N. Nemoto, Segmental Orientations and Deformation Mechanism of Poly(ether- block -amide) Films, *Macromolecules*. 37 (2004) 6219–6226.
- [10] S.R. Armstrong, D.R. Paul, A. Hiltner, Permeability of Poly (ether block amide) (PEBAX): Effect of Orientation, in: *Abstracts of Papers, 240th ACS National Meeting*, Boston, MA, American Chemical Society, 2010: p. PMSE – 193.

- [11] A. Car, C. Stropnik, W. Yave, K.-V. Peinemann, Tailor-made Polymeric Membranes based on Segmented Block Copolymers for CO<sub>2</sub> Separation, *Advanced Functional Materials*. 18 (2008) 2815–2823.
- [12] D. Husken, T. Visser, M. Wessling, R.J. Gaymans, CO<sub>2</sub> permeation properties of poly(ethylene oxide)-based segmented block copolymers, *Journal of Membrane Science*. 346 (2010) 194–201.
- [13] S.R. Reijerkerk, A. Arun, R.J. Gaymans, K. Nijmeijer, M. Wessling, Tuning of mass transport properties of multi-block copolymers for CO<sub>2</sub> capture applications, *Journal of Membrane Science*. 359 (2010) 54–63.
- [14] S. Matteucci, Y.P. Yampolskii, B.D. Freeman, I. Pinnau, Transport of Gases and Vapors in Glassy and Rubbery Polymers, in: Y. Yampolskii, I. Pinnau, B.D. Freeman (Eds.), *Materials Science of Membranes for Gas and Vapor Separation*, 1st ed., Wiley, 2006.
- [15] T.C. Merkel, V.I. Bondar, K. Nagai, B.D. Freeman, I. Pinnau, Gas sorption, diffusion, and permeation in poly(dimethylsiloxane), *Journal of Polymer Science Part B: Polymer Physics*. 38 (2000) 415–434.
- [16] H. Lin, E. Van Wagner, J.S. Swinnea, B.D. Freeman, S. Pas, A.J. Hill, et al., Transport and structural characteristics of crosslinked poly(ethylene oxide) rubbers, *Journal of Membrane Science*. 276 (2006) 145–161.
- [17] L.M. Robeson, B.D. Freeman, D.R. Paul, B.W. Rowe, An empirical correlation of gas permeability and permselectivity in polymers and its theoretical basis, *Journal of Membrane Science*. 341 (2009) 178–185.
- [18] L.M. Costello, W.J. Koros, Temperature dependence of gas sorption and transport properties in polymers: measurement and applications, *Industrial & Engineering Chemistry Research*. 31 (1992) 2708–2714.
- [19] H. Lin, *Solubility Selective Membrane Materials for Carbon Dioxide Removal from Mixtures with Light Gases*, The University of Texas at Austin, 2005.
- [20] D.R. Paul, R. Clarke, Modeling of modified atmosphere packaging based on designs with a membrane and perforations, *Journal of Membrane Science*. 208 (2002) 269–283.
- [21] B.S. Kirkland, R. Clarke, D.R. Paul, A versatile membrane system for bulk storage and shipping of produce in a modified atmosphere, *Journal of Membrane Science*. 324 (2008) 119–127.

- [22] R.W. Baker, *Membrane Technology and Applications*, 2nd ed., West Sussex, John Wiley & Sons, Ltd., 2004.
- [23] A. Exama, J. Arul, R.W. Lencki, L.Z. Lee, C. Toupin, Suitability of Plastic Films for Modified Atmosphere Packaging of Fruits and Vegetables, *Journal of Food Science*. 58 (1993) 1365–1370.
- [24] S. Mangaraj, T.K. Goswami, P. V. Mahajan, Applications of Plastic Films for Modified Atmosphere Packaging of Fruits and Vegetables: A Review, *Food Engineering Reviews*. 1 (2009) 133–158.
- [25] K.L. Yam, D.S. Lee, Design of modified atmosphere packaging for fresh produce, in: M.L. Rooney (Ed.), *Active Food Packaging*, Blackie Academic & Professional, 1995: pp. 55–73.
- [26] F. Chu, T. Yamaoka, H. Ide, Y. Kimura, Microvoid formation process during the plastic deformation of  $\beta$ -form polypropylene, *Polymer*. 35 (1994) 3442–3448.
- [27] F. Chu, Structure and gas permeability of microporous films prepared by biaxial drawing of  $\beta$ -form polypropylene, *Polymer*. 37 (1996) 573–579.
- [28] A.W. Myers, V. Stannett, M. Szwarc, The permeability of polypropylene to gases and vapors, *Journal of Polymer Science*. 35 (1959) 285–288.
- [29] J. Kerns, A. Hsieh, A. Hiltner, E. Baer, Mechanical Behavior of Polymer Microlayers, *Macromolecular Symposium*. 147 (1999) 15–25.

## Chapter 7. Conclusions and Recommendations

### 7.1 CONCLUSIONS

#### 7.1.1 Porosity of Thermally Annealed $\beta$ -iPP Films

The crystallinity of extruded  $\beta$  nucleated isotactic polypropylene ( $\beta$ -iPP) materials was influenced by the MFI of the iPP used, the extrusion conditions, and by the annealing treatment applied to the extruded films. An accounting of the crystallinity in these films by DSC and XRD techniques enabled the development of useful metrics of  $\beta$  crystallinity in these materials. These metrics can be used to predict the porosity of the films when they are biaxially stretched under comparable conditions. The growth of stable  $\beta_1$  crystals in  $\beta$ -iPP materials, which was facilitated by appropriate post-extrusion annealing, was the most important factor in creating highly porous films. The mechanism of pore formation in biaxially stretched  $\beta$ -iPP films was clarified and used to explain pore formation in the films. This model is based on an understanding of the physical processes occurring during the extrusion, thermal annealing, early biaxial stretching, and late biaxial stretching stages of porous film production.

A variety of iPP materials and precursor thermal annealing conditions can be used to successfully create microporous membranes with this approach, compared with the more strict processing requirements of row-nucleated materials such as Celgard. This flexibility makes  $\beta$ -iPP microporous films attractive in their own right or for use in

---

Portions of this chapter have been adapted with permission from the following articles:  
G.T. Offord (author, primary experimentalist), S.R. Armstrong (editor, sample preparation), B.D. Freeman (editor), E. Baer (editor), A. Hiltner (editor), J.S. Swinnea (XRD experiments), D.R. Paul (editor), *Polymer*. 54 (2013) 2577–2589.  
G.T. Offord (author, primary experimentalist), S.R. Armstrong (editor, sample preparation), B.D. Freeman (editor), E. Baer (editor), A. Hiltner (editor), D.R. Paul (editor), *Polymer*. 54 (2013) 2796–2807.

multilayered composite membranes where the temperature, viscosity, or other requirements for the nonporous material limit the range of extrusion conditions that can be used.

### **7.1.2 Factors Influencing Permeability of $\beta$ -iPP Films**

The relationship between the amount of well-developed  $\beta$  crystalline material and the extent of pore formation upon stretching in a  $\beta$ -iPP film is affected by the stretching temperature, reflecting differences in stress during stretching and the different transformation modes of  $\beta$  crystals with temperature. Measured differences in porosity and permeability are qualitatively reflected in SEM imaging of  $\beta$ -iPP stretched films as a function of annealing and stretching temperature. Stretched  $\beta$ -iPP film permeability tracks film porosity, similar to other polypropylene films in the literature and to commercially manufactured porous films. The high permeability of our  $\beta$ -iPP films was comparable to these quality commercial films. The pore size distributions for the films were narrow relative to other  $\beta$ -iPP films, and the mean values were in the ultrafiltration range. Permselectivity measurements and the pore size were used in conjunction to demonstrate the transport mechanism of gas through the membranes, which was primarily in the Knudsen diffusion regime. The high permeability and narrow pore size distribution were achieved across a range of iPP resin viscosities and stretching treatments. This process flexibility indicates that  $\beta$ -iPP materials are potentially a good candidate to provide a porous support layer in coextruded composite membranes, enabling the manufacture of economically advantageous and environmentally friendly separations technologies.

### **7.1.3 Production and Characterization of Multilayered Membranes for Modified Atmosphere Packaging (MAP)**

The permeabilities to several gases of PEBAX grades containing poly(ethylene oxide) (PEO) and poly(tetramethylene oxide) (PTMO) were measured over a range of transmembrane pressures and experimental temperatures. It was found that PEO-based grades exhibit higher selectivities to CO<sub>2</sub> over light gases than PTMO-based grades, but that PTMO-based grades exhibit higher permeabilities. The permeability of these materials is dependent upon the PE soft block content, with greater PE contents resulting in higher permeabilities and, to a certain point, higher selectivities of CO<sub>2</sub> over light gases due to its strong interaction with ether oxygen linkages. One PEO-based PEBAX film and one PTMO-based film were studied for their usefulness in MAP applications by examining the temperature dependence of their transport properties. Although the PEO-based grade had a high CO<sub>2</sub>/O<sub>2</sub> selectivity, its low permeability over a range of temperatures made it less useful than the PTMO-based grade.

The two materials were compared to a commercial MAP product (Landec Intellipac), and it was determined that a layer of less than 1  $\mu\text{m}$  would be required to meet its high O<sub>2</sub> permeance. The high selectivity of these PEBAX grades, however, makes these materials of some interest for the preservation of produce like apples. Their performance was modeled for a hypothetical standard package of apples, and the required combination of membrane area and storage temperature for each material was determined. The high throughput PTMO-based PEBAX required less area and lower storage temperatures than the PEO-based grade.

Multilayered films of  $\beta$ -iPP and the PTMO-based PEBAX were produced, and their performance was studied over a range of biaxial draw ratios, layer counts, and PEBAX content. No discernable trend was found in the performance of the films based

on draw ratio. Generally, 3-layer films performed better than 17-layer films, and higher PEBAX contents resulted in films with higher selectivities but lower permeances. Comparison of the multilayer results with those of single layer PEBAX films indicated the imperfect nature of the pore formation in multilayered films, and this was modeled using two parameters with distinct physical meaning. This effort showed that large areas of intact, nonporous PP still existed in all of the multilayered films, inhibiting the transport properties. The performance of the multilayered films in the context of MAP was also determined, with very large membrane areas required to obtain even middling packaging performance. Thermal annealing the multilayered films slightly improved O<sub>2</sub> permeance, but it does not qualitatively change the assessment of these films as unsuitable for MAP applications.

## **7.2 RECOMMENDATIONS FOR FUTURE STUDIES**

### **7.2.1 Improved Crystallinity for Pore Formation in $\beta$ -iPP**

The quantity of perfected  $\beta$  material, which is indexed by the volume fraction of  $\beta_1$  determined by DSC experiments, is the primary factor in  $\beta$ -iPP pore formation. Other studies have shown that different  $\beta$  nucleators and nucleator loading influence the amount and development of crystallinity [1]. Depending upon the nucleator and its loading,  $\beta$ -iPP can exhibit exclusively  $\beta_1$  peaks, perhaps indicating a more suitable material for pore formation than the  $\beta$ -iPP we studied, which had double peak behavior. Many  $\beta$  nucleators also nucleate  $\alpha$  crystallinity [2], which could influence the stretching behavior of films and, therefore, pore formation. Different  $\beta$  nucleators have been used in the production of porous  $\beta$ -iPP films, but there have been no systematic studies of nucleator type or loading on pore formation. A more effective nucleator might improve pore formation not just in

single layer films, but also in multilayered films, where it was observed that confinement resulted in areas of intact PP.

### **7.2.2 Microporous $\beta$ -iPP Films for Liquid Separations**

Very few studies have previously examined  $\beta$ -iPP microporous films for separations in the liquid phase [3,4]. The pore size distribution in the materials studied in this dissertation is narrow, and the mean pore size is in the ultrafiltration size range. Because the porous membranes were biaxially stretched, they can be expected to have excellent mechanical properties in the machine and transverse directions, unlike other extruded porous films such as Celgard [3]. These advantages make them potentially attractive as battery separators, where separator integrity is an important characteristic [5]. Porosity and gas permeability are often used as proxies for transport of ions in the liquid phase for this application, and the properties of  $\beta$ -iPP films are comparable to Celgard films in this regard. Direct characterization of the transport of ions in the liquid phase would further demonstrate the utility of these materials as separators. The measurement of water transport through  $\beta$ -iPP films would also prove to be a useful first step if they are to be used as supports for potential extruded nanofiltration or reverse osmosis (RO) membranes.

### **7.2.3 Pore Formation of $\beta$ -iPP in Confined Environments**

The good pore formation of  $\beta$ -iPP films is mitigated by PEBAX confinement, with pore formation inhibited in the PP over large areas, and thicknesses of several hundred nanometers of intact PP per layer remaining in these areas. It is not currently known whether the influence of PEBAX is strongest due to its influence on the crystallization of  $\beta$ -iPP or its influence on the stretching process. Fundamentally, it would be interesting to know how pore formation is influenced by contact with different

materials (e.g., thermoplastic elastomers like PEBAX, glassy polymers, or even polymers in the melt at the applied stretching temperature). Practically, this issue must be understood so that useful multilayered membranes with a porous support can be produced.

The simplest conceivable experiment along these lines would be to coextrude  $\beta$ -iPP and a rheology-matched rubbery polymer which would provide “soft” confinement. These could be coextruded in a 3-layer configuration, with two rubbery layers sandwiching the  $\beta$ -iPP layer. After coextrusion, one of two protocols could be followed:

1. Soxhlet extraction to remove the rubbery material followed by biaxial stretching of the recovered PP
2. Biaxial stretching of the multilayered film followed by Soxhlet extraction to remove the rubbery material

Polypropylene is quite resistant to dissolution in many common solvents, so many combinations of rubbery polymers and solvents would be possible. The resulting  $\beta$ -iPP films could be compared to one another for porosity and permeability as described previously, and also compared to extruded single layer  $\beta$ -iPP films. The interpretation of the results would be relatively straightforward. If the first protocol shows significantly better pore formation than the second, confinement during stretching is the primary inhibitor. If single layer extruded  $\beta$ -iPP films show better pore formation than the multilayered films, layer confinement causes crystallization that is unfavorable to pore formation upon stretching. This general outline could be refined to include the effects of relative layer thicknesses and the nature of the confinement by altering the amount and identity of the confining material.

#### 7.2.4 Optimized Multilayered Membranes for MAP Applications

The primary challenge associated with fabricating extruded multilayered membranes for MAP is their low O<sub>2</sub> permeance. There are three basic strategies to address this challenge:

1. Improve the pore formation process
2. Decrease the total thickness of the active layer(s)
3. Increase the permeability of the active layer(s)

The first strategy is discussed elsewhere in this chapter. In the context of MAP applications with the materials currently being used, extruding a two-layer film with the minimal amount of PEBAX possible would likely yield the best results due to the reduced likelihood of interactions between the PEBAX and its support layer during crystallization or stretching.

The second strategy may be possible if the coextruded materials are exceptionally compatible, and the flow of the thin active layer in the melt remains intact. This strategy will not be further discussed because it is largely empirical, and the desired properties of the layer materials are generally given higher priority than rheological compatibility.

The final strategy is of most interest, because there have been a number of advances beyond PEBAX in the area of polyether-containing block copolymers. One such method to increase O<sub>2</sub> permeability that was of interest but not attempted during this project was the incorporation of poly(ethylene glycol) (PEG) into PEBAX to form a blend with higher ether oxygen concentrations. These materials have been studied elsewhere, and exhibit both higher permeabilities and higher CO<sub>2</sub>/O<sub>2</sub> selectivities than native PEBAX materials [6]. The viscosity of the blend would also decrease with increasing PEG content, providing some measure of melt rheology control. Another possibility is the synthesis of custom block copolymers with enhanced phase separation

compared to PEBAX, resulting in higher permeability through the polyether phase [7]. The lack of material availability would be the main challenge of this approach, so it would likely be less attractive than using PEG/PEBAX blends.

Beyond strategies for improving O<sub>2</sub> permeance, a practical consideration for any MAP membrane is the fact that produce packages are a highly humid environment (80 to 90% relative humidity) [8] and that the transport of water vapor in these materials may influence the transport of other gases [9]. Both single layer films of the separating material as well as any multilayered films produced should therefore be tested for their permeabilities under different humidity conditions, an experiment which is now possible in our labs since the construction of a mixed gas permeation system with water vapor injection. This realistic environment would give a true indication of the performance of any MAP membranes produced.

### **7.2.5 Coextruded Membranes with Porous Supports**

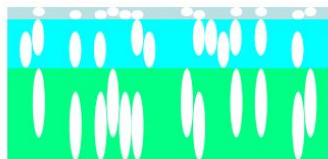
In conjunction with projects meant to further understand and improve pore formation in  $\beta$ -iPP films, several multilayered membranes should be investigated. Revisiting the battery separator application, it may be possible to coextrude a trilayer battery separator [5,10] with enhanced shutdown response if porous  $\beta$ -iPP layers can be combined with a lower-melting material that can be made porous through, for example, the inclusion of fillers. This would represent a processing improvement over current trilayer films, which are constructed using a lamination process.

Several other promising applications are depicted in Figure 7.1. Pseudo-asymmetric membranes for applications such as ultrafiltration may also be fabricated using multilayer coextrusion. Using a single grade of iPP, different types or loadings of  $\beta$  nucleators could be masterbatched to obtain several iPP feedstocks with identical or very

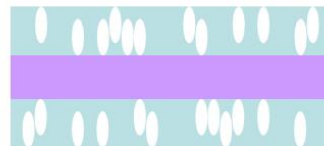
similar rheology but distinct crystallization behavior [11]. These feedstocks could be coextruded and biaxially stretched so that each layer has different porosities and pore size distributions. Ideally, they could be arranged in descending order of pore size, so that the separating layer has mechanical support from the other layer(s).

As mentioned previously, extruded RO membranes are also a possible application using this technology. Coextruded membranes for this application are currently being investigated. The separating layer is made of disulfonated poly(arylene ether sulfone) (BPS) materials, a chlorine-resistant, high flux RO material, which is impregnated with poly(ethylene glycol) (PEG) to achieve rheological compatibility with  $\beta$ -iPP by lowering the BPS  $T_g$ . Compatibility between the support layer and active layer has proven to be the main challenge to this point in these studies. It would also be possible to improve rheological compatibility by implementing reactive extrusion techniques, which degrade PP chains and reduce melt viscosity [12]. This technique has already been demonstrated for  $\beta$  nucleated polypropylenes.

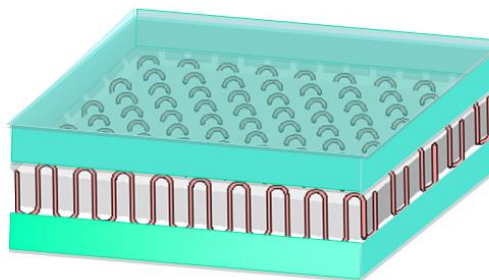
A final intriguing possibility for multilayered films is in  $\text{CO}_2/\text{CH}_4$  separations via the introduction of poly(4-methyl-1-pentene) (P4M1P) as the active layer. Like syndiotactic polypropylene, P4M1P is one of the few materials with a crystalline phase less dense than the amorphous phase and where appreciable mass transfer occurs through the crystalline phase in permeation experiments [13]. The size of a  $\text{CH}_4$  molecule is comparable to the spacing in the crystalline lattice, and so estimates of its diffusion in the pure crystalline phase show a large reduction relative to smaller gases [13]. Previously, it has been demonstrated with PEO that orientation in a confined configuration can result in single crystal sheets [14]. If the crystallinity of P4M1P can be enhanced through orientation in a multilayered configuration while a porous support is simultaneously formed, a very efficient membrane for  $\text{CH}_4$  separations would be the result.



Support Layer: Porous PP (large  $D_{\text{pore}}$ )  
 Active Layer: Porous PP (small  $D_{\text{pore}}$ )



Support Layer: Porous PP  
 Active Layer: PEG-BPS Blend



Support Layer: Porous PP  
 Active Layer: Confined Crystalline P4M1P

Figure 7.1. Three potential multilayered membranes and their constituent materials.

### 7.3 REFERENCES

- [1] J. Varga, I. Mudra, G.W. Ehrenstein, Highly active thermally stable  $\beta$ -nucleating agents for isotactic polypropylene, *Journal of Applied Polymer Science*. 74 (1999) 2357–2368.
- [2] M. Gahleitner, C. Grein, S. Kheirandish, J. Wolfschwenger, Nucleation of Polypropylene Homo- and Copolymers, *International Polymer Processing: The Journal of the Polymer Processing Society*. XXVI (2011) 2–20.
- [3] W. Zhu, X. Zhang, C. Zhao, W. Wu, J. Hou, M. Xu, A Novel Polypropylene Microporous Film, *Polymers for Advanced Technologies*. 7 (1996) 743–748.
- [4] G. Shi, X. Zhang, J. Zheng, G. Zhou, Microporous Film, Made from  $\beta$ -Crystalline Phase Polypropylene, *International Polymer Processing*. 10 (1995) 330–333.
- [5] G. Venugopal, J. Moore, J. Howard, S. Pandalwar, Characterization of microporous separators for lithium-ion batteries, *Journal of Power Sources*. 77 (1999) 34–41.
- [6] A. Car, C. Stropnik, W. Yave, K.-V. Peinemann, PEG modified poly (amide-b-ethylene oxide) membranes for CO<sub>2</sub> separation, *Journal of Membrane Science*. 307 (2008) 88–95.
- [7] S.R. Reijerkerk, M.H. Knoef, K. Nijmeijer, M. Wessling, Poly(ethylene glycol) and poly(dimethyl siloxane): Combining their advantages into efficient CO<sub>2</sub> gas separation membranes, *Journal of Membrane Science*. 352 (2010) 126–135.
- [8] K.L. Yam, D.S. Lee, Design of modified atmosphere packaging for fresh produce, in: M.L. Rooney (Ed.), *Active Food Packaging*, Blackie Academic & Professional, 1995: pp. 55–73.
- [9] S.J. Metz, W.J.C. Van De Ven, J. Potreck, M.H. V Mulder, M. Wessling, Transport of water vapor and inert gas mixtures through highly selective and highly permeable polymer membranes, *Journal of Membrane Science*. 251 (2005) 29–41.
- [10] P. Arora, Z.J. Zhang, Battery separators., *Chemical Reviews*. 104 (2004) 4419–62.
- [11] J. Varga,  $\beta$ -Modification of Isotactic Polypropylene: Preparation, Structure, Processing, Properties, and Application, *Journal of Macromolecular Science, Part B*. 41 (2002) 1121–1171.

- [12] J. Fan, J. Feng, Study on  $\beta$ -Nucleated Controlled-Rheological Polypropylene Random Copolymer: Crystallization Behavior and a Possible Degradation Mechanism, *Industrial & Engineering Chemistry Research*. 52 (2013) 761–770.
- [13] A.C. Puleo, D.R. Paul, P.K. Wong, Gas sorption and transport in semicrystalline poly(4-methyl-1-pentene), *Polymer*. 30 (1989) 1357–1366.
- [14] H. Wang, J.K. Keum, A. Hiltner, E. Baer, B.D. Freeman, A. Rozanski, et al., Confined Crystallization of Polyethylene Oxide in Nanolayer Assemblies, *Science*. 323 (2009) 757–760.

## Bibliography

- Aboulfaraj, M., G'Sell, C., Ulrich, B., & Dahoun, A. (1995). In situ observation of the plastic deformation of polypropylene spherulites under uniaxial tension and simple shear in the scanning electron microscope. *Polymer*, *36*(4), 731–742. doi:10.1016/0032-3861(95)93102-R
- Armstrong, S., Freeman, B., Hiltner, A., & Baer, E. (2012). Gas permeability of melt-processed poly(ether block amide) copolymers and the effects of orientation. *Polymer*, *53*(6), 1383–1392. doi:10.1016/j.polymer.2012.01.037
- Armstrong, S. R., Paul, D. R., & Hiltner, A. (2010). Permeability of Poly (ether block amide) (PEBAX): Effect of Orientation. *Abstracts of Papers, 240th ACS National Meeting* (p. PMSE – 193). Boston, MA: American Chemical Society.
- Arora, P., & Zhang, Z. J. (2004). Battery separators. *Chemical reviews*, *104*(10), 4419–62.
- Asano, T., Yamamoto, T., Mina, M. F., Fujiwara, Y., Takahashi, H., & Hatta, I. (1999). Melting behavior of the oriented  $\beta$ -phase polypropylene texture crystallized by the temperature slope method. *Journal of Macromolecular Science, Part B*, *38*(1), 163–175. doi:10.1080/00222349908248112
- ASTM D3985: Standard Test Method for Oxygen Gas Transmission Rate Through Plastic Film and Sheeting Using a Coulometric Sensor. *ASTM Book of Standards, 15.10*. doi:10.1520/D3985-05R10E01
- ASTM F2476: Test Method for the Determination of Carbon Dioxide Gas Transmission Rate (CO<sub>2</sub> TR) Through Barrier Materials Using An Infrared Detector. *ASTM Book of Standards, 15.10*. doi:10.1520/F2476-05
- Baer, E., Hiltner, A., & Jarus, D. (1999). Relationship of Hierarchical Structure to Mechanical Properties. *Macromolecular Symposium*, *147*, 37–61.
- Bai, F., Li, F., Calhoun, B. H., Quirk, R. P., & Cheng, S. Z. D. (1999). Physical Constants of Poly(propylene). In J. Brandrup, E. H. Immergut, & E. A. Grulke (Eds.), *Polymer Handbook* (4th ed., p. V/21–V/30). New York: John Wiley & Sons, Inc.

- Bai, H., Luo, F., Zhou, T., Deng, H., Wang, K., & Fu, Q. (2011). New insight on the annealing induced microstructural changes and their roles in the toughening of  $\beta$ -form polypropylene. *Polymer*, 52(10), 2351–2360. doi:10.1016/j.polymer.2011.03.017
- Bai, H., Wang, Y., Zhang, Z., Han, L., Li, Y., Liu, L., Zhou, Z., et al. (2009). Influence of Annealing on Microstructure and Mechanical Properties of Isotactic Polypropylene with  $\beta$ -Phase Nucleating Agent. *Macromolecules*, 42(17), 6647–6655. doi:10.1021/ma9001269
- Baker, R. W. (2004). *Membrane Technology and Applications. Membrane Technology and Applications* (2nd ed.). West Sussex: John Wiley & Sons, Ltd.
- Barbi, V., Funari, S. S., Gehrke, R., Scharnagl, N., & Stribeck, N. (2003). SAXS and the Gas Transport in Polyether- b lock -polyamide Copolymer Membranes. *Macromolecules*, 36(3), 749–758. doi:10.1021/ma0213403
- Bernal-Lara, T. E., Masirek, R., Hiltner, A., Baer, E., Piorowska, E., & Galeski, A. (2006). Morphology studies of multilayered HDPE/PS systems. *Journal of Applied Polymer Science*, 99(2), 597–612. doi:10.1002/app.22178
- Bernardo, P., Drioli, E., & Golemme, G. (2009). Membrane Gas Separation: A Review/State of the Art. *Industrial & Engineering Chemistry Research*, 48(10), 4638–4663. doi:10.1021/ie8019032
- Bierenbaum, H., Plainfield, R., Isaacson, R., & Lantos, P. (1969). Breathable Medical Dressing. US3426754.
- Bondar, V. I., Freeman, B. D., & Pinnau, I. (1999). Gas sorption and characterization of poly(ether-b-amide) segmented block copolymers. *Journal of Polymer Science Part B: Polymer Physics*, 37(17), 2463–2475. doi:10.1002/(SICI)1099-0488(19990901)37:17<2463::AID-POLB18>3.0.CO;2-H
- Bondar, V. I., Freeman, B. D., & Pinnau, I. (2000). Gas transport properties of poly(ether-b-amide) segmented block copolymers. *Journal of Polymer Science Part B: Polymer Physics*, 38(15), 2051–2062. doi:10.1002/1099-0488(20000801)38:15<2051::AID-POLB100>3.0.CO;2-D
- Cai, Z., Zhang, Y., Li, J., Xue, F., Shang, Y., He, X., Feng, J., et al. (2012). Real time synchrotron SAXS and WAXS investigations on temperature related deformation and transitions of  $\beta$ -iPP with uniaxial stretching. *Polymer*, 53(7), 1593–1601. doi:10.1016/j.polymer.2012.02.012

- Car, A., Stropnik, C., Yave, W., & Peinemann, K.-V. (2008a). Tailor-made Polymeric Membranes based on Segmented Block Copolymers for CO<sub>2</sub> Separation. *Advanced Functional Materials*, 18(18), 2815–2823. doi:10.1002/adfm.200800436
- Car, A., Stropnik, C., Yave, W., & Peinemann, K.-V. (2008b). PEG modified poly (amide-b-ethylene oxide) membranes for CO<sub>2</sub> separation. *Journal of Membrane Science*, 307, 88–95. doi:10.1016/j.memsci.2007.09.023
- Celgard. (2009). *Celgard Product Comparison, Company Literature Item #10002* (Vol. 2200).
- Celgard. (2010). *Celgard Overview Brochure, Company Literature Item #10003*.
- Chu, F. (1996). Structure and gas permeability of microporous films prepared by biaxial drawing of  $\beta$ -form polypropylene. *Polymer*, 37(4), 573–579. doi:10.1016/0032-3861(96)83143-0
- Chu, F., Yamaoka, T., Ide, H., & Kimura, Y. (1994). Microvoid formation process during the plastic deformation of  $\beta$ -form polypropylene. *Polymer*, 35(16), 3442–3448. doi:10.1016/0032-3861(94)90906-7
- Chu, F., Yamaoka, T., & Kimura, Y. (1995). Crystal transformation and micropore formation during uniaxial drawing of  $\beta$ -form polypropylene film. *Polymer*, 36(13), 2523–2530. doi:10.1016/0032-3861(95)91197-F
- Costello, L. M., & Koros, W. J. (1992). Temperature dependence of gas sorption and transport properties in polymers: measurement and applications. *Industrial & Engineering Chemistry Research*, 31(12), 2708–2714. doi:10.1021/ie00012a012
- Dong, M., Guo, Z., Su, Z., & Yu, J. (2011). The effects of crystallization condition on the microstructure and thermal stability of isotactic polypropylene nucleated by  $\beta$ -form nucleating agent. *Journal of Applied Polymer Science*, 119(3), 1374–1382. doi:10.1002/app.32487
- Dong, M., Guo, Z., Yu, J., & Su, Z. (2009). Study of the assembled morphology of aryl amide derivative and its influence on the nonisothermal crystallizations of isotactic polypropylene. *Journal of Polymer Science Part B: Polymer Physics*, 47(3), 314–325. doi:10.1002/polb.21642

- Druin, M. L., Loft, J. T., & Plovon, S. G. (1972). Novel Open-Celled Microporous Film. *US3679538*.
- Exama, A., Arul, J., Lencki, R. W., Lee, L. Z., & Toupin, C. (1993). Suitability of Plastic Films for Modified Atmosphere Packaging of Fruits and Vegetables. *Journal of Food Science*, *58*(6), 1365–1370. doi:10.1111/j.1365-2621.1993.tb06184.x
- Fan, J., & Feng, J. (2013). Study on  $\beta$ -Nucleated Controlled-Rheological Polypropylene Random Copolymer: Crystallization Behavior and a Possible Degradation Mechanism. *Industrial & Engineering Chemistry Research*, *52*(2), 761–770. doi:10.1021/ie302474b
- Fane, A. G. (2002). Membrane bioreactors: design & operational options. *Filtration & Separation*, *39*(5), 26–29. doi:10.1016/S0015-1882(02)80168-9
- Ferrer-Balas, D., Maspoch, M. L., Martinez, A. B., & Santana, O. O. (2001). Influence of annealing on the microstructural, tensile and fracture properties of polypropylene films. *Polymer*, *42*(4), 1697–1705. doi:10.1016/S0032-3861(00)00487-0
- Fisher, H. M., & Wensley, G. C. (2002). Polypropylene microporous membrane for battery separator. *US6368742*.
- Fujiwara, Y. (1975). Das Doppelschmelzverhalten der  $\beta$ -Phase des isotaktischen Polypropylens. *Colloid and Polymer Science*, *253*(4), 273–282. doi:10.1007/BF02352075
- Fujiyama, M. (1996). Structures and properties of injection moldings of beta-crystal nucleator-added polypropylenes. *International Polymer Processing*, *11*(3), 271–274.
- Fujiyama, Mitsuyoshi, Kawamura, Y., Wakino, T., & Okamoto, T. (1988). Study on Rough-Surface Biaxially Oriented Polypropylene Film. I. Formation of  $\beta$ -Form Crystals in Sheet Cast with T-Die Extruder. *Journal of Applied Polymer Science*, *36*, 985–993.
- Gahleitner, M., Grein, C., Kheirandish, S., & Wolfschwenger, J. (2011). Nucleation of Polypropylene Homo- and Copolymers. *International Polymer Processing: The Journal of the Polymer Processing Society*, *XXVI*(01), 2–20. doi:10.3139/217.2411
- Gigova, A. (2006). Investigation of the porous structure of battery separators using various porometric methods. *Journal of Power Sources*, *158*(2), 1054–1061. doi:10.1016/j.jpowsour.2005.11.006
- Gore, R. W. (1976). Process for producing porous products. *US3953566*.

- Greener, J., Ng, K. C., Vaeth, K. M., & Smith, T. M. (2007). Moisture permeability through multilayered barrier films as applied to flexible OLED display. *Journal of Applied Polymer Science*, 106(5), 3534–3542. doi:10.1002/app.26863
- Grein, C., Plummer, C. J. G., Kausch, H.-H., Germain, Y., & Béguelin, P. (2002). Influence of  $\beta$  nucleation on the mechanical properties of isotactic polypropylene and rubber modified isotactic polypropylene. *Polymer*, 43(11), 3279–3293. doi:10.1016/S0032-3861(02)00135-0
- Grein, Christelle. (2005). Toughness of Neat, Rubber Modified and Filled  $\beta$ -Nucleated Polypropylene: From Fundamentals to Applications. *Advances in Polymer Science*, 188(September), 43–104. doi:10.1007/b136972
- Hernandez, A. (1996). Pore size distributions in microporous membranes. A critical analysis of the bubble point extended method. *Journal of Membrane Science*, 112(1), 1–12. doi:10.1016/0376-7388(95)00025-9
- Humbert, S., Lame, O., Chenal, J. M., Rochas, C., & Vigier, G. (2010). New Insight on Initiation of Cavitation in Semicrystalline Polymers: In-Situ SAXS Measurements. *Macromolecules*, 43(17), 7212–7221. doi:10.1021/ma101042d
- Husken, D., Visser, T., Wessling, M., & Gaymans, R. J. (2010). CO<sub>2</sub> permeation properties of poly(ethylene oxide)-based segmented block copolymers. *Journal of Membrane Science*, 346(1), 194–201. doi:10.1016/j.memsci.2009.09.034
- Isaacson, R. B., & Bierenbaum, H. S. (1971). Process for Preparing Microporous Film. US3558764.
- Jacoby, P., Bersted, B. H., Kissel, W. J., & Smith, C. E. (1986). Studies on the  $\beta$ -Crystalline form of Isotactic Polypropylene. *Journal of Polymer Science Part B: Polymer Physics*, 24, 461–491.
- Jacoby, Philip, Bauer, C. W., Clingman, S. R., & Tapp, W. T. (1994). Oriented polymeric microporous films. US5317035.
- Jacoby, Philip, Bauer, C. W., Clingman, S. R., & Tapp, W. T. (1997). Oriented polymeric microporous films. US5594070.
- Jarus, D. (2002). Barrier properties of polypropylene/polyamide blends produced by microlayer coextrusion. *Polymer*, 43(8), 2401–2408. doi:10.1016/S0032-3861(01)00790-X

- Jin, Y., Tai, H., Hiltner, A., Baer, E., & Shirk, J. S. (2007). New class of bioinspired lenses with a gradient refractive index. *Journal of Applied Polymer Science*, *103*(3), 1834–1841. doi:10.1002/app.25404
- Johnson, M. B., & Wilkes, G. L. (2001). Microporous membranes of polyoxymethylene from a melt-extrusion process: (I) effects of resin variables and extrusion conditions. *Journal of Applied Polymer Science*, *81*(12), 2944–2963. doi:10.1002/app.1745
- Johnson, M. B., & Wilkes, G. L. (2002a). Microporous membranes of polyoxymethylene from a melt-extrusion process: (II) Effects of thermal annealing and stretching on porosity. *Journal of Applied Polymer Science*, *84*(9), 1762–1780. doi:10.1002/app.10587
- Johnson, M. B., & Wilkes, G. L. (2002b). Microporous membranes of isotactic poly(4-methyl-1-pentene) from a melt-extrusion process. I. Effects of resin variables and extrusion conditions. *Journal of Applied Polymer Science*, *83*(10), 2095–2113. doi:10.1002/app.10164
- Johnson, M. B., & Wilkes, G. L. (2002c). Microporous membranes of isotactic poly(4-methyl-1-pentene) from a melt-extrusion process. II. Effects of thermal annealing and stretching on porosity. *Journal of Applied Polymer Science*, *84*(5), 1076–1100. doi:10.1002/app.10395
- Kalakkunnath, S., Kalika, D. S., Lin, H., & Freeman, B. D. (2005). Segmental Relaxation Characteristics of Cross-Linked Poly(ethylene oxide) Copolymer Networks. *Macromolecules*, *38*(23), 9679–9687. doi:10.1021/ma051741t
- Kelman, S. D., Matteucci, S., Bielawski, C. W., & Freeman, B. D. (2007). Crosslinking poly(1-trimethylsilyl-1-propyne) and its effect on solvent resistance and transport properties. *Polymer*, *48*(23), 6881–6892. doi:10.1016/j.polymer.2007.08.063
- Kerns, J., Hsieh, A., Hiltner, A., & Baer, E. (1999). Mechanical Behavior of Polymer Microlayers. *Macromolecular Symposium*, *147*, 15–25.
- Kim, J. H., Ha, S. Y., & Lee, Y. M. (2001). Gas permeation of poly (amide-6b-ethylene oxide) copolymer. *Journal of Membrane Science*, *190*(February), 179–193.
- Kirkland, B. S., Clarke, R., & Paul, D. R. (2008). A versatile membrane system for bulk storage and shipping of produce in a modified atmosphere. *Journal of Membrane Science*, *324*, 119–127. doi:10.1016/j.memsci.2008.07.001

- Kjellander, R., & Florin, E. (1981). Water structure and changes in thermal stability of the system poly(ethylene oxide)-water. *Journal of the Chemical Society, Faraday Transactions 1*, 77(9), 2053–2077. doi:10.1039/f19817702053
- Koros, W. J., Paul, D. R., & Rocha, A. A. (1976). Carbon Dioxide Sorption and Transport in Polycarbonate. *Journal of Polymer Science Part B: Polymer Physics*, 14(4), 687–702.
- Kotek, J., Raab, M., Baldrian, J., & Grellmann, W. (2002). The effect of specific  $\beta$ -nucleation on morphology and mechanical behavior of isotactic polypropylene. *Journal of Applied Polymer Science*, 85(6), 1174–1184. doi:10.1002/app.10701
- Kusuma, V. A., Freeman, B. D., Borns, M. A., & Kalika, D. S. (2009). Influence of chemical structure of short chain pendant groups on gas transport properties of cross-linked poly(ethylene oxide) copolymers. *Journal of Membrane Science*, 327(1-2), 195–207. doi:10.1016/j.memsci.2008.11.022
- Kusuma, V. A., Gunawan, G., Smith, Z. P., & Freeman, B. D. (2010). Gas permeability of cross-linked poly(ethylene-oxide) based on poly(ethylene glycol) dimethacrylate and a miscible siloxane co-monomer. *Polymer*, 51(24), 5734–5743. doi:10.1016/j.polymer.2010.09.069
- Li, H., Freeman, B. D., & Ekiner, O. M. (2010). Gas permeation properties of poly(urethane-urea)s containing different polyethers. *Journal of Membrane Science*, 369(1-2), 49–58. doi:10.1016/j.memsci.2010.11.024
- Li, J. X., & Cheung, W. L. (1998). On the deformation mechanisms of  $\beta$ -polypropylene: 1. Effect of necking on  $\beta$ -phase PP crystals. *Polymer*, 39(26), 6935–6940. doi:10.1016/S0032-3861(98)00144-X
- Li, J. X., & Cheung, W. L. (2000). A Correction Function to Determine the  $\beta$ -Fusion Heat in a Mixture of  $\alpha$ - and  $\beta$ -PP. *Journal of Thermal Analysis and Calorimetry*, 61, 757–762.
- Li, J. X., Cheung, W. L., & Chan, C. M. (1999). On deformation mechanisms of  $\beta$ -polypropylene 3. Lamella structures after necking and cold drawing. *Polymer*, 40(13), 3641–3656. doi:10.1016/S0032-3861(98)00578-3
- Li, J. X., Cheung, W. L., & Jia, D. (1999). A study on the heat of fusion of  $\beta$ -polypropylene. *Polymer*, 40(5), 1219–1222. doi:10.1016/S0032-3861(98)00345-0

- Li, X., Wu, H., Huang, T., Shi, Y., Wang, Y., Xiang, F., & Zhou, Z. (2010).  $\beta/\alpha$  Transformation of  $\beta$ -polypropylene during tensile deformation: effect of crystalline morphology. *Colloid and Polymer Science*, 288(16-17), 1539–1549. doi:10.1007/s00396-010-2275-x
- Lin, H. (2005). *Solubility Selective Membrane Materials for Carbon Dioxide Removal from Mixtures with Light Gases*. The University of Texas at Austin.
- Lin, H., & Freeman, B. D. (2004). Gas solubility, diffusivity and permeability in poly(ethylene oxide). *Journal of Membrane Science*, 239, 105–117. doi:10.1016/j.memsci.2003.08.031
- Lin, H., & Freeman, B. D. (2005a). Materials selection guidelines for membranes that remove CO<sub>2</sub> from gas mixtures. *Journal of Molecular Structure*, 739(1-3), 57–74. doi:10.1016/j.molstruc.2004.07.045
- Lin, H., & Freeman, B. D. (2005b). Gas and Vapor Solubility in Cross-Linked Poly(ethylene Glycol Diacrylate). *Macromolecules*, 38(20), 8394–8407. doi:10.1021/ma051218e
- Lin, H., & Freeman, B. D. (2006a). Gas Permeation and Diffusion in Cross-Linked Poly(ethylene glycol diacrylate). *Macromolecules*, 39(10), 3568–3580. doi:10.1021/ma051686o
- Lin, H., & Freeman, B. D. (2006b). Springer Handbook Part C: Measurement Methods for Materials Properties, Ch. 7 Sect. 6, Permeation and Diffusion. *Springer Handbook*.
- Lin, H., Van Wagner, E., Swinnea, J. S., Freeman, B. D., Pas, S., Hill, A. J., Kalakkunnath, S., et al. (2006). Transport and structural characteristics of crosslinked poly(ethylene oxide) rubbers. *Journal of Membrane Science*, 276(1-2), 145–161. doi:10.1016/j.memsci.2005.09.040
- Lin, K.-Y., Xanthos, M., & Sirkar, K. K. (2009). Novel polypropylene-based microporous membranes via spherulitic deformation. *Journal of Membrane Science*, 330(1-2), 267–278. doi:10.1016/j.memsci.2008.12.060
- Liu, R. Y. F., Bernal-Lara, T. E., Hiltner, A., & Baer, E. (2005). Polymer Interphase Materials by Forced Assembly. *Macromolecules*, 38(11), 4819–4827. doi:10.1021/ma047292z

- Liu, R. Y. F., Ranade, A. P., Wang, H. P., Bernal-Lara, T. E., Hiltner, A., & Baer, E. (2005). Forced Assembly of Polymer Nanolayers Thinner Than the Interphase. *Macromolecules*, 38(26), 10721–10727. doi:10.1021/ma051649x
- Loeb, S., & Sourirajan, S. (1963). Sea Water Demineralization by Means of an Osmotic Membrane. In R. F. Gould (Ed.), *Saline Water Conversion II* (Vol. 38, pp. 117–132). Advances in Chemistry Series Number 38, American Chemical Society.
- Lonsdale, H. K., Merten, U., & Riley, R. L. (1965). Transport properties of cellulose acetate osmotic membranes. *Journal of Applied Polymer Science*, 9(4), 1341–1362. doi:10.1002/app.1965.070090413
- Lotz, B., Wittmann, J. C., & Lovinger, A. J. (1996). Structure and morphology of poly(propylenes): a molecular analysis. *Polymer*, 37(22), 4979–4992. doi:10.1016/0032-3861(96)00370-9
- Mangaraj, S., Goswami, T. K., & Mahajan, P. V. (2009). Applications of Plastic Films for Modified Atmosphere Packaging of Fruits and Vegetables: A Review. *Food Engineering Reviews*, 1(2), 133–158. doi:10.1007/s12393-009-9007-3
- Matteucci, S., Yampolskii, Y. P., Freeman, B. D., & Pinnau, I. (2006). Transport of Gases and Vapors in Glassy and Rubbery Polymers. In Y. Yampolskii, I. Pinnau, & B. D. Freeman (Eds.), *Materials Science of Membranes for Gas and Vapor Separation* (1st ed.). Wiley.
- Meille, S. V., Ferro, D. R., Brueckner, S., Lovinger, A. J., & Padden, F. J. (1994). Structure of  $\beta$ -Isotactic Polypropylene: A Long-Standing Structural Puzzle. *Macromolecules*, 27(9), 2615–2622. doi:10.1021/ma00087a034
- Menyhárd, A., Varga, J., & Molnár, G. (2006). Comparison of different -nucleators for isotactic polypropylene, characterisation by DSC and temperature-modulated DSC (TMDSC) measurements. *Journal of Thermal Analysis and Calorimetry*, 83(3), 625–630. doi:10.1007/s10973-005-7498-6
- Merkel, T. C., Bondar, V. I., Nagai, K., Freeman, B. D., & Pinnau, I. (2000). Gas sorption, diffusion, and permeation in poly(dimethylsiloxane). *Journal of Polymer Science Part B: Polymer Physics*, 38(3), 415–434. doi:10.1002/(SICI)1099-0488(20000201)38:3<415::AID-POLB8>3.0.CO;2-Z
- Metz, S. J., Mulder, M. H. V., & Wessling, M. (2004). Gas-Permeation Properties of Poly(ethylene oxide) Poly(butylene terephthalate) Block Copolymers. *Macromolecules*, 37(12), 4590–4597. doi:10.1021/ma049847w

- Metz, S. J., Ven, W. J. C. Van De, Potreck, J., Mulder, M. H. V., & Wessling, M. (2005). Transport of water vapor and inert gas mixtures through highly selective and highly permeable polymer membranes. *Journal of Membrane Science*, 251, 29–41. doi:10.1016/j.memsci.2004.08.036
- Mizutani, Y., Nakamura, S., Kaneko, S., & Okamura, K. (1993). Microporous Polypropylene Sheets. *Industrial & Engineering Chemistry Research*, 32(1), 221–227. doi:10.1021/ie00013a029
- Mueller, C. D., Kerns, J., Ebeling, T., Nazarenko, S., Hiltner, A., & Baer, E. (1997). Microlayer Coextrusion: Processing and Applications. *Polymer Process Engineering* 97 (pp. 137–157).
- Mueller, C. D., Nazarenko, S., Ebeling, T., Schuman, T. L., Hiltner, A., & Baer, E. (1997). Novel Structures by Microlayer Coextrusion - Talc-Filled PP, PC/SAN, and HDPE/LLDPE. *Polymer Engineering & Science*, 37(2), 355–362.
- Mueller, C. D., Topolkaev, V., Soerens, D., Hiltner, A., & Baer, E. (2000). Breathable Polymer Films Produced by the Microlayer Coextrusion Process. *Journal of Applied Polymer Science*, 78, 816–828.
- Murphy, Thomas M., Langhe, D. S., Ponting, M., Baer, E., Freeman, B. D., & Paul, D. R. (2011). Physical aging of layered glassy polymer films via gas permeability tracking. *Polymer*, 52(26), 6117–6125. doi:10.1016/j.polymer.2011.10.061
- Murphy, Tom M, Offord, G. T., & Paul, D. R. (2009). Fundamentals of Membrane Gas Separation. In E. Drioli & L. Giorno (Eds.), *Membrane Operations: Innovative Separations and Transformations* (pp. 63–82). Wiley-VCH.
- Myers, A. W., Stannett, V., & Szwarc, M. (1959). The permeability of polypropylene to gases and vapors. *Journal of Polymer Science*, 35(128), 285–288. doi:10.1002/pol.1959.1203512830
- Nagō, S., & Mizutani, Y. (1998). Microporous polypropylene sheets containing CaCO<sub>3</sub> filler: Effects of stretching ratio and removing CaCO<sub>3</sub> filler. *Journal of Applied Polymer Science*, 68(10), 1543–1553. doi:10.1002/(SICI)1097-4628(19980606)68:10<1543::AID-APP1>3.3.CO;2-W
- Natta, G., & Corradini, P. (1960). Structure and Properties of Isotactic Polypropylene. *Del Nuovo Cimento*, 15(10), 40–51.
- Nazarenko, S., Hiltner, A., & Baer, E. (1999). Polymer microlayer structures with anisotropic conductivity. *Journal of Materials Science*, 34, 1461 – 1470.

- Nguyen, Q. T., Sublet, J., Langevin, D., Chappey, C., Marais, S., Valleton, J.-M., & Poncin-Epaillard, F. (2010). CO<sub>2</sub> Permeation with Pebax®-based Membranes for Global Warming Reduction. In B. D. Freeman & Y. Yampolskii (Eds.), *Membrane Gas Separation* (Galley Pro., pp. 255–278). West Sussex: John Wiley & Sons, Ltd.
- Offord, G. T., Armstrong, S. R., Freeman, B. D., Baer, E., Hiltner, A., & Paul, D. R. (2013). Influence of Processing Strategies on Porosity and Permeability of  $\beta$  Nucleated Isotactic Polypropylene Stretched Films. *Polymer, Accepted*. doi:10.1016/j.polymer.2013.03.050
- Offord, G. T., Armstrong, S. R., Freeman, B. D., Baer, E., Hiltner, A., Swinnea, J. S., & Paul, D. R. (2013). Porosity Enhancement in  $\beta$  Nucleated Isotactic Polypropylene Stretched Films by Thermal Annealing. *Polymer, Accepted*. doi:10.1016/j.polymer.2013.03.026
- Okamoto, K., Fuji, M., Okamoto, S., Suzuki, H., Tanaka, K., & Kita, H. (1995). Gas permeation properties of poly(ether imide) segmented copolymers. *Macromolecules*, 28(20), 6950–6956. doi:10.1021/ma00124a035
- Paul, D. R., & Clarke, R. (2002). Modeling of modified atmosphere packaging based on designs with a membrane and perforations. *Journal of Membrane Science*, 208(1-2), 269–283. doi:10.1016/S0376-7388(02)00303-4
- Peinador, R. I., Calvo, J. I., Prádanos, P., Palacio, L., & Hernández, A. (2010). Characterisation of polymeric UF membranes by liquid–liquid displacement porosimetry. *Journal of Membrane Science*, 348(1-2), 238–244. doi:10.1016/j.memsci.2009.11.008
- Phillips, R. A., & Wolkowicz, M. D. (2005). Polypropylene Morphology. In N. Pasquini (Ed.), *Polypropylene Handbook* (2nd ed., pp. 147–264). Hanser Gardner.
- Poussin, L., Bertin, Y. A., Parisot, J., Brassy, C., De, M., Physique, D., & Cnrs, U. R. A. (1998). Influence of thermal treatment on the structure of an isotactic polypropylene. *Polymer*, 39(18), 4261–4265.
- Puleo, A. C., Paul, D. R., & Wong, P. K. (1989). Gas sorption and transport in semicrystalline poly(4-methyl-1-pentene). *Polymer*, 30(July), 1357–1366.
- Raharjo, R. D., Freeman, B. D., Paul, D. R., Sarti, G. C., & Sanders, E. S. (2007). Pure and mixed gas CH<sub>4</sub> and n-C<sub>4</sub>H<sub>10</sub> permeability and diffusivity in poly(dimethylsiloxane). *Journal of Membrane Science*, 306, 75–92. doi:10.1016/j.memsci.2007.08.014

- Ran, S., & Xu, M. (2004). Studies on the Pore Formation Mechanism of  $\beta$ -Crystalline Polypropylene Under Stretching. *Chinese Journal of Polymer Science*, 22(2), 123–130.
- Reif, O. W. (2006). Microfiltration Membranes: Characteristics and Manufacturing. *Adv. Biochem. Engin/Biotechnol*, 73– 103. doi:10.1007/b104245
- Reijerkerk, S. R., Arun, A., Gaymans, R. J., Nijmeijer, K., & Wessling, M. (2010). Tuning of mass transport properties of multi-block copolymers for CO<sub>2</sub> capture applications. *Journal of Membrane Science*, 359(1-2), 54–63. doi:10.1016/j.memsci.2009.09.045
- Reijerkerk, S. R., Jordana, R., Nijmeijer, K., & Wessling, M. (2011). Highly hydrophilic, rubbery membranes for CO<sub>2</sub> capture and dehydration of flue gas. *International Journal of Greenhouse Gas Control*, 5(1), 26–36. doi:10.1016/j.ijggc.2010.06.014
- Reijerkerk, S. R., Knoef, M. H., Nijmeijer, K., & Wessling, M. (2010). Poly(ethylene glycol) and poly(dimethyl siloxane): Combining their advantages into efficient CO<sub>2</sub> gas separation membranes. *Journal of Membrane Science*, 352(1-2), 126–135. doi:10.1016/j.memsci.2010.02.008
- Reijerkerk, S. R., Nijmeijer, K., Ribeiro, C. P., Freeman, B. D., & Wessling, M. (2011). On the effects of plasticization in CO<sub>2</sub>/light gas separation using polymeric solubility selective membranes. *Journal of Membrane Science*, 367(1-2), 33–44. doi:10.1016/j.memsci.2010.10.035
- Rezac, M. E., John, T., & Pfromm, P. H. (1997). Effect of copolymer composition on the solubility and diffusivity of water and methanol in a series of polyether amides. *Journal of Applied Polymer Science*, 65(10), 1983–1993. doi:10.1002/(SICI)1097-4628(19970906)65:10<1983::AID-APP16>3.0.CO;2-Y
- Robeson, L. M., Freeman, B. D., Paul, D. R., & Rowe, B. W. (2009). An empirical correlation of gas permeability and permselectivity in polymers and its theoretical basis. *Journal of Membrane Science*, 341(1-2), 178–185. doi:10.1016/j.memsci.2009.06.005
- Sadeghi, F. (2005). Study of Polypropylene Morphology Obtained from Blown and Cast Film Processes: Initial Morphology Requirements for Making Porous Membrane by Stretching. *Journal of Plastic Film and Sheeting*, 21(3), 199–216. doi:10.1177/8756087905057085

- Sadeghi, Farhad, Aji, A., & Carreau, P. J. (2007a). Analysis of row nucleated lamellar morphology of polypropylene obtained from the cast film process: Effect of melt rheology and process conditions. *Polymer Engineering & Science*, 47(7), 1170–1178. doi:10.1002/pen.20837
- Sadeghi, Farhad, Aji, A., & Carreau, P. J. (2007b). Analysis of microporous membranes obtained from polypropylene films by stretching. *Journal of Membrane Science*, 292(1-2), 62–71. doi:10.1016/j.memsci.2007.01.023
- Sadeghi, Farhad, Aji, A., & Carreau, P. J. (2008). Microporous membranes obtained from polypropylene blends with superior permeability properties. *Journal of Polymer Science Part B: Polymer Physics*, 46(2), 148–157. doi:10.1002/polb.21350
- Sandhya. (2010). Modified atmosphere packaging of fresh produce: Current status and future needs. *LWT - Food Science and Technology*, 43(3), 381–392. doi:10.1016/j.lwt.2009.05.018
- Schofield, R. W., Fane, A. G., & Fell, C. J. D. (1990). Gas and Vapour Transport Through Microporous Membranes. I. Knudsen-Poiseuille Transition. *Journal of Membrane Science*, 53, 159–171.
- Schuman, T. L., Stepanov, E. V, Nazarenko, S., Capaccio, G., Hiltner, A., & Baer, E. (1998). Interdiffusion of Linear and Branched Polyethylene in Microlayers Studied via Melting Behavior. *Macromolecules*, 31, 4551–4561.
- Shi, G., Chu, F., Zhou, G., & Han, Z. (1989). Plastic Deformation and Solid-Phase Transformation in  $\beta$ -Phase Polypropylene. *Die Makromolekulare Chemie*, 190(4), 907–913.
- Shi, G., Zhang, X., Zheng, J., & Zhou, G. (1995). Microporous Film, Made from  $\beta$ -Crystalline Phase Polypropylene. *International Polymer Processing*, 10(4), 330–333.
- Song, Y., Yamamoto, H., & Nemoto, N. (2004). Segmental Orientations and Deformation Mechanism of Poly(ether- block -amide) Films. *Macromolecules*, 37(16), 6219–6226. doi:10.1021/ma0400620
- Stocker, W., Schumacher, M., Graff, S., Thierry, A., Wittmann, J.-C., & Lotz, B. (1998). Epitaxial Crystallization and AFM Investigation of a Frustrated Polymer Structure: Isotactic Poly(propylene),  $\beta$  Phase. *Macromolecules*, 31(3), 807–814. doi:10.1021/ma971345d

- Tabatabaei, S. H., Carreau, P. J., & Ajji, A. (2008). Microporous membranes obtained from polypropylene blend films by stretching. *Journal of Membrane Science*, 325(2), 772–782. doi:10.1016/j.memsci.2008.09.001
- Tabatabaei, S. H., Carreau, P. J., & Ajji, A. (2009a). Effect of processing on the crystalline orientation, morphology, and mechanical properties of polypropylene cast films and microporous membrane formation. *Polymer*, 50(17), 4228–4240. doi:10.1016/j.polymer.2009.06.071
- Tabatabaei, S. H., Carreau, P. J., & Ajji, A. (2009b). Structure and properties of MDO stretched polypropylene. *Polymer*, 50(16), 3981–3989. doi:10.1016/j.polymer.2009.06.059
- Takahashi, S., Yoshida, M., Asano, M., & Nakagawa, T. (2004). Gas-Permeation Control by PET Membranes with Nanosized Pores. *Polymer Journal*, 36(1), 50–53. doi:10.1295/polymj.36.50
- Tangirala, R., Baer, E., Hiltner, A., & Weder, C. (2004). Photopatternable Reflective Films Produced by Nanolayer Extrusion. *Advanced Functional Materials*, 14(6), 595–604. doi:10.1002/adfm.200305446
- Turner Jones, A., Aizlewood, J. M., & Beckett, D. R. (1964). Crystalline Forms of Isotactic Polypropylene. *Die Makromolekulare Chemie*, 75, 134–158.
- Ulbricht, M. (2006). Advanced functional polymer membranes. *Polymer*, 47(7), 2217–2262. doi:10.1016/j.polymer.2006.01.084
- Varga, J. (1989).  $\beta$ -Modification of polypropylene and its two-component systems. *Journal of Thermal Analysis*, 35(6), 1891–1912. doi:10.1007/BF01911675
- Varga, J. (1986). Melting memory effect of the  $\beta$ -modification of polypropylene. *Journal of Thermal Analysis*, 31(1), 165–172. doi:10.1007/BF01913897
- Varga, J., Mudra, I., & Ehrenstein, G. W. (1999). Crystallization and Melting of  $\beta$ -Nucleated Isotactic Polypropylene. *Journal of Thermal Analysis and Calorimetry*, 56(3), 1047–1057.
- Varga, József. (2002).  $\beta$ -Modification of Isotactic Polypropylene: Preparation, Structure, Processing, Properties, and Application. *Journal of Macromolecular Science, Part B*, 41(4), 1121–1171. doi:10.1081/MB-120013089

- Varga, József, Mudra, I., & Ehrenstein, G. W. (1999). Highly active thermally stable  $\beta$ -nucleating agents for isotactic polypropylene. *Journal of Applied Polymer Science*, 74(10), 2357–2368.
- Varga, József, Tóth, F., & Hummel, D. O. (1986). Annealing of the  $\beta$ -modification of polypropylene. *Makromolekulare Chemie. Macromolecular Symposia*, 5(1), 213–223. doi:10.1002/masy.19860050120
- Venugopal, G., Moore, J., Howard, J., & Pandalwar, S. (1999). Characterization of microporous separators for lithium-ion batteries. *Journal of Power Sources*, 77, 34–41.
- Wang, H., Keum, J. K., Hiltner, A., Baer, E., Freeman, B. D., Rozanski, A., & Galeski, A. (2009). Confined Crystallization of Polyethylene Oxide in Nanolayer Assemblies. *Science*, 323(6 February 2009), 757–760. doi:10.1126/science.1164601
- Washburn, E. W. (1921). The Dynamics of Capillary Flow. *Physical Review*, 17(3), 273–283. doi:10.1103/PhysRev.17.273
- Wijmans, J. G., & Baker, R. W. (1995). The solution-diffusion model: a review. *Journal of Membrane Science*, 107, 1–21.
- Xu, M., Hu, S., Guan, J., Sun, X., Wu, W., Zhu, W., Zhang, X., et al. (1992). Polypropylene microporous film. *US5134174*.
- Yam, K. L., & Lee, D. S. (1995). Design of modified atmosphere packaging for fresh produce. In M. L. Rooney (Ed.), *Active Food Packaging* (pp. 55–73). Blackie Academic & Professional.
- Yamamoto, Y., Inoue, Y., Onai, T., Doshu, C., Takahashi, H., & Uehara, H. (2007). Deconvolution Analyses of Differential Scanning Calorimetry Profiles of  $\beta$ -Crystallized Polypropylenes with Synchronized X-ray Measurements. *Macromolecules*, 40(8), 2745–2750. doi:10.1021/ma062784s
- Yoshino, M., Ito, K., Kita, H., & Okamoto, K. (2000). Effects of hard-segment polymers on CO<sub>2</sub>/N<sub>2</sub> gas-separation properties of poly(ethylene oxide)-segmented copolymers. *Journal of Polymer Science Part B: Polymer Physics*, 38(13), 1707–1715. doi:10.1002/1099-0488(20000701)38:13<1707::AID-POLB40>3.0.CO;2-W
- Zhou, G., He, Z., Yu, J., & Han, Z. (1986). Characterization of the  $\beta$ -form and study of the  $\beta$ - $\alpha$  transition during heating by wide angle X-ray diffraction. *Die Makromolekulare Chemie*, 187(3), 633–642.

Zhu, W., Zhang, X., Zhao, C., Wu, W., Hou, J., & Xu, M. (1996). A Novel Polypropylene Microporous Film. *Polymers for Advanced Technologies*, 7(9), 743–748. doi:10.1002/(SICI)1099-1581(199609)7:9<743::AID-PAT548>3.0.CO;2-W

## **Vita**

Grant Thomas Offord arrived in Texas in August of 1983, the first of two sons born to Spencer and Suzan Offord. During a brief hiatus from Texas, he graduated from Oklahoma State University with a Bachelor of Science degree in Chemical Engineering. Grant then began his graduate studies at the University of Texas at Austin under the supervision of Professors Don Paul and Benny Freeman, where he held Texas Longhorns football season tickets for five consecutive years. After taking a Master of Science degree in Chemical Engineering, Grant completed his dissertation and mounted a successful defense. In May of 2013, the degree of Doctor of Philosophy in Chemical Engineering was conferred upon him. Dr. Offord has accepted an offer of employment with Eastman Chemical Company in Longview, Texas.

Permanent e-mail: [gtofford@utexas.edu](mailto:gtofford@utexas.edu)

This dissertation was typed by the author.